Inverted Brayton Cycles for Exhaust Gas Energy Recovery

Chen, Zhihang

Award date:
2019

Inverted Brayton Cycles for Exhaust Gas Energy Recovery

Zhihang Chen

A thesis submitted for the degree of Doctor of Philosophy

University of Bath

Department of Mechanical Engineering

April 2019

I declare that the work in this thesis is my own and relevant citations are included to acknowledge the work of others.

Zhihang Chen

Abstract

The exhaust gas from an internal combustion engine contains approximately 30% of the thermal energy of combustion. Waste heat recovery (WHR) systems aim to reclaim a proportion of this energy in a bottoming thermodynamic cycle to raise the overall system thermal efficiency. One of promising heat recovery approaches is to employ an inverted Brayton cycle (IBC) immediately downstream of the primary cycle. However, it is a little-studied approach as a potential exhaust-gas heat-recovery system, especially when applied to small automotive power-plants. Thus, this thesis presents comprehensive study of IBC as wasted heat recovery (WHR) system for a 2-litre turbocharged gasoline internal combustion (IC) engine.

The basic IBC system consists of a radial turbine, a heat exchanger, and a centrifugal compressor in sequence. The use of the radial turbine is to further expand the exhaust gases from the turbocharged engine down to subatmospheric, so that the high turbine expansion ratio can be achieved. At the given turbine efficiency, the high turbine expansion ratio leads to the high specific power that generates by the turbine. Then, the residual heat in the expanded exhaust gas is rejected by the downstream heat exchanger in order to reduce the temperature of the exhaust gases. By doing so, the lower exhaust gas temperature leads to the higher gas density, thereby decreasing the compressor power consumption for the given compression ratio. The use of the centrifugal compressor is to pressurize the cooled gas back up to ambient. The IBC net power is the power differential between the turbine power generation and compressor power consumption.

The main advantage of the IBC system is that the exhaust gases can be expanded below atmospheric pressure in the IBC turbine, thereby increasing the potential to recover thermal energy from the exhaust gases. The heat exchanger implemented between the turbine and compressor aims to lower the temperature

of the exhaust gases prior to the compression process. Since the role of this heat exchanger is to reject as much heat as possible, a liquid coolant loop with inexpensive materials offers a relatively light-weight, cost-effective solution. In addition, although the IBC system is installed immediately downstream of the top cycle and utilizes the exhaust gases as the operating fluid, it is still possible to leave the top cycle unaffected by adjusting its working pressure, that is, there is no back pressure caused by the employment of the IBC system. Finally, the characteristics of the IBC system is the simple configuration and relatively light weight. The key components – centrifugal compressor and radial turbine are quite mature technologies which has been widely used as turbochargers for automotive applications.

The core of this thesis contains four main divisions. First, the IBC thermodynamic model was created by using finite-time thermodynamics (FTT) to perform the parametric study. The simulation results show that the increase of IBC inlet temperature, pressure, and turbomachinery efficiencies are beneficial to the IBC systemic performance at the given IBC expansion ratio. Moreover, there exists an optimum IBC expansion ratio that delivers the maximum specific power. Thus, the IBC system should be optimised according to the design conditions.

In the second section, the correlated gasoline engine model was coupled with the high-fidelity IBC 1D model, in order to demonstrate the IBC heat-recovery capability as a bottoming WHR system for a commercial engine. The moderate improvement in the systematic performance was expected at engine high-load and high-speed conditions, due to the employment of an IBC system. Later, engine mini-map points for the Worldwide Harmonised Light Vehicle Test Procedure (WLTP) driving cycle were selected as the design conditions for the IBC prototype, as such mini-map points can fully represented the engine operating conditions during real-world driving. IBC 1D simulations were conducted to give the guidance of the turbomachinery selection. However, due to the limited access to the commercial turbomachinery, the selected compressor and turbine suffer the suboptimal performance at the design point.

Thus, the third section presented the performance optimisation of the selected compressor and turbine. The 3D modelling method was employed to evaluate the performance of all compressor and turbine design candidates. Due to the limited time, the compressor and turbine blades were trimmed to achieve the optimal performance. It is a common practice in the turbomachinery industry to optimise the existing design at the new design points. The optimal trimmed compressor and turbine, delivering the T-S efficiency of 72.32% and 77.38% respectively, were manufactured and employed in the IBC prototype. In parallel to the experiments of the IBC prototype, the compressor in-house design and optimisation procedure was created in order to achieve a high-performance compressor at the design points. By integrating Generic Algorithm (GA) optimisation method with the compressor design process, the final compressor design was able to reach at the T-S efficiency of 77.67%, which is 5.35 percentage points higher than that of the trimmed commercial compressor.

The experiments of the IBC prototype were conducted in the gas stand in University of Bath. This is the first experimental demonstration of the IBC application for the automotive use. The test results show that the IBC prototype is able to generate the net power when the selected IC engine works at motorway cruise conditions. The parametric study of the IBC prototype was also conducted in tests. Finally, an IBC 1D model was correlated to the test data, and then utilized to predict the corresponding power generation over all engine mini-map points. Besides, the correlated IBC model can be utilized for the further development of the IBC system.

Acknowledgement

First, I would like to express my great gratitude to Dr. Colin Copeland for his continuous support throughout my PhD. Without his guidance and persistent help this dissertation would not have been possible. Additionally, his patience, encouragement, and vision let me successfully transfer from a manufacturing engineer to a vehicle engineer.

I also would like to express my sincere thanks to all the colleagues at PVRC for their emotional and technical support throughout my research, Dr. Dian Liu, Dr. Huayin Tang, Dr. Ian Kennedy, Dr. Lupeng Fei, Dr. Liu Dai, Dr. Pin Lu, Dr. Pavlos Dimitriou, Dr. Qiyou Deng, Dr. Tomasz Duda, Dr. Zhangqing Ning, Stefan Tüchler, and Linzhen Tan. I really enjoyed in working with all of you.

Very special and sincere thanks to my girlfriend, Danni He, for her support during the writing-up phase in my research. It was a tough time, but she made it wonderful.

Last but not the least, I would like to thank my parents, Jun Chen and Yangwan Gui, for their unflagging support and encouragement. 谢谢爸爸和妈妈的鼓励和支持，我爱你们！

Nomenclature

A	area
ρ	density
$\dot{m}$	mass flow rate
α_1	discharge flow angle
$\dot{W}$	power extracted from the working fluid
U	turbine blade tip speed
W	gas velocity relative to the rotor blades
C	absolute gas velocity
C_p	specific isobaric heat capacity
R_g	gas constant of the working fluid
C_v	specific isochoric heat capacity
k	ratio of the specific heats
p	pressure
T	temperature
T_0	average temperature
r	pressure ratio
h	enthalpy
C_r	ratio of heat capacity rates
W	specific work
$\dot{Q}$	heat rate
B	the constant related to heat-transfer
V	volume

v	the velocity of the piston
P	power
f	friction force
v	the velocity of the piston
L	piston stroke length
N	engine speed
x_1	piston position at maximum volume
x_2	piston position at minimum volume
ε_2	pressure drop ratio at state 2
ε_4	pressure drop ratio at state 4
n	number of compression stages
m	flow mass
C_f	skin friction coefficient
Dp	length of mass element in flow direction
D	equivalent diameter
$Cpresure$	pressure loss coefficient
A_s	heat transfer surface area
H	heat transfer coefficient
T_{fluid}	equivalent diameter
T_{wall}	pressure loss coefficient
RPM	turbocharger speed
y^+	dimensionless wall distance
y	distance to the nearest wall
u_τ	turbulent eddy viscosity
w	work

PR	pressure ratio

Greek Symbols

θ	azimuth angle
η	efficiency
γ	compression ratio of the engine
μ	friction loss coefficient

Subscripts

i	turbine rotor inducer
e	turbine rotor exducer
air	mass flow rate of the intake air
a	actual processes
am	ambient condition
c	compression process inside the cylinder
$cool$	coolant used in the inverted Brayton cycle
e	expansion process inside the cylinder
ex	heat exchanger
final	final exhaust outlet
hl	bypass heat leakage
ic	compressor in the inverted Brayton cycle
ict	whole compression processes in the inverted Brayton cycle
IBC	inverted Brayton cycle
it	turbine in the inverted Brayton cycle
in	input

loss	heat loss through the cylinder wall
low	subatmospheric pressure
max	Maximum value
mean	Mean velocity of the piston
net	net value
opt	optimum value
out	output
O	Otto cycle
t	turbocharger
tc	turbocharger compressor
tt	turbocharger turbine
s	ideal processes
μ	friction loss

Abbreviations

IC	internal combustion
IBC	inverted Brayton cycle
GDI	gasoline direct injection
WHR	waste heat recovery
A/R	area to radius
FGT	fixed geometry turbine
VGT	variable geometry
ATEG	automotive thermoelectric generator
TEGs	thermoelectric generators
ICE	internal combustion engine
QW	quantum-well

SUV	sports utility vehicle
RC	Rankine cycle
ORC	organic Rankine cycle
ETEIR	engine thermal efficiency increasing ratio
PBC	pressurized Brayton cycle
CVT	continuously variable transmission
APT	atmospheric pressure turbine
PES	primary energy saving
EGR	exhaust gas recirculation system
HAT	humid air turbine
CAD	computer-aided design
GA	genetic algorithms
ANN	artificial neural network
CFD	computational fluid dynamics
OF	objective function
T-T	total-to-total
DOE	design of experiments
FTT	finite-time thermodynamics
WLTP	worldwide harmonized light vehicles test procedures
NTU	number of transfer units
T-S	total-to-static
BMEP	brake mean effective pressure
BSFC	brake-specific fuel consumption
PMEP	pumping mean effective pressure
SST	shear stress transport
RMS	residual mean square

Table of Contents

List of Figures

List of Tables

Chapter 1 – Introduction

1.1 Background and Motivation

The development of sustainable energy technologies is a key part of the global scientific agenda and is one of the most difficult challenges facing engineers today. Observing that internal combustion engines are the most widely used source of primary power for machinery critical to the transportation, construction and agricultural sectors, one of the greatest areas for impact is the improvement in engine technology due to its extraordinary growth, especially in rapidly industrializing nations. Notably in transportation applications，the amount of CO_2 gas released from engine takes up 25% of global CO_2 emissions [1]. In addition, the global demand of vehicles increases steadily and dramatically. Figure 1.1 shows the number of passenger and commercial vehicles sold worldwide from 1990 to 2017, and a forecast for 2018 [2]. The number of the total vehicle production significantly increased in 2015, then kept at a stable and sustainable pace from 2015 to 2017. In 2018, it is expected to reach at around 81 million. Despite developments in fuel cell and electric vehicle technology, it is now widely recognized that a large fraction of future vehicles will still rely on the internal combustion (IC) engine. Therefore, the use of IC engine in transportation is a major issue with the respect to concerns about energy conservation and environmental sustainability. Given the concerns above, the development of systems for energy recovery, electrification and storage are becoming the hot

research topics to improve the overall heat-work conversion efficiency and, therefore, reduce IC engine fuel consumption.

In this thesis, a promising energy recovery system – inverted Brayton cycle (IBC) device will be comprehensively discussed using 0D, 1D, 3D simulations, and experimental tests. The IBC system is an exhaust-gas heat-recovery system which harvests thermal energy from the high-temperature exhaust gas expelled from IC engines, thereby increasing the overall thermal efficiency and, therefore, reducing emissions and carbon dioxide. It should be noted that it is also able to recover pressure energy from the exhaust gas, namely, that resulting from 'blowdown' at the end of the power stoke. The basic IBC device consists of a radial turbine, a heat exchanger, and a centrifugal compressor in sequence, referred as a single-stage IBC system due to the employment of single cooling and compression process.

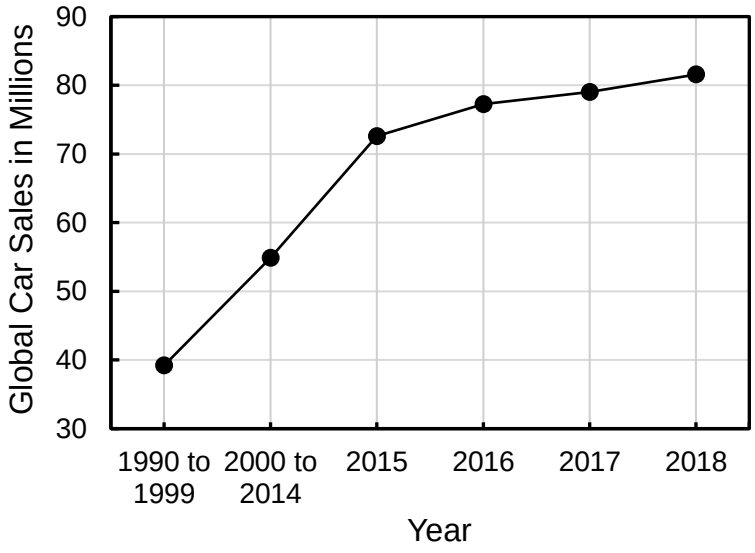

Figure 1.1 Number of vehicles sold worldwide from 1990 to 2018

1.2 IC Engine Energy Flow

To achieve the thermal efficiency improvement, the energy balance and exergy balance in IC engine should be analysed, which allows engineers focus on addressing the most significant parasitic losses of the fuel energy. Extensive

studies on the energy flow reveal that waste heat produced during the thermal combustion process could be as high as 30-40% which is rejected to the environment through an exhaust pipe in the form of heat, while only 12-30% of the available energy in a fuel can be converted to the mechanical work or brake work [3-5]. One reason for this is that maximum compression ratio of IC engines is limited by several factors, such as engine knocking, even though the high compression ratio is desired due to the resulting efficient combustion and subsequent expansion stroke. Thus, the combusted gases released by the combustion chamber, referred as the exhaust gas, still contains various forms of energy due to an insufficient expansion stroke. Especially under part load, the energy contained by the exhaust gas is up to around 36% of the fuel energy. However, the exhaust gas energy is considered by some to be low-grade energy due to its high temperature but low pressure [6].

Liu et al. [7] presented an energy flow analysis in a turbocharged, gasoline direct-injection (GDI) engine. As shown in Figure 1.2 (a), energy utilization efficiency of a modern gasoline engine is still low. The fuel energy can be divided into several parts – effective work, exhaust gas energy, coolant energy and other loss (unburned fuel energy and engine surface heat transfer). Under part load, the percentage of effective work changes from 27.8% to 33.5%, while that of exhaust gas energy varies between 23.7% and 35.8%. In most cases, exhaust gas energy almost equals effective work in quantity. However, the exhaust gas energy cannot be fully reused since it is a kind of low-grade energy. Therefore, engine exergy balance analysis was carried out, shown in Figure 1.2 (b). It can be observed that the percentage of exhaust gas exergy is always lower than that of effective exergy, but it is larger than the percentage of heat transfer exergy under most of conditions. Under part load, the percentage of exhaust gas exergy changes from 9.4% to 16.8%, and it demonstrates a great potential for engine fuel economy improvement by the exhaust gas energy recovery.

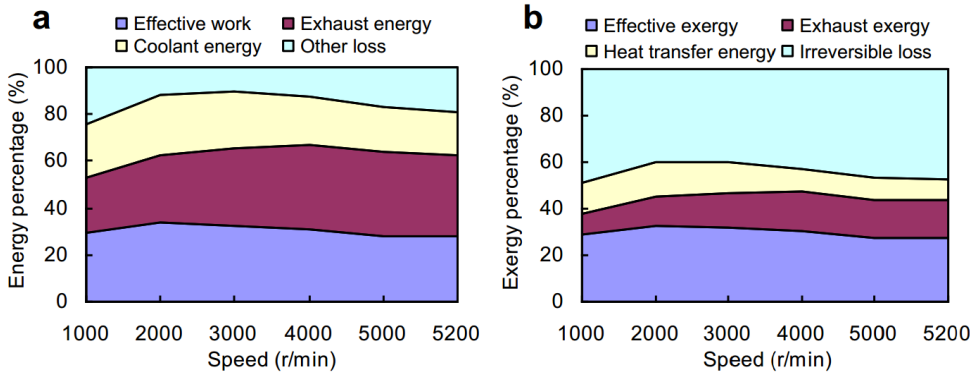

Figure 1.2 Energy and exergy distribution of a turbocharged, direct injection gasoline. (a) Energy distribution of GDI engine. (b) Exergy distribution of GDI engine. [7]

Ozkan et al. [8] analysed the energy balance and exergy balance of a Ford 1.8 L, four-cylinder, four-stroke, direct-injection compression ignition diesel engine. The test has been performed at the engine speed of 2000 rpm and the engine load of 50%. According to the energy distribution shown in Figure 1.3, the percentage of energy contained by the exhaust gas is 32%, which is only slightly lower than that utilized by the drivetrain. Furthermore, the exergy distribution of the considered diesel engine, shown in Figure 1.4, reveals that 7.94% exhaust gas exergy is expected.

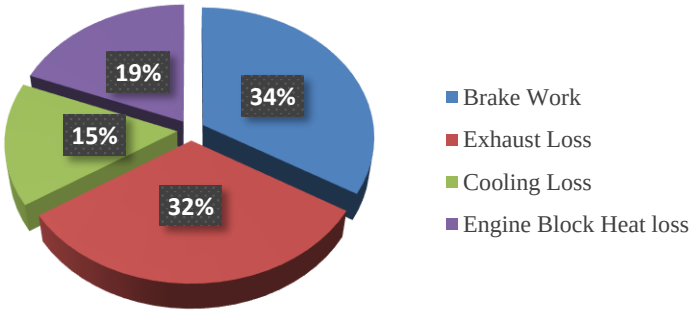

Figure 1.3 Energy distribution of a Ford diesel engine

In order to quantify exhaust energy available for the heat recovery system, exhaust gas from a typical light duty 4 cylinder spark ignition engine has been analysed by Chammas and Clodic [9]. The results show that the corresponding available exhaust gas energy ranges from 4.6 to 120 kW depending on the engine

operating conditions. However, given the conversion efficiency and the parasitic losses of the exhaust-gas heat-recovery systems, the maximum recoverable work is from 1.7 to 45 kW when the regeneration system operates between the average temperature of the exhaust gases and the outdoor temperature.

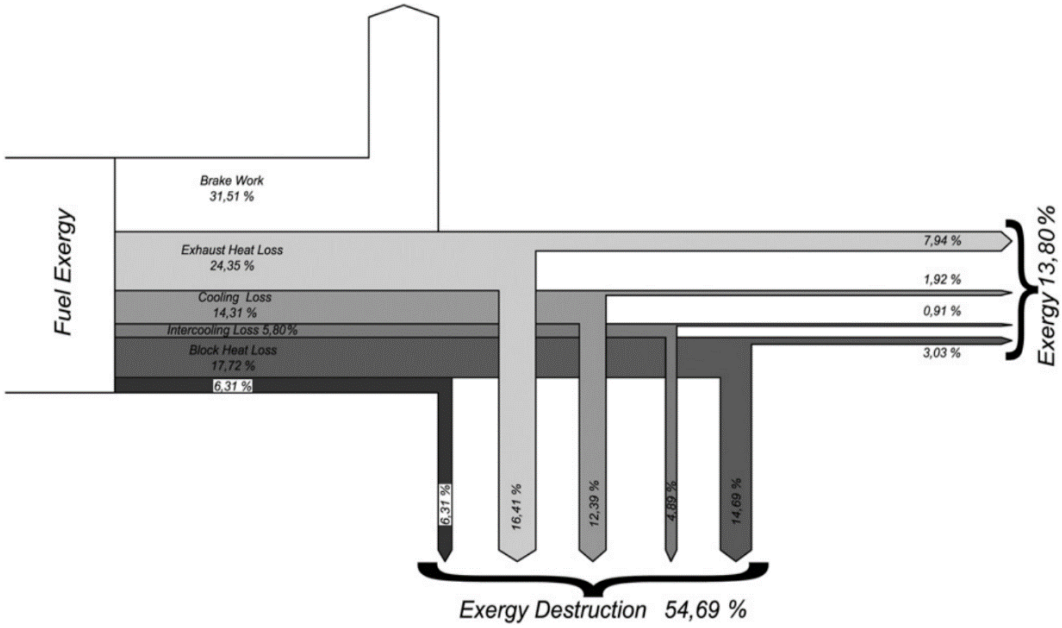

Figure 1.4 Exergy distribution of a Ford diesel engine [8]

These observations in terms of the energy quantity and quality of the gasoline and diesel engines exhaust gas have given rise to a recent trend for wasted heat recovery, as they point to the significant amount of energy in exhaust gas could be recovered that is otherwise simply wasted by discharging exhaust gas to the ambient.

1.3 Exhaust Gas Energy

As a major part of the loss from an internal combustion engine, the exhaust gas contains various forms of energy, and the main characteristic of the exhaust gas energy is unsteady caused by the working cycle and engine various operating conditions. Generally, the exhaust-gas flow energy can be classified into terms of kinetic energy, pressure energy, and thermal energy [7]. The kinetic energy can be neglected since it only accounts for small proportion of the total exhaust

gas energy, or more precisely, is lower than 0.6% at most engine operating conditions [6]. The remaining pressure energy in the exhaust gas is high-grade mechanical energy and can be directly recovered by an expansion process like that which occurs within a turbo-compounding turbine placed in the exhaust system. Theoretically, the recovery efficiency is limited by the component efficiency and the parasitic energy losses of an expansion device. After expansion, the remaining thermal energy could be considered as low-grade thermodynamic energy that can be recovered by some indirect or direct methods. In fact, the thermal energy occupies more than 90% of the exhaust energy under full load conditions and also represents the largest proportion under part load [6]. However, this thermal energy is impossible to completely convert into high-grade energy such as mechanical energy and electrical energy, and the corresponding recovery efficiency is limited by cycle and heat transfer efficiencies [10].

1.4 Waste Heat Recovery System

Although various vehicle-mounted thermal utilities adopted to recover energy from exhaust gas have been intensively investigated, the exhaust steam still contains high-grade heat content. The turbocharger is an example of this since it is widely employed to IC engines as an exhaust-gas energy-recovery device. The direct recovery method used by the turbocharger mainly aims to reclaim the pressure energy resulting from ‘blowdown’ at the end of the expansion. The blowdown event refers to the pressure pulse in the exhaust gas forming as the exhaust valve is opened. To be specific, due to the cylinder expansion ratio usually being insufficient to fully expand the gas to ambient pressure, the pressure in the cylinder is much higher than that in the exhaust manifold when the exhaust valve opens, especially before the piston reach top death centre. Therefore, once the exhaust valve is opened, any remaining combustion pressure in the cylinder is suddenly released producing a sudden pressure rise in the manifold [11]. The energy extracted by the turbine is used to compress the engine intake air, thereby allowing more fuel to be burnt and an increased engine power density. Thus, the employment of the turbocharger can offer a route to fuel

economy through downsizing. However, at many engine operation conditions, there is much more energy available to a turbine than that consumed by a compressor. The wastegate of the turbine, therefore, is introduced to divert a fraction of the exhaust gas, thereby reducing the power driving the turbine wheel to match the power required for a given boost level. By doing so, energy that could have been reclaimed is wasted. Thus, a significant amount of heat energy is available for a waste heat recovery (WHR) system conceived as bottoming cycle. Similar to the first stage of the exhaust-gas energy-recovery system, bottoming WHR cycles could further profitably exploit this discharged heat not only by direct recovery through exhaust gas expansion but also indirect recovery through heat transfer.

In this thesis, the aim is to introduce IBC system as a bottoming WHR cycle of a turbocharged engine, instead of replacing the turbocharger. This is because that the turbocharger is not only designed for reducing the engine fuel consumption in some engine operating envelope, but achieve significant power gains and, therefore, provide a route towards engine downsizing. The benefits of engine downsizing are friction reduction as well as reduced thermal loss. Moreover, any reduction in engine mass can, in turn, lead a reduction in chassis, drivetrain and suspension masses. Thus, given that the turbocharger is highly beneficial to engine performance, the IBC system is designed and mounted downstream of the turbocharger turbine, even though an IBC system is able to recover more wasted energy without the turbocharger due to the higher exhaust temperature.

1.5 Centrifugal Compressor

A centrifugal compressor is the key component in IBC system. It is a fluid-flow machine that deliver a pressure rise by adding the kinetic energy to the working fluid through the rotor or impeller and, then, slowing the fluid in the diffuser to increase its static pressure. A cutaway view and a sketch of a centrifugal compressor are presented in Figure 1.5 and 1.6, respectively. Centrifugal compressors have several advantages. For instance, they are less sensitive to

changes in the mass flowrate, have low manufacturing cost, generate a higher pressure ratio per stage, have wide range of rotational speed and are easy to assemble [12].

1.5.1 Compressor Inlet Casing

The function of the inlet casing is to deliver the fluid to the impeller with minimum loss and to provide a uniform velocity profile at the impeller inlet. Typically, the stationary inlet casing is a simple pipe. In some applications, an air filter and noise reducing baffles are provided at the inlet casing. In addition, an inlet guide vane is sometimes placed at the inlet to impart a defined pre-swirl motion in order to achieve a desired aerodynamic performance. The variable inlet guide vane is able to regulate both the flow rate and the power consumption [13].

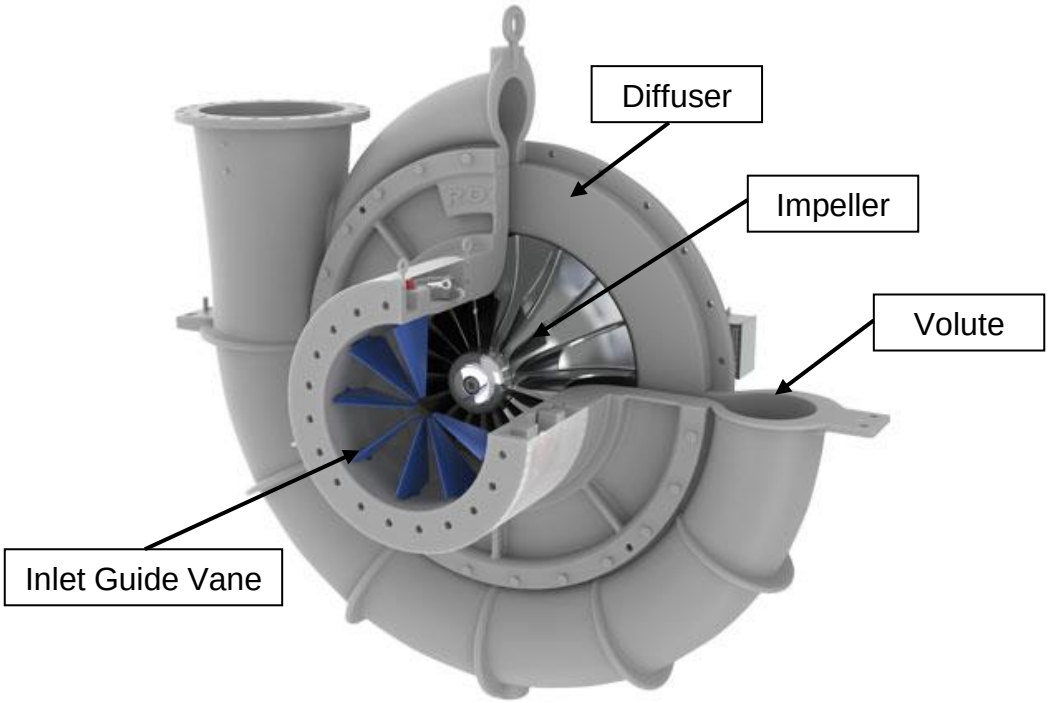

Figure 1.5 Cutaway view of a centrifugal compressor [14]

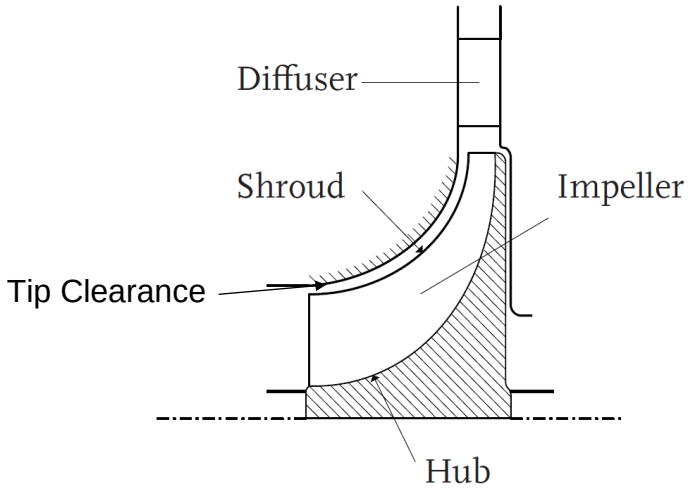

Figure 1.6 A sketch of a centrifugal compressor

1.5.2 Compressor Impeller

For the centrifugal compressor, the function of the impeller is to accelerate the working fluid through the impeller passages by the rotation of its aerodynamic surface that are highly curved and twisted, thereby gradually increasing the angular momentum of the fluid. By doing so, both the static pressure and the velocity are increased by the impeller.

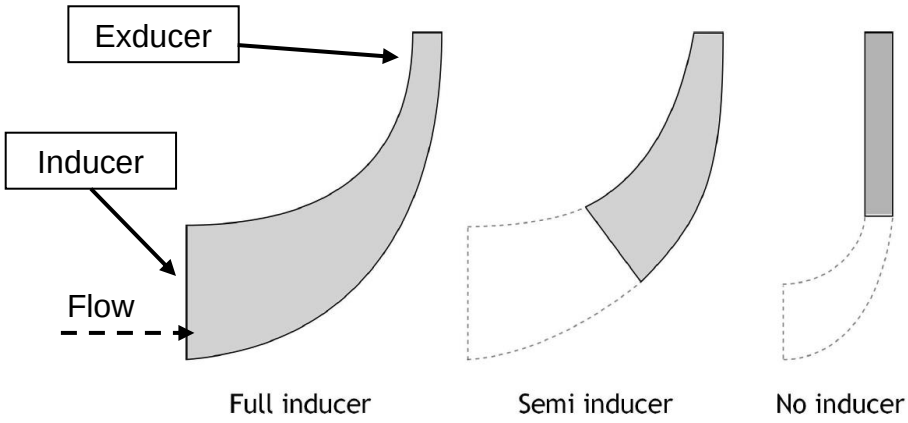

Figure 1.7 Different kind of impeller inducers. Blades are shaded gray, for the semi inducer and no inducer impeller the compressor inlet is shown dotted.

In Figure 1.7, the axial inlet of the impeller is referred as the inducer. In practice, the inducer may not being axial, or employ no inducer at all [12]. Example of three

different types of inducers is depicted in Figure 1.7. Aungier [15] claimed that the flow coefficient, representing the dimensionless mass flow into the compressor, was significantly impacted by the general shape of the impeller, especially the inducer. Generally, the impeller without the inducer, shown as the right one in Figure 1.7, has the smallest flow coefficient. In other words, it would provide the highest resistance to the working flow. In contrast, the impeller with the full inducer, shown to the left in Figure 1.7 has the largest flow coefficient. Although this type of impeller suffers the high manufacturing cost due to the complicated three-dimensional blade shape, the resulting highest efficiency among three kinds of impellers contributes to the wide use in automotive turbochargers. However, the efficiency of the full-inducer impeller is limited by its strong curvature needed to turn the inlet axial flow into radial. Naturally, the semi-inducer impeller would be expected to have flow coefficient and efficiency somewhere in between two to former examples. For a centrifugal compressor, the semi-inducer impeller blades sometimes are introduced and placed between two full-inducer impeller blades, in order to increase the operating range and efficiency at the off-design conditions [16]. The reason of this could be explained by follows. It is a common practice to increase the number of impellers, thereby providing more guidance to the flow towards the impeller exit and minimizing blockage at the compressor inducer. However, the parasitic aerodynamic friction loss that is increased with the blade number can lead to a deterioration in the compressor efficiency. In addition, the blade number should be limited by the manufacturing cost, impeller weight, hub stresses, and desired inertia. Since the transient operation of the engine is of great important in its everyday operating condition, the turbocharger should be designed with a low inertia, in order to responding quickly to the transient changes of the engine [17]. Given the above analysis of the impeller blades, the semi-inducer impellers could be introduced between two full length blades to provide extra guidance to the flow in the impeller passage with minor additional aerodynamic friction loss and weight, while still keeping the number of blades at the compressor inlet. The semi-inducer impeller blade is usually referred as the splitter.

Another critical region is the clearance gap between the tip of the rotating blades and the stationary shroud, shown in Figure 1.6. Unlike the large compressor

design, the conventional centrifugal compressor for automotive use is unshrouded, meaning that the shroud just outside the impeller is formed by the stationary housing. The main benefit of unshrouded impellers is that the mechanical stresses is much lower than that of the shrouded impeller, due to the less mass at the end of the blade tips. However, it has been proved that leakage flow over the blade tips is the most critical contributor to performance degradation [18]. Strong pressure gradients over the blade tips encourage leakage flows that distort the main flow pattern and, therefore, lead to a performance loss. Thus, the larger the tip clearance is, the lower the compressor efficiency and pressure capability. However, it is hard to keep the tip clearance small due to the thermal expansion and the component mechanical tolerance stacking requiring accurate alignment between the impeller and the diffuser, especially when a long rotating shaft is employed.

The compressor performance is also significantly affected by the outlet of the compressor impeller, referred as exducer shown in Figure 1.7. Since the diffuser downstream of the compressor exducer prefers a flow that is relatively uniform in tangential and axial direction, the impeller exducer should be designed properly to provide a good guidance for the exit flow. There are three types impeller exducer – radial, forward swept, and backward swept, illustrated in Figure 1.8 with outlet velocity triangles at exit. The radial impellers are widely employed due to their ease of manufacture [16]. In addition, the radial impeller only suffers from tensile stress under the rotating centrifugal force, while the forward and backward swept impeller need to consider the bending force. The backward swept impellers are widely utilized for automotive use, due to its wider operating range and broader efficiency characteristics. To be specific, at given shaft speed, the backward swept impeller reduces the Mach number in the diffuser and delivers a more favorable angle, thereby reducing the energy loss in the diffuser. However, Wang et al. [19] claimed that generally the lower pressure ratio is delivered by the backward impeller, compared to the radial impeller. This is because that increasing the back swept angle contributes to form the shock waves on splitter blade roots, which can cause a loss of total pressure.

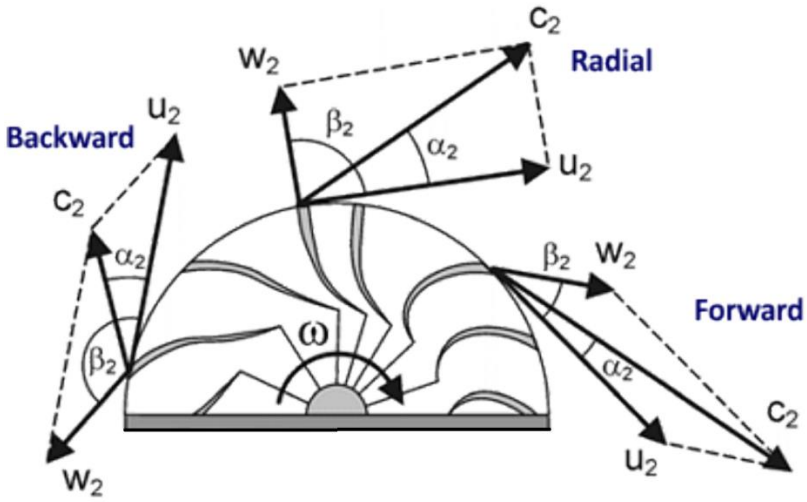

Figure 1.8 Three types impeller exducer – radial, forward swept, and backward swept

1.5.3 Compressor Diffuser

The diffuser is a stationary component that is fitted directly downstream of the impeller. The function of the diffuser is to deaccelerate or 'diffuse' high-velocity fluid leaving the impeller and, therefore, further convert the kinetic energy into static pressure. The basic diffuser comprises two parallel walls which form a radial channel, referred as vaneless diffuser shown in Figure 1.9. Although the vaneless diffuser appears to be a geometrically simple device, it is a critical for the compressor efficiency due to the resulting high loss in stagnation pressure. It is beset by three serious fluid mechanical problems. The primary problem is the tendency of the flow boundary layers to separate from the diffuser walls if the diffusion rate is too rapid resulting in flow mixing. On the contrary, if the diffusion rate is too small, the fluid is exposed to a longer fluid path in diffuser and, therefore, the fluid friction losses become excessive. Additionally, the approximately half of the fluid energy at the impeller exit is kinetic energy. Thus, high velocity of the fluid leads to large viscous drag on the walls, thereby reducing the pressure recovery. [20]

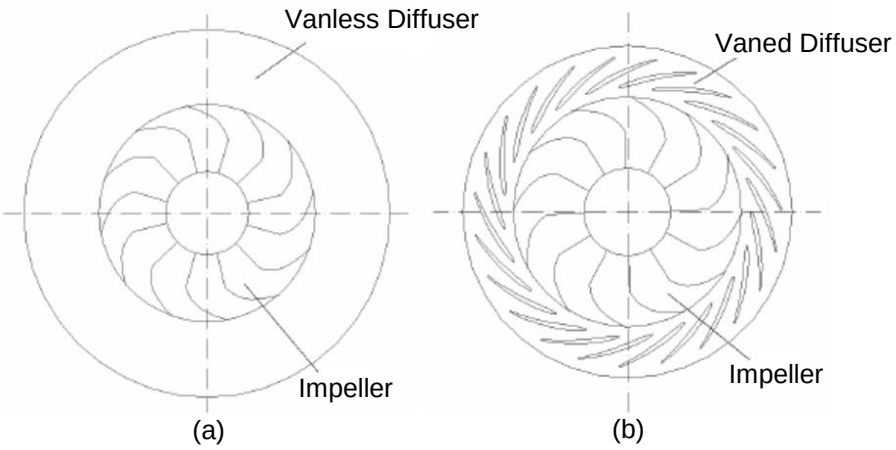

Figure 1.9 Vaneless (a) and vaned (b) diffusers

In contrast, the vaned diffuser utilizes vanes to guide the flow to achieve a desired flow field. Thus, at the design operating point the compressor with a vaned diffuser can deliver a better operating efficiency than that with vaneless diffuser. In addition, due to the higher diffusion rate of the vaned diffuser, a smaller diffuser diameter is required to deliver the target pressure recovery. Thus, the vaned diffuser is clearly advantageous where a small unit size is important [20]. However, at off-design operating points, the flow angle at the impeller exit is no longer aligned with the inlet angle of diffuser vanes. Thus, the incidence loss at the diffuser vane entry will increase as the air flow angle departs from the vane inlet angle, thereby deteriorating the compressor efficiency. As a result, the efficient operating range of the compressor with the vaned diffuser is limited.

1.6 Radial Turbine

Radial turbine is also the key component in IBC system. In a radial turbine, kinetic and thermal energy of the working medium is converted into shaft energy in passing from a large radius to a small radius. Figure 1.10 shows a radial turbine in the commercial Borg-warner turbocharger.

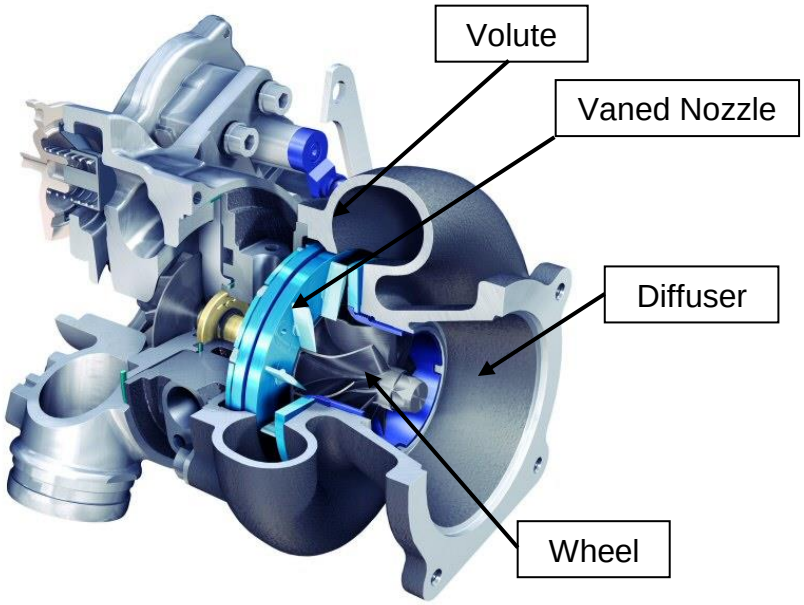

Figure 1.10 Cutaway view of a turbocharger radial turbine [21]

The working principle of the radial turbine is described as follows. The high-temperature or high-pressure working fluid enters the inlet of turbine volute and is guided to the vaned or vaneless nozzle where the flow is turned into a direction tangential to the rotor. Then, the downstream rotor turns it into the axial direction in a controlled manner, causing a change in tangential momentum and a force to be exerted on the rotor blades. The velocity of the fluid discharging from the rotor is considerable. Thus, in order to further recover the kinetic energy, an axial diffuser is incorporated at the radial turbine exit.

Radial turbines are extensively used in automotive turbocharger due to their several advantages. First, compared to the axial-flow turbine, the radial turbine is able to deliver better performance at lower flow rates when engine works in low load condition. Additionally, it can maintain good off-design performance. This is favorable characteristic to automotive engines which typically behave in a highly transient manner. Thus, the radial turbine is generally more beneficial to engine performance then the axial one. Moreover, the low manufacturing and maintaining cost, high level of robustness, and simple packaging requirements make the radial turbine more attractive for automobile applications. Given all

advantages presented above, a radial turbine is employed in IBC system to harvest energy by expanding the exhaust gas.

1.6.1 Turbine Volute

The primary function of the turbine volute is to feed the nozzle vanes or the rotor with uniform flow at the desired angle in order to optimise its overall performance. A spiral type of volute, shown in Figure 1.11, is typically used with radial inflow turbines. The working fluid enters the volute in a tangential direction, turned following the geometry of the volute to ideally distribute a uniform gas flow, and provide the required tangential momentum to the rotor by accelerating the flow. In addition to the flow distribution and acceleration, the volute should deliver the desired flow angle distribution at the volute exit to reduce the incidence losses caused by the mismatch between the flow angle and the inlet angle of the nozzle vanes or the rotor blades.

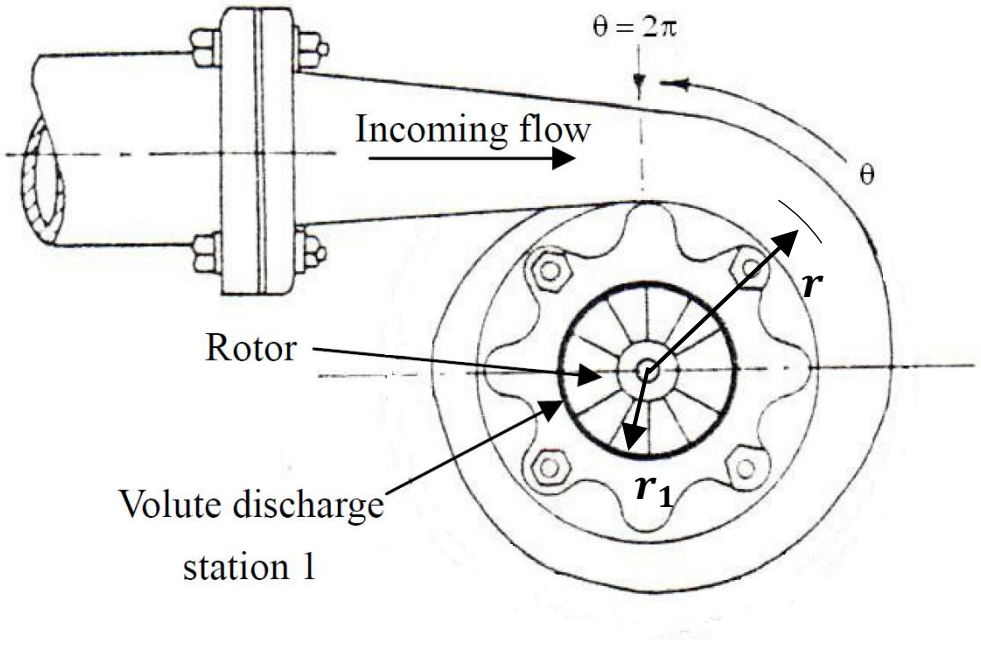

Figure 1.11 Spiral casing of a radial inflow turbine

The distribution of area to radius (A/R) ratio in circumferential direction is one of the key parameters to define the volute geometry. The parameter A/R is the ratio of volute cross-sectional area and its centroid distance to rotational center. The

distribution of A/R directly influences the flow angle distribution at the rotor inlet and, therefore, has a significant impact on the turbine performance. The parameter A/R can be deduced using incompressible theory with the consumption of uniform pressure distribution.

See Figure 1.11, for incompressible flow, the mass flow rate going through a cross section at any azimuth angle θ is

$$\dot{m}_\theta = A_\theta \rho_\theta V_{\theta r} \tag{1.1}$$

where A_θ and ρ_θ are the area and gas density at any azimuth angle θ, respectively. $V_{\theta r}$ is the corresponding radial component of the gas velocity.

For uniform mass flow distribution, the mass flow rate at given azimuth angle θ also is

$$\dot{m}_\theta = \dot{m}_1 \times \frac{\theta}{2\pi} \tag{1.2}$$

where $\dot{m}_1$ is the mass flow rate at volute discharge station 1.

Apply the free-vortex assumption, the tangential velocity at the centroid of this section is obtained once the radius of the centroid is known

$$V_{\theta t} = V_{1t} \times \frac{r_1}{r} \tag{1.3}$$

Therefore, combine equation (1), (2), and (3), the expression of the parameter A/R is obtained with the consumption of constant gas density

$$\begin{aligned} \left(\frac{A_\theta}{A_1}\right)\left(\frac{\rho_\theta}{\rho_1}\right)\left(\frac{r_1}{r_\theta}\right) &= \frac{\theta}{2\pi}\tan^{-1}\alpha_1 \\ \frac{A_\theta}{r_\theta} &= \frac{A_1}{r_1} \times \frac{\theta}{2\pi} \times \tan^{-1}\alpha_1 \end{aligned} \tag{1.4}$$

where α_1 is the discharge flow angle defined as $\alpha_1 = \tan^{-1}(V_{1\theta}/V_{1t})$.

Note that the desired α_1 is determined by the desired inlet angle of the rotor, and A_1/r_1 is a constant value once the size of the rotor is fixed. Hence, the parameter A/R is the linear function of the angle θ. This simple expression is widely used in design practice due to the difficulty in obtaining the density variation inside the volute.

On the same note, the volute cross-sectional shape is a key geometry which links the area and radius in the A/R. The optimal turbine performance can be achieved by optimizing volute cross sectional shape. However, the volute cross-sectional shape can sometimes be compromised for the engine level packaging.

1.6.2 Turbine Nozzle

As discussed in previous section, the volute provides most of the swirl required for correct incidence into the rotor if there is no vane existed in the nozzle. Thus, the vaneless nozzle can be used to simply stabilize the flow entering the turbine rotor. The resulting benefit is the low manufacture cost and high reliability since there is no complex geometry component exiting between two parallel walls of the nozzle.

However, due to the benefits of vaned nozzle, it is becoming favorable in automotive turbocharger industry. Given the simplicity and reliability of the nozzle vans, it is common to use uncambered aerofoils with quite robust trailing edges which could distribute and accelerate the flow equally around the turbine rotor inlet with an optimum angle. The example of uncambered aerofoil nozzles is shown in Figure 1.12. Waston and Janota [22] claimed that the large number of the nozzle vanes can provide better flow guidance at the penalty of increased frictional losses and flow blockage. It should be noted that the issue of the flow blockage is critical for the internal combustion engine application. This is because blockage resulting from a choked flow can limit the flow capability and reduce the efficiency due to the induced shock wave, thereby lowering the engine performance. Thus, the nozzle opening will be sized to pass the range of engine mass flows without choking occurring in the throat of the passage at high pressure ratio [23].

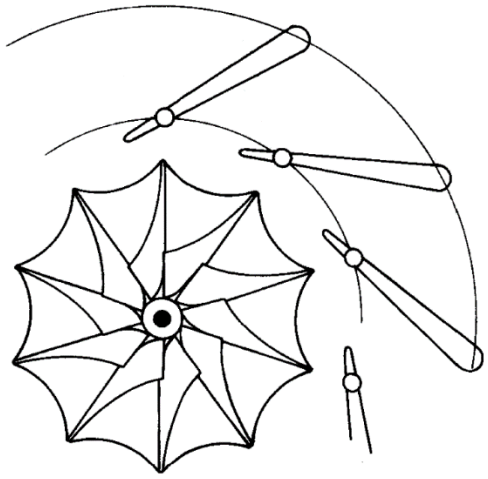

Figure 1.12 Uncambered aerofoil nozzles

Turbine nozzle vans could be stationary and is often referred as a fixed geometry turbine (FGT). The corresponding limitation is poor performance at off-design condition. A FGT is optimised for a specific engine condition. Given the wide operating envelop of the internal combustion engine, the turbine efficiency is limited at the majority of working condition. However, the existence of wastegate can avoid the efficiency drop at high mass flow by diverting excess exhaust gases away from the turbine. A wastegate is a simple valve that controls the flow of exhaust gas through the turbine and, therefore, control the boost pressure. It should be noted that the throttling loss is induced when the wastegate valve is open.

Considering the advantages and disadvantages of FGT discussed herein, variable geometry turbine (VGT) is proposed and designed to increase boost pressure at low speeds, reduce response times, and decrease the boost at high engine speeds to prevent over-boosting. The variable geometry can be achieved by altering cross sectional area at turbine nozzle, referred as pivoting vane turbine. It has a ring of vanes mounted on pins that allow them to rotate axially. By doing so, the angle of the vanes is able to change in order to a position that provides the desired cross section between vanes, demonstrated in Figure 1.13. Vanes are closed when the engine mass flow is low in order to accelerate the airflow entering the rotor. With increasing the exhaust mass flow rate, the vane

open to prevent choke. Thus, the overall efficiency of a VGT is greater than that of a FGT due to the larger operating range.

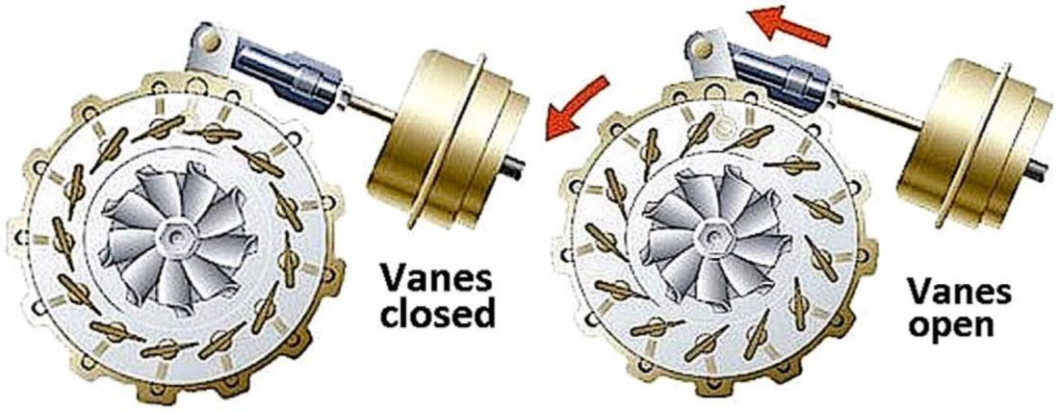

Figure 1.13 Pivoting vane turbine in fully closed (left) and fully open (right) positions [24]

Despite the outstanding advantages of VGT, the peak efficiency of a VGT is often lower than a FGT equivalent, partially due to the leakage in the turbine casing and around the mountings of moving components. In addition, since the exhaust temperature is quite high 850 °C for diesel engines and 1000 °C for petrol engines, the thermal expansion of each component in VGT increase the metal-to-metal friction, which can cause the pivoting mechanism to stick. This will significantly reduce performance. [24]

1.6.3 Turbine Wheel

Similar to compressor rotor, the turbine rotor is composed of a solid hub with blades, shown in Figure 1.14. The main function of the turbine rotor is to extract energy from the working fluid and hence there is drop in enthalpy, pressure and absolute velocity. The discharged working fluid from the vaned nozzle goes into the radial portion of the rotor at the inlet, referred as inducer, then exist at the axial portion at the outlet, called as exducer.

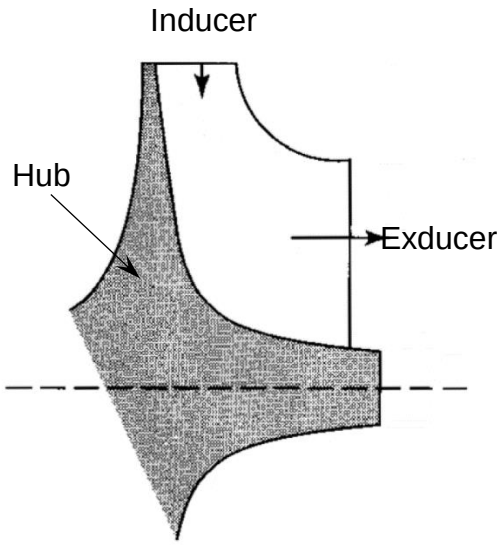

Figure 1.14 A sketch of a radial turbine rotor

By analyzing the velocity triangles at turbine rotor inducer and exducer, the following energy transfer equation in the rotor can be derived,

$$\dot{W} = \frac{1}{2}\dot{m}[(U_i^2 - U_e^2) - (W_i^2 - W_e^2) + (C_i^2 - C_e^2)] \tag{1.5}$$

where $\dot{W}$ is the power extracted from the working fluid. $\dot{m}$ is the mass flow rate. U is the blade tip speed. W is the gas velocity relative to the rotor blades. C is the absolute gas velocity. The subscript 'i' denotes the rotor inducer, while 'e' denotes the rotor exducer.

Eq. 1.5 gives an indication of how the turbine rotor should be designed to maximize the energy transfer. The first term shows that the larger change in radius from the inlet to outlet is desirable with respect to the shaft power. The second term shows that the relative velocity at exducer must exceed that at inducer for positive work, that is, the flow must accelerate through the rotor passage in the relative frame of the reference. The last term illustrates that the absolute exit gas velocity must be minimized since this is a direct loss of the potential work. Thus, the exit swirl should be reduced, ideally to zero.

The incident angle is defined as the difference between rotor inlet flow angle and blade angle at the rotor leading edge. According to Japikse and Baines [25], the optimum incidence for radial turbine is in the region of - 20° and - 40°. At the optimum incidence range, the rotor is typically tolerant to changes of only up to 10° without a significant drop in efficiency. However, the nature of the reciprocation engine is the wide operating conditions, that is, the wide range of exhaust mass flow rates. Thus, the focus of turbine design for the automotive application should shift to off-design operation condition. Thus, the mixed flow turbine has been extensively studied to improve the efficiency over a wide range of the mass flow rate. The main difference between radial turbine and mixed flow turbine is shown in Figure 1.15. It could be clearly seen that the blade inlet angle at inducer is zero for the radial turbine rotor, while none-zero inlet blade angle results from a mixed flow turbine rotor.

It is common knowledge that the optimal efficiency of the radial turbine could be achieved at the relatively high velocity ratio of around 0.7, whereas the peak efficiency for mixed flow turbines is at lower velocity ratios [26], which refers to the operating condition of high exhaust gas velocity and low turbine rotational speed. The velocity ratio is one of the key design parameters of turbines and defined as the ratio of the rotor tip velocity in relation to the isentropic spouting velocity which could be achieved if the available total-to-static enthalpy drop would be converted into kinetic energy by an isentropic process. The lower velocity ratio achieved by mixed flow turbines is also desirable for automotive application. This can be explained by follows. When exhaust energy is the greatest, the high pressure ratio and the associated low velocity ratio will mean that the turbine is operating near to its maximum shaft power. Thus, it is advantageous to reach the peak efficiency at the low velocity ratio, which the mixed flow turbine is designed for.

As discussed with regard to the turbine energy transfer, the energy associated with the exit swirl velocity represents energy loss and efficiency reduction. To be specific, in a radial turbine, rotor losses could be reduced if there is an accelerating flow along the turbine rotor passage, so that the relative velocity at exducer should be high. In contrast, the absolute velocity at outlet should be low.

Thus, the exducer annulus area should be relatively large to reduce the exit dynamic head to a minimum. However, the ratio of the diameter of exducer tip to that of the exducer hub should be limited to avoid overstressing the blade, especially the blade surface at the exducer tip.

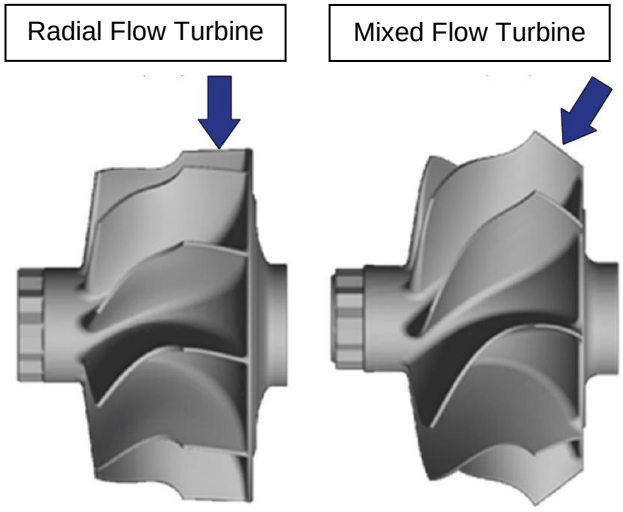

Figure 1.15 Radial versus mixed flow turbines [26]

1.7 Aim and Objectives

The principle aim of this research is to fully study the heat recovery capability of IBC system as the bottom WHR cycle of an automotive IC engine, by numerical simulations and experimental tests. Thus, the main objectives are defined as follows:

1. To review the literature in the field of exhaust-gas heat-recovery cycles, especially IBC system, and justify the contribution of investigating IBC system.

2. To perform the parametric study of IBC system by numerical simulations to enhance the understanding of IBC performance at various operating boundary conditions.

3. To design, manufacture, and test the prototype of IBC system at a selected IC engine operating condition on the basis of the numerical analysis results.

4. To calibrate IBC system model against the test for the further use in IBC system development.

1.8 Thesis Outline

Chapter 1: Introduction

This chapter introduces the importance and necessity of the extensive studies on the exhaust-gas heat-recovery devices for the automotive applications. Then, two critical IBC components – centrifugal compressor and radial turbine are introduced and discussed.

Chapter 2: Literature Survey

In this chapter, the published literature is reviewed to demonstrate the current state-of-the-art WHR technologies. In particular, WHR technologies include automotive thermoelectric generators, Rankine cycle, pressurized Brayton cycle, turbo-compounding, and inverted Brayton cycle. Then, the published turbomachinery design optimisation methods will be summarized, as centrifugal compressor and radial turbine for the IBC system will be designed and optimised in this research.

Chapter 3: IBC Thermodynamic Modelling and Analysis

This chapter contains the detailed description of IBC working principle as well as the thermodynamic model. Then, the parametric study of IBC system will be performed to fully understand its heat recovery capability. Afterwards, a 2-litre gasoline engine will be selected as the primary upper cycle for IBC system, in order to investigate the benefits of IBC system over a real-world driving cycle.

Chapter 4: IBC 1D Modelling and Analysis

Higher fidelity engine and IBC system models will be developed and utilized to study the IBC system performance over various operating conditions. Since 1D models allows the employment of the compressor and turbine characteristic maps for the IBC system, the compressor/turbine size optimisation will be conducted at design conditions. Based on the optimisation results, a commercial compressor and turbine will be selected as the baseline turbomachinery designs for the IBC prototype.

Chapter 5: Compressor and Turbine Design

In this chapter, the further optimisation of the selected commercial compressor and turbine will be performed by 3D simulations with the blade trimming technology. The optimal turbomachinery will be manufactured for the IBC prototype. However, the blade trimming technology is only a simple method to optimise the existing turbomachinery geometry at the design condition. Thus, due to the limitation of the blade trimming technology, a compressor design and optimisation process will be developed to generate new compressor design which has better performance than the trimmed commercial compressor.

Chapter 6: Experimental Procedure and Results

The experimental facilities and test procedure used in this research will be presented. This chapter contains three sections. In the first section, the necessary changes and required setup for the existing gas stand cell will be described. The second section will show the test limitations and the test results analysis. Finally, the test data will be utilized to correlate the 1D IBC model.

Chapter 7: Summary

The final chapter will present the major finding of this thesis, and makes recommendations for the further research.

Chapter 2 – Literature Survey

2.1 Introduction

This chapter will present a comprehensive review of current WHR technologies available in public domain. According to the characteristic of IC engines exhaust gas, there are two categories of WHR systems – indirect recovery and direct recovery technologies. The definition of each category will be detailed, following by the review of the research and production examples of the dominate technologies in each category. Note that the WHR technologies comparison, discussion, and summary are heavily bias to IBC system.

The second section in this chapter summaries the optimisation methods for the compressor and turbine designs. In general, there are two common optimisation methods applying to turbomachinery design – gradient-based optimisation and genetic algorithm optimisation. The advantages and disadvantages of each optimisation method will be analysed in order to select a proper optimisation method for this research.

2.2 Waste Heat Recovery System

As discussed in Introduction chapter, the exhaust-gas heat energy can be categorized into kinetic energy, pressure energy, and thermal energy. In

accordance with the characteristic of exhaust gas, the exhaust-gas heat-recovery methods can be divided into direct recovery, utilizing an expansion device, and indirect recovery through heat transfer and thermodynamic cycle.

2.2.1 Indirect Recovery Based on Thermodynamic Cycle

In general, the indirect recovery approaches utilize the wasted exhaust heat as an intermediate heat source for a separate bottoming power cycle. In order to integrate the bottoming cycle with the primary cycle, a binary fluid system is obtained in which the operating fluid of the bottoming cycle exploits heat from the primary cycle exhaust gas in a heat exchanger. In this scenario, the working pressure of the bottoming cycle is decoupled with engine exhaust back pressure by transferring heat in the heat exchanger. Therefore, the performance of the heat exchanger plays a very important role in an indirect exhaust-gas heat-recovery system.

The other critical factor is the working medium in the bottoming cycle, which determines exhaust gas energy recovery efficiency. Based on the operating characteristics of the working medium, there are two main kinds of the working medium forms – liquid working medium and gas working medium. The advantage of the liquid working medium is that it can achieve high working pressure with little compression work consumption. Furthermore, the phase change process of liquid is a very efficient way to store and release energy. However, the phase change process can increase the volume of the liquid working medium, thereby imposing problems on the flow path design, such as requiring a large-diameter turbine and heat exchanger. On the other hand, the bottoming cycle with gas working medium will be much simpler since no phase change process is involved during the heat transfer process. Moreover, the bottoming cycle can be designed as an open cycle and, therefore, there is no need for a condenser. Thus, it could be argued that it is more logical to consider the bottoming cycle with a gas working medium for automotive heat recovery.[7]

2.1.1.1 Automotive Thermoelectric Generators

Automotive Thermoelectric Generators (ATEG) is one of the promising indirect recovery approaches for automotive use without any parasitic pollution. This technology converts thermal energy from the different temperature gradients, existing between hot and cold ends of a semiconductor, directly into electric energy, as shown in Figure 2.1. The advantages of ATEG include free maintenance, silent operation and high reliability since there is no moving and complex mechanical parts involved. Furthermore, ATEG is able to operate without any loads supplied by the engine drive trains. As a result, this would help to reduce the engine weight and direct the most of the increased power to the drive shaft, which would in turn help to improve the performance and fuel economy [27]. More importantly, this energy recovery technology can be applied without significant redesign, development and calibration of established engine sub-systems.

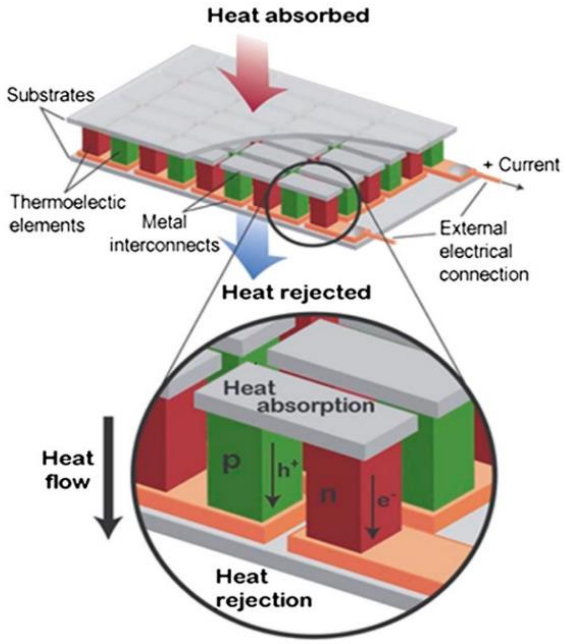

Figure 2.1 Schematic of a typical thermoelectric device [28]

The thermoelectric generators (TEGs) can generate electric power only when it is mounted where a temperature gradient exists. Therefore, in terms of the automotive engine, there are two main potential mounting allocations for ATEG

– the radiator and the exhaust gas system that are the two main heat outputs of the internal combustion engines. The radiators are used to reject the heat of the coolant that takes out the excess heat of the automotive engine in order to avoid overheating and seizure [29]. The main structure of the exhaust gas system is the exhaust manifold which is designed to discharge the expanded exhaust gas containing high-grade heat content. However, given its simplicity and low influence on the operation of the engine, present thermoelectric technologies are mostly mounted in the exhaust gas system, instead of the exhaust manifold [29]. Therefore, the typical layout of ATEG system consists of an exhaust gas system, a heat exchanger, a thermoelectric generator, a power conditioning system, and a battery pack, shown in Figure 2.2.

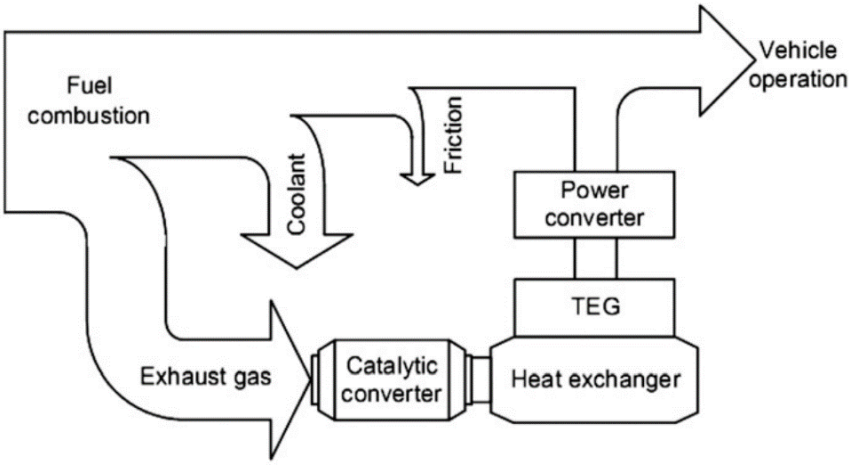

Figure 2.2 A typical ATEG system [28]

The ATEG operating process can be described as follow:

(1) During the operation of ICEs, the waste heat rejected through the exhaust manifold is extracted by the heat exchanger mounted directly downstream of the catalytic converter of the exhaust gas system.

(2) The thermal energy captured by the heat exchanger is transferred to the thermoelectric system to form the different temperature gradients, thereby producing electric power by the semiconductor.

(3) Power conditioning is performed by the power converter to achieve maximum power transfer.

The performance of ATEG system is affected by several factors, such as the temperature of the exhaust gas available from the primary cycle, the effectiveness of the heat exchanger, and the thermoelectric materials. As the primary challenge of the employment of ATEG system, the thermoelectric materials have been extensively investigated within recent years. As far as author's knowledge, Mori et al. [30] firstly stated that the application of thermoelectric in automobiles should require special design philosophy compared to general applications, but there is not enough information pointing out the special requirements, such as how far away from optimal performance a material may be. In order to determine essential elements in thermoelectric technology to be used specifically for automobile heat recovery applications, Mori et al. evaluated the effect of a thermoelectric system on fuel economy by applying commercially available thermoelectric materials and typical industrial techniques on a 2.0-litre midsize gasoline vehicle. The optimised parameter of ATEG system is the height of elements, which plays a very important role in terms of module performance. The height of elements determines the temperature difference of a module, thus affecting its electric motive force under certain thermal condition. Furthermore, it also determines the internal resistance of a module which affects current flow during electric power generation. The performance of ATEG has been evaluated under optimised specifications at four different driving modes. The results show that although the specifications of thermoelectric units have been optimised, only very modest improvement of the fuel economy was predicted. The maximum fuel economy improvement was 0.36% predicted under highway driving condition. The analysis of the energy flow of ATEG system indicated that the largest loss is due to the lack of the performance in thermoelectric material. In addition, the performance losses due to assembly and heat exchanger also occupies large proportion of the efficiency loss.

Stobart et al. [31] also ascertained that the major barriers to a successful application of ATEG is the conversion efficiency of the thermoelectric material. In their study, ATEGs models mounted in four types of engines have been built and validated with the corresponding experiments. An annual fuel saving of 3.9 – 4.7% was predicted due to the installation of ATEG in the exhaust system of each engine. The predicted power output of ATEG system could potentially replace the

alternator of a small passenger vehicle. However, the economic analysis of ATEGs system applied in passenger vehicles revealed that the used modules would have to have 1/10th of the current unit cost with current thermoelectric materials. The further improvement of the conversion efficiency of thermoelectric materials are required to realize the practical application in vehicles.

Karri et al. [32] presented predictions of the power produced and fuel saved when exhaust energy was recovered using a thermoelectric generator composed of two promising thermoelectric materials – quantum-well (QW) structured materials and commercially available Bi_2Te_3. The considered TEGs were simulated with an assumption that it is mounted in the exhaust stream of a sports utility vehicle (SUV). The coolant flow rate of the ATEG system and the aspect ratio of the thermoelectric legs have been optimised to maximum the power recovered by the thermoelectric generator. The results in terms of fuel saving are shown in Figure 2.3. Positive fuel saving was predicted at all vehicle speeds when TEG was made of the QW materials. The corresponding maximum fuel improvement of around 1.5% was observed at a vehicle speed of 112.7 km/h. However, negative fuel gains were registered at vehicle speeds of 48.3 and 80.6 km/h using Bi_2Te_3. This is because the parasitic losses associated with the employment of ATEG exceeded the power produced by the exhaust-gas heat-recovery system at lower vehicle speeds. To be specific, the dominant parasitic loss causing by using ATEG is the rolling resistance parasitic loss due to the TEG system weight. Moreover, it increases with vehicle speed. The power utilized to circulating the coolant in ATEG is less significant. The type of power loss is almost independent of the vehicle speed because the coolant system by-pass valve maintains an approximately constant pressure drop across the heater core even as the engine speed changes. It should be noted that the exhaust energy was underutilized because of space limitations, especially at higher vehicle speeds due to resulting higher temperature of the exhaust gas.

Within the recent years, the revival of interests into the improvement of heat-to-electricity conversion efficiency of the thermoelectric materials has brought many promising materials into the attention of many scientists and engineers. For example, BiTe (bismuth telluride), CeFeSb (skutterudite), ZnBe (zinc-beryllium),

SiGe (silicon-germanium), SnTe (tin telluride) and new nano-crystaline or nano-wire thermoelectric materials are currently in development stage to improve the performance of ATEG. For studies in the thermoelectric materials applied in vehicles, the most of them intend to use BiTe-based bulk in ATEG due to its availability in the market and high applicability in low and high temperature range [33].

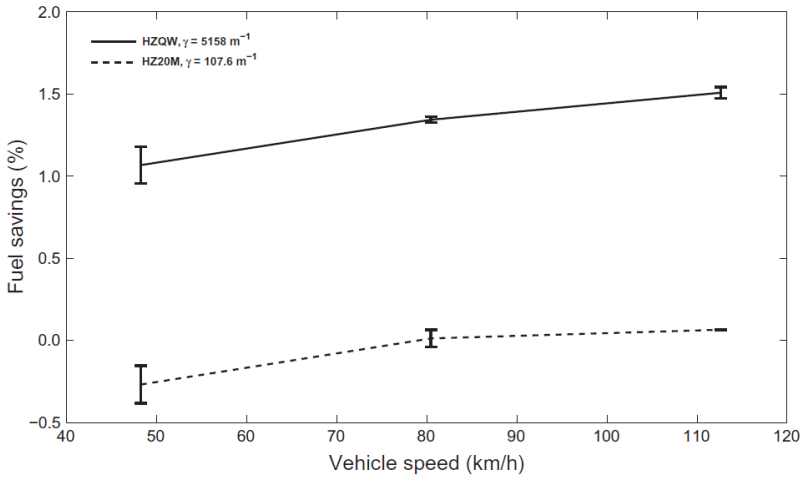

Figure 2.3 Fuel saving caused by the employment of two kinds of ATEGs [32]

In conclusion, ATEG is a potential exhaust-gas heat-recovery system and extensive studies have been performed to evaluate its heat recovery capability. To improve the current modest performance of ATEG, many promising thermoelectric materials with high conversion efficiency are in development stage. However, the poor conversion efficiency of ATEGs, typically lower than 4%, is still the primary challenge currently which hinder their adoption in the on-road market [34]. Without significant breakthroughs, the thermoelectric generator might be unfeasible to install in the exhaust system of the vehicle for the purpose of recovering wasted energy.

2.1.1.2 Rankine Bottoming Cycle

The other indirect recovery concept is to introduce a thermodynamic bottoming cycle at the exhaust system to generate electric power. In terms of researches on the thermodynamic bottoming cycles, one of the most popular basic working cycles is the Rankine cycle (RC). The basic configuration of Rankine bottoming

cycle is shown in Figure 2.4. By integrating an RC with the primary cycle, a binary fluid system is obtained in which the RC's working fluid exploits heat from the primary cycle exhaust gas in a vaporizer heat exchanger, produces output power during the expansion process in a expander, and discharges residual heat to the environment in a condenser [35]. For continuation of the cycle, the working medium is pumped from low to high pressure and returned to the heat exchanger. As the working medium is a liquid, the compression process in the pump consumes little energy to achieve high pressure.

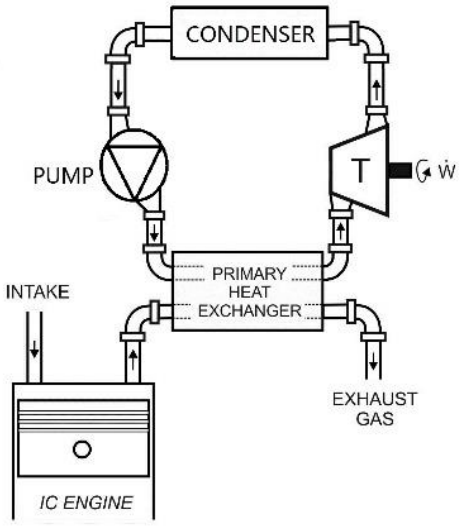

Figure 2.4 Layout of Rankine bottoming cycle mounted immediately downstream of an IC engine

Applications of the RC on an on-road vehicle as a the bottoming heat-recovery system were first investigated during the energy crisis in 1970s [36-38], but mainly for heavy duty trucks. For instance, Patel and Doyle from Mack Trucks [39] designed and built a prototype of such a system operating on the exhaust gas of a 288 HD truck engine in 1976. A 450 km on-road test demonstrated the technical feasibility of the system and its economic advantage with an improvement of 12.5% in fuel consumption. Following this, based on the work by Thermo Electron Corporation, Heywood [40] claimed a prediction in 1981 that a reduction of fuel consumption by 10–15% could be obtained with a RC–EHR system on diesel engines.

Recently, intensive efforts have been concentrated on the Organic Rankine cycle (ORC) applied as bottoming heat-recovery cycle for the internal combustion engine. This is due to the potentially low-grade temperature of the exhaust gas available from the transport engine and the organic fluids are superior to water when the required power is limited and the heat sourced temperature is low [41]. More specifically, the properties of the organic fluids mean that these working mediums often have lower heat of vaporization and can better follow the heat source to be cooled, thus reducing temperature differences and, consequently, irreversibilities at the evaporator. Furthermore, the turbine for organic cycles can provide higher efficiency at part load and are usually less complex due to the lower enthalpy drop of the fluids. It means that the ORC plant typically requires only a single-stage expander, resulting in a simple and more economical system in terms of capital costs and maintenance [42]. For the reasons presented herein, the thermodynamic characteristic of the potential organic working fluids has been extensively discussed under different engine operating conditions. Chen et al. [43] stated that a working fluid must not only have the necessary thermo-physical properties that match the application but also possess adequate chemical stability in the desired temperature range. They recommended that the thermodynamic and physical properties, stability, environmental impacts, safety and compatibility, and availability and cost are among the considerations when selecting a working fluid. In their study, the performance predictions of 35 different types of the organic working fluids under various working conditions indicate that the best working fluids with the highest efficiency cycles may not be the same for different operating conditions.

Yang et al. [44] tested the combined system consisting of a six-cylinder four-stroke diesel engine and a ORC with the working fluids of R245fa at the whole operating range of the selected engine. It should be noted that the evaporating pressure was considered as a variable. The research shows that, with an evaporating pressure of 3MPa, engine speed of 2200r/min and engine torque of 1200N·m, the net power output of the ORC system, engine thermal efficiency increasing ratio (ETEIR), and the improvement ratio of BSFC all hit the maximum values, being 22.41kW, 8.085%, 7.423% respectively. Hountalas et al. [45] found that a 7% improvement in fuel efficiency was expected when an ORC technique

was applied to a high-efficiency, low-emissions, dual-fuel, low temperature combustion engine.

In order to further improve the performance of the Rankine bottoming cycle, the modification of the basic Rankine cycle configuration have been proposed. The automotive manufacturer, BMW, conducted a two-loop Rankine cycle system on a four-cylinder gasoline engine to recover waste heat from the exhaust gas and the cooling system. The water and ethanol were selected as the working medium for two loops, respectively. The test bench measurements showed that an additional power of about 10% can be produced at typical highway cruising speeds [46].

Vaja et al. [41] also proposed a ORC system to exploit the thermal energy from the exhaust gas and the engine cooling system. They claimed that up to a 12% increase in efficiency was observed by adopting this proposed cycle to a supercharged, natural gas engine. However, the resulting complexity and capital costs lead to a long payback period. In fact, ORCs only applied to the exhaust system still hold the most significant promise owing to cost, packaging, weight, and working fluid safety concerns. Furthermore, in the case of steam bottoming, the need for a high-pressure steam generator, a steam turbine, and a condenser might be unfeasible on a small scale.

2.1.1.3 Pressurized Brayton Cycle

Given the complexity of the conventional Rankin bottoming cycle, a much simpler thermodynamic cycle, the pressurized Brayton cycle (PBC), shown in Figure 2.5, was proposed as an alternative exhaust-gas heat-recovery system [47]. The pressurized Brayton cycle is a modified gas turbine cycle where the combustor is substituted by a heat exchanger which exploits thermal energy from the available hot gas stream from the primary topping cycle. Thus, the basic PBC consists of a compressor, a gas-gas heat exchanger, and a turbine. The ‘pressurized’ term is referred to a bottoming cycle loop that is above atmospheric pressure during heat addition. The working medium air is boosted to a certain pressure in the compressor, and then fed into the heat exchanger. After capturing the thermal

energy from the exhaust gas rejected by the primary cycle in the heat exchanger, the pressurized and heated air is able to drive the turbine to produce rotating work, and then rejected to the ambient. The work produced by the turbine proportionally transfer to the compressor by a shaft, in order to complete the compression process. The rest is to generate the electric power, which is regards as the net work produced by PBC.

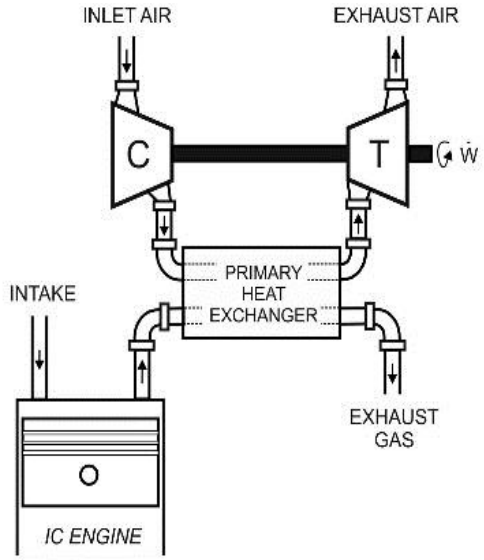

Figure 2.5 Layout of pressurized Brayton cycle mounted immediately downstream of an IC engine

Since this kind of combined cycle decouples the working pressure of bottom cycle from the engine exhaust back pressure by the method of heat transfer, the parasitic loss for the engine is only caused by the pressure drops through the heat exchanger, which can cause the increase in the back pressure of the primary cycle. Then, the resulting increase of the pumping work can deteriorate the engine performance. For this reason, the exchanger is an important component in terms of the efficiency of the entire configuration. Furthermore, the other important parameters impacting the optimum selection of the heat exchanger is temperature differential [48]. High efficiencies of the cycle are achieved for small temperature differences in the heat exchanger, although this results in a large size of heat exchanger.

Romanov et al. [49] presented a comprehensive parametric study of a system consisting of gas turbine and PBC. The results show a high capability of energy recovery in terms of PBC. Approximately 11%-20% and 4%-6% increase in power output and efficiency respectively are expected depending on both the systematic operating condition and design parameters.

Liu et al. [7] studied a SI engine model to identify the benefits of PBC as the bottoming heat-recovery cycle. The efficiency of the turbine and compressor was assumed to be 0.75 and 0.78, respectively. The effectiveness of the heat exchanger was fixed as 0.95. The performance predictions showed that the output power produced by PBC was quite low, only around 0.6 kW, due to the poor cycle efficiency. The reason was that the effective output work of this bottom cycle depended on the difference between the expansion work of turbine and the work consumed by the compressor. Furthermore, the working medium air did not fully expand in the turbine, that is, the air temperature after expansion was still every high. As a result, quite a number of the thermal energy was wasted again. The results also revealed that the heat exchanger effectiveness was quite sensitive to the air flow rate in PBC loop and even able to reach as low as 80%, which hinder the further performance improvement. Moreover, the other challenge of this technology has been specified as the intensive thermal stresses in the gas-gas heat exchanger.

To improve the efficiency of PBC installations, the more complex configurations have been proposed by Czaja et al. [48]. Then, the performance of all considered PBCs have been analyzed with a typical gas turbine, shown in Figure 2.6. The GT10 gas turbine has been selected as the primary cycle. As shown in Figure 2.6, regarding the complex PBC system in case 2, an extra compressor is adopted immediately downstream of an intercooling process. A first compressor stage compresses ambient air. Then, the compressed air is conveyed to an intercooler and cooled to the lowest possible temperature. After intercooling the compressed air is again compressed in a second air compressor and then air is heated up in the heat exchanger. The intercooler mounted between two compressors is to keep the temperature of the compressed air low before compression and make the work of compression more efficient. For the complex

PBC system in case 3, two additional compression processes are introduced before the original compressor. The increase in mechanical power output of three proposed cycles are plotted with various inlet pressure of the heat exchanger in Figure 2.7.

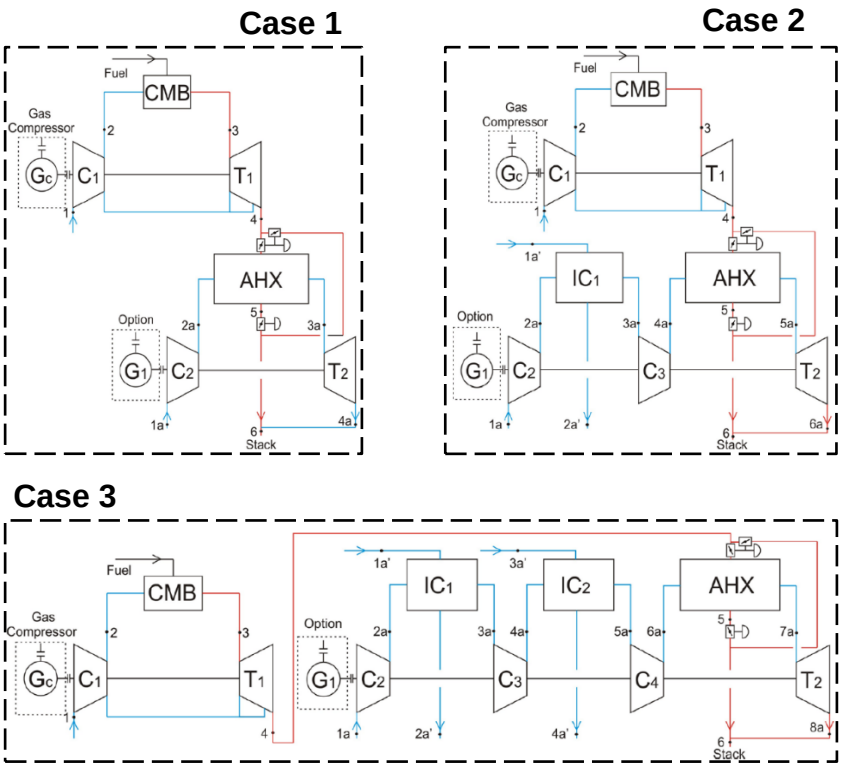

Figure 2.6 Configurations of three proposed cycles [48]

The results showed that the additional compression process can contribute to further improve the performance of the combined system. The significant improvement caused by adding one extra compression process can be observed, while only modest increase in output power was found when the third compression stage is introduced. Furthermore, the pressure drops through the heat exchanger significantly deteriorated the PBC performance in all three cases. It should be noted that there exists an optimal inlet pressure of the heat exchanger that delivers the maximum performance improvement.

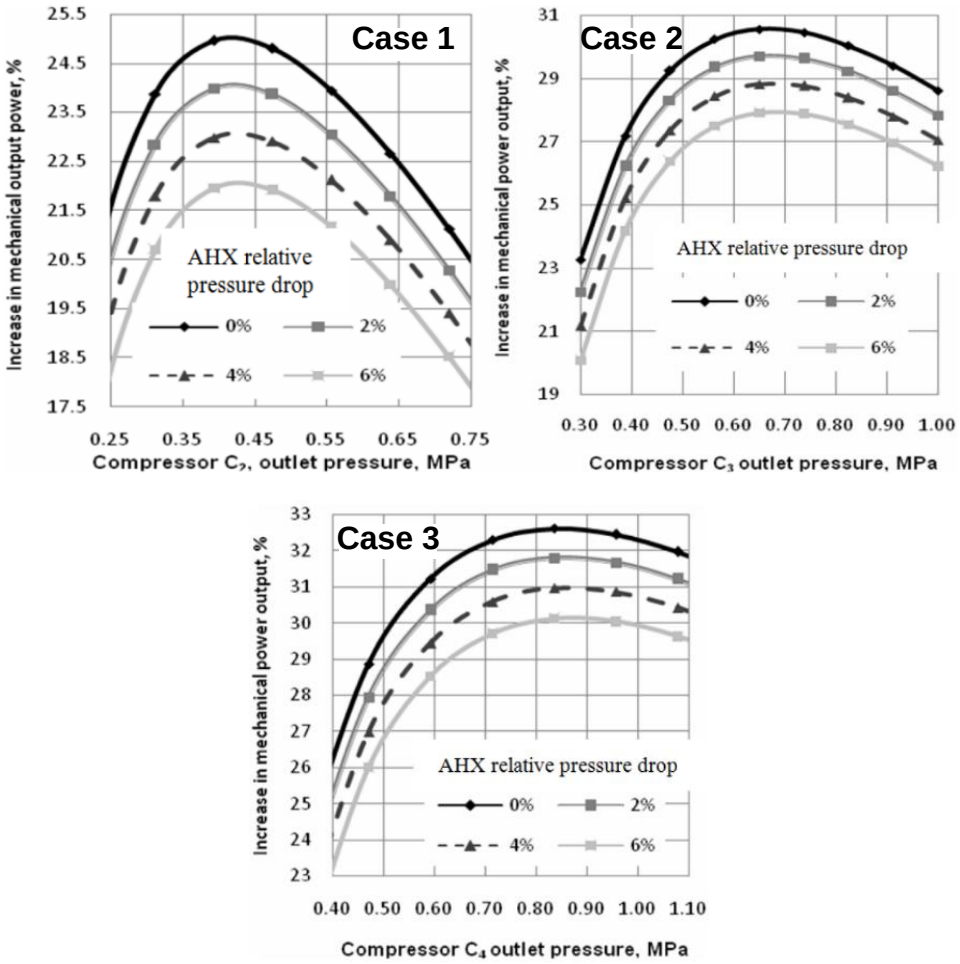

Figure 2.7 Mechanical power output of three proposed cycles as a function of pressure ratio [48]

2.2.2 Direct Recovery Approaches

Due to the limitation of the engine expansion ratio and various irreversible processes occurring in the cylinder, the exhaust gas does not fully expand in the firing cylinder. Therefore, once the exhaust valve is opened, any remaining combustion pressure in the cylinder is suddenly released producing a pressure pulse. This kind of energy can be exploited by a turbine to produce shaft work. This is the principle behind turbocharging system. However, as the additional expansion devices are directly connected to engine exhaust system, the level of working pressure in a bottom cycle will affect the engine's pumping losses, thereby affecting the working performance of engine firing cylinder. Thus, how to

match the bottom cycles with the working cycles of engine firing cylinder can become a technical difficulty.

2.2.2.1 Turbo-compounding

In terms of direct recovery approaches, an additional expansion process is usually required to fully expand the exhaust gas for energy recovery, shown in Figure 2.8. Therefore, the simple power turbine has been implemented immediately downstream of the turbocharger, known as the turbo-compounding system. The exhaust gas energy recovered by the additional turbine is transformed into shaft work which is either added to the engine torque directly or utilized to generate the electrical power, referred as the mechanical and electrical turbo-compounding respectively. The drawback of turbo-compounding system is that the maximum energy could be exploited by the power-turbine is limited by the pressure available to expand over. In theory, the best that turbo-compounding system can achieved is to only expand the gases from the blowdown pressure to the atmospheric pressure. Thus, the only way to increase the power-turbine expansion ratio is to raise the exhaust back-pressure in the turbocharger turbine and, therefore, the working pressure in the exhaust manifold. Consequently, the engine needs to work harder to expel the burned gases, which is represented by the increase in pumping loss. In addition, higher exhaust back-pressure on the engine can result in increased residual gases, delayed combustion, increased heat transfer in the cylinder, and disruption of engine thermodynamic balance [50].

The turbo-compounding application was firstly utilized in aircraft piston engine before the 1930s [51]. There are two main advantages of introducing the turbo-compounding into aircraft propulsion: 1) aircraft piston engines are designed for long hours of operation at constant high load. This resulting high exhaust pressure and temperature that are desirable for a turbo-compounding system, 2) the low ambient pressure at high altitude encourages turbo-compounding to deliver high pressure ratio and, therefore, recover more energy from the exhaust gas.

In the 1950s and 1960s, the turbo-compounding applications were extensively found in boat and train engines, as these engines typically operate at high load for extended periods of time [52]. With intensive researches and developments, the modern power plants applied in maritime ships can achieve total efficiencies up to around 50% [53].

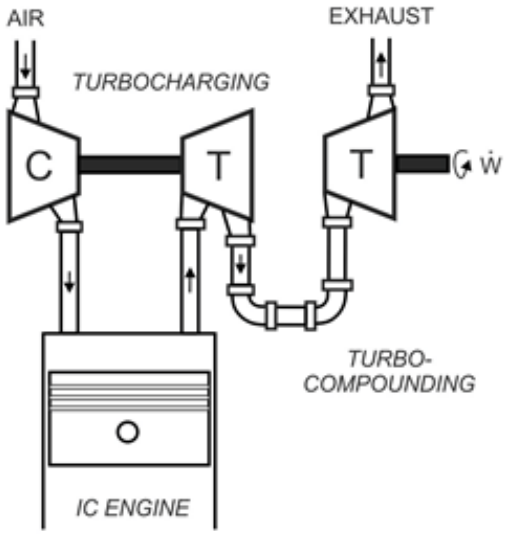

Figure 2.8 Turbocharging and turbo-compounding

With the successful utilization of the turbo-compounding system as an exhaust-gas heat-recovery device in the heavy-duty engines, construction equipment manufacturers such as Caterpillar started to exploit such compound systems to improve their high-duty diesel engines. The first commercialized compound truck engines were lunched by Cummins in 1981 [54]. Over a 50,000-mile highway driving test in the USA, the turbo-compounding system leads to a 4.7% reduction in the fuel consumption [55]. Caterpillar developed a 14.6L heavy-duty Diesel engine with a mechanical turbo-compounding system which adds the recovered energy to the engine crankshaft mechanically by a gearbox. Although up to 6% reduction in fuel consumption at full load was achieved due to the employment of the mechanical turbo-compounding system, the inefficient high-speed gearbox was the major weakness of this heat-energy recovery architecture [55]. Afterwards, the various compounded systems were mainly investigated and applied to high-displacement, high-load Diesel engine, such as Scania's 6-

cylinder 11L DTC 1101 Diesel engine, Isuzu's Ceramic IDI, and Volvo's D12-500TC [56].

Although the fuel economy benefits of the turbo-compounding system were presented by academic researches and industrial R&Ds, this technology is still not widely applied to the road vehicle engine. This is due to several limitations, such as low available energy for the power turbine at low and part engine load, overall low power turbine efficiency due to variability requirements for each engine load, and the resulting higher exhaust back-pressure that deteriorates the engine performance by increasing the pumping loss. In addition, from the power turbine point of view, the gear ratio between the engine crank and the power turbine should vary depending upon the engine load points in order to maintain high efficiency of the power turbine and achieve fast response to engine loads changes. The variable speed of the power turbine can be achieved by the employment of the continuously variable transmission (CVT) for the mechanical turbo-compounding, or an electric generator for the electric variant. However, given the cost, packaging, efficiency, and the operating requirements, CVTs and electric generators for the turbo-compounding are still too immature to be applied for this particular use.

In conclusion, the turbo-compounding technology is an exhaust-gas heat-recovery system which adds a power turbine in the exhaust line to extract the wasted exhaust available from the primary cycle – mainly internal combustion engines. Due to the characteristics of the turbo-compounding device, its favourable primary cycle should operate at high load for extended periods of time. Thus, commercialized turbo-compounding systems are mainly found in aircraft piston engines, boat and train powertrains, and heavy-duty trucks. Although the basic turbo-compounding architecture is able to deliver decent improvement in the fuel economy with the additional benefit of simplicity, there are several limitations to the prospects for a wide spread application of turbo-compounding in the automotive industry. This is mainly because that the heavily transient engine operating conditions from low to high load in automotive use requires wide operating range of the power turbine. Moreover, the energy recovery capacity of the turbo-compounding is significantly dependent on the available expansion

ratio of the power turbine. The achievable expansion ratio for this technology only can be increased with the exhaust back pressure. However, as the power turbine is directly connected to engine exhaust system, the increasing exhaust pressure makes expelling burned gasses from the combustion chamber difficult, that is, by increasing the engine pumping loss. In addition, other system components, such as electric generators and CVT systems, still should be properly designed and developed to improve the overall performance of the turbo-compounding system so that it could be utilized widely in road vehicle engines. [53]

2.2.2.2 Inverted Brayton Cycle

Due to the drawbacks of the turbo-compounding system, a simple modification of the turbo-compounding system with a downstream heat exchanger and compressors with intercooling, termed as the Braysson cycle, has been proposed by Frost et al. [57]. The Braysson cycle, shown in Figure 2.9, consists of a conventional gas-turbine worked as the high-temperature heat addition process and the Ericsson cycle as the low-temperature heat rejection process.

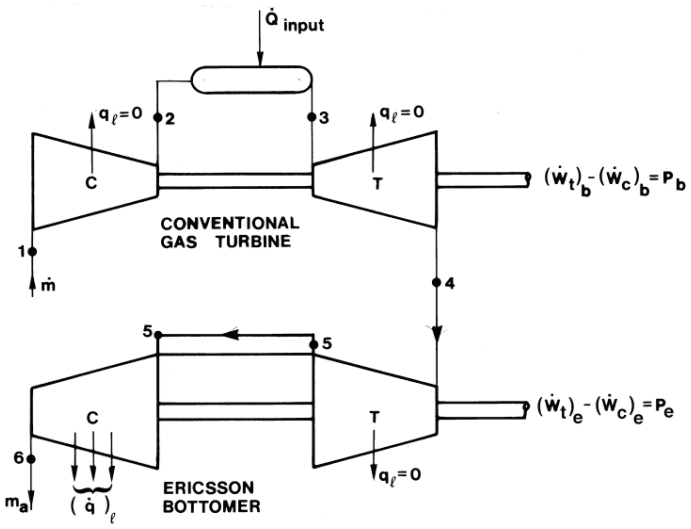

Figure 2.9 Layout of a combined Brayton and Ericsson bottomer gas turbine [35]

Frost et al. [57] performed the First Law analysis for the Braysson cycle. The exergy analysis of an irreversible Braysson cycle has also been studied by Zheng et al. [58]. Furthermore, performance analysis and optimum criteria of an

endoreversible and irreversible Braysson heat engine have been intensively studied by using a concept of the finite-time thermodynamic for a typical set of operating condition [59-62]. The corresponding results revealed that there is a window of pressure ratio in the upper Brayton cycle where the Braysson cycle shows a significant improvement over the best that can be achieved with either the non-regenerative or the regenerative Brayton cycle, even over the conventional combined gas and steam turbines in a certain range of operating condition. However, the high vacuum (up to 0.04 bar) in the bottom cycle requires a large turbine and the cooling technique implemented with the compression process to obtain isothermal compression, that may hinder the practical application especially considering the added manufacturing difficulty and cost [63]. Thus, given the feasibility of Braysson cycle application, the Ericsson cycle should be improved by adding a heat sink – heat exchanger and replacing intercooled compressors with conventional compressors. In other words, the novel proposed architecture consists of a conventional turbine, heat exchangers, and compressors, referred as inverted Brayton cycle (IBC). The schematic diagram of the basic IBC system with an IC engine is shown in Figure 2.10.

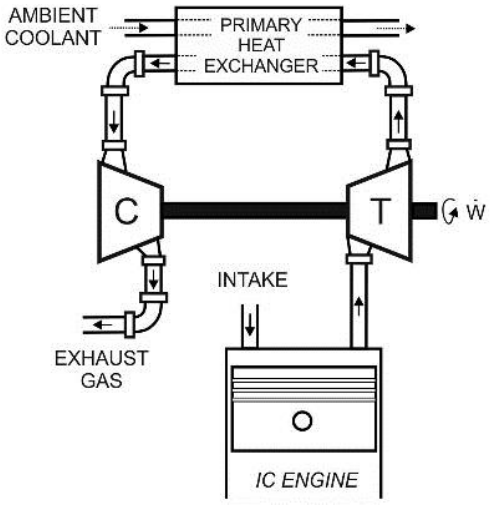

Figure 2.10 Layout of inverted Brayton cycle mounted immediately downstream of an IC engine

As far as authors' knowledge, the concept of inverted Brayton cycle has been first proposed and studied by Kohler in 1919 [64]. Instead of utilizing a heat exchanger,

a steam generator and condenser were employed to cool the working fluid after expansion. In 1944, the alternative cooling applications, using surface or spray type coolers, were studied by Hingst [65] to improve the overall performance. In 1955, the function of IBC inlet temperature and turbine pressure ratio was established by Hodge [66], to evaluate the IBC overall thermal efficiency and specific power output. The function shows that the cycle inlet temperature plays a vital role in the IBC performance, as both the thermal efficiency and the optimum pressure ratio increases with the cycle inlet temperature. Thus, given the characteristic of IBC cycle, the preferable primary cycle should deliver high temperature exhaust gas in order to enhance the hear-recovery capability of IBC cycle.

Preliminary analysis on the IBC has been concentrated on the case of an IBC as a bottoming cycle to a gas turbine, which is dubbed the mirror gas turbine. The first investigation was performed by Wilson and Dunteman [67], who were inspired from a business case about a Ruston and Hornsby commercial gas turbine. In order to increase the overall energy generated by this gas turbine system, a waste-heat boiler was incorporated as a heat source for other uses by harvesting some remaining heat from the turbine exhaust. The downside of the additional heat boiler is that the parasitic pressure drop contributes to the increase of the turbine exhaust pressure, thereby reducing the pressure ratio across the turbine and, therefore, the corresponding power output. One customer attempted to eliminate this negative influence of the waste-heat boiler by employing a downstream induced draft fan to reduce the turbine exhaust pressure back to atmospheric. The customer reported that although the induced draft fan consumed the electric power to remain the atmospheric pressure at the turbine exit, the overall net power benefited from the increased power generated by the gas turbine itself. The resulting power gain encouraged Wilson to further improve this architecture by introducing an additional turbine between the main turbine and a waste-heat boiler, that is, inverted Brayton cycle as a bottoming cycle. In Wilson's research, the thermodynamic performance and return on investment of IBC system were investigated based on the reasonable assumptions with respect to the technology at the time. The results showed that there is a window of IBC inlet temperature and pressure ratio where the cycle is

competitive with other methods of waste-heat utilization. Moreover, the average return on investment for the IBC device was up to 30 percent. This large return on investment was calculated on the assumption that the exhaust gas would be discharged into IBC at any operating points. It should be noted that the resulting back pressure will be negligible at design point, but undoubtedly increase at off-design points. However, the gas turbine power loss caused by the back pressure was ignored in their research. Consequently, the return on investment were overestimated. The other limitation of their study is that the IBC system was only evaluated at one operating condition. In addition, a proper optimisation of the pressure ratio of the IBC turbine should be employed to maximum the IBC heat-recovery capability in their study.

Afterwards, Holmes [68] conducted a thermodynamic analysis of the combined system of marine gas turbine and IBC, in order to investigate performance, efficiency and fuel-consumption effects on marine gas turbine. The results showed a maximum increase in power and efficiency of around 12%. In addition, he reckoned that the upper cycle, which was marine gas turbine in his research, should be optimised to gain benefits from the employment of an IBC system. Thus, a matching process should be conducted when IBC system is introduced to any existing upper cycle.

Tsujikawa at el. [69] performed a comprehensive parametric study of IBC system to reveal the influence of the IBC inlet temperature, pressure ratio, turbomachinery efficiencies, and the stage number of intercooling. Then, a conventional gas turbine and IBC system - mirror gas turbine were optimised to maximize the power output and thermal efficiency of the combined system. The results showed that even at atmospheric pressure the waste energy can be recovered successfully from the high temperature gas by employing IBC system as a bottoming heat-recovery cycle. Moreover, by introducing three stages intercooling, the IBC thermal efficiency can be improved by approximately 10 percent when the IBC overall pressure ratio was limited up to 10. Finally, they found that the optimal combined system of a Brayton cycle and IBC was able to deliver up to 60% thermal efficiency in the case of a turbine inlet temperature of 1500°C. However, since the IBC inlet pressure in the combined system was fixed

as 1 bar in their research, the influence of IBC inlet pressure on the whole system was not revealed. It should be noted that the benefit of multi-stages IBC, constructed from a expander followed by multiple heat exchangers and compressors, was also investigated by Kaneko [70]. The results showed that the improved systematic performance could be expected by an increase in the number of compression stages. In addition, a combined system between two-stage IBC and a combustor, referred as two-stage atmospheric pressure turbine (APT), was able to achieve maximum overall thermal efficiency of 65% [71]. Figure 2.11 shows the basic configuration of an APT. Basically, it consists of a combustor and IBC system. The unpressurized burned gas with high temperature discharged by combustor is utilized as the energy source for IBC system. Thus, research above showed that multi-stages IBC are promising and should be considered as a potential bottoming heat recovery cycle.

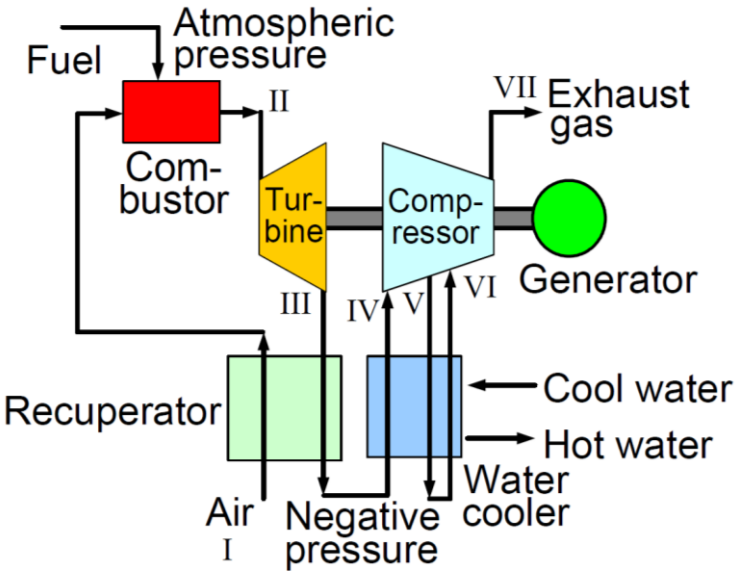

Figure 2.11 Schematic diagram of APT [71]

In Agnew's research [63], the influence of IBC inlet pressure on the system thermal efficiency of a mirror gas turbine was revealed by an optimisation study which was performed with a fixed upper cycle turbine inlet temperature, constant stack pressure and pressure, and real component efficiencies. This study indicated that the maximum specific work output and efficiency of the mirror gas turbine could be obtained when the inlet pressure to the bottom cycle is above atmospheric pressure.

Bianchi et al. [72, 73] investigated the used of IBC as an exhaust-gas heat-recovery cycle for low-temperature cogenerative applications and repowering the existing gas turbines. Their studies showed that although the thermal efficiencies of cogenerative applications were deteriorated by the existing of IBC, the overall electrical efficiency increased by about 5%. Due to the thermal efficiency reduction of the cogenerative applications, they introduced an IBC as a bottoming cycle for gas turbines to avoid its side effects. The most widespread gas turbines on the market were selected as the main cycle to perform the IBC preliminary design. The results showed the maximum percentage of electrical power increased range from 10 to 30%. However, optimistic component efficiencies were assumed in their research.

IBC performance was compared with various potential combination of Rankine and Brayton cycles by Alabdoadaim et al. [74-76]. In their studies, the baseline configuration introduced a simple IBC as the bottom cycle, while there were three alternative upper cycles – simple Brayton cycle, Brayton cycle with regeneration, and one with reheat. The results showed that the optimum value of bottom cycle expansion pressure was different for each cycle configuration. Furthermore, the regeneration cycle attained best efficiency value of 49.36% with component size similar to that of a simple gas turbine. In order to further exploit the heat energy carried by the exhaust, a Rankin cycle was introduced to recover the heat rejected by the cooler in IBC. There were two IBCs in parallel in their proposed novel configuration, shown in Figure 2.12. The use of two IBCs provides an opportunity for the stream in the Rankin cycle to be heated in two locations – one as an evaporator and the other as a superheater. This unconventional combined system attained a high thermal efficiency of 54 percent. The following study showed that the removal of the compressor of the second IBC contributes to the increase of the maximum thermal efficiency – up to 57.7%. However, the manufacturing difficulties and cost hinder the employment of their novel proposed configurations in practice.

Moreover, further comparisons were conducted by Bhargave et al. [35]. Three small/medium power (100 kW to 30 MW) rating gas turbines and a microturbine are selected as the topping cycle to perform the systematic thermodynamic

performance evaluation and comparison among IBC, PBC, and ORC. The Primary Energy Saving (PES) index were introduced to quantify the overall system performance. Generally, ORC provides comparatively better results in terms of PES index and the overall electric efficiency. However, for the selected microturbine, IBC offer the best performance enhancement. The limitation of their research is that the component efficiencies of the bottoming cycle were fixed across over all simulations. Additionally, only one design point for each upper cycle was introduced to evaluate and compare proposed heat recovery technologies.

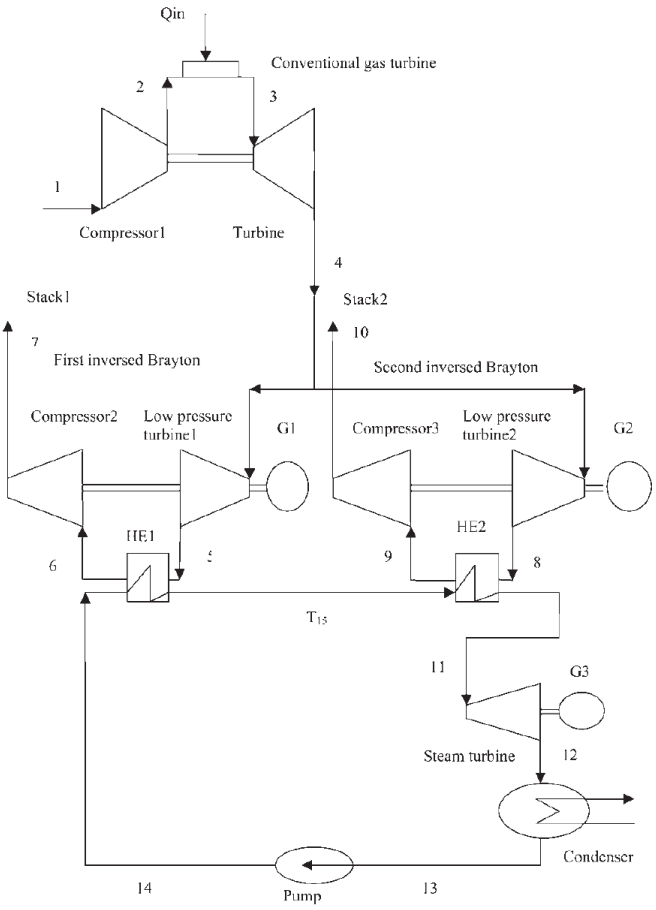

Figure 2.12 System layout of conventional gas turnine with two IBCs in parallel [75]

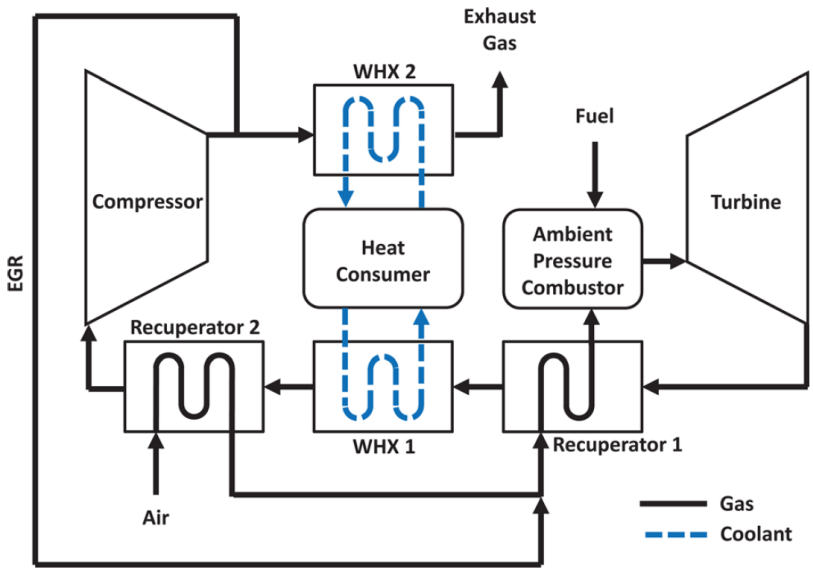

Figure 2.13 Schematic overview of the IBC with a second recuperator and EGR [77]

Microturbines are also considered as the potential top cycle for IBC. The major drawback of this technology is the employment of smaller turbocharger components which suffers low efficiency and low pressure ratio due to the high tip leakage loss. However, the low pressure level of the IBC results in high volumetric gas flows, thereby enabling the use of large, highly efficiency turbochargers components [78]. Tanaka et al. [79] developed a 50kW output power atmospheric pressure turbine (APT). In their research, it was designed to harvest heat energy from the exhaust gas available from industrial furnaces. The simulation results show that the overall electric efficiency of the proposed system is approximately 20%. Henke et al. [77] increased the complexity of an IBC by using two water heat exchangers, two recuperators, and exhaust gas recirculation system (EGR), shown in Figure 2.13. Compared with a conventional microturbines operating on the recuperated Brayton cycle, the total efficiency gain achieved by non-EGR configuration is from ~2% to ~4% points, varying with the coolant temperature. However, the total efficiency improves by additional 10% to 15% points when EGR is used with a recirculation rate of 85%. Kuifang [80] claims that the electrical efficiency of microturbines is typically about 30% which is limited by a state-of-the-art turbine inlet temperature – maximum around 950 °C. However, the microturbines performance could be enhanced by the employment

of humid air turbine (HAT). The resulting electric efficiency can reach up to 40%. Their study aims to further increase the electric efficiency of the microturbine based on HAT (mHAT) by introducing IBC as bottomer of a mHAT. The electric efficiency and specific work of mHAT with IBC are 2% points and 20% higher than of HAT cycle respectively when the turbine inlet temperature reaches the maximum – 950 °C.

Although extensive studies about IBC as exhaust-gas heat-recovery system have been performed, there has been few experimental investigations. Fujii et al. [81] firstly conducted two basic experiments to investigate the performance of IBC at different working condition. The first one was to confirm the operation of inverted process of expansion, cooling, and compression by running IBC system without extracting power from IBC shaft, while the second one is to confirm the power generation by decoupling the IBC turbine and compressor. By doing so, the power harvested by IBC turbine was measured by the connected compressor, while the power consumed by IBC compressor equals to that by the motored compressor. Although in the first experiment IBC turbine and compressor successfully run at several idling speeds without generating any net power, the power out of IBC system in the second test were extremely low due to the maximum system thermal efficiency of approximately 1%. They reckoned that the low efficiency turbine, around 50% at all test points, deteriorated the system thermal efficiency. The further thermodynamic analysis shows that increasing the inlet temperature or turbomachinery efficiency of IBC can promote the performance of mirror gas turbine, but also ignored the influence of the IBC inlet pressure.

In 2006, a prototype atmospheric pressure turbine (APT) was constructed and tested by Tanaka et al. [79]. The design pressure ratio was set to 3.3. The compressor and turbine were single-stage centrifugal and radial-flow devices respectively, and no intermediate cooling was introduced in the compression stage. The target power output of 3.3 kW was successfully delivered by the prototype. However, during the continuous operation at the speed of 96000rpm, a gas leak was found in the negative pressure part. Thus, the measured thermal efficiency was only 5.8% with the gas leak, while it was increased to 7.4% with

the improvement of seal performance. In order to further improve the performance of APT, better heat insulation on pipes were built. The final output power and thermal efficiency achieved by the prototype were 3.5 kW and 8.7%, respectively. Their key conclusion on the prototype bench test is that the mechanical and dissipative heat losses of such devices occupy large proportion of the total loss and, therefore, should be reduced to attain higher efficiency. Agelidou et al. [82] presented an experimental study of a conventional MGT operated in IBC mode. The test range of IBC rotation speed is from 180 000 rpm and 240 000 rpm. The turbine outlet pressure varies between 0.5 bar at part load and 0.3 bar at full load. Due to unexpected high mechanical losses on the shaft, the IBC system is unable to produce positive power output.

As far as authors' knowledge, the performance evaluation of the inverted Brayton cycle applied to a piston engine as an exhaust-gas heat-recovery system has *only* been performed by Bailey in 1985 [83], which aims to compare with the other two alternative power cycles – the Rankin cycle and the pressurized cycle. The common baseline for the comparison was the adiabatic-turbocompound high-power diesel engine. The results indicated that, in terms of engine rated specific fuel consumption, all three alternative power cycles as the bottom heat-recovery system offer a significant improvement over the turbocompound diesel baseline. More specifically, the inverted and pressurized Brayton cycles delivered approximately half of the improvement in system thermal efficiency compared the Rankin bottoming cycle. However, given that many of the proposed organic Rankine systems tend to be complex, costly and on occasion, toxic, it seems logical to consider much simpler air Brayton systems for automotive heat recovery. Then, the comparison between pressurized and inverted Brayton cycle indicated that the performance of both cycles becomes competitive with each other, depended on the thermal characteristics of the heat exchanger. It should be noted that the recent study, conducted by Bhargava et al. [35], offers a performance comparison of the pressurized and inverted Brayton cycles as the bottoming heat-recovery thermodynamic cycles and shows IBC is superior to PBC.

2.3 Turbomachinery Design Optimisation

Essentially, turbomachinery design optimisation mainly includes two engineering problems – geometry design and optimisation methods. Regarding design techniques for turbomachinery, it could be broadly divided into two categories: direct and inverse methods. The direct methods require a sensible first base design as a starting point. Then, a trial-and-error procedure is employed to repeatedly adjust the base design and evaluate the corresponding performance, until a satisfactory solution is accomplished. Typically, optimisation techniques are introduced into the trial-and-error procedure to guide the perturbations to geometrical parameters and reduce the computation cost. The optimisation fitness function should be integrated properly with the constraints and design parameters. Thus, the sensitivities that indicate how to change the geometry to achieve the design target can be studied by optimizing the fitness function. This approach is the most popular current way of performing the optimisation since computer capacities are continuously increasing. The inverse methods require the engineer to find a well-posited pressure or velocity distribution on the boundaries that reaches the design requirements and then determining a geometry that yields this target pressure or velocity. Although this design approach could deliver the final design with low and affordable computational cost due to the pre-defined specification of the flow field, its success highly depends on the engineers' experience and insight. Moreover, it is usually difficult to directly apply constraints in the inverse design. [84, 85]

Therefore, given the advance in the high-performance computing, the direct methods are better suited to the turbomachinery design, especially taking account into the extremely complex flow field and various constraints of the rotating device. Since the optimisation is required in the direct design, the design problem is posed as an optimisation problem, which the requirements are translated into an objective function dependent on geometric and other parameters of the design object. Thus, an efficient direct design should select a proper optimisation method based on the nature of the design problem, in order to achieve the design requirements with reasonable computation cost. Srinivasan [86] provides a general review of the optimisation techniques applied for the direct

design method. These optimisation techniques can be broadly classified into following groups: a) gradient-based optimisation techniques, b) global optimisation techniques.

2.3.1 Gradient-based optimisation

Gradient-based optimisations are typically local algorithms to find the minimum of the cost function by utilizing the gradient information of the function at each iteration. All variants of gradient-based optimisation techniques have been widely studied and applied to a variety of engineering problems. Their main advantage is the smaller number of function evaluations required to find the optimum, due to rapid convergence rates. In addition, they have capabilities of solving problems with a large numbers of design variables, especially when the number of design variables is considerably greater than the number of objectives and constraints. However, since the nature of gradient-based algorithms require that the objective functions are differentiable and continuous, they have difficulty solving discrete optimisation problems. Moreover, good initial design points are critical to increase the possibility of preventing locating a local optimum and, therefore, finding a better optimum solution. It should be noted that seeking for the global optimum is achievable by gradient-based optimisations when multiple random initial design points are presented in the design space. However, by doing so, the corresponding computational burden significantly increases due to the lack of effective guidance of the search direction.[86-88]

The example of applying the gradient-based optimisation to a large and complex industrial design problem is shown below. Odeh [87] proposed and investigated one gradient-based algorithms – the MacNeal-Schwendler Corporation (MSC) Nastran optimisation technique in solving the weight optimisation of different metallic and composite laminated aircraft wing structures. Two key objectives are emphasized. First, the procedure of generating good initial starting points for the discrete and continues design variables should be properly established with consideration of the trade-off between covering whole design space and avoiding large number of design points. However, there is no clear methodology available to guide the selection of starting design points. Thus, the number of initial design

points and how to distribute them in the design space are conducted by intuition and previous experience. Second, since the design space of this aircraft wings weight optimisation is too large, tremendous design variables of different sensitivities, and highly nonlinear objective functions, a practical optimisation framework is critical to achieve the final optimised optimum design in a cost-effective manner. In their study, an improved strategy, shown in Figure 2.14, was proposed. The key feature of this strategy is to take advantage of the previous optimal solution by introducing it as the initial candidates for the next optimisation process. Such iteration procedure was terminated when the aircraft wing mass of the optimised solution at each iteration is converged and all design requirements are satisfied.

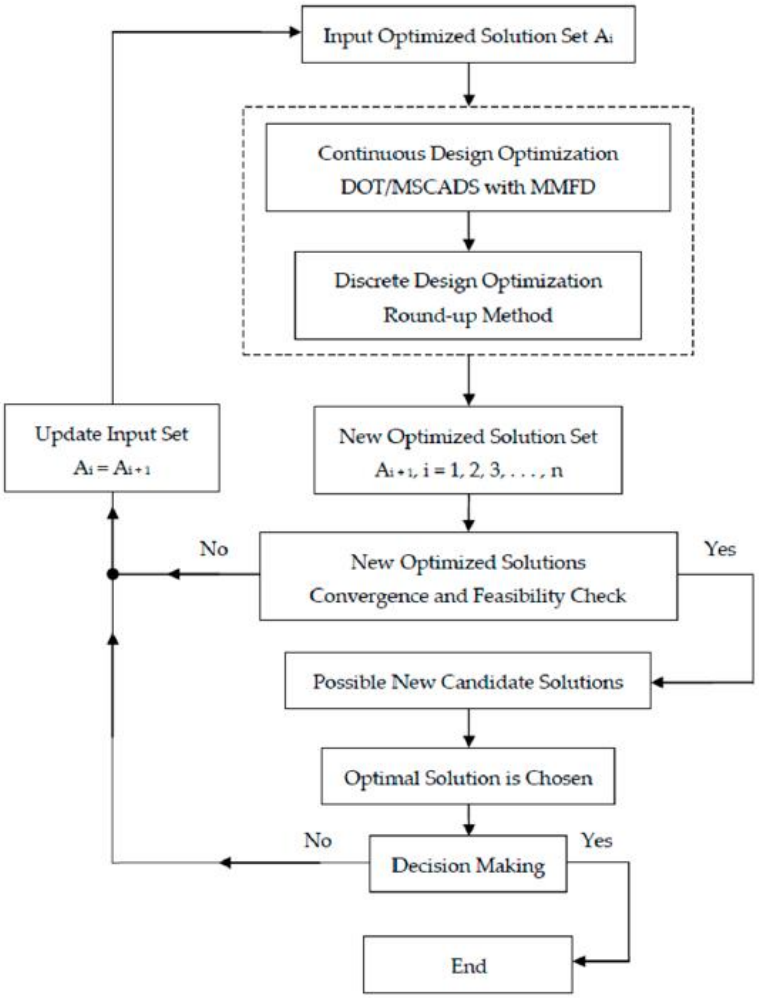

Figure 2.14 Flowchart of the improvement search for an optimum solution [87]

Gradient-based optimisation methods have been used to optimise the geometry of turbomachinery applications with various purposes, range from single blade row [89-91] to multi-row and multi-stage architectures [85, 92-94]. Regarding the integration of the optimisation approach with the geometric design, one of main challenge recognized by these studies is that proper parameterization methods and tools should be chosen to define the optimisation variables and the corresponding design space, with the consideration of the computational cost, the mechanical and manufacturing requirements. Some parameterization methods, such as Hicks-Henne shape functions, free-form deformation, and the surface nodes of the computation grids, possess a large degree of freedom and provide sensitivity derivatives at low computational efforts, which make them quite attractive for gradient-based optimisation methods. However, the disadvantage of these parameterization methods is that there is no direct connection to the computer-aided design (CAD) model. In other words, based on the afore-mentioned parameterization methods, the optimised grid point positions are the final output, while the geometry in most industrial CAD software typically consists of high-order surface such as non-uniform rational B-spline (NURBS) surfaces. Thus, Becker et al. [95] proposed an advanced NURBS fitting procedure for a post processor which is able to translates a given set of grid points into a NURBS surface with high accuracy. Figure 2.15 shows an example of translation process from an unstructured triangular parameterization with the computed control point, to an approximated NUERBS surface. The challenge is that the unstructured grid can be seen as an arbitrary point cloud with four known corner points. It should be noted that no matter how accurate the fitting procedure is, there still are fitting or approximation errors which may impair the optimality of the final design.

On the other hand, the such parameterization methods lack the consideration of geometric constraints related to mechanical and manufacturing requirements, as only mathematic principles are applied for the parameterization [96]. This disadvantage may make the optimisation procedure computationally expensive, due to the high possibility of investigating an unfeasible design. Thus, a parametric CAD model should be introduced into the optimisation procedure, in order to facilitate the integration of constraints in the optimisation process and

allows design parameters to be easily varied while sustaining the geometric features feasible. In Lasse's study [96], parametric blades of turbocharger radial turbine are optimised by a gradient-based optimisation algorithm to maximize the corresponding the total-to-static efficiency at multiple operating points. They claimed that the gradient-based optimisations are efficient for the optimisation problems with large design space, such as the blade shape optimisation, as the resulting computational cost is essentially dependent on the number of the defined objective and constraint functions, instead of the design variables. This benefit makes the gradient-based optimisations particularly suitable for the industrial design processes where the nature are the time restrictions and complex constraints with respect to manufacturing feasibility. Therefore, a gradient-based optimisation approach available in a commercial optimisation package – Sparse Nonlinear Optimiser is utilized by Lasse to optimise the turbine blade shape. The selected algorithm handles constraints by forming a smooth augmented Lagrangian merit function. The in-house CAD software is used to parameterize the turbine blades and predict the corresponding performance with the following design variables: meridional flow path, camber line surface, blade thickness distribution, and the number of blades. Figure 2.16 shows an example of the approach to parameterize the turbine blades hub and shroud in meridional flow path. The constraint of this optimisation is to remain the output power and the choking mass flow. Over all three design points, up to 4 percentage points of total-to-static efficiency improvement are achieved by the final optimal design.

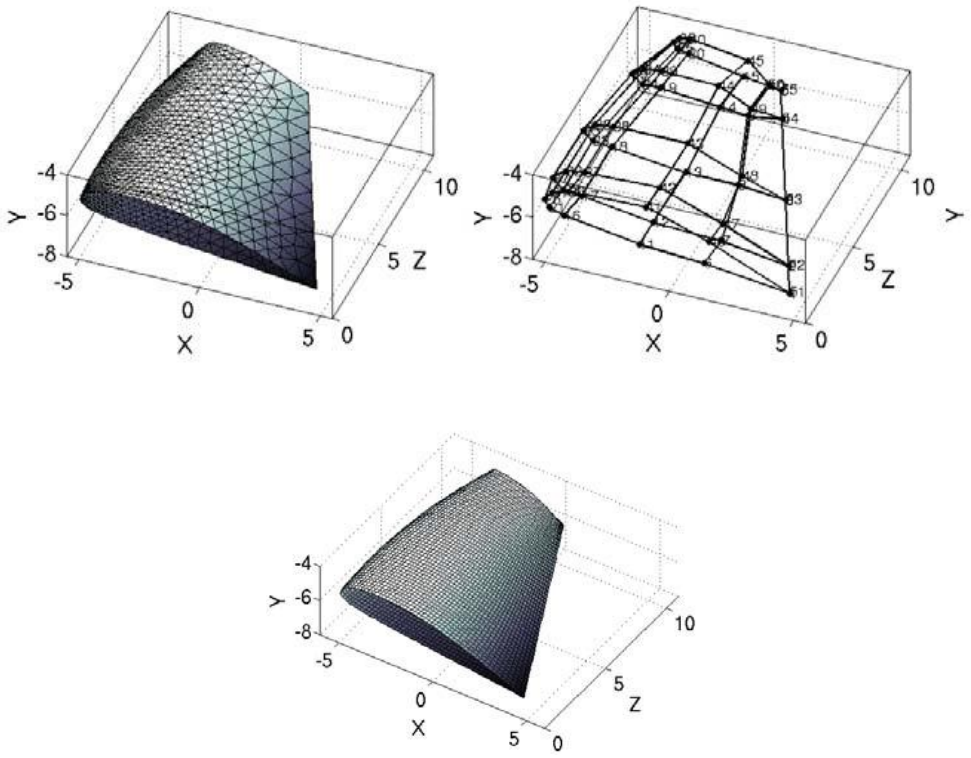

Figure 2.15 Wing 3D model with the unstructured triangular grid and the computed control points. The structured grid with approximated NURBS surfaces. [95]

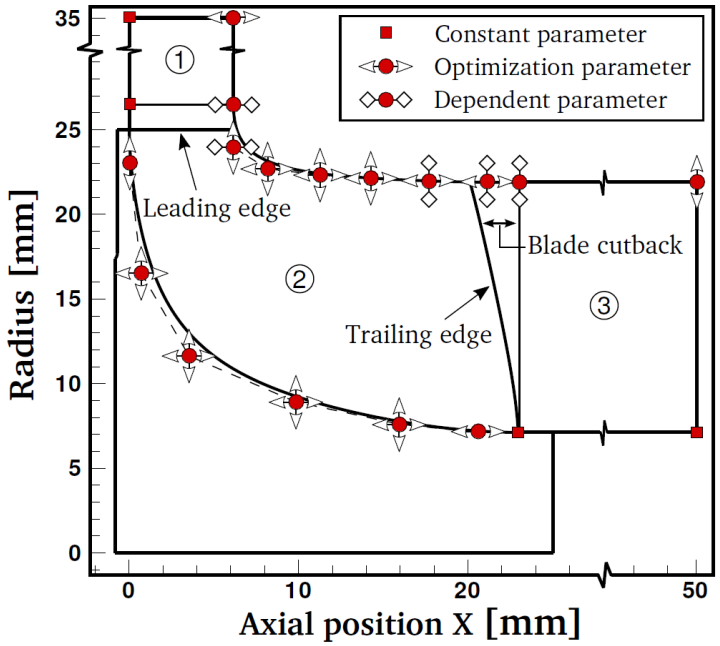

Figure 2.16 Parameterization of the meridional flow path with three patches 1-3 [96]

2.3.2 Global Optimisation – Genetic Algorithm

Global optimisation techniques aim to find the global optimal solution to discrete and combinatorial optimisation problems that contain multiple local maxima or minima without any gradient information of the objective function. It is important to note that no algorithm can guarantee convergence on a global optimum in the general sense. Thus, it may be more accurate to refer to global optimisation algorithms as having global properties. Most of the global optimisation algorithms need quite large initial populations to cover the whole design space and initiate the optimisation process. Therefore, the problems with fewer design variables are favourable for the global optimisation algorithms in order to avoid numerous starting points and, therefore, reduce the computational cost. Venter [88] claims that global algorithms are well suited for optimisation problems with the design variables less than 50.

One of global optimisation techniques – genetic algorithms (GA) has become very popular in the last decade. This method is generic population-based metaheuristic optimisation algorithm. To be specific, it heuristically mimics biological evolution such as reproduction, mutation, recombination, and selection. GA is metaheuristic inspired by the process of natural selection, which was initially introduced by John Holland in 1975 and developed by Goldberg in 1989. Then, it has been employed for solving numerical optimisation problems in a wide variety of application fields including engineering, biology, economics, agriculture, business, telecommunications, and manufacturing [97]. Generally, the genetic algorithm is designed to drive a population of candidate solutions of an optimisation problem to evolve toward better solutions. Essential differences that distinguish GA from other optimisation methods are that GA aims to cover the entire design space and thus reduce the probability to get trapped in a local minimum and that it is no longer necessary to compute the gradient of the objective function [98, 99].

The main difficulty of turbomachinery design optimisation is that the objective function has numerous local optimum, due to the complex flow structures and geometrical parameters. Thus, given that GA could perform the global

optimisation efficiently, extensive studies shows the employment of GA on turbomachinery geometry optimisation.

Benini [100] proposed to utilise GA combined with a commercial CFD code to maximise the impeller peak efficiency with the present of constraints on the impeller pressure ratio and operation range. In his study, Bezier curves are used to describe the shape of the blade on each layer. In addition, Bezier curves on each layer are defined as a function of meridional coordinates. By doing so, the surfaces of the compressor impeller are easy to manipulate parametrically and have continuous derivatives up to any required order. Thus, the outlined procedure is able to generate pairs of very good blade shapes using 14–16 parameters. Figure 2.17 shows the described 3D parameterization of main and splitter blade shapes.

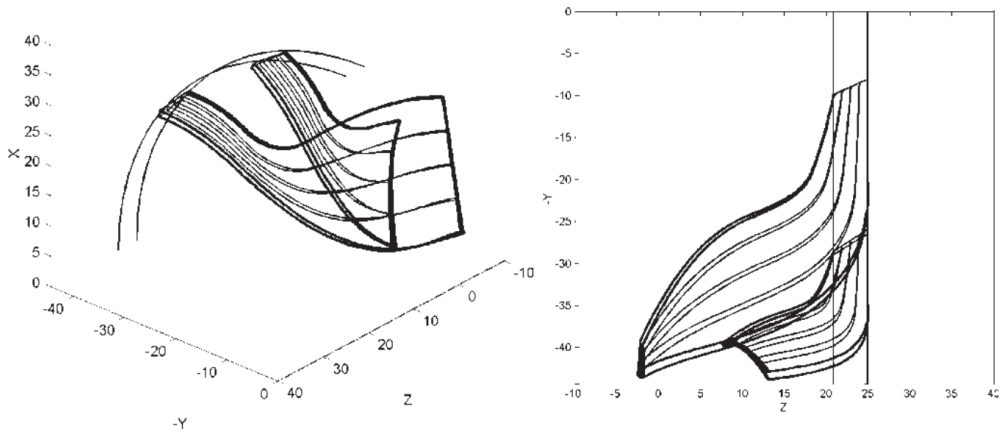

Figure 2.17 3D parameterization of main and splitter blade shapes [100]

Alexander et al. [101] performed a surface shape optimisation of the main blades and splitters of a centrifugal compressor by the combined optimisation method – artificial neural network (ANN) and GA. The objectives are to increase the isentropic efficiency and reduce the acoustic signature at multiple operating points. With implementing control points of each curve, the Bézier curves, B-spline, and interpolated curve are used to parameterise the hub, shroud, blade leading edges and camber curves. It should be noted that three dependently camber curves are defined at near-hub, near-shroud and mid-span of blades respectively, to ensure that arbitrary blade surfaces are investigated and,

therefore, it is more likely to achieve a better optimal design. In total, 45 optimisation parameters and 8 objective functions are defined to accomplish the design requirements. The results show that 1.4% points of the total-to-static efficiency and 23% reduction of the shock strength are achieved by the optimised compressor.

In Lbaraki's study [102], a similar approach combining ANN and GA was also applied to enhance the performance of the centrifugal compressor by optimizing the compressor impeller. Moreover, two optimised compressor designs were manufactured and tested to verify the proposed optimisation method to be valid. The test results showed the improvement of efficiency and the extension of operating range as promised by the optimisation method. The compressor characteristics of two optimised compressor designs are shown in Figure 2.18. OPT1 shows a higher maximum efficiency by 0.5% in the proximity of pressure ratio 1.8, and higher efficiency by 1% at the pressure ratio 2.2. However, OPT2 has a lower maximum efficiency by 1% but an extended operating range compared with the baseline impeller. In addition, the reverse analysis of the obtained impellers using CFD was conducted to understand the internal flow structure and mechanism of efficiency improvement.

Cho et al. [12] proposed to use the combination of design of experiments (DOE), ANN and GA to optimise the compressor blade. DoE was applied to generate the initial data space to train the ANN and GA was utilized to improve the accuracy of ANN during the optimisation process. Therefore, authors reckoned that the proposed combined optimisation process could decrease the computational time while obtaining the globally optimised result. In their research, Bézier curve was adopted to express the shape of the blades as this curve is superior in terms of smoothness and continuity. As shown in Figure 2.19, the flow passage was redesigned using a Bezier curve formulated by six control points at the hub and shroud, while only two control points of each Bézier curve is considered as design variables. For the camber curves defined at near-hub and near-shroud, 8 control points are implemented for the Bezier curve, while only 2 control points are design variables, shown in Figure 2.19. The performance of each design points was

evaluated by CFD on a single flow passage including portions of the inlet and diffuser. It should be noted that the $k - \varepsilon$ model is selected for turbulence closure.

The efficiency and the pressure ratio are considered together as the objective function as follows:

$$\mathrm{OF} = (1 - \eta_{t-t}) + \max\left[\left(\frac{|\Pi - \Pi_{req}|}{\Pi_{req}} - 0.1\right), 0\right] \tag{2.1}$$

where OF is the objective function for the optimisation process. η_{t-t} and Π is the total-to-total efficiency and pressure ratio, respectively. Π_{req} is the prescribed pressure ratio.

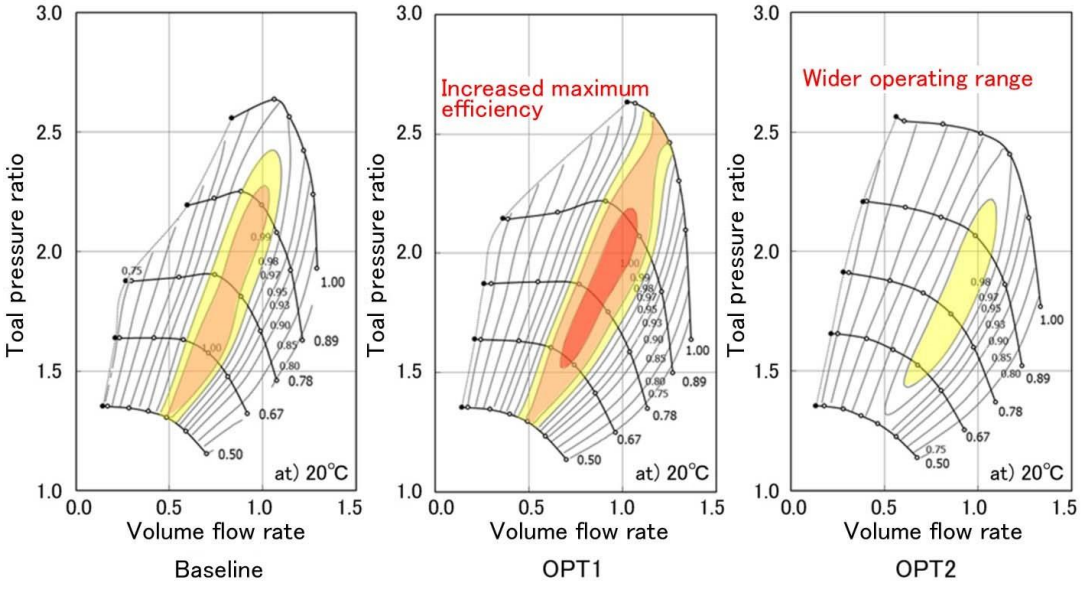

Figure 2.18 Compressor map comparison between baseline and two optimised geometries, where OPT1 features increased peak efficiency and OPT2 a wider operating range [102]

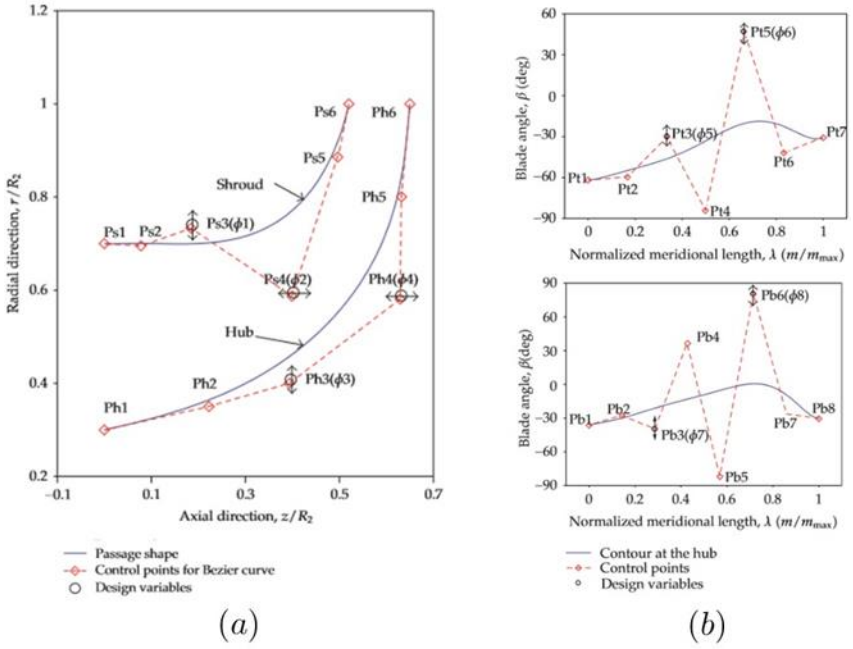

Figure 2.19 (a) Parameterization of the flow passage. (b) parameterization of camber curves defined at near-hub and near-shroud.[12]

The objective function is minimized during the optimisation function. Therefore, the maximum efficiency is obtained when the value of $1-\eta_{t-t}$ is minimized. However, the expected range was set within 1% of the prescribed pressure ratio. Thus, $max\left[\left(\frac{|\Pi-\Pi_{req}|}{\Pi_{req}}-0.1\right),0\right]$ could introduce a positive value of the penalty into the objective function when the pressure ratio error is over 1%. The optimisation process delivered a compressor design with the efficiency improvement of 1.4% while pressure ratio error is less than 1%.

The combined optimisation process – DOE, ANN and GA was also applied to optimise the turbine blade in Van den Braembussche' study [103]. However, his aim was to demonstrate the capability of this combined optimisation method to solve complex design problem by considering multiple operating points and multidisciplinary, referred as multi-objective optimisation. He reckoned that a good design must not only provide good off-design performance which could be delivered by multipoint optimisation, but respect the mechanical and manufacturing constraints, referred as multidisciplinary. For each operating point, four penalty terms were introduced to concern the mechanical stresses, efficiency,

mass flow, and Mach number, respectively. Although an improved turbine design was achieved, he found that the outcome of this combined optimisation process still depends on the input of the designer in terms of a careful selection of design parameters, a clear definition of objectives and constraints as well as validation of results.

Multi-objective optimisation of a centrifugal compressor impeller was also performed by Kim et al. [104] with the target of maximising both pressure ratio and isentropic efficiency of a vaneless radial compressor. A fast and elitist non-dominated sorting genetic algorithm (NSGA-II) with a ε-constraint strategy for local search coupled with a surrogate model was used for this multi-objective optimisation. Four design variables are selected from two control points for constructing the shroud and hub contours. By doing so, the meridian flow path is optimised to achieve the required targets. The optimisation process starts with a DoE. Then, the objective functions at each DoE point are evaluated to create the radial basis neural network. Subsequently, the neural network inputs – four variables are optimised by NSGA-II to get the maximum outputs of the neural network. The detailed optimisation procedure is shown in Figure 2.20.

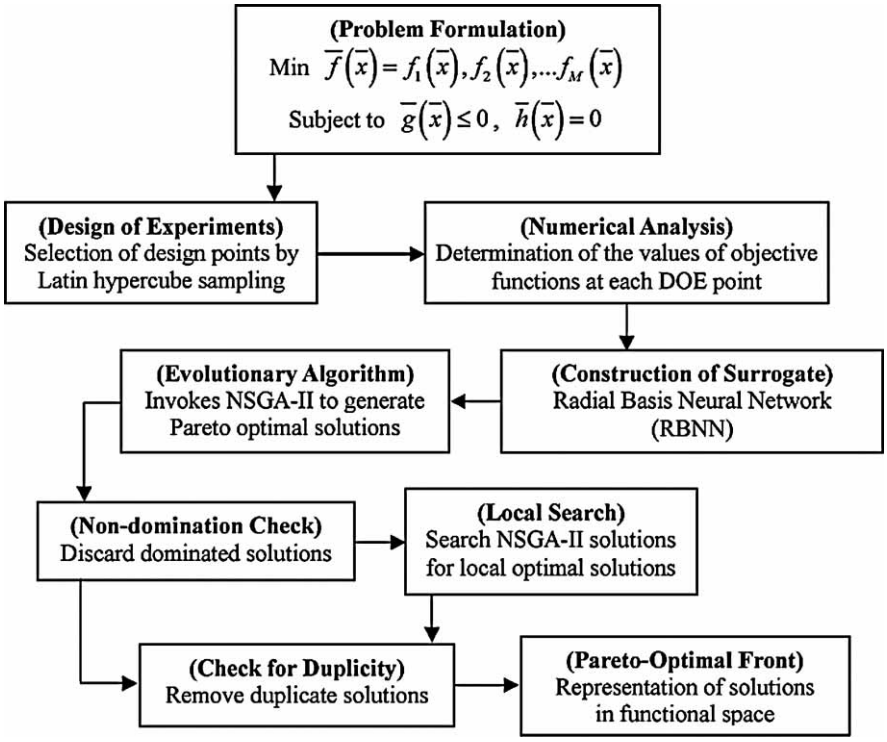

Figure 2.20 Multi-objective optimisation procedure [104]

The outcome of the hybrid multi-objective optimisation is a Pareto-optimal solution, shown in Figure 2.21. It reveals the competing nature of pressure ratio and isentropic efficiency, where any improvement of optimisation objective leads to the deterioration of the other optimisation objective. The conclusion made by Kim is that the proposed surrogate-based multi-objective evolutionary optimisation can be effectively used for various turbomachinery applications including fans, turbines, pumps, and so on.

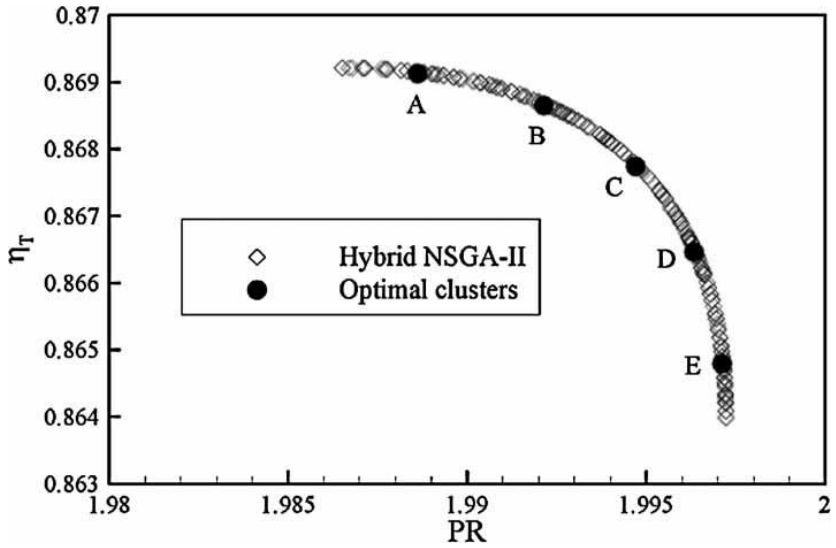

Figure 2.21 Pareto-optimal solution [104]

2.4 Summary

Firstly, this chapter reviewed the fundamentals, research and studies of favorable WHR technologies in the public domain. Give that the exhaust-gas heat energy consists of kinetic energy, pressure energy, and thermal energy, the exhaust-gas heat-recovery methods can be categorized into indirect and direct recovery approaches.

Regarding indirect recovery approaches, the heat contained in IC engine exhaust gas will pass through a binary fluid system, typically a heat exchanger, and harvest by a separate bottoming power cycle. The advantage of the indirect recovery approaches is that the negative effect of the WHR applications on the primary cycle is minimized. This is, the only interaction between the primary cycle and the indirect WHR bottoming cycle is the back pressure caused by the

pressure drop of the heat exchanger, typically which is minor. Thus, three favorable indirect heat recovery technologies were reviewed – automotive thermoelectric generators (ATEG), Rankin bottoming cycle, and pressurized Brayton cycle.

In conclusion, ATEG is a potential exhaust-gas heat-recovery system. To improve the performance of ATEG, many promising thermoelectric materials with high conversion efficiency are in development stage. However, the poor conversion efficiency of ATEGs, typically lower than 4%, is still the primary challenge currently which hinder their adoption in the on-road market [34]. Without significant breakthroughs, the thermoelectric generator might be unfeasible to install in the exhaust system of the vehicle for the purpose of recovering the wasted energy.

On the other hand, although Rankine bottoming cycle has relatively complex configuration, the resulting net power is desirable. In an application to utilize low-grade heat power conversion, such as the application for the automotive use, the organic working fluids with low boiling points should be selected to achieve better performance. Several studies show that the Organic Rankine cycle, as a bottoming WHR cycle, is able to deliver up to 12% increase in efficiency. However, the manufacturing cost, packaging issue, weight, and working fluid safety concerns of ORCs are primary challenges for its adaption on the transport engine.

Given the complexity of the conventional Rankin bottoming cycle, a simplified cycle - the pressurized Brayton cycle was proposed and studied as an alternative exhaust-gas heat-recovery system. This technology is more favorable for gas turbines, instead of IC engines. This is due to the wide operating range in terms of the exhaust mass flow in IC engines. In addition, the poor gas-gas heat exchanger performance is the barrier to the successful application of this technology for automotive use.

Direct recovery approaches directly utilize the exhaust gas as the working fluid to recover the wasted energy. Typically, an expender is introduced into the exhaust gas system to further expand the exhaust gas. By doing so, all sorts of exhaust

gas energy can be exploited to some extent. However, the resulting downside is the non-negligible back pressure generated by the expender.

The simplest direct recovery approach is the turbo-compounding system, which just implement a power turbine immediately downstream of the turbocharged engine. This technology has been heavily applied on heavy-duty engines for aircraft piston engines, boat and train powertrains, and the heavy-duty engines for trucks, while rarely for the road vehicle engines due to its downsides, such as low overall turbine efficiency, high resulting back pressure, limited achievable expansion ratio, etc.

In order to overcome the drawbacks of the turbo-compounding system, one or several stages of cooling and compression processes were introduced downstream of the power turbine in order to reduce the resulting back pressure and increase the achievable expansion ratio. The proposed system is referred as inverted Brayton cycle (IBC). This technology was extensively studied as the WHR bottoming cycle for gas turbine and decent power recovery capability was expected. In addition, various thermodynamic cycles were combined with IBC in order to further increase the recovered power. Regarding IBC applications for IC engines, only few related researches were found in public domain. The limited knowledge about IBC were gained by these researches.

In summary, the indirect exhaust-gas heat-recovery applications include ATEGs, ORCs and pressurized Brayton cycle. ATEGs suffer from the poor conversion efficiency. To be specific, the conversion efficiency of the thermoelectric modules used commercially is less than about 10% and overall efficiency of ATEG devices is about 5 – 10% [105]. However, their advantages are free maintenance, silent operation due to no moving mechanical parts involved, and low resulting engine back pressure. Although ORCs are more attractive considering their heat recovery capability, the cost and size of ORC are primary challenges for its adaption on the transport engine. Moreover, the performance of pressurized Brayton cycle is limited due to the low effectiveness and the large size of the gas-gas heat exchanger.

In contrast, the thermal characteristic of the inverted Brayton cycle seems quite suitable for automotive use due to its high performance and simple configuration. Although extensive parametric studies have been presented to discover the effect of various IBC boundary conditions in the gas turbine system, very little effort has been made to study the potential power system comprising a turbocharged engine and the inverted Brayton cycle. Moreover, there is no any experiment test to demonstrate the IC engine performance improvement by employing IBC as the bottoming heat recovery system.

Chapter 3 – IBC Thermodynamic Modelling and Analysis

3.1 Introduction

In this chapter, a parametric study of the inverted Brayton cycle (in isolation from the primary cycle) will be presented based on different boundary conditions. Following this, pressurized Brayton and turbocompounding systems, which can make use of conventional radial turbomachinery to recover thermal energy in a Brayton bottoming cycle, will be compared with IBC by using a turbocharged gasoline engine (Otto cycle) model as a base. All three alternative heat recovery systems are demonstrated in Figure 3.1.

All thermodynamic models in this chapter are constructed using finite-time thermodynamics (FTT). Since classical thermodynamic analyses based on thermodynamic equilibrium do not consider the irreversibilities originating from finite-time and finite-size constraints, the finite-time thermodynamic approach is an important alternative method to optimise and analyse real thermal system [106-108]. In the irreversible Otto cycle model to be presented, the following internal irreversibility are included: engine compression and expansion efficiencies, temperature variant specific heats, pressure drop during the heat addition and rejection processes, heat loss through the cylinder wall, frictional loss as a function of mean piston velocity and a heat leak rate. The isentropic efficiencies of the turbine and compressor are applied to describe the actual

behaviour of the compressor and turbine. The intent is to demonstrate the cycle power output and thermal efficiency when various parameters of the inverted Brayton cycle are varied. The inverted Brayton cycle is also compared with pressurized Brayton cycle and turbo-compounding system to assess the advantages and disadvantages to this technique.

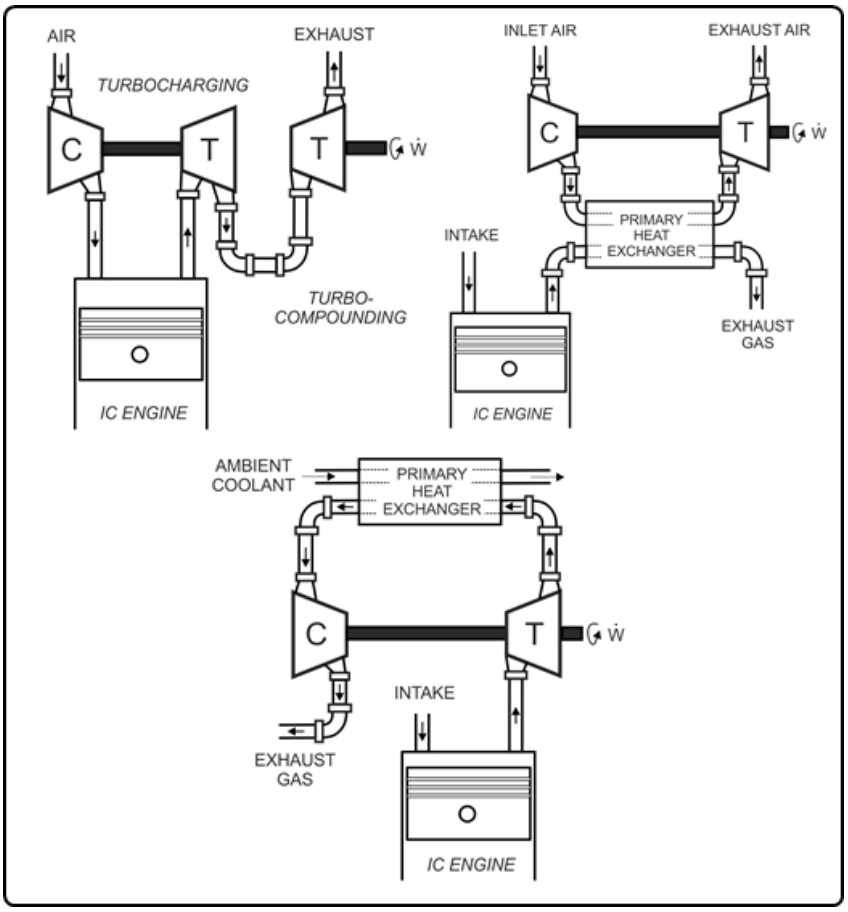

Figure 3.1 [Top left] Turbocharging & Turbo-compounding; [Top right] Pressurized Brayton; [Bottom] Inverted Brayton

IBC system also is considered with the data from a 2.0L gasoline turbocharged engine operating over a drive cycle to quantify its benefits. The IBC thermodynamic model is still constructed using FTT. The outlet boundary conditions of the IBC thermodynamic model are fixed as the ambient, while its inlet boundary conditions are set using experimental exhaust data taken from a turbocharged vehicle progressing through the worldwide harmonized light vehicles test procedures (WLTP). This real-world on-road test procedure – WLTP defines a global harmonized standard for determining the levels of pollutants,

CO2 emissions, and fuel consumption. It is published due to the growing gap between official laboratory and real-world on-road emission value [109]. The influences of both single stage and two-stage IBC systems on the objective engine have been presented in this chapter. Further, an optimisation of the turbine pressure ratio in the single stage IBC has been performed to reveal the corresponding maximum benefits.

It should be noted that the contents from Section 3.2 to Section 3.5.3 in this chapter have been published as a journal paper [110] in Journal of Engineering for Gas Turbines and Power. Furthermore, the contents in Section 3.5.4 have been published as a journal paper [111] in Journal of Engineering for Gas Turbines and Power.

3.2 Principle of inverted Brayton cycle

In this chapter, the performance of the IBC with various design parameters will be analysed as a bottoming exhaust-gas heat-recovery cycle integrated with a turbocharged engine. The schematic layout of proposed combined is shown in Figure 3.2.

As shown in Figure 3.2, the inverted Brayton cycle consists of a turbine further exploiting the exhaust gas available from the upper cycle, a heat exchanger removing the residual heat of the expanded gas, and a compressor boosting the exhaust gas up to atmospheric condition. As only one compressor is employed in IBC in Figure 3.2, this proposed bottoming cycle is referred as single-stage IBC.

The temperature-entropy diagram of the combined cycle power plant of the turbocharged engine and three-stage IBC system is shown in Figure 3.3. The subscript ‘s’ denotes an ideal state at the actual ending pressure of each process but at the same entropy value as the beginning thus describing the idealized processes. IBC is represented by the power cycle $\mathbf{6} \rightarrow \mathbf{7} \rightarrow \mathbf{8} \rightarrow \mathbf{9}$. The rest of the temperature-entropy diagram represent the temperature and entropy changes in the engine turbocharger and combustion chambers. The main processes of the IBC system are listed as below:

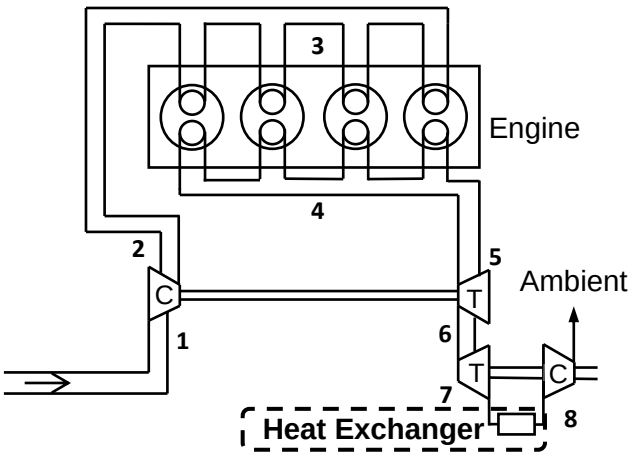

Figure 3.2 A combined system consisting of a turbocharged engine and single-stage inverted Brayton cycle

1. The expanded exhaust gas stream discharged by the turbocharged turbine is further expanded in the IBC turbine (T) section to below ambient pressure, thereby reclaiming energy from the exhaust. The mechanical power extracted during sub-atmospheric expansion is partially utilized to supply the subsequent compression process and overcome any parasitic energy loss of the IBC turbomachinery, such as the heat loss and mechanical friction. The rest, referred as the IBC net power, is converted into either the electric power by an electricity generator connected to the IBC turbo machine mechanically, or the shaft work which is added to the engine torque directly.

2. The remainder of the heat in the exhaust after expansion is rejected by the downstream heat exchanger. The more effective the heat rejection, the greater the performance of the IBC system. That is, the lower the temperature of the exhaust gas after the heat exchanger the less the work required by IBC compressor for the same pressure ratio. However, the existence of pressure loss across the heat exchanger can deteriorated the system performance by lowering the inlet pressure of the IBC compressor and, therefore, increasing the energy for the corresponding compression process. Therefore, the heat exchanger effectiveness and the pressure

loss are considered as significant influences when considering the IBC performance.

3. The cooled gases are re-compressed back up to the atmospheric pressure in the compressor section (C) and discharged to the ambient.

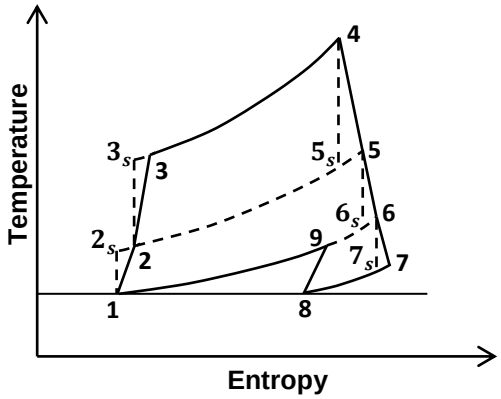

Figure 3.3 Temperature and Entropy Diagram of the Turbocharged Engine with a single-stage IBC

3.3 Model Description

The turbocharged, gasoline (Otto cycle) engine was selected as a basis to perform a comparison between three alternative heat recovery cycles. The three alternatives considered are the inverted Brayton cycle, the turbocompounding system, and the pressurized Brayton cycle. However, the inverted Brayton cycle could equally be applied to other engine types, including non-turbocharged range extenders and large diesel engines which are more likely to operate at a fixed speed, high-load point suitable for heat recovery. The layout of the thermodynamic model of the turbocharged engine with the inverted Brayton cycle is illustrated schematically in Figure 3.4. The bottoming cycle is shown with three stages of compression processes as an example. To be specific, the model is composed of three components as shown in Figure 3.4: a 2-litre four-stroke, four-cylinder gasoline engine, a turbocharger with a single stage of compression and expansion and the inverted Brayton cycle with three stages compression

processes. The corresponding temperature-entropy diagram of the process is shown in Figure 3.5.

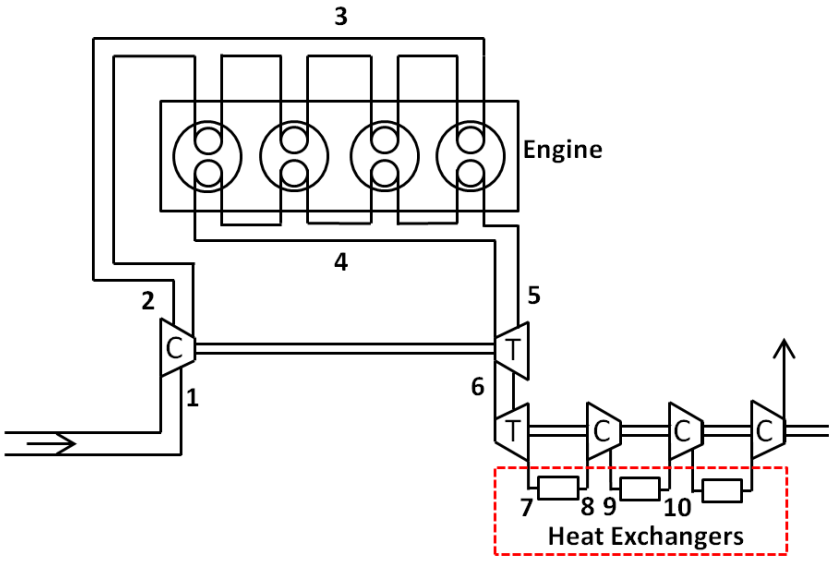

Figure 3.4 Schematic of the turbocharged engine with three stages of IBC

Based on Figure 3.5, the entire processes of this combined system can be described as below. The air enters the cycle at state 1 through the turbo compressor, where it is pressurized and then leaves at state 2 into the Otto cycle. The air standard Otto cycle consists of four internally reversible branches: an isentropic compression process $\mathbf{2} \rightarrow \mathbf{3_s}$, a constant volume heat addition process $\mathbf{3_s} \rightarrow \mathbf{4}$, an isentropic expansion process $\mathbf{4} \rightarrow \mathbf{5_s}$ and a constant volume heat rejection process$\mathbf{5_s} \rightarrow \mathbf{2}$. Considering the internal irreversibility during the real compression and expansion processes, the high pressure gas at state 2 is compressed to state 3, and is heated at a constant volume to state 4, and is expanded to state 5. It subsequently expands and drops in temperature over the turbocharger turbine before leaving at state 6. The effect of a pressure drop inside the cylinder on the performance of the Otto cycle is presented in Figure 3.6. At state 6, the gas still carries a large amount of thermal energy, which is able to drive the turbine to produce further work. For the inverted Brayton cycle, this means that the gas is over-expanded within the next turbine to state 7 where the pressure of the gas can be below atmosphere. The depressurized gas then passes through an intercooler to remove the remainder of the heat (state 8)

before the gas is compressed back up to atmospheric pressure by one or more compressors.

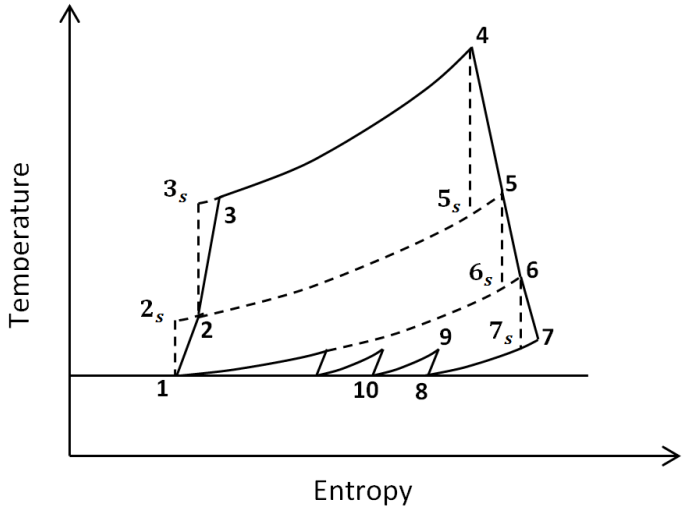

Figure 3.5 Temperature and Entropy diagram of a turbocharged engine with IBC

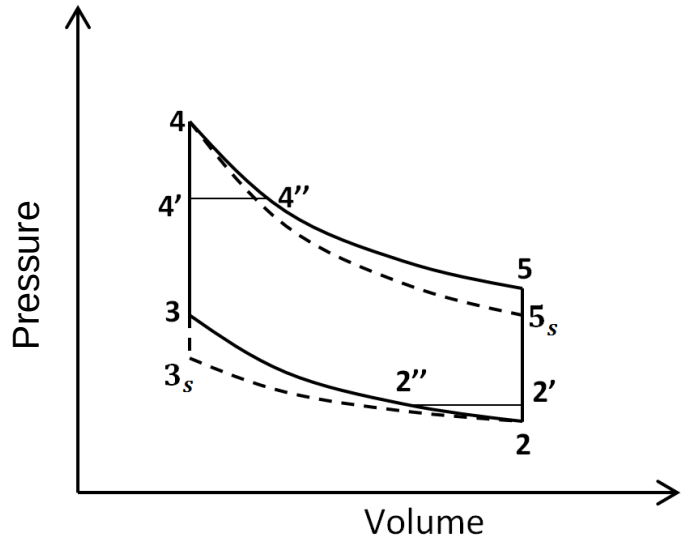

Figure 3.6 P-V diagram of the air standard Otto cycle

3.4 Thermodynamic Model

3.4.1 IBC Turbine

In the ideal cycle, the working fluid is assumed to behave as an ideal gas with constant specific heats. However, in order to improve the accuracy of the predicted IBC performance, the specific heat with constant pressure (C_p) varying with temperature is introduced in the IBC thermodynamic model. According to reference [108], for temperature range from 300 K to 3500 K, the specific heat with constant pressure can be expressed as a function of temperature as follows:

$$C_p(T) = 2.506 \times 10^{-11}T^2 + 1.454 \times 10^{-7}T^{1.5} - 4.246 \times 10^{-7}T + 3.162 \times 10^{-5}T^{0.5} + 1.3303 - 1.512 \times 10^{-4}T^{-1.5} + 3.063 \times 10^{5}T^{-2} - 2.212 \times 10^{7}T^{-3} \quad (3.1)$$

The relation between specific heat at constant pressure and constant volume is defined as:

$$C_v = C_p - R_g \quad (3.2)$$

where $R_g = 0.281$ kJ/(kg K) is the gas constant of the working fluid.

Any of reversible adiabatic processes can be broken up into a large number of infinitesimally-small processes with an infinitesimally-small change in temperature dT and pressure dp of the working fluid. Thus, for the ideal compression of the compressor and expansion of the turbine, the equation in terms of an infinitesimally-small process can be written as follows,

$$\frac{p^{(k-1)/k}}{T} = \frac{(p+dp)^{(k-1)/k}}{T+dT} \quad (3.3)$$

where *k* is the specific heat ratio and equals to C_p/C_v .

Specific heat ratio k can be regarded as a constant for each of these infinitesimally-small processes when k varies with temperature. Therefore, for

the reversible adiabatic process between states i and j, the equation can be derived after natural logarithm processing of

$$C_p(T)\mathrm{In}\,(T_j/T_i) = R_g\mathrm{In}\,(p_j/p_i) \tag{3.4}$$

where the temperature in the equation of C_p is $T = (T_j - T_i)/\mathrm{In}(T_j/T_i)$.

Therefore, the equation for isentropic process can be written as

$$C_p(T)\mathrm{In}\frac{T_{7s}}{T_6} = R_g\mathrm{In}\,\frac{1}{r_{it}} \tag{3.5}$$

where r_{it} is the expansion ratio across the turbocharger turbine. The subscript 's' denotes an ideal state at the actual end of each process.

Therefore, knowing the turbine inlet temperature and the turbine pressure ratio, the idealized outlet temperature of the turbine, T_{7s}, can be determined by the previous equation, thereby calculating the real outlet temperature T_2.

The turbine is considered as an open system due to mass flow across its boundaries. Thus, the specific work produced by the turbine is

$$W_{it} = h_6 - h_7 = \eta_{it}\int_{T_{7s}}^{T_6} C_p(T)\,dT \tag{3.6}$$

where η_{it} is the isentropic efficiency of the IBC turbine.

3.4.2 Heat Exchanger

A simple counter-flow heat exchanger built by the Number of Transfer Units (NTU) method is employed with the consideration of the pressure loss. The NTU is utilized to calculate the rate of heat transfer in the heat exchanger and, therefore, yield the exhaust temperature at the heat exchanger outlet, when there is insufficient information to the perform a high-level accurate simulation. In this considered thermodynamic model, it is assumed that the NTU, defined as Eq. 3.7, is a fixed value during the entire WLTP driving cycle.

$$NTU = \frac{1}{C_r - 1} \ln\left(\frac{\varepsilon - 1}{\varepsilon\, C_r - 1}\right) \tag{3.7}$$

where ε is the heat exchanger effectiveness and C_r is the ratio of heat capacity rates.

The heat capacity rate is defined as the quantity of heat absorbed or released per unit temperature change per unit time for a certain mass flow rate. Therefore, C_e and C_{cool} for the exhaust gas and the coolant respectively are expressed as Eq. 3.8, and denoting the smaller one as C_{min} and the larger one as C_{max}.

$$\begin{aligned} C_e &= \dot{m}_e * C_p(T) \\ C_{cool} &= \dot{m}_{cool} * C_{pcool} \end{aligned} \tag{3.8}$$

where $\dot{m}_e$ is the mass flow rate of the exhaust gas. $\dot{m}_{cool}$ is the coolant mass flow rate. C_{pcool} is the specific heat capacity at constant volume for the coolant.

Therefore, the ratio of heat capacity rates is defined as follows,

$$C_r = \frac{C_{min}}{C_{max}} \tag{3.9}$$

In the thermodynamic model considered in this chapter, a design operating point for the heat exchanger have been specified to calculate the NTU based on Eq. 3.7. Then, for each operating point the C_r can be re-calculated by the Eqs. 3.8 and 3.9. As the NTU is assumed as a constant at the entire WLTP driving cycle, the corresponding heat exchanger effectiveness can be calculated as follows,

$$\eta_{ex} = \frac{1 - \exp[-NTU(1 - C_r)]}{1 - C_r \exp[-NTU(1 - C_r)]} \tag{3.10}$$

Therefore, knowing the heat exchanger effectiveness, exhaust temperature at HE inlet, and the coolant inlet temperature, the exhaust temperature at heat exchanger outlet can be calculated by the following expression,

$$T_{out} = T_{in} - \eta_{ex} (T_{in} - T_{cool}) \tag{3.11}$$

where T_{in} and T_{out} is the temperature at the inlet and outlet of the heat exchanger, respectively. T_{cool} is the coolant inlet temperature.

The reason of why the pressure loss has been considered in this study is that the IBC performance is deteriorated by the present of the pressure loss across the heat exchanger. The pressure drop between the inlet and outlet of the heat exchanger can lower the inlet pressure of the IBC compressor, thereby increasing the power consumed by the IBC compressor to pressurize the exhaust gas from sub-atmospheric pressure to the ambient. In this considered thermodynamic model, the pressure loss across heat exchanger is assumed as a quadratic function of the mass flow rate, given as follows,

$$p_{loss} = A * \dot{m}_e{}^2 \tag{3.12}$$

where p_{loss} is the pressure loss and A is coefficient of the pressure loss.

The coefficient of the pressure loss is calculated by Eq. 3.12 with the exhaust mass flow rate and the pressure loss at the design operating point and fixed as a constant at the whole WLTP driving cycle. Thus, for each operating point the corresponding pressure loss can be calculated by Eq. 3.12 with the corresponding exhaust mass flow rate.

3.4.3 IBC Compressor

As in the case for the turbine, the equation for the isentropic compression process can be written as:

$$C_p(T)\ln\frac{T_{9s}}{T_8} = R_g \ln r_{ic} \tag{3.13}$$

According to Eq. 3.13, the idealized outlet temperature of the compressor, T_{4s}, can be deduced by the compressor ratio and the compressor inlet temperature, thereby calculating the real outlet temperature T_4.

As the compressor is an open system, the specific work by the compressor can be expressed as

$$W_{ic} = h_4 - h_3 = (1/\eta_{ic}) \int_{T_3}^{T_{4s}} C_p(T)\, dT \tag{3.14}$$

where η_{ic} is the isentropic efficiency of the IBC compressor.

Since the outlet pressure of the bottoming compressor is assumed as 1.05 bar, the pressure ratio across all the compression processes in IBC system, r_{mc} , is determined by the turbine outlet pressure termed as subatmospheric pressure p_{low}. The relation can be written as: $r_{ict} = 1.05/p_{low}$. According to reference [84], in order to maximize the power extracted by the inverted Brayton cycle, the optimal split of pressure between more than one compressor stages is considered as

$$r_{ic} = {r_{ict}}^{1/n} \tag{3.15}$$

where *n* is the number of compressors stages in IBC system.

Since there are *n* stages of compressors, the total IBC compression specific work is

$$W_{ict} = \underbrace{W_{8,9} + W_{10,11} + W_{12,13}}_{n} \cdots\cdots \tag{3.16}$$

3.4.4 IBC System Performance

Based on all the analysis above, the IBC net specific work and efficiency is expressed as

$$W_{IBC} = W_{it} - W_{ic}$$
$$\eta_{IBC} = W_{IBC} \Big/ \int_{T_{IBC,oulet}}^{T_6} C_p(T)\, dT \tag{3.17}$$

where $T_{IBC,oulet}$ is the temperature at the IBC outlet, that is, the compressor outlet.

3.4.5 Internal Combustion Engine

Figure 3.6 shows a schematic of the air standard Otto cycle with different modes of irreversibility: cycle 2 $\rightarrow 3_s \rightarrow$ 4 $\rightarrow 5_s \rightarrow$ 2 represents the ideal Otto cycle. According to Mahmoud [107], process 3 $\rightarrow 4'$ is the heat-addition at constant volume while process $4' \rightarrow 4''$ is the heat-addition at constant pressure due to the pressure drop. Similarly, process 5 $\rightarrow 2'$ is the heat-rejection at constant volume while process $2' \rightarrow 2''$ is the heat-rejection at constant pressure. The pressure at state $4'$ and state $4''$ are defined as follows,

$$p_{4'} = p_{4''} = \varepsilon_4 p_4 \tag{3.18}$$

where $\boldsymbol{\varepsilon_4}$ is the pressure drop ratio at state 4 and the range of its value is 0 to 1. Similarly, the pressure at state $\mathbf{2}'$ and state $\mathbf{2}''$ are defined as follows:

$$p_{2'} = p_{2''} = \frac{p_2}{\varepsilon_2} \tag{3.19}$$

where ε_2 is the pressure drop ratio at state 2 and the range of its value is 0 to 1.

Using definitions (18) and (19) along with the thermodynamic relation, it is possible to calculate the temperatures at points $2'$, $2''$, $4'$ and $4''$. The temperatures at these points are written as follows:

$$T_{2,} = T_2 \,/\varepsilon_2 \qquad T_{2,,} = {\varepsilon_2}^{(1-k)/k}\, T_2$$
$$T_{4,} = \varepsilon_4 T_4 \qquad T_{4,,} = {\varepsilon_4}^{(k-1)/k}\, T_4 \tag{3.20}$$

Considering the interval irreversibilities of the heat engine during the compression and expansion processes, the compression and expansion efficiencies are defined respectively as,

$$\eta_c = \frac{T_2 - T_{3s}}{T_2 - T_3} \tag{3.21}$$

$$\eta_e = \frac{T_4 - T_5}{T_4 - T_{5s}} \tag{3.22}$$

Any of reversible adiabatic processes can be broken up into a large number of infinitesimally-small processes with an infinitesimally-small change in temperature dT and volume dV of the working fluid. Thus, the equation for the ideal compression and expansion processes in the cylinder can be written as follows.

$$TV^{k-1} = (T + dT)(V + dV)^{k-1} \tag{3.23}$$

Specific heat ratio *k* can be regarded as a constant for each of these infinitesimally-small processes when *k* varies with temperature. Therefore, for the reversible adiabatic process between states *i* and *j*, the equation can be derived after natural logarithm processing of Eq. 3.23,

$$C_v(T)\mathrm{In}\,(T_j/T_i) = R_g \mathrm{In}\,(p_i/p_j) \tag{3.24}$$

where the temperature of C_v in the equation is $T = (T_j - T_i)/\mathrm{In}(T_j/T_i)$.

Therefore, equations for reversible adiabatic processes 2 → 3_s and 4 → 5_s are respectively as follows

$$C_v(T)\mathrm{In}\frac{T_{3s}}{T_2} = R_g \mathrm{In}\,\gamma \qquad C_v(T)\mathrm{In}\frac{T_4}{T_{5s}} = R_g \mathrm{In}\,\gamma \tag{3.25}$$

where γ is the compression ratio of the engine.

Based on the bypass heat-leakage model advanced by Bejan [106], it is assumed that there exists a constant rate of bypass heat leakage (Q) from the heat reservoir to the heat sink. In this case, the temperature of the heat reservoir and the heat sink is defined as T_4 and T_2 respectively. Thus, the bypass heat leak rate is given by the following expression

$$\dot{Q}_{hl} = C(T_4 - T_2) \tag{3.26}$$

where C is heat leak coefficient.

Given the pressure drop during the compression and expression processes, the heat added to the heat engine consists of the constant volume process 3 → $4'$ and the constant volume process $4' \rightarrow 4''$. Thus, the heat input with the three different modes of irreversibility (pressure drop, internal irreversibility, and heat leak) is given by:

$$(\dot{Q}_O)_{in} = \dot{m}_{air}\left(\int_{T_3}^{T_{4'}} C_v(T)\,dT + \int_{T_{4'}}^{T_{4''}} C_p(T)\,dT + \dot{Q}_{hl}\right) \tag{3.27}$$

where $\dot{m}_{air}$ is the mass flow rate of the intake air.

The heat rejected by the heat engine consists of the constant volume process 5 → $2'$ and the constant volume process $2' \rightarrow 2''$. Thus, the heat output is:

$$(\dot{Q}_O)_{out} = \dot{m}_{air}\left(\int_{T_{2'}}^{T_5} C_v(T)\,dT + \int_{T_{2''}}^{T_{2'}} C_p(T)\,dT + \dot{Q}_{hl}\right) \tag{3.28}$$

For a real Otto-cycle, the heat loss through the cylinder wall is not negligible. Thus, the present approach assumes that the heat loss through the cylinder wall

is proportional to the average temperature of both the working fluid and the cylinder wall. The wall temperature is treated as a constant. So the heat leak is given by the following linear equation

$$\dot{Q}_{loss} = \dot{m}_{air} B(T_3 + T_4 - 2T_0) \tag{3.29}$$

where B is the constant related to heat-transfer, T_0 is the average temperature of the working fluid and cylinder walls, and it is given by, $T_0 = (T_4 - T_3)/\ln(T_4/T_3)$.

Taking into account the friction loss of the piston, Ge [108] recommend that the dissipation term can be represented by a friction force which in a linear function of the velocity, expressed as,

$$f_\mu = \mu v = \mu(dx/dt) \tag{3.30}$$

where μ is a coefficient of friction loss, v is the velocity of the piston, and x is the piston displacement. Then the lost power due to friction is,

$$P_\mu = dW_\mu/dt = \mu(dx/dt)(dx/dt) = \mu(v_{mean})^2 \tag{3.31}$$

where v_{mean} is the mean velocity of the piston.

As the engine in our model is a four-stroke engine, the total distance the piston travels per cycles is,

$$4L = 4(x_1 - x_2) \tag{3.32}$$

where x_1 and x_2 are the piston position at maximum and minimum volume respectively. *L* is the piston stroke length. If the engine operates at N cycles per second, the mean velocity of the piston is,

$$V_{mean} = 4LN \tag{3.33}$$

Due to the four-cylinder engine in our model, the total lost power can be expressed as,

$$P_{\mu} = 4\mu(4LN)^2 \tag{3.34}$$

Thus, the net power of the Otto cycle is

$$(P_O)_{net} = (\dot{Q}_O)_{in} - (\dot{Q}_O)_{out} - P_{\mu} \tag{3.35}$$

The power input of the Otto cycle is

$$(P_O)_{in} = (\dot{Q}_O)_{in} + \dot{Q}_{loss} \tag{3.36}$$

3.4.6 Turbocharger Compressor and Turbine

The thermodynamic models of the compressor and turbine presented in the previous section are utilized to simulate the performance of the turbocharger. Thus, the power required for the turbocharger compressor is

$$P_{tc} = \dot{m}_{air} * (h_1 - h_2) = (\dot{m} * \eta_{tc}) \int_{T_1}^{T_{2s}} C_p(T)\, dT \tag{3.37}$$

Where η_{tc} is the isentropic efficiency of the turbocharger compressor.

The required power of the turbocharger compressor is provided by the turbine. Therefore, the power done P_{tt} by the turbine is expressed as

$$\begin{aligned} P_{tc} = P_{tt} &= (\dot{m}_e * \eta_{tt}) \int_{T_{6s}}^{T_5} C_p(T) dT \\ &= \dot{m}_e \int_{T_6}^{T_5} C_p(T) dT \end{aligned} \tag{3.38}$$

where η_{tt} is the isentropic efficiency of the turbocharger turbine.

3.5 Thermodynamic Simulation Results and Discussion

In order to perform this study, the following assumptions have been made:

- The effect of all duct pressure losses and leaving losses external to rotating components are neglected. In addition, fuel added on mass flow rate is ignored, that is, $\dot{m}_e$ equals to $\dot{m}_{air}$.

- The pressure and temperature of the intake air are considered as, T_1=T_{am}=300 K, p_1=p_{am}=1.013 bar. The exhaust pressure of each model is taken as 1.04 bar.

- The maximum temperature at the inlet of each turbine is considered as 1300 K due to the limitation of the maximum temperature that conventional radial turbines can withstand, while the maximum temperature in the cylinder is chosen as 2200 K according to the material limits of the existing components.

- In terms of IBC, the maximum turbomachinery efficiencies are chosen as 0.85 and 0.9 for the compressor and turbine respectively and the mechanical efficiency of the turbo machines is assumed to be 0.95. The turbocharger turbine and compressor isentropic efficiencies are assumed as a constant 0.75. The heat loss or gain on the turbomachinery components is not considered.

Table 3.1 Engine parameters

Description	value
Compression Ratio, γ	8
Exhaust mass flow rate, $\dot{m}_e$	0.15 kg/s
Piston stroke length, L	$1 \times 10^{-2}\ m$
Engine speed, N	3000 rpm
Pressure drop ratio at states 2, ε_2	0.6
Pressure drop ratio at states 4, ε_4	0.6
Engine compression and expansion efficiencies, η_c and η_e	0.97
Coefficient of friction loss, μ	12.9 $N \cdot s/m$
Heat leak coefficient, C	0.05 $kJ/kg \cdot K$
Heat loss coefficient, B	0.2 $kJ/kg \cdot K$

- A gas-liquid heat exchanger is adopted in the IBC to reject heat. The temperature of the liquid coolant is assumed to be 300 K.

- A four-stroke, four-cylinder turbocharged gasoline engine is established as the baseline model. The engine parameters are listed in Table 3.1. All coefficients of various energy losses in this thermodynamic model have been calibrated with the GT-power model which is built based on the same engine geometry

3.5.1 Inverted Brayton Cycle Parametric Study

This section will consider the performance of the Inverted Brayton cycle in isolation from the engine. The *T-s* diagram for a three-stage intercooled inverted Brayton cycle has been shown in Figure 3.5, represented by the cycle from state 7 to the final exhaust outlet. According to previous assumptions, the inlet pressure of the turbine, p_6 , and the outlet pressure of the compressor, p_{final} , are considered as 1.013 and 1.04 bar respectively. The baseline inlet temperature of the inverted Brayton cycle is assumed as 1000 K since the inverted Brayton cycle is adopted downstream of the engine and, therefore, high temperature exhaust gas flows directly into the IBC turbine. The isentropic efficiencies are chosen as 0.75 and 0.8 for the compressor and turbine respectively. An effectiveness of 0.95 may be considered as the maximum value attainable in a gas-to-liquid heat exchanger adopted between each component in the inverted Brayton cycle.

Figure 3.7 shows the effect of the number of IBC compression stages on the specific work for six values of subatmospheric pressure p_{low}. This reveals that introducing an extra compression process can contribute to an increase in the specific work whatever the subatmospheric pressure is.

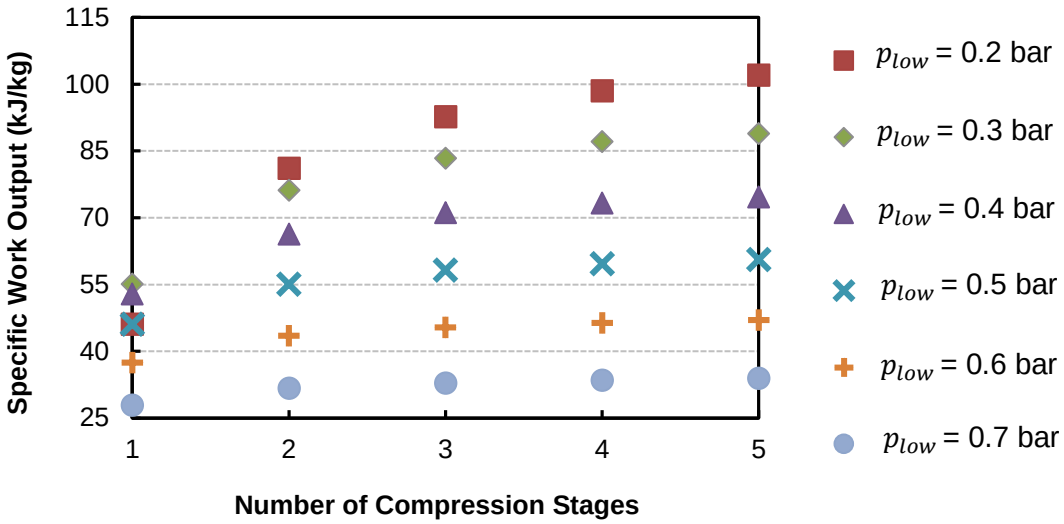

Figure 3.7 System specific work output as a function of subatmospheric pressure and number of IBC compression stages

The improvement caused by the additional IBC stages can be explained as following. Typically, actual compression process of the centrifugal compressor is defined as polytropic process due to the heat loss during the process. The corresponding *p-v* diagrams is shown in Figure 3.8. However, there is a compression process that requires less amount of work, referred as isothermal compression. This type of compression process occurs when the fluid temperature remains constant during the compression. The pressure versus volume variation for isothermal compression is also illustrated in Figure 3.8. Although isothermal compression is able to minimize the compressor work, it is difficult to achieve isothermal compression by centrifugal compressors due to the difficulty of implementing sufficient cooling during the whole process. Thus, in practice, multiple stages of intercooling and compressors are introduced to approximate the isothermal compression. By doing so, the fluid is cooled between two compressions instead of during the compression in isothermal compression. In Figure 3.8, the red line shows the process path of introducing one-stage intercooling and compression. It should be noted that cooling process is assumed as isobaric process.

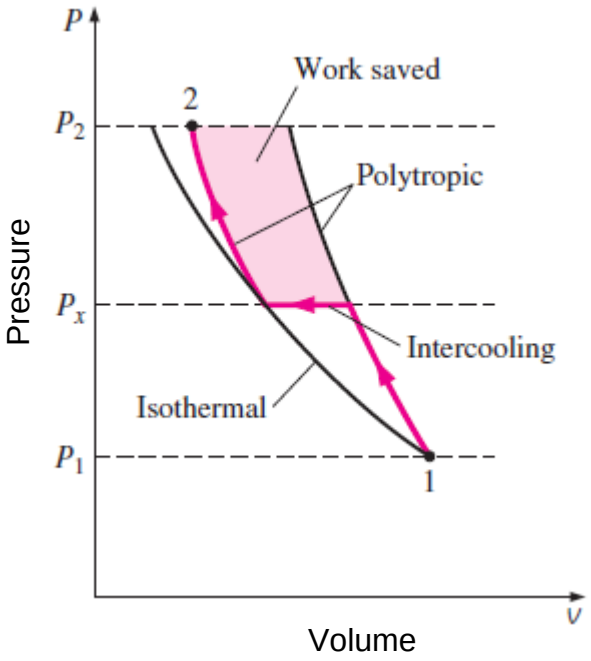

Figure 3.8 Comparison of the process paths of isothermal, polytropic, and two-stage intercooling compression [112]

Figure 3.8 shows that the process path of three afore-mentioned compression for the same inlet state and exit pressure. Regarding the two-stage compression with intercooling, the gas is compressed in the first stage from P_1 to an intermediate P_x, cooled at constant pressure to the initial temperature T_1, and finally compressed to P_2 by the second stage of the compression. Comparing with the one-stage polytropic compression, the coloured area represents the work saved as a result of an additional compression with intercooling. Similarly, for same overall compression ratio, introducing compression stages with intercooling can reduce the power consumption of compression process, thereby increasing IBC net power output.

However as shown in Figure 3.7, the thermal efficiency increment diminishes significantly moving from one to two stages and beyond. Moreover, the performance improvement is more sensitive to the number of compression stages when a lower sub-atmospheric pressure is achieved. Considering the cases with the same number of compression stages, it can be found that a decrease in the sub-atmospheric pressure results in an increasing turbine expansion ratio and thus a significant rise in performance. The exception is the case of the single-

stage IBC where a sub-atmospheric pressure of 0.2 produces less power output than that of 0.3 or even 0.4. Note that this characteristic is heavily dependent on the efficiency of the IBC components and the exhaust temperature.

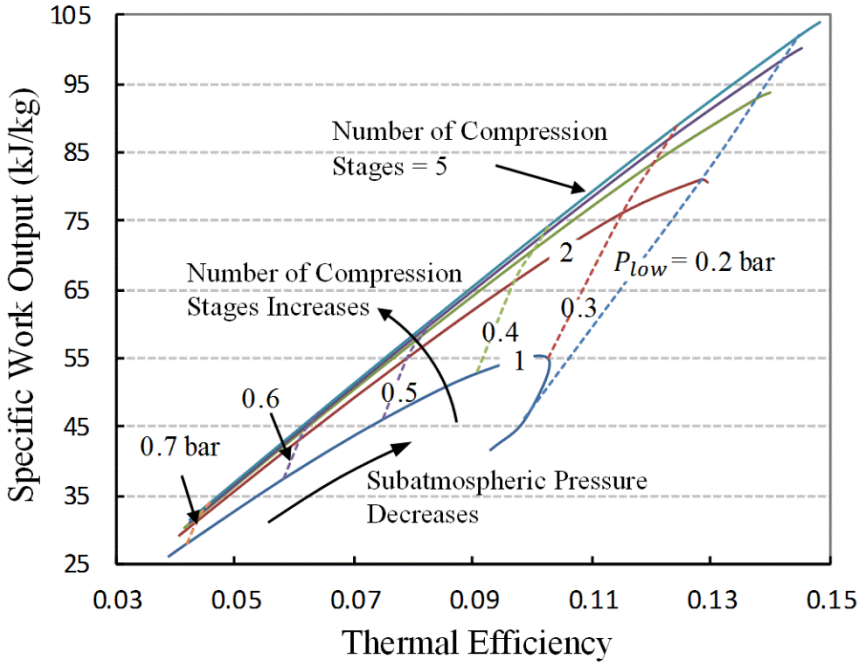

Figure 3.9 Effect of compression stages and subatmospheric pressure on the thermal efficiency

In order to further reveal the performance characteristics of the inverted Brayton cycle, the $W_{IBC} \sim \eta_{IBC}$ curves are plotted in Figure 3.9, where W_{IBC} and η_{IBC} are, respectively, the specific work output and thermal efficiency of the IBC. The $W_{IBC} \sim \eta_{IBC}$ curves are presented for different numbers of the compression stages. For a fixed sub-atmospheric pressure (or fixed turbine expansion ratio), there is only a relatively slight change in the thermal efficiency with an increase in the number of compression stages. The maximum efficiency change is approximately 3.6 percentage points in the case of a sub-atmospheric pressure of 0.2 bar when the single-stage IBC is compared with that of two stages of compression. The thermal efficiency strongly depends on the sub-atmospheric pressure at any chosen value of compression stages. A six-percentage point improvement in the thermal efficiency for the single-stage IBC is expected as the working fluid at the outlet of the turbine is depressurized from 0.7 bar to 0.2 bar. It should also be noted that, similar to the trend of the specific work output

observed in Figure 3.7, a thermal efficiency drop for the single-stage IBC is predicted when the sub-atmospheric pressure decreases from 0.3 to 0.2.

Regarding the number of compression stages, Figure 3.9 shows that the largest specific work rise is observed between one and two stages of IBC. This suggests that three compression stages or fewer appears most sensible. However, the number of compression processes has a weaker effect on the thermal efficiency of the IBC (in isolation). Moreover, an extra stage needs to adopt one more compressor and heat exchanger with the associated additional complexity and cost. Hence, the single-stage inverted Brayton may be considered as a good cost-to-benefit solution for applying a bottoming cycle for exhaust gas energy recovery in automotive applications.

The variables that influence the thermal efficiency and the specific work of the single-stage inverted Brayton cycle are the isentropic efficiency of compression and expansion, η_{ic} and η_{it} , the inlet pressure and temperature of the inverted Brayton cycle, p_6 and T_6 , subatmospheric pressure p_{low} , the turbine expansion ratio r_{it} and the effectiveness of the heat exchanger η_{ex} . Therefore, a numerical sensitivity study of the single-stage configuration is presented below to demonstrate the influence of the afore-mentioned variables. The baseline boundary conditions are assumed as T_6 = 1000 K, η_{ic} = 0.75, η_{it} = 0.8, η_{ex} = 0.95, and p_6 = 1.013 bar. The rest of boundary conditions are considered as the same as that of previous analysis considering the multi-stage IBC.

3.5.1.1 Effect of the inlet temperature T_6 and the subatmospheric pressure p_{low} (r_{it}) at fixed η_{ic} (0.75), η_{it} (0.8), η_{ex} (0.95) and P_6 (1.013 bar)

Since the inlet pressure p_6 is fixed for this analysis, the turbine expansion ratio r_{it} is a fixed value when the subatmospheric pressure p_{low} is assumed. Figures 3.10 and 3.11 illustrate the specific work and thermal efficiency as a function of the turbine outlet pressure p_{low} , for different inlet temperatures T_6 . The line that is highlighted with symbols indicates the baseline operating condition. Figure 3.10 shows that the specific work output is a monotonically increasing function of the

IBC inlet temperature T_6 . Simply, the higher the IBC inlet temperature, the larger the amount of energy carried by the exhaust gas and consequently the more power that can be exploited by the inverted Brayton cycle. Moreover, a large reduction in the specific work can be expected when the inlet temperature decreases significantly. For example, from 1400 K to 1000 K with the sub-atmospheric pressure at 0.2 bar (and an expansion ratio of 5.06), the reduction in specific work is 133.13 kJ/kg. Moreover, when the inlet temperature descends below to a certain value, there is no work generated by the IBC. For example, in this model, if T_6 decreases below the threshold value of 544 K, the IBC net specific work is negative at any chosen value of the sub-atmospheric pressure.

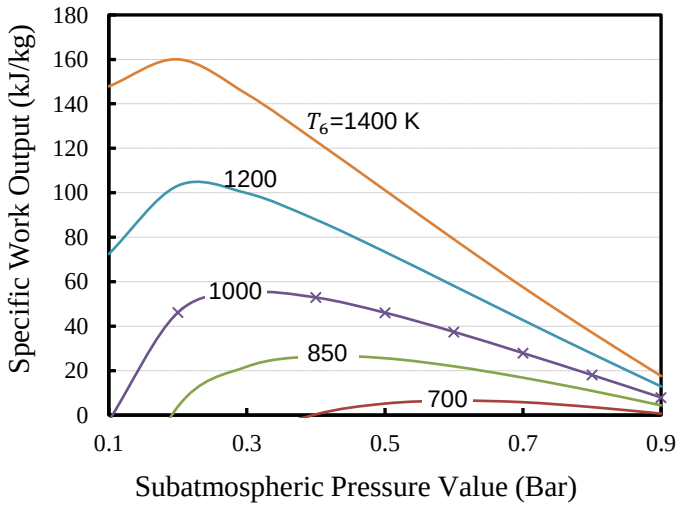

Figure 3.10 Specific work output variation depending on the bottoming turbine inlet temperature and subatmospheric pressure

It can also be observed in Figure 3.10 that for a given inlet temperature T_6 , as the p_{low} decreases, the power output peaks and then decreases. The sub-atmospheric pressure p_{low} that produces maximum power increases with a reduction in the IBC inlet temperature T_6 . That is, maximum power is obtained for a turbine pressure ratio which tends to be lower when T_6 is lower. Therefore, there is an optimum sub-atmospheric pressure (or turbine pressure ratio) which changes with the variation of the inlet temperature.

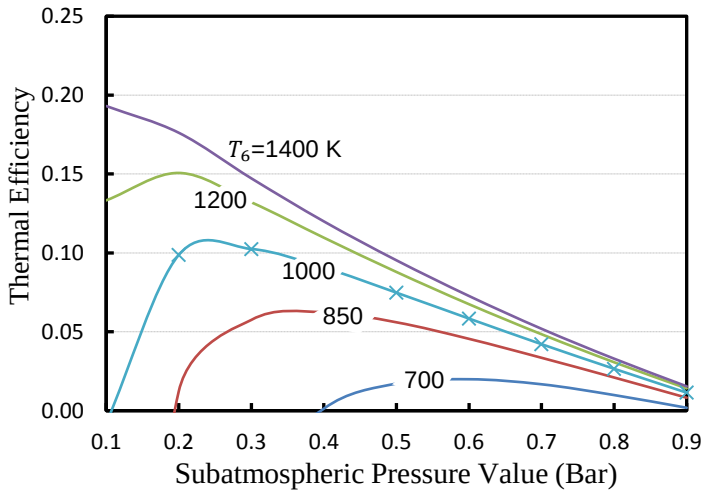

Figure 3.11 . Thermal efficiency variation depending on the bottom compressor inlet temperature and subatmospheric pressure

The IBC thermal efficiency for the same conditions is presented in Figure 3.11. An increasing trend in the thermal efficiency can be expected with an increase in T_6 . However, the efficiency increment provided by the increase of T_6 from 1000 K to 1400 K is smaller than that from 700 K to 1000 K. The characteristic of thermal efficiency with the variation of p_{low} is similar to that of the specific work, namely, there is an optimum sub-atmospheric pressure that delivers a peak efficiency. Moreover, the optimal p_{low} decreases as the turbine inlet temperature T_6 increases. When IBC inlet temperature increases beyond a certain value, the thermal efficiency is monotonically decreasing function of IBC inlet temperature T_6 .

3.5.1.2 Effect of the turbomachinery efficiencies (η_{ic} and η_{it}) and the subatmospheric pressure $p_{low}(r_{it})$ at fixed p_6 (1.013 bar), η_{ex} (0.95) and T_6 (1000 K)

Figure 3.12 shows the effect of the turbomachinery efficiency on the specific work and the thermal efficiency, respectively. The trend with increasing turbomachinery efficiency is clear, that is, a significant rise in IBC performance is to be expected as the component isentropic efficiencies approach unity. The optimum subatmospheric pressure $(p_{low})_{opt}$ that delivers the maximum specific

work $(W_{IBC})_{max}$ and the maximum IBC cycle efficiency $(\eta_{IBC})_{max}$ increases as the turbine and compressor become less efficient.

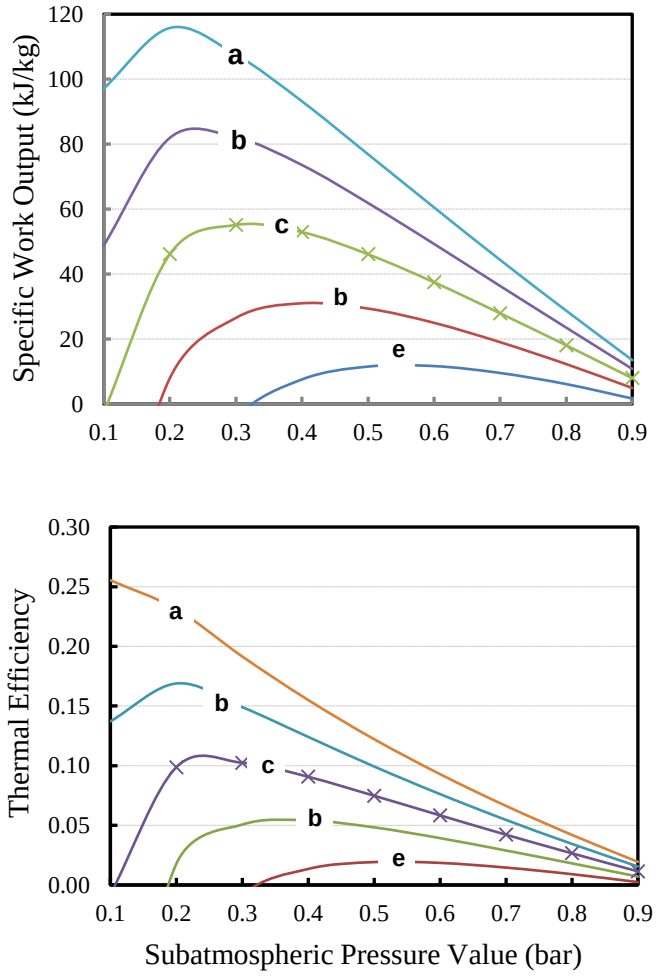

Figure 3.12 IBC performance versus subatmospheric pressure value is plotted for different values of turbomachinery efficiency (Turbine isentropic efficiency – η_{it}, Compressor isentropic efficiency – η_{ic}). The values are (a) 0.9, 0.85; (b) 0.85, 0.8; (c) 0.8, 0.75; (d) 0.75, 0.7; (e) 0.7, 0.65.

3.5.1.3 Effect of the inlet pressure p_6 and IBC expansion ratio r_{it} (p_{low}) at fixed η_{ic} (0.75), η_{it} (0.8), η_{ex} (0.95) and T_6 (1000 K)

In Figure 3.13, the solid lines indicate the variation of the specific work and thermal efficiency when the sub-atmospheric pressure changes from the 0.9 bar to 0.1 bar at different values of the turbine inlet pressure. The dash lines are turbine pressure ratio r_{it} contours. Both the specific work and thermal efficiency

are monotonically increasing function of the inlet pressure at any chosen values of the turbine expansion ratio. However, increasing the IBC inlet pressure leads to a higher back pressure of the engine which can negatively influence its performance. Hence, a system compromise is required to select the optimum IBC inlet pressure. In addition, Figure 3.13 shows that the optimum turbine pressure ratio $(r_{it})_{opt}$ corresponding to the maximum specific work $(W_{IBC})_{max}$ increases with the increases of p_6. The thermal efficiency at maximum power output point increases with the increases of p_6 as well. When the IBC inlet pressure p_6 is fixed, with an increasing turbine pressure ratio r_{it}, the power and efficiency of the IBC first increases and then decreases beyond an optimum value.

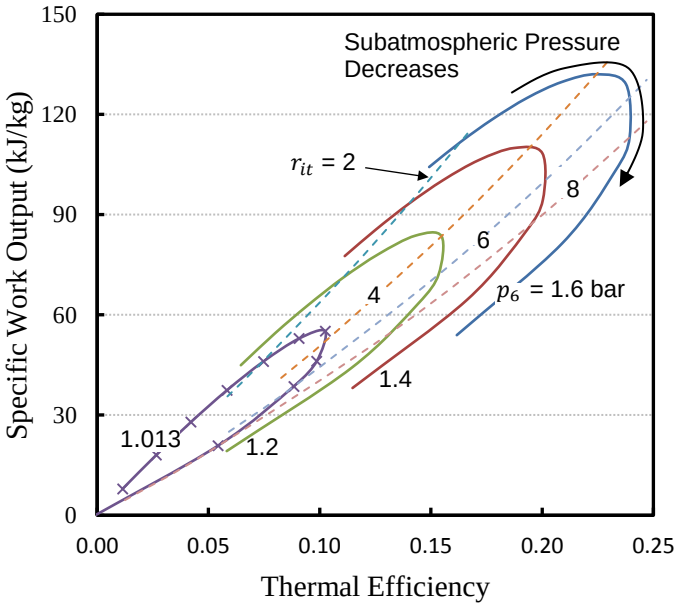

Figure 3.13 . W_{IBC}~ η_{IBC} curves varying with p_6 and r_{it}

3.5.1.4 Effect of the subatmospheric pressure p_{low} (r_{it}) and the effectiveness of the heat exchanger η_{ex} at fixed η_{ic} (0.75), η_{it} (0.8), p_6 (1.013 bar) and T_6 (1000 K)

The W_{IBC}~ η_{IBC} curves, with a variation in the heat exchanger effectiveness and atmospheric pressure, are plotted in Figure 3.14. The solid lines indicate the variation of the IBC performance characteristic caused by p_{low} approaching 0.2 bar at different values of the heat exchanger effectiveness. The effectiveness decreases from 0.95 to 0.75 with an interval of 0.05 and the dash lines represent

turbine pressure ratio contours. An increase in the effectiveness of the heat exchanger can contribute to a significant improvement in the IBC performance at this level of turbomachinery efficiencies (0.75/0.8 for compressor/turbine respectively). An increase in the effectiveness η_{ex} lowers the outlet temperature of the heat exchanger, thereby increasing the density of the exhaust gas and increasing the pressure ratio across the compressor for same power input. Consequently, the resulting lower backpressure of the turbine can contribute to an increase the expansion ratio, thereby increasing the energy extracted from the exhaust gas.

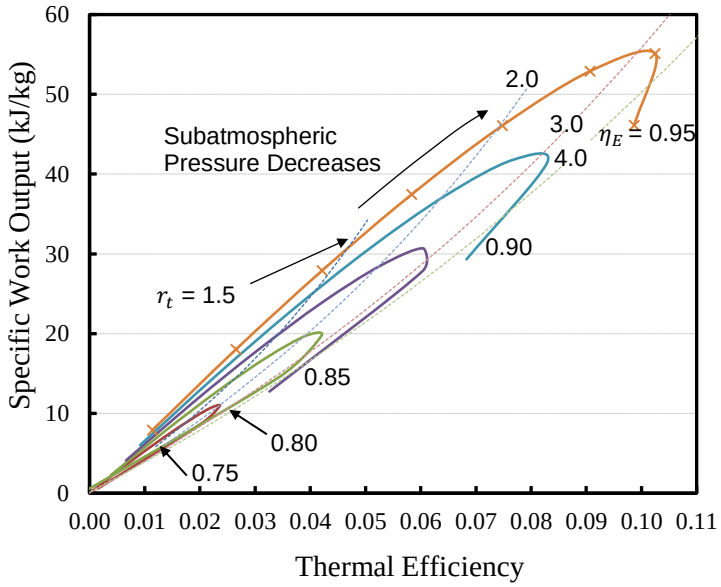

Figure 3.14 The W_{IBC}~ η_{IBC} curves varying with p_{low} and η_{ex}

3.5.2 System Study of Internal Combustion Engine with Three Alternative Cycles

In order to specify the strengths and weaknesses of three alternative cycles – IBC, pressurized Brayton cycle, and a turbocompounding system, an irreversible Otto-cycle model with an array of losses is used as a base for the bottoming cycle. The input power of the whole system equals to the thermal input to the Otto cycle, while the output power of the system consists of two parts - the net power of the

Otto cycle and the net power produced by the bottoming cycle. Therefore, the efficiency of the whole system is

$$\eta = \frac{P_{output}}{(P_O)_{in}} = \frac{(P_O)_{net} + W_{IBC} * \dot{m}_{air}}{(\dot{Q}_O)_{in} + \dot{Q}_{loss}} \tag{3.39}$$

As discussed in the introduction to this chapter, it is also possible to construct a bottoming Brayton cycle that is arranged in a similar way to a standard gas turbine, referred to the pressurized Brayton cycle. The difference is that the combustor in the gas turbine is replaced by a heat exchanger working as the heat addition process as shown in Figure 3.15. Thus, it is interesting to compare the inverted Brayton cycle to the pressurized Brayton cycle to understand their relative merits. Moreover, the turbocharged engine with an IBC can be considered as an extension of a turbo-compounding engine that only consists of a power-turbine. Thus, turbo-compounding, pressurized and inverted Brayton cycle systems are all compared as potential heat recovery systems for use with a turbocharged gasoline engine which has been fully described in the thermodynamic model. The comparison is made in terms of the system thermal efficiency, to highlight the strengths and weaknesses of each configuration.

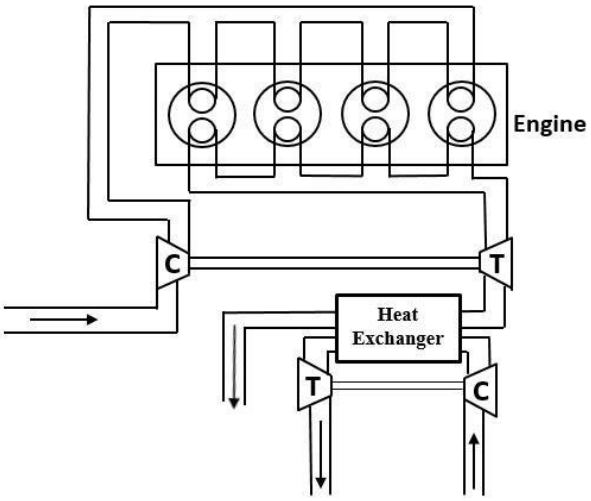

Figure 3.15 Schematic of the turbocharged engine with the pressurized Brayton cycle

Besides the mean pressure over which they operate, one of the main differences between the inverted and pressurized Brayton cycles is the operation of the heat

exchanger. A pressurized Brayton must have an air-to-air heat exchanger with material that is able to operate at high exhaust gas temperatures whereas the heat exchanger in an inverted Brayton cycle must reject a large amount of heat, but this can be achieved via a liquid coolant. It also has the advantage of only being exposed to exhaust gases that have already been expanded across the turbine.

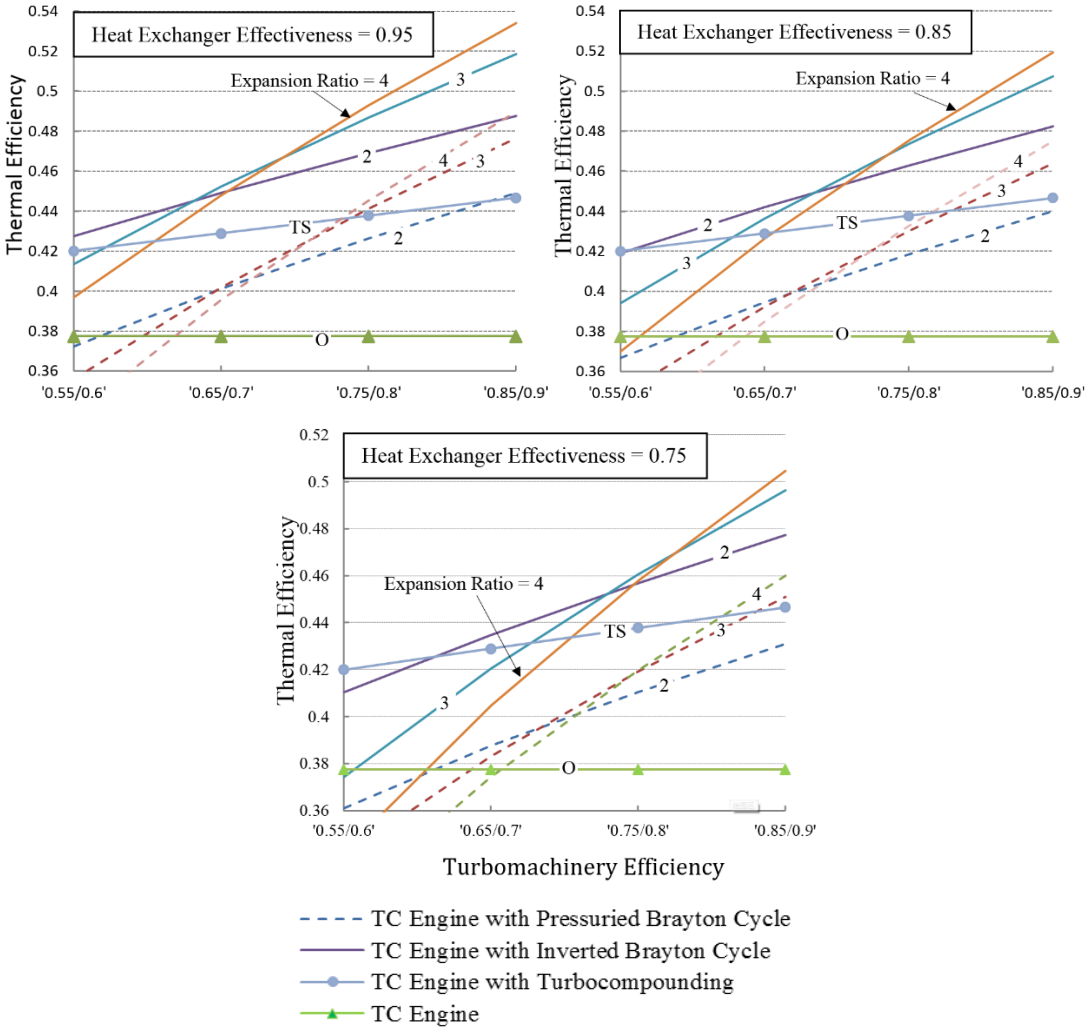

Figure 3.16 Comparison three alternative power cycles at different values of the turbomachinery efficiency, heat exchanger effectiveness and turbine pressure ratio

In Figure 3.16, the solid lines with numbers indicate the variation of the thermal efficiency in terms of the turbocharged engine with the inverted Brayton cycle, while the dash lines with numbers indicate the pressurized Brayton cycle and the solid line with 'TS' represent turbo-compounding system. The numbers represent

the expansion ratio of the bottoming turbine in the pressurized and inverted Brayton cycle. The baseline configuration of the turbocharged engine without heat recovery is shown with the solid line with 'O'. The power produced by the bottoming cycle is converted into shaft work which is added to the engine torque directly. The transmission efficiency is assumed to be 0.95. The horizontal axis represents the compressor/turbine isentropic efficiency of the inverted Brayton cycle as well as the pressurized Brayton cycle. The outlet temperature and pressure from the turbocharger turbine, (1112.6 K and 1.54 bar respectively), are calculated based on the thermodynamic relations in turbocharged gasoline engine and the boundary condition of the system intake air. Figure 26 shows that the base model system thermal efficiency is slightly under 38% (BSFC ~ 215 g/kWh) which is a typical peak of a gasoline engine. For the pressurized and inverted Brayton cycle, there exists a window of turbomachinery efficiency for which those cycles can always improve the performance of the turbocharged engine. The maximum efficiency rise is produced by the inverted Brayton cycle (single stage is considered here) with a pressure ratio of 4. However, with the decrease of turbomachinery efficiency, the thermal efficiency of systems with high expansion ratios will, at some critical value, decrease below the same system with a lower expansion ratio. One of the most important outcomes is that for a set of bottoming cycle boundary conditions (turbomachinery efficiency, heat exchanger effectiveness, and turbine expansion ratio), the improvement in the engine system efficiency caused by adopting the inverted Brayton cycle is significantly greater than that achieved by the pressurized Brayton cycle.

In this simplified model, the turbine efficiency of the turbocompounding turbine varies from 0.6 to 0.9. The results show a significant efficiency improvement over the base configuration despite simply using the remaining blowdown pressure after the turbocharger. This simple model suggests that the pressurized Brayton cycle rarely out-performs the turbo-compounding device apart from the highest pressure ratios and component efficiencies. The inverted Brayton cycle, however, generally improves system efficiency beyond the turbo-compounding option for reasonable values of component efficiencies. When the turbine expansion ratio increases, or the heat exchange effectiveness decreases, higher turbomachinery performance in IBC is required in order to achieve superior system efficiencies

compared to the turbo-compounding system. It should be noted, however, that the model assumes that the turbo-compounding device does not increase engine pumping work but purely reclaims the remaining pressure after the turbocharger turbine.

3.5.3 System Effect of IBC Compression Stages

The earlier section concerning the isolated inverted Brayton cycle reveals that introducing additional compression stage can promote the performance improvement from the IBC and less than 3 compression stages seem most sensible considering complexity and cost. Therefore, Figure 3.17 shows the influence of introducing a second compression stage on the performance of the whole system at the different values of the IBC turbine expansion ratio. The parameters of the engine model are the same as the previous section. The effectiveness of the heat exchanger is selected to be a conservative 0.85.

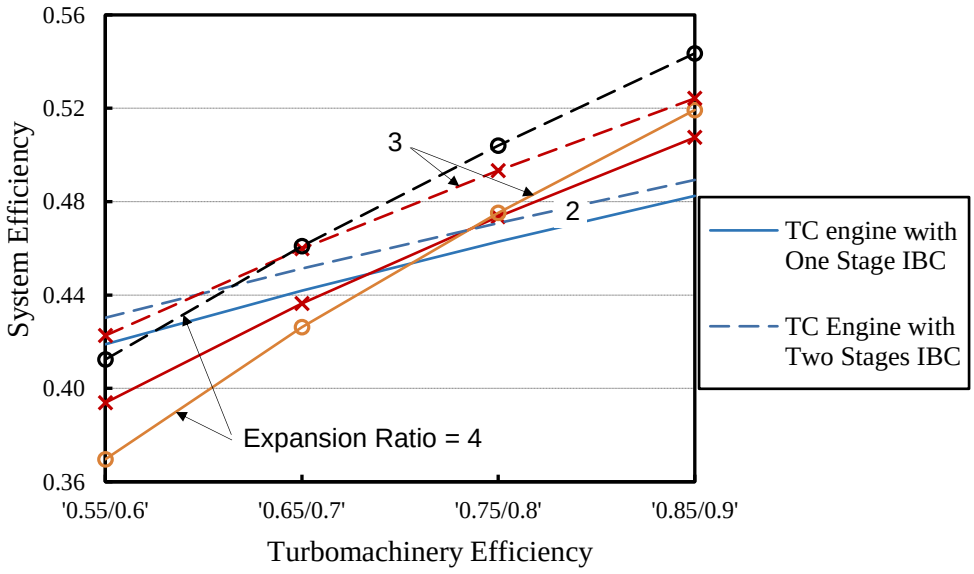

Figure 3.17 Efficiency of turbocharged engine with various stages IBC versus system efficiency

In Figure 3.17, the solid lines indicate the turbocharged engine with the one stage IBC, while the dashed lines represent that with two stages. The number related to each line shows the value of the IBC turbine pressure ratio. Comparing cases

with same expansion ratio, the system efficiency increments due to introducing an extra compression stage can be expected. At any chosen values of the turbomachinery efficiency, the system efficiency increment is larger when the IBC turbine pressure ratio is 4. It seems that higher expansion ratios across the IBC turbine can contribute to a higher system efficiency increment with added compression and intercooling stages. This trend is the same as that found in the analysis of the isolated inverted Brayton cycle. Not only does an extra compression stage help at higher efficiencies, it also helps to minimize the drop in system efficiency that occurs when the turbomachinery efficiency drops. This is especially true for cases with high expansion ratios that drop off quicker when the turbomachinery is not performing at peak efficiency.

3.5.4 IBC Performance over Driving Cycle

In this section, the exhaust conditions available from the engine test bench data were introduced as the inlet conditions of the IBC thermodynamic model to quantify the power recovered by IBC, thereby revealing the benefits of IBC to this particular engine. It should be noted that the test bench data of the baseline engine were collected by WLTP. It defines a global harmonized standard for determining the levels of pollutants and CO2 emissions, fuel consumption. The IBC thermodynamic model will be simulated with the following variables: IBC inlet pressure, turbine pressure ratio, heat exchanger effectiveness, turbomachinery efficiencies, and the IBC compression stage. The aim of this section is to analysis the performance of IBC system when it is applied to a light-duty automotive engine operating in a real-world driving cycle.

3.5.4.1 Engine Bench Test Data

A 2.0L gasoline turbocharged engine is selected as a primary power cycle to assess the benefits of the IBC system. The selected turbocharged engine has been tested over the WLTP in an SUV vehicle and the measured exhaust conditions have been utilized as the boundary conditions of the IBC thermodynamic model. It should be noted that the engine speed and torque are used to deduce the brake power output. The WLTP Class 3 test cycle, shown in

Figure 3.18, consists of four parts for Low, Medium, High, and Extra High speed. Table 3.2 provides the main descriptive parameters of WLTP class 3 test cycle.

Table 3.2 Main descriptive parameters of WLTP class 3 test cycle

	low	Medium	High	Extra High	Total
Duration (s)	589	433	455	323	1800
Stop Duration (S)	156	48	31	7	242
% of Stops	26.5%	11.1%	6.8%	2.2%	13.4%
Maximum Speed (Km/h)	56.5	76.6	97.4	131.3	

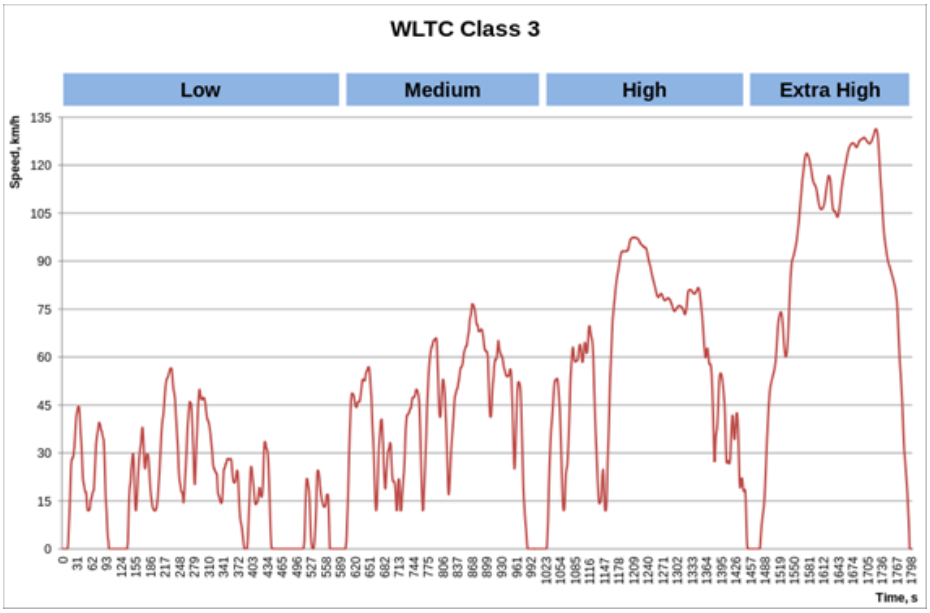

Figure 3.18 WLTP driving cycle

Figure 3.19 shows the time distribution of engine operating points on the engine map. Since the sampling frequencies for each measured data, such as engine speed and exhaust temperature, are different, the lowest frequency of these channels is chosen as the global sampling frequency for data collection of the various engine parameters.

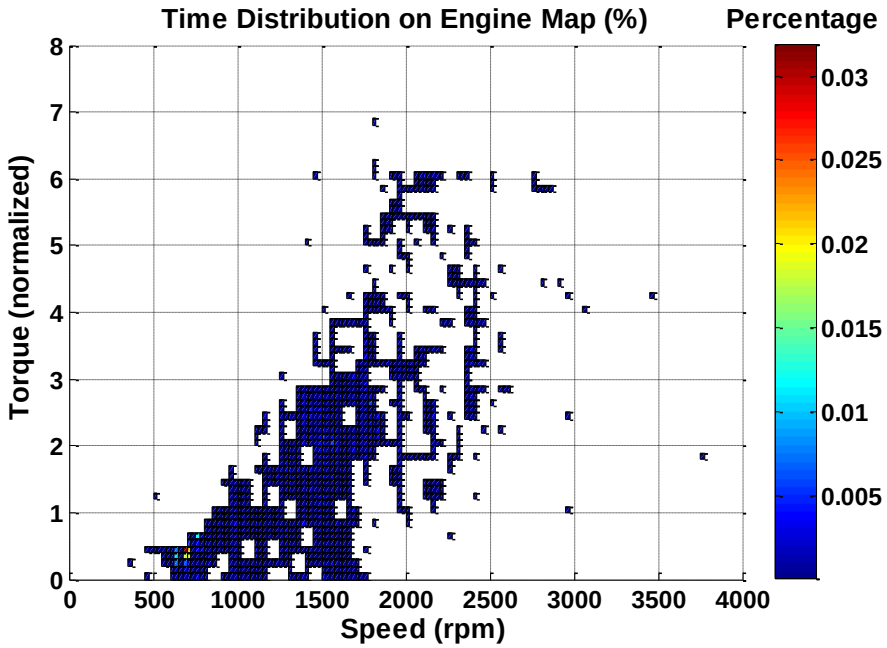

Figure 3.19 Time distribution of engine operating points on the engine map

As the WLTP driving cycle is designed to represent real world vehicle operation on urban and extra-urban roads, motorways, and freeways, the predicted IBC performance regarding to WLTP testing data should represent the practical use of an IBC in a vehicle. The exhaust conditions required by the IBC thermodynamic model are the exhaust temperature, the exhaust pressure, and the exhaust mass flow rate. According to the previous IBC study in this Chapter the higher the inlet pressure of the IBC, the greater the energy derived from the IBC system. However, since the IBC system is adopted directly downstream of the turbocharged engine, higher IBC inlet pressure can deteriorate the engine performance by raising the engine back pressure and, therefore, increasing the parasitic pumping work. Additionally, the influences of the engine back pressure on its performance are absent in the IBC thermodynamic model presented here. Thus, throughout this section, the IBC inlet pressure is fixed at 1 bar to leave the engine unaffected by the existence of IBC system. The exhaust mass flow rate and temperature directly downstream of the turbocharged engine are plotted in Figure 3.20 and 3.21, respectively. It should be noted that in most applications, it would be desirable to place the IBC after catalyst. Thus, the author emphasis that the present analysis uses pre-catalyst temperature and, thus, would need to be re-assessed using post-catalyst temperature. In some cases, this may result in greater heat due to the exothermic reaction in the catalyst.

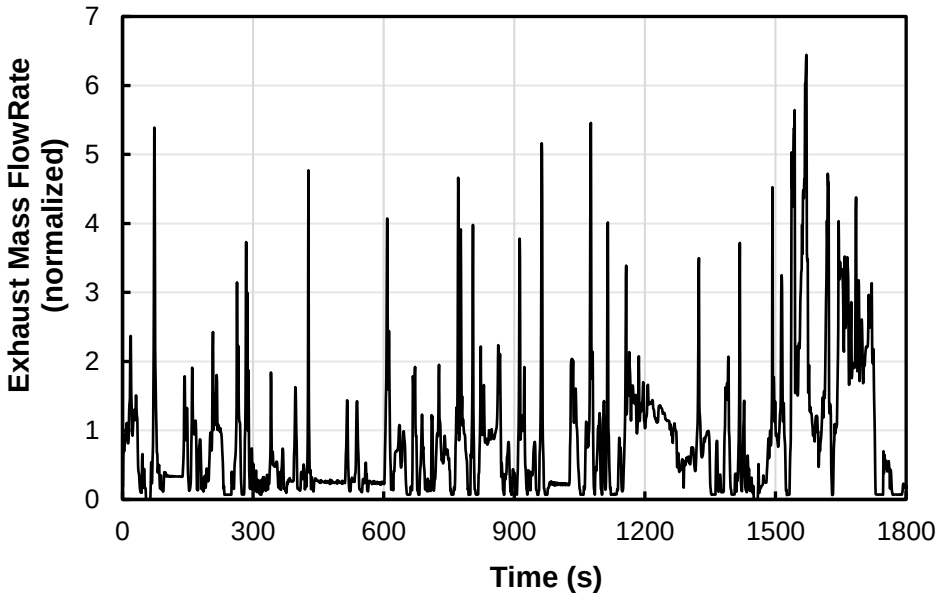

Figure 3.20 Exhaust mass flow rate

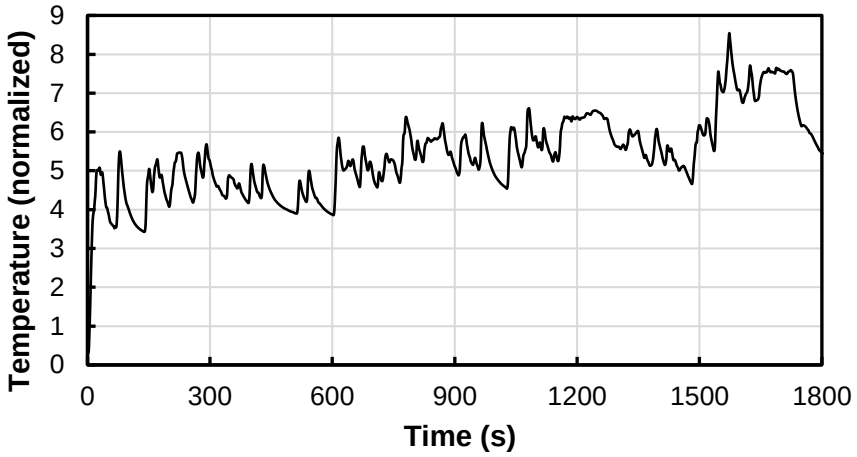

Figure 3.21 Exhaust temperature

3.5.4.2 Model Conclusion and Assumptions

In this section, the exhaust outlet boundary condition (the temperature, pressure and mass flow rate of the exhaust gas) available from the objective engine bench testing is introduced as the inlet boundary conditions of the IBC thermodynamic model to quantify the energy recovered by the IBC system. In order to perform this study, the following additional assumptions have been made:

- A liquid-to-air counter-flow heat exchanger is adopted in the IBC to simply reject heat. Water is considered as the coolant and the corresponding

specific heat at constant pressure is assumed as 4.2 $kJ/(kg\,K)$. The coolant inlet temperature and mass flow rate are assumed to be 315 K and 0.4 kg/s, respectively. The design point for the heat exchanger is taken as 600 K exhaust temperature and 0.1 kg/s exhaust mass flow rate. The design point heat exchanger effectiveness is considered as 0.9. Finally, the pressure loss across the heat exchanger is 0.025 bar at the design operating point.

- The mechanical connection is employed to transfer the recovered power from the turbo machines to the engine shaft. Thus, the transmission efficiency (η_m) of 0.95 is considered to represent any parasitic mechanical loss.

- The deviation of the turbomachinery from the idealized behaviour is described by the isentropic component efficiencies. A range of turbomachinery isentropic efficiencies between 0.7 – 0.8 for both the compressor and turbine are considered in this study. Note that the isentropic efficiencies of the compressor and turbine are assumed as a fixed value during the entire WLTP driving cycle. The author recognize that the fixed turbomachinery efficiencies are difficult to achieve in practice, but this assumption aims to reveal the influence of turbomachinery performance at the system level.

The specific work extracted by IBC turbine can be calculated using Eq. 3.6 with the inlet and idealized outlet temperatures (T_6 and T_{7s}, respectively), and the IBC turbine isentropic efficiency η_t. Then, the turbine power is equal to the turbine specific work times the mass flow rate of the working fluid $\dot{m}_e$, It should be noted that the inlet temperature (T_6) and exhaust mass flow rate ($\dot{m}_e$) of an IBC system are taken from the vehicle test data. The isentropic efficiencies of the IBC compressors are equal and represented by η_{ic}. The power added to the working fluid by the individual compressor is equal to the work specific work in Eq. 3.14 times the exhaust mass flow rate $\dot{m}_e$. Therefore, the net power P_{IBC} produced by IBC system is defined as the difference between the power produced by the IBC turbine and that consumed by the IBC compressor(s). Since it is assumed that

the power recovered by the IBC is converted into shaft power which is added to engine torque directly, the mechanical loss is represented by a transmission efficiency η_m in the thermodynamic model.

The performance of the system is represented as brake specific fuel consumption (BSFC) defined as follow,

$$BSFC = \frac{m_f}{P_{system}} \tag{3.40}$$

where m_f is the fuel consumption rate and P_{system} is the power produced by the system.

As the engine speed and torque have been measured over the WLTP drive cycle, the engine brake power P_{IC} can be calculated by multiplying the engine speed by the brake torque. The benefits of IBC system are defined as the resulting BSFC improvement expressed as,

$$\begin{aligned} BSFC\ Improvement &= \frac{BSFC_{IC} - BSFC_{combined}}{BSFC_{IC}} \\ &= \frac{\frac{m_f}{P_{IC}} - \frac{m_f}{P_{IC} + \eta_m * P_{IBC}}}{\frac{m_f}{P_{IC}}} \\ &= \frac{\eta_m * P_{IBC}}{P_{IC} + \eta_m * P_{IBC}} \end{aligned} \tag{3.41}$$

where $BSFC_{IC}$ is the brake specific fuel consumption of the objective engine. $BSFC_{combined}$ is the brake specific fuel consumption of the combined system – the objective engine integrating with IBC.

It should be noted that the fuel consumption rate is eliminated during the deduction of the BSFC improvement. Thus, the BSFC improvement is evaluated by the engine brake power and IBC power output every second, then averaged over the testing time to yield the average BSFC improvement.

3.5.4.3 Single-stage IBC System

This section presents the influence of the single-stage IBC system on the system efficiency in terms of drive cycle BSFC improvement. Figure 3.22 shows the effect of the IBC turbomachinery efficiency on the average BFSC improvement for five values of the turbine pressure ratio. The compressor and turbine efficiencies are assumed to be equal and increases from 0.7 to 0.8 with an interval of 0.05. The trend with increasing turbomachinery efficiency is clear, that is, a significantly rise in the average BSFC improvement at a given turbine pressure ratio. When the turbomachinery efficiencies are 0.7, the average BSFC improvement is lower than 0.5%, even approaches zero as the turbine pressure ratio reaches at 3.5. It reveals that when the IBC turbomachinery efficiency descends below a certain value, there is no work generated by IBC and, therefore, the IBC system should be bypassed.

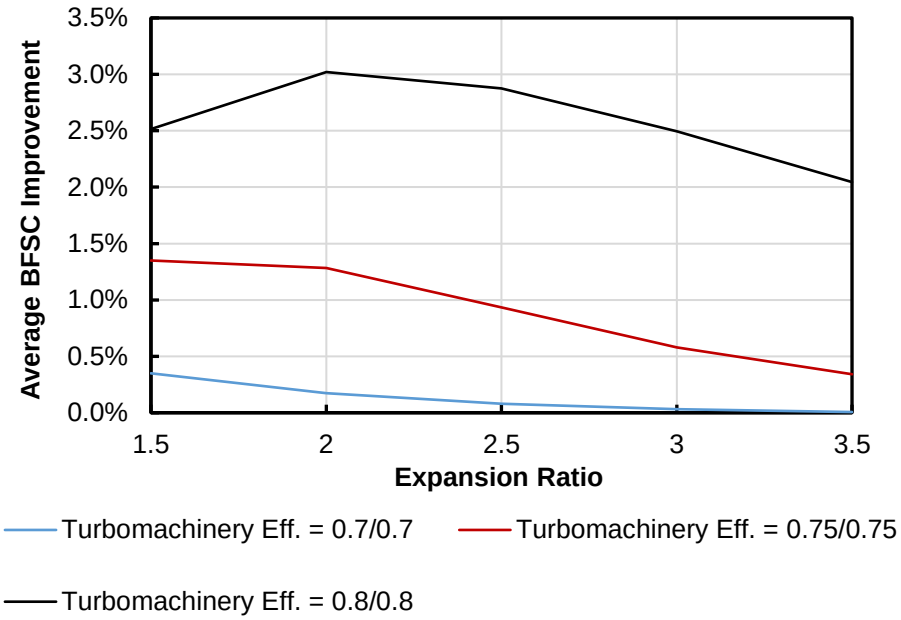

Figure 3.22 The benefits of single stage IBC

According to the previous IBC study in this Chapter, an optimum turbine pressure ratio exists that delivers the maximum average BFSC improvement. This theory can be clearly observed in Figure 3.22 when the turbomachinery efficiencies are 0.8/0.8. Here the average BSFC improvement reaches a peak of 3.02% and the decreases as the turbine pressure ratio increases. It should be noted that the

average BSFC improvement is calculated over the entire duration of WLTP driving cycle and the engine stop phase accounts for 13.4%. At the turbomachinery efficiencies of both 0.75/0.75 and 0.7/0.7, the average BSFC improvement is a monotonically decreasing function of the turbine pressure ratio. Thus, the optimum turbine ratio should be below 1.5 for both two cases. This suggests that for WLTP driving cycle, the objective engine should be integrated with low pressure ratio IBC system when the IBC turbomachinery is unable to achieve high efficiencies.

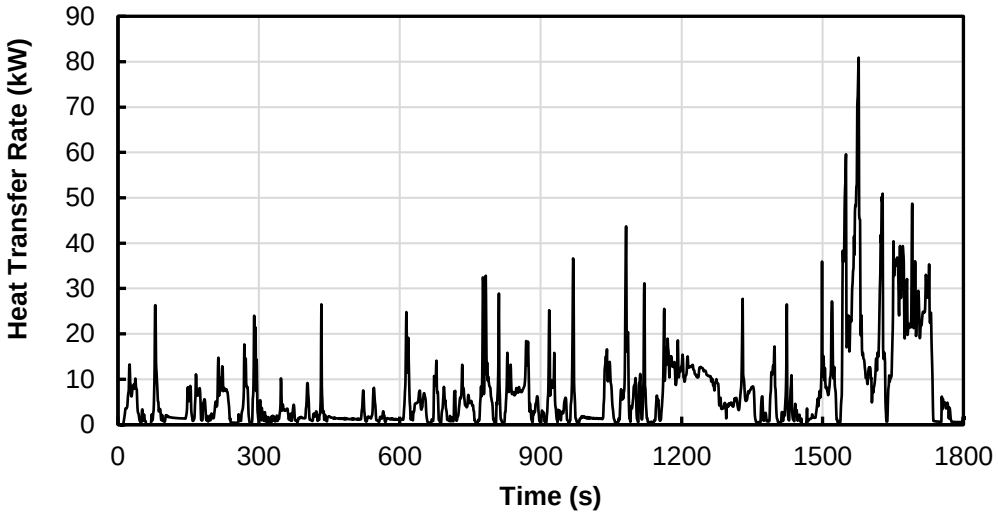

Figure 3.23 Heat transfer rate in the heat exchanger

Figure 3.23 shows the required heat transfer rate in the IBC heat exchanger during WLTP driving cycle when the turbomachinery efficiencies are 0.8/0.8 and the turbine pressure is 2. Unsurprisingly, the relative higher rate of heat rejection is expected at the part of the extra high engine speed. The corresponding average effectiveness of the heat exchanger is 0.92. The maximum heat transfer rate is 80.89 kW, which indicates that a relatively large size of the heat exchanger should be adopted. However, it should be noted that there is only 21 seconds when heat transfer rate in heat exchanger exceeds 40 kW, while the duration of WLTP driving cycle is 1800 seconds. Therefore, there is no need to employ a relatively large and heavy heat exchanger to meet all required heat transfer rate during WLTP driving cycle. A reasonable compromise between the system performance and the heat exchanger size should be reached.

3.5.4.4 Effect of IBC Compression Stages

According to the previous IBC study in this Chapter, an extra stage of compression processes in IBC system is a benefit to its specific power output. A rise in the IBC specific power output is found as the number of compression stages increase, depending on the expansion pressure in IBC. In addition, the IBC performance improvement is quite small when the third compression process is introduced. It should be noted that the extra compression stage needs to adopt one more compressor and heat exchanger. Thus, given the complexity and tiny improvement associated with the third compression stage, two-stage or single stage IBC should be considered as the most sensible configuration for automotive application. Considering the discussion above, the benefits of introducing a second compression stage is presented in this section. The additional heat exchanger is presented by the same thermodynamic heat exchanger model used in the 'Single-stage IBC system' section.

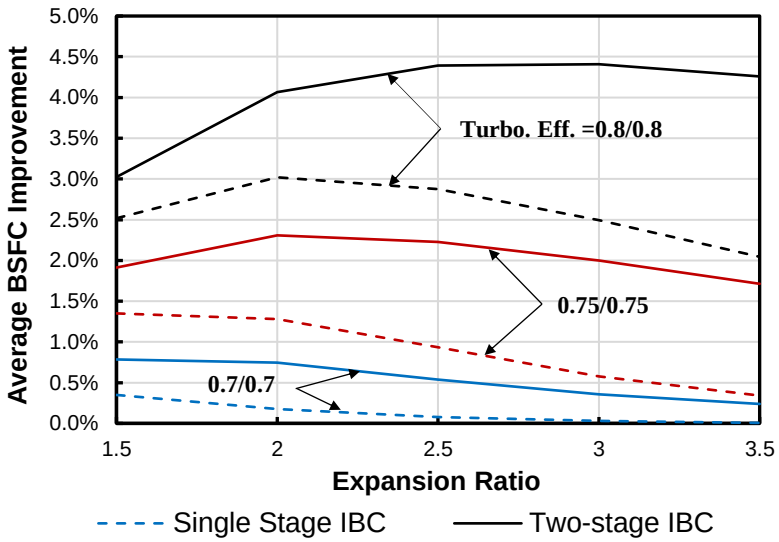

Figure 3.24 Average BSFC improvement due to various stages IBC versus IBC expansion ratio

Figure 3.24 shows the influence of adopting a second compression stage on the performance of the combined cycle power plant for three levels of turbomachinery performance. The solid lines indicate the turbocharged engine with the two stage IBC, while the dashed lines represent that with a single stage. Compared cases with same turbomachinery efficiencies, the increment of the average BFSC

improvement due to the employment of the second compression stage can be expected and seems more sensitive when a higher expansion ratio is achieved. For example, a 2.24 percentage point increment of the average BFSC improvement is predicted due to the existence of the second compressor when the turbomachinery efficiencies are 0.8/0.8 and the expansion ratio is 3.5. However, with reducing the turbomachinery efficiencies to 0.7/0.7, only 0.5 percentage point increment is expected. In addition, for the highest level of turbomachinery performance assumed in this study, the expansion ratio of the two-stage IBC that delivers the maximum BSFC improvement (4.41%) is 3, while that of the single stage IBC is only 2. Therefore, given the optimum expansion ratio and the benefits of the second stage compression, the high turbine pressure ratio should be achieved to maximize the performance improvement when the two-stage IBC system is employed as the exhaust-gas heat-recovery system.

On the other hand, it seems that the higher turbomachinery efficiency can contribute to a higher system performance improvement with the additional compression stage. The maximum increment of the average BSFC improvement is only 1.37% and 0.57% when the turbomachinery efficiencies are 0.75/0.75 and 0.7/0.7, respectively. Therefore, the second compression and intercooling stage should be employed to promote the system performance only if high efficiencies of the turbomachinery are achieved.

3.5.4.5 IBC Turbine Pressure Ratio Optimisation

The optimum turbine pressure ratio varies with the IBC inlet boundary conditions – exhaust temperature and pressure when all component efficiencies are fixed. Therefore, the objective of the optimisation is to find the optimum turbine pressure ratio of single stage IBC that maximizes the average BSFC improvement at certain component efficiencies. Since the impact of the engine back pressure is absent in the current thermodynamic model, the IBC inlet pressure is fixed at 1 bar in the optimisation process. In the case of the fixed IBC inlet pressure, the optimum expansion ratio across IBC turbine only varies with the exhaust temperature. In addition, the average exhaust temperature at each part of WLTP driving cycle varies significantly due to the different corresponding engine speed.

Therefore, the IBC turbine pressure ratio will be optimised to deliver maximum BSFC improvement at each individual part of WLTP driving cycle – low, medium, high, and extra high speeds. The IBC turbine and compressor efficiencies are chosen as 0.8.

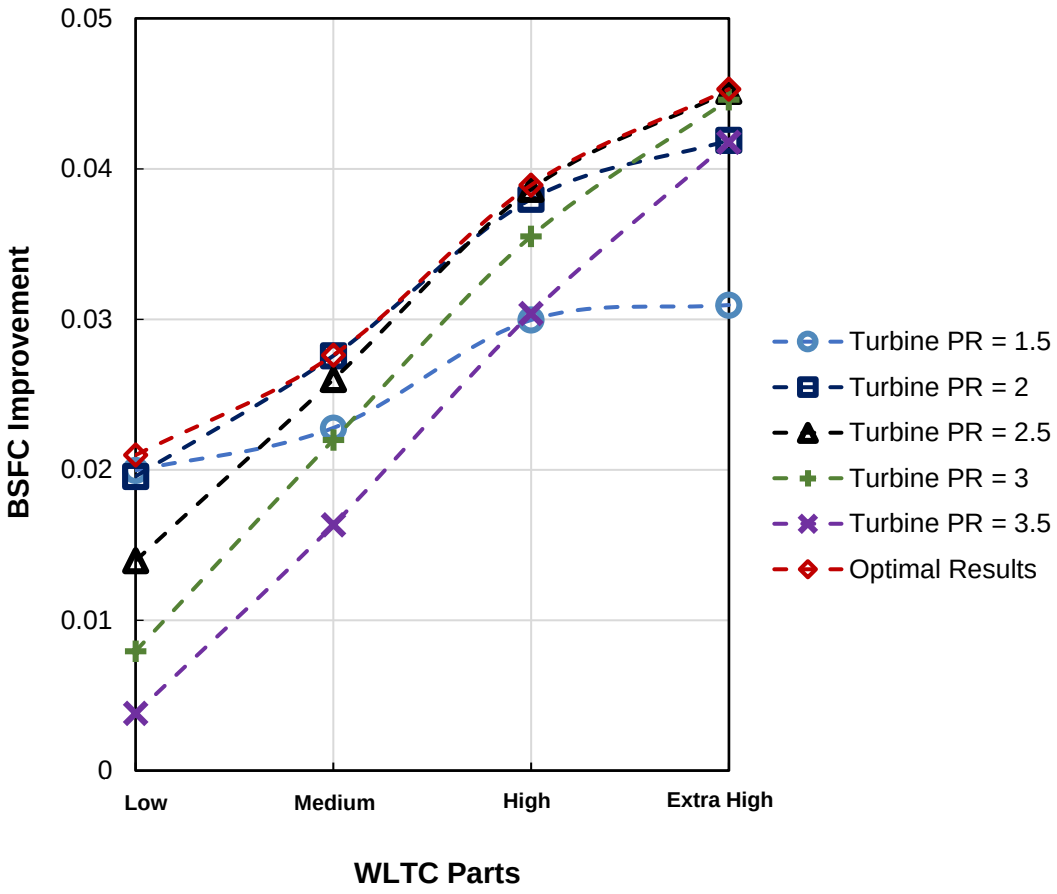

Figure 3.25 Comparison between optimised IBC with that of fixed expansion ratio

The optimisation tool in Matlab – 'fminbnd' is utilized to solve this single variable optimisation problem. Its algorithm is based on golden section search and parabolic interpolation. Figure 3.25 shows the predicted performance of the optimised IBC system compared with cases of the fixed expansion ratio. The horizontal axis represents the four parts of the WLTP driving cycle. It should be noted that individual dots should be used to present the BSFC improvement at each WLTC part, because the X axis in Figure 3.25 is discrete. However,

continuous dashed lines are used in order to clearly show the tendency of the BSFC improvement across over all WLTC parts.

With the turbomachinery efficiencies of 0.8/0.8, the maximum average BSFC improvement in all cases of single stage IBC system can be expected when the expansion ratio is 2. Thus, both the optimisation results and the case with the expansion ratio of 2 are listed in Table 3.3.

Table 3.3 Optimisation results

	% of Whole Driving Cycle	Average BSFC Improvement (%)		Optimum Turbine Pressure Ratio
		Turbine PR = 2	Optimal Turbine PR	
Whole Driving Cycle		**3.02%**	**3.15%**	
Low	32.70%	1.96%	2.10%	1.70
Medium	24.05%	2.76%	2.76%	2.07
High	25.25%	3.80%	3.89%	2.26
Extra High	18.00%	4.19%	4.53%	2.65

As is shown in Table 3.3, the higher optimum turbine pressure ratio is expected when the engine load and vehicle speed increases from low to extra high. Since the exhaust gas temperature is the only variable which affects the optimum expansion ratio, it means that the optimum expansion ratio increases with the increase of the exhaust temperature. Since the average exhaust mass flow rate increases with engine speed as well, may be possible to match a fixed geometry turbomachine that operates near to the optimum expansion ratio during the entire WLTP driving cycle.

Compared with the case of the expansion ratio of 2, only 0.13 percentage increment of the average BSFC improvement can be expected when the turbine pressure ratio is optimised. This is because that a small increment of the average BSFC improvement caused by the expansion ratio optimisation can be predicted due to the low-grade heat energy contained in the low-temperature exhaust gas.

The ‘Low’ part counts for 32.7% of the whole WLTP driving cycle. The relative higher increment of the average BSFC improvement is expected at the Extra High part. However, the Extra High part only occupies 18% of the whole WLTLP driving cycle.

3.6 Thermodynamic Simulation Conclusion

The inverted Brayton bottoming cycle applied to a standard internal combustion engine has been modelled with an Otto cycle and a Brayton cycle. The intent is to understand the viability of Brayton cycles (in particular the intercooled, inverted variety) to reclaim thermal energy from current automotive power plants. Although the potential for heat recovery may be somewhat less compared to the Rankine cycle, the appeal of the Brayton cycle is its relative simplicity and the use of readily available radial turbomachinery components.

In order to understand the performance of the inverted Brayton bottoming cycle in isolation, the parametric study presented in this research has shown the potential to deliver a reasonable specific power output from heat recovery. The rise in IBC performance has been shown to be dependent on five factors to varying degrees - the number of compression stages, the cycle inlet temperature and pressure, the isentropic efficiency of the turbomachinery and the effectiveness of the heat exchanger. However, in order to achieve the maximum specific power, this will correspond to a specific optimal expansion ratio that is dependent on the boundary condition of the IBC. The following specific conclusions have been derived from this research:

1. An extra stage of compression processes in the inverted Brayton cycle is a benefit to the specific power output. A rise in the IBC thermal efficiency is found as the compression stages increase, depending on the subatmospheric pressure in IBC. However, an extra compression stage consists of one additional compressor and heat exchanger. Thus, given a

benefit versus complexity/cost analysis, one stage could thus be considered as the most sensible configuration for automotive applications.

2. With an increase in the expansion ratio of the IBC (reduction in post-turbine pressure), the maximum specific power output peaks and then can drop depending on the turbine inlet temperature and component efficiencies. Thus, the optimum expansion ratio will dependent on these boundary conditions. Thus, careful design of IBC turbomachinery will be needed to match the optimal operating point to the upstream hardware.

3. There is a minimum threshold value of the IBC inlet temperature and/or turbomachinery efficiency that is needed to ensure that there is positive work produced by the inverted Brayton cycle. Unsurprisingly, increasing the inlet temperature and/or turbomachinery performance leads to higher specific power output.

4. The IBC performance is a monotonically increasing function of the turbomachinery efficiency. Moreover, a significantly improvement in the maximum specific power can be expected if the turbine and compressor isentropic efficiencies increase from 0.7/0.65 to 0.9/0.85.

5. Similarly, a large increase of the power output is found with an increase in the IBC inlet pressure. However, it should be highlighted that the performance of the engine may be deteriorated by this higher back pressure. In contrast to a turbocompounding device, the strength of the IBC is that it does not need to operate with high backpressures to operate successfully.

6. Increasing the effectiveness of the heat exchanger increasing the density of the gases in the IBC compressor and thus, increase the pressure ratio for the same power input. The resulting lower backpressure of the turbine increases the expansion ratio and the energy exploited from the exhaust gas. Hence, the effectiveness of heat exchanger can positively affect the IBC performance.

Then, the system benefits from adding an inverted Brayton cycle to a turbocharged Otto cycle has been analysed. In addition, a comparison of the

inverted Brayton cycle, turbocompounding system and the pressurized Brayton cycle is also made. The following conclusions can be drawn from this research:

7. The maximum system efficiency improvement is produced by adopting the inverted Brayton cycle as a bottoming heat-recovery cycle. That is, the IBC is the best of the three options if the component efficiencies can be maintained. The IBC is substantially better compared to the pressurized Brayton cycle.

8. The highest system efficiency predicted for the Otto cycle with a single stage IBC is 53% with a pressure ratio of 4 and component efficiencies of η_{ic} (0.85), η_{it} (0.9), η_{ex} (0.95). This is a substantial increment over the base configurations and illustrates the potential of heat recovery in raising system BSFC.

9. A minimum requirement for turbomachinery efficiency is needed to improve beyond the turbo-compounding system. Therefore, the inverted Brayton cycle offers an excellent bottoming heat-recovery cycle only if high performances of the turbomachinery and heat exchanger are achieved.

10. The system performance improvement caused by adopting the second compression stage is clear and expected. The corresponding efficiency improvement is more sensitive when the pressure ratio of the bottoming turbine is higher.

Moreover, since the IBC system is adopted directly downstream of the engine, the exhaust conditions of the upper cycle should be introduced as the inlet boundary conditions of the IBC thermodynamic model. Thus, experimental exhaust data from a 2.0L turbocharged gasoline engine operating over a WLTP driving cycle have been used as the boundary conditions. Since it is assumed in this research that the IBC should not impose any additional backpressure post catalyst the IBC inlet and outlet boundary conditions are fixed at 1 bar. Note that the WLTP driving cycle is designed to represent real world vehicle operation. Thus, the predicted performance of IBC system based on WLTP testing data could reasonably represented the practical use of IBC system on a vehicle.

In terms of the single stage IBC system integrated with the objective engine, the maximum resulting average BSFC improvement is 3.02% when the IBC turbomachinery efficiencies is 0.8/0.8 and the expansion ratio is 2. It should be noted that the average BSFC improvement is deduced on the whole WLTP driving cycle and that 13.4% of WLTP is engine stop phase. Unsurprisingly, the system performance is deteriorated by the decrease of turbomachinery efficiency. When the IBC turbomachinery efficiency descends below a certain value, there is no work generated by IBC and, therefore, the IBC system should be bypassed. The two-stage IBC system should be employed when the high performance of IBC turbo machine can be achieved. In addition, the IBC turbine in the two-stage IBC needs to operate with a high expansion ratio area to deliver the maximum improvement of the system performance.

The optimisation of the expansion ratio in a single stage turbine has been presented. The results show that an increase in the optimum expansion ratio can be expected when the WLTP driving cycle move from the ‘Low’ part to the ‘High’ part. Since the average exhaust mass flow rate increases from the ‘Low’ part and ‘High’ part as well, this trend could be matched to a fixed geometry turbo machine that is designed to operate at the optimum expansion ratio during the whole WLTP driving cycle.

Chapter 4 – IBC 1D Modelling and Analysis

4.1 Introduction

In this chapter, a validated 2-litre downsized turbocharged SI engine model has been built and simulated under steady state condition by GT-Power code, in order to quantify the performance improvement due to the employment of the inverted Brayton cycle (IBC). GT-Power code is a commercial engine performance analysis code built on one-dimensional computational fluid dynamics (CFD) which is capable of predicting various operating parameters of the internal combustion engine and its developed configurations [113]. Real characteristic maps of turbine and compressor provided by the manufacturers was optimised by scaling the map mass flow rate to achieve the lowest break specific fuel consumption (BSFC). Based on optimised characteristic maps, the IBC systematic thermodynamic performance was evaluated with two variables – the expansion pressure ratio and turbomachinery efficiency, under various engine loads.

In order to demonstrate the IBC heat-recovery capability in real world driving cycle, the real characteristic maps of turbine and compressor was introduced and re-sized at one mini-map point. Mini-map points are a set of steady state engine operating points with the allocated weighting, which are typically utilized to present a particular driving cycle. Then, the performance of IBC system with the matched turbine and compressor were predicted at the rest of mini-map points.

Finally, based on the re-sized characteristic maps of turbine and compressor, a commercial compressor and turbine were selected to perform the 3D simulation for the further performance improvement.

It should be noted that the contents from Section 4.3 to Section 4.4.3 have been published as a conference paper [114] in JSAE/SAE 2015 International Powertrains, Fuels & Lubricants Meeting. Moreover, the contents in Section 4.4.4 have been published as a conference paper [115] in Proceedings of the 2nd Conference on Engine Process.

4.2 1D Modelling Approach

Nowadays, the demand of the engine modelling is extensively increasing in the engine design and development process. It enables engineers to develop and demonstrate new technology concepts which are potentially beneficial to engine performance, even before the first prototypes are available. In addition, it is useful in predicting engine performance and simulating parameters that are difficult or impossible to measure in experiments. There are several favourable engine models utilized in the state-of-the-art engine development – black box model, mean value model, 1D model and multi-dimensional model. Typically, for a particular research, the modelling approaches should be selected with respect to the simulation accuracy requirement, computational cost, model capability and availability.

In this study, the 1D modelling approach was chosen to simulate and analyse the combined system – IC engine and IBC system, due to its accuracy, limited available simulation time, and the flexibility and capability of integrating different models. The 1D engine model was provided by research partners and fully correlated with engine bench tests. The simulation environment of this 1D engine model is GT-power which is commercial 1D fluid dynamic simulation code developed and licensed by Gamma Technologies Inc. Basically, engine simulation performed in GT-power code can be described as follows. The Navier-

Stokes equations are solved in one dimension for the working fluid in pipes and flowsplits. Moreover, simplified models, such as maps and look-up tables, are employed to predict the performance of other critical engine components, for example valves, throttles, turbocharger, non-predictive combustion model, and so on. Typically, extensive test data is required to correlate these simplified models, so as to ensure the simulation accuracy.

In the following sub-sections, the brief descriptions of the simulation methods for critical engine components are presented.

4.2.1 Flow Modelling

The flow modelling in pipes are extremely critical, as the majority of components in engine air path system can be essentially categorized as pipes. In order to achieve high simulation accuracy, firstly the whole piping system should represent the geometry of the corresponding real engine. Secondly, the proper simulation method should be employed. In GT-power, the flow model involves the solution of the Navier-Stokes equations, namely the conservation of continuity, momentum and energy equations. These equations are solved in one dimension, which means that all quantities are averaged across the flow direction [116].

Before introducing the Navier-Stokes equations, two available solvers for these equations are described first. Basically, the different time integration methods are utilized in these two solvers – explicit and implicit solvers. The explicit solver should be used when wave dynamic is important and crank angle resolved results are required. It is beneficial to simulate highly unsteady flow which occurs in engine air flow and fuel injection systems. However, although this solver produces more accurate prediction of pressure wave dynamic, the associated small time scale cause high computational cost. On the contrary, the implicit solution is more efficient where high frequency pressure fluctuations are not of interest. The corresponding use cases are non-engine simulations, such as exhaust system warm-up and cooling system. In this study, the explicit solver is selected for all 1D simulations due to the existence of IC engine in the combined system.

The solver aims to solve the Navier-Stokes equations within the defined sub-volumes in each pipe. The aim of discretizing the piping system into many sub-volumes is to improve the model fidelity and simulation accuracy. The type of discretization is referred to as a staggered grid, shown in Figure 4.1.

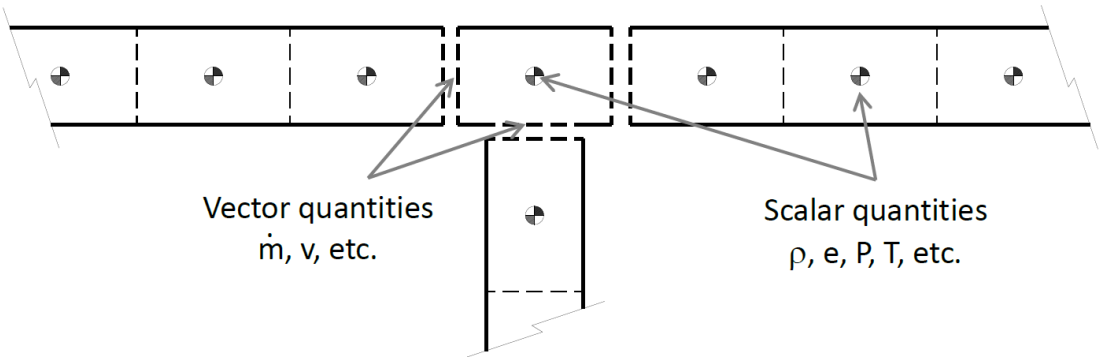

Figure 4.1 Schematic of staggered grid approach [116]

As shown in Figure 4.1, these sub-volumes are connected by boundaries. The scalar variables, such as pressure, temperature, density, and internal energy, are assumed to be uniform over each sub-volume and calculated at centroid. The vector variables, such as mass flux, velocity and mass fraction fluxes, are calculated at boundaries.

After sub-volumes creation, the Navier-Stokes equations – conservation of mass, energy and momentum are solved by the explicit and implicit solvers inside the sub-volumes and at boundaries. Mass conservation states that the rate of change of mass within a sub volume equals the sum of mass flux in and out of the sub volume:

$$\frac{dm}{dt} = \sum_{boundaries} \dot{m} \tag{4.1}$$

where $\dot{m}$ is the boundary mass flux into the volume and $\dot{m}$ is the mass of the volume.

Momentum conservation states that the rate of change of momentum in the sub volume is equal to the net pressure forces and wall shear forces acting in a system plus the net flow of momentum in and out of the sub volume:

$$\frac{d\dot{m}}{dt} = \frac{dpA + \sum_{boundaries}(\dot{m}u) - 4C_f \frac{\rho\mu|\mu|}{2}\frac{dxA}{D} - C_{presure}\left(\frac{1}{2}\rho\mu|\mu|\right)A}{dx} \quad (4.2)$$

Where:

$\dot{m}$	boundary mass flux into the volume
dp	pressure differential across dx
A	flow area
μ	velocity at boundary
C_f	skin friction coefficient
Dp	length of mass element in flow direction
ρ	density
D	equivalent diameter
$Cpresure$	pressure loss coefficient

Energy conservation states that the rate of change of energy in a sub volume is equal to the sum of energy transfer in and out of the sub volume. Energy transfer in the volume involves energy connected to work, mass flow and heat transfer:

$$\frac{d(me)}{dt} = -p\frac{dV}{dt} + \sum_{boundaries}(\dot{m}h) - HA_s\left(T_{fluid} - T_{wall}\right) \quad (4.3)$$

Where:

m	mass of the volume
e	total internal energy per unit mass
p	pressure
V	volume
h	total enthalpy
A_s	Heat transfer surface area
H	Heat transfer coefficient
T_{fluid}	equivalent diameter
T_{wall}	pressure loss coefficient

4.2.2 Combustion Modelling

When the working fluid has been predicted in the air path system, a well calibrated combustion model is required to predict the amount of chemical energy released as heat in the cylinder during the combustion phase. In GT-power, combustion models can be categorized into predictive, non-predictive, and semi-predictive modelling. The combustion model selection depends on the intended use of the engine model and the availability of experimental data.

In theory, predictive combustion models are an appropriate choice for all engine simulation, as any change of in-cylinder combustion caused by varying engine parameters or operating conditions could be accurately captured by a well calibrated predictive combustion model. However, numerous efforts and test data are required to calibrate the predictive combustion model. In addition, due to the high-level complexity of calculation associated with the predictive combustion model, the corresponding computation time is significantly higher. Thus, it is recommended when the simulations aim to study a variable that has a direct and significant effect on in-cylinder combustion.

On the contrary, the non-predictive combustion models simply impose a fixed burn rate as a function of crank angle. The burn rate is the instantaneous rate of fuel consumption within the cylinder combustion process and utilized to describe the corresponding heat releasing. Thus, the combustion is fixed regardless of any change of in-cylinder conditions, such as changes in residual fraction or injecting time. In conclusion, the non-predictive models are recommended when the variables of interest have a minimal effect on the burn rate.

Compared with the predictive combustion models, a semi-predictive combustion models have less physical sub-models to predict the in-cylinder combustion. The function of the absent physical sub-models is achieved by imposing the combustion burn rates in non-predictive combustion models. It means that the changes of the combustion burn rate will be predicted based on operating conditions, such as engine speed, intake manifold, and spark time in gasoline

engines. The method provides limited predictability without the significant computation penalty.

Since the engine hardware in this research was available, extensive experiments have been conducted to measure any parameters related to engine combustion, then calculate the combustion heat release. Therefore, the predictability of the combustion model was not required. In addition, the engine block geometries remain unchanged in the investigation of IBC system. Moreover, the control parameters were not to be varied in a wide range in simulation studies. Thus, non-predictive combustion model – 'EngCylCombSIWiebe' was selected to simulate engine combustion. This combustion model utilizes the Wiebe function to fit the SI combustion burn rate profile. The spark-50% burn duration, 10% to 90% duration, and exponent are the required inputs of Wiebe function. These inputs have been calibrated with the experiment data.

4.2.3 Turbocharger modelling

4.2.3.1 Compressor and Turbine Modelling

Since IBC system consists of a turbine and one or several compressors, the turbocharger simulation methodology is vital for the IBC systematic simulation. Generally, turbocharger simulations can be categorized into 0D, 1D and 3D, with respect to the simulation complexities. In GT-power, the turbine and compressor are simulated as 0D elements. In other words, the performance maps of the turbine and compressor should be provided by the user and utilized to model the corresponding performance. This simulation method is widely used in 1D engine simulations due to the simplicity and the reasonable accuracy in the measured operating range. However, the extrapolation method is also available in GT-power to enable the prediction capability when the turbine and compressor work at the operating points where there is no test data available.

Typically, the turbocharger manufacturers supply turbine and compressor performance maps. They are summarized as a series of performance data points measured in experiments, each of which describes the operating condition by speed, pressure ratio, mass flow rate, and thermodynamic efficiency. However,

in order to avoid the effects of the variations in the measurement condition and applications, the provided performance maps have been corrected to a reference condition. To be specific, the inlet temperature and inlet total pressure for each of the data points should be corrected to a chosen reference temperature and pressure. The reference temperature and pressure are provided along with the performance maps. In terms of the speed and mass flow rate, the formulas to perform the corrections are given below:

$$RPM_{corrected} = RPM_{actual} \Big/ \sqrt{\frac{T_{inlet-total}}{T_{reference}}}$$
$$\dot{m}_{corrected} = \dot{m}_{actual} * \sqrt{\frac{T_{inlet-total}}{T_{reference}}} \Big/ \frac{p_{inlet-total}}{p_{reference}} \quad (4.4)$$

where $RPM_{corrected}$ is the corrected turbocharger speed of compressor or turbine RPM_{actual} is the physical turbocharger speed $T_{inlet-total}$ is the total temperature at inlet of compressor or turbine $T_{reference}$ is the chosen reference temperature $p_{inlet-total}$ is the total pressure at inlet of compressor or turbine $p_{reference}$ is the chosen reference pressure

Once the performance maps of the turbine and compressor are introduced in GT-power models, the turbocharger speed and pressure ratio will be utilized as inputs to the performance maps. Then, the mass flow rate and thermodynamic efficiency are looked up in the performance maps and imposed in the solution. It should be noted that the pressure ratio and efficiency of the compressor are usually total-to-total values which are directly linked to compressor power, while total-to-static values are typical for turbines. This is because the kinetic energy of the working fluid at the turbine outlet are usually not utilized for the turbocharged engine. Nevertheless, standards vary among the turbocharger manufacturers. Care must be taken when comparing and using the turbocharger performance maps, since the flow characteristics and efficiency might be changed when different methods are used. In this study, total-to-total values are used for compressors and total-to-static values are used for turbines.

4.2.3.2 Shaft Modelling

The other critical component in turbocharger is the shaft which is used to mechanically connect the compressor and turbine. In GT-power, shaft connections should be introduced to represent the total rotational inertia of the turbine wheel, compressor wheel, and shaft. In addition, the power balance across the shaft is calculated instantaneously for the simulation of power imbalance at the turbocharger shaft. At steady-state simulations, it is recommended that the turbo inertia should be set quite high for the first three of four engine cycles so that the turbo speed does not experience a dip while the velocity in the manifolds is developing. Then, the inertia should be made very low to allow the simulation to reach steady state very quickly. Finally, the real value of the turbo inertia provided by the turbocharger manufacturers should be used to the rest of the simulation. On the other hand, since the turbo inertia will significantly affect the turbo speed transient response and, therefore, the transient engine performance, it is very important that an accurate value for the turbo inertia is specified in transient simulations.

In theory, the turbocharger bearing mechanical loss should be specified in the simulation. However, most turbocharger suppliers use the compressor as load when the turbine is mapped on a conventional gas-stand. Thus, the bearing mechanical loss has been lumped in the turbine efficiency map. In this case, there is no need to specify any mechanical loss torque or efficiency in this simulation. In this research, the bearing friction was modelled implicitly in the turbine efficiency, as it has been included in the turbine efficiency map.

4.3 Model Description

In order to reveal the energy saving potential of an IBC, a 2-litre 4-cylinder turbocharged gasoline engine was considered as the primary cycle in this research. The engine boosting system consists of a turbocharger and a supercharger placed in series. The 1D detail model of the considered engine is

developed in GT-power and integrated with the proposed bottoming cycle, shown in Figure 4.1. The proposed SI engine model was built based on the design geometry and validated with the test bench data in order to improve the accuracy of the predicted results. Boundary conditions of the system at inlet and outlet are fixed as the parameters of standard atmospheric state – the pressure of 0.99 bar and temperature of 298 K. The SI Wiebe combustion sub-model is employed to describe the heat release during combustion. The S-shaped Wiebe function associated with this combustion model is empirical constructed and able to define combustion profile approximately but quite accurately. The other boundary conditions, such as mechanical friction loss, combustion efficiency, flow coefficient of intake and exhaust valve, were calibrated by the tested data of this gasoline engine.

The efficiency of electric generator connected to IBC is considered as 95%. For the sake of simplicity, 95% power retrieved by the bottoming cycle is transferred directly to the engine by a GT-power module which can add energy to any connected objective part by effectively providing a speed-dependent torque.

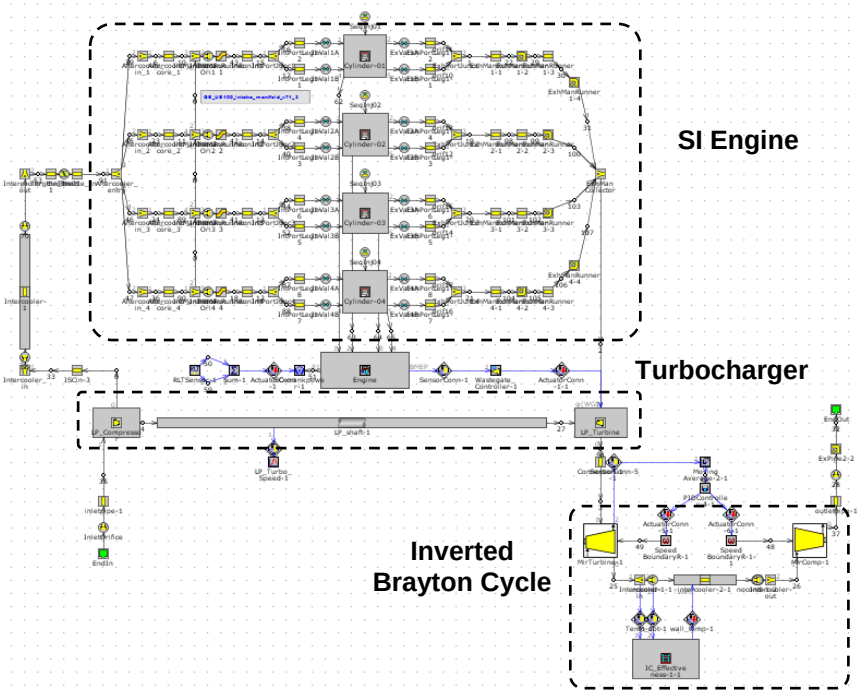

Figure 4.2 Numerical model of the combined system in GT-Power

Although ideally the turbocharging system should be re-matched to deliver the optimal system performance, the original turbocharging system was unchanged to ensure that all variables are related to the proposed heat-recovery cycle.

The operating speed of IBC turbomachinery is controlled to achieve the fixed pressure ratio target. The corresponding isentropic efficiency is set as a constant by scaling the map efficiency. In this case, the sensitivity of IBC conditions to the performance of the combined system can be evaluated.

The heat exchanger is built as a simple pipe in GT-power. The effectiveness of the heat exchanger is mainly influenced by the heat capacity of the two kinds of working fluids when the design parameters are fixed. That is, the effectiveness might vary with the operating condition of two working mediums, such as the mass flow rate, temperature, and working pressure. Nevertheless, the heat exchanger effectiveness in this research was fixed as 0.85 by varying the wall temperature, in order to evaluate the systematic performance with various heat exchanger performances. The temperature of coolant fluid was assumed as 300K.

In this chapter, real characteristic maps for the turbine and compressor in the primary cycle was firstly re-sized for IBC turbine at the engine speed of 4500 rpm and the full-load Brake Mean Effective Pressure (BMEP) of 30.9 bar. Then, the optimised IBC was utilized to perform a parametric study at engine speed 4500 rpm with various engine loads. Since engine speed in these investigations is fixed as 4500 rpm, the second stage, the supercharger, is declutched. This means that only the turbocharging system boosts the intake air and affects the system performance at this engine speed. Therefore, the target engine can be regarded as a turbocharged engine to investigate the influence of IBC on it. The valve timing, cam profiles and profile control terminate value for the SI Wiebe combustion model have been fixed throughout all simulations to ensure the predicted effect on the engine performance was due to IBC only.

In order to achieve the turbomachinery re-sizing, the attribute ‘Mass Multiplier’ within the GT-power IBC turbine module is selected to scale the reference map mass flow rate. The GT-power code calculates the instantaneous pressure ratio

and speed, then looks up the mass flow rate in the map. Consequently, the rate is multiplied by the value of that attribute before it is imposed. Thus, the attribute 'Mass Multiplier' for the turbine was considered as a design variable. The rest of design variables were the 'Mass Multiplier' of the IBC compressor and the torque applied on the shaft of IBC turbomachinery as the power extraction. Thus, an optimisation method required in this research should be able to solve a multi-variable optimisation problem. The genetic algorithm (GA) was employed as the optimisation approach in this research, as it has the capability to mimic the process of natural evolution and is thus considered to be one of the most useful approaches to solve this kind of problem [117].

Later, the IBC expansion ratio was optimised over the entire operating range of the target engine. The engine baseline GT-power model was utilized to predict the exhaust condition at the turbocharger outlet which was considered as the IBC inlet. The computational cost of the IBC GT-power model is too high to perform the proposed optimisation. Thus, IBC thermodynamic model presented in Chapter 3 was employed for the proposed optimisation.

4.4 Result and Discussion

4.4.1 IBC Compressor/Turbine Size Optimisation

The single-objective optimisation process was carried out by varying the load applied to the IBC turbomachinery shaft, mass flow multipliers of IBC turbine and compressor. The engine operating point is 4500 rpm with a BMEP of 30.9 bar and the BSFC is selected as the optimal objective function to be minimized. The optimal values of design parameters and corresponding predicted results are list in Table 4.1. The original turbocharged SI engine is referred as the baseline, which the turbocharged engine with IBC is as the combination.

Table 4.1 shows that, compared to the baseline, the pumping loss of the combined system is increased. Nevertheless, the corresponding fuel economy

(BSFC) is reduced by 5.91%. This is because that the optimised IBC system has the capability of recovering more than the parasitic power lost caused by the higher back pressures due to the presence of IBC components. In theory, the thermodynamic behaviour of IBC determines that the primary cycle could be unaffected by mounting IBC as the bottom heat-recovery cycle with properly turbomachinery matching. In other words, IBC is able to extract the wasted energy from the exhaust system without any additional back pressure of engine and, thus, no parasitic power lost is present. However, the increased exhaust manifold pressure is observed in the result from the GA optimisation. This is due to the optimal trade-off performance between the recovered power and the resulting power loss. On the other hand, since the real characteristic maps of the turbocharger in this proposed system are optimised and applied for IBC turbomachinery and both 'Mass Multiplier' values of IBC compressor and turbine modules are more than a unit, the physical size of the IBC turbomachinery should be bigger than that of the turbocharger in the primary cycle in order to deliver maximum performance improvement.

Table 4.1 GA optimisation results

Optimisation Results	Turbine/Compressor Mass Multiplier = 1.37/2.04 Torque = 1.43 N-m		
	Baseline	Combination	Improvement
BMEP (bar)	30.926	30.926	
BSFC (g/kW*h)	233.984	220.163	5.91%
PMEP (bar)	0.458	0.848	
System efficiency	35.88	38.24	2.25 percent points

The optimisation process in this section is to establish proper characteristic turbomachinery maps to perform the parametric study and provide guidance for the design of practical IBC applications, which is not a normal matching process. Therefore, although only 2.25 percent points in terms of systematic efficiency improvement is predicted shown in Table 4.1, the further performance improvement of the combined system can be achieved by performing proper matching processing for IBC turbomachinery.

4.4.2 Parametric Study of the Combined System based on the Optimal Turbine and Compressor Maps

Although the parametric study of the IBC system in isolation from the engine has been performed in the previous chapter by 0D modelling, the interactions between engine and IBC system are not investigated. Thus, parametric study of the combined system of SI engine and IBC system is performed in this section. To be specific, the operational characteristics of turbocharged engine incorporating IBC are evaluated under a range of conditions from low engine loads (BMEP = 12bar) to very high loads (BMEP = 40bar) at a fixed engine speed of 4500 rpm and the IBC expansion ratio of 3. As described in Model Description section, the operating speed of IBC turbomachinery is controlled to ensure that the turbine delivers the pressure ratio of 3. In addition, the map efficiency of the turbine and compressor is scaled to achieve the desired isentropic efficiency. Three cases are considered and listed in Table 4.2.

Table 4.2 IBC turbomachinery efficiencies

CASE	Compressor	Turbine
1	0.8	0.85
2	0.6	0.65
3	none	none

In case 1, the performance of the turbocharged engine with IBC is evaluated at the IBC turbine/compressor efficiency of 0.85/0.8 respectively, while only 0.65/0.6 in case 2. Case 3 is to present the performance investigation of the original turbocharged engine (without the IBC) as the reference case. The solid lines indicate the system efficiency of three cases, while the dash lines represent the corresponding efficiency increment in case 1 and 2 respectively. In theory, at any IBC boundary conditions, the fixed IBC expansion ratio can be achieved by adjusting the turbomachinery speed which is controlled by the torque on its shaft. The corresponding BSFC is plotted in Figure 4.3.

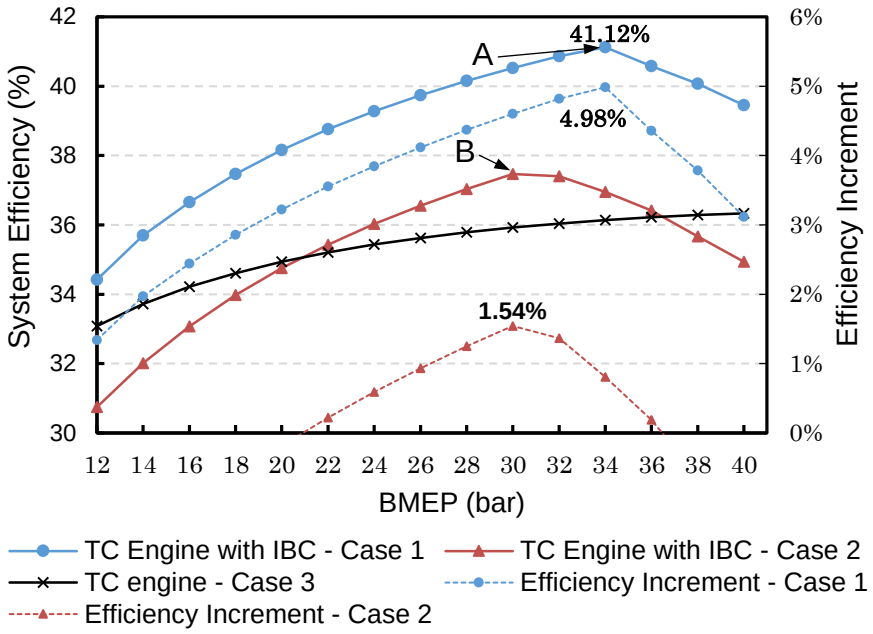

Figure 4.3 Variation of the system efficiency at different values of BMEP

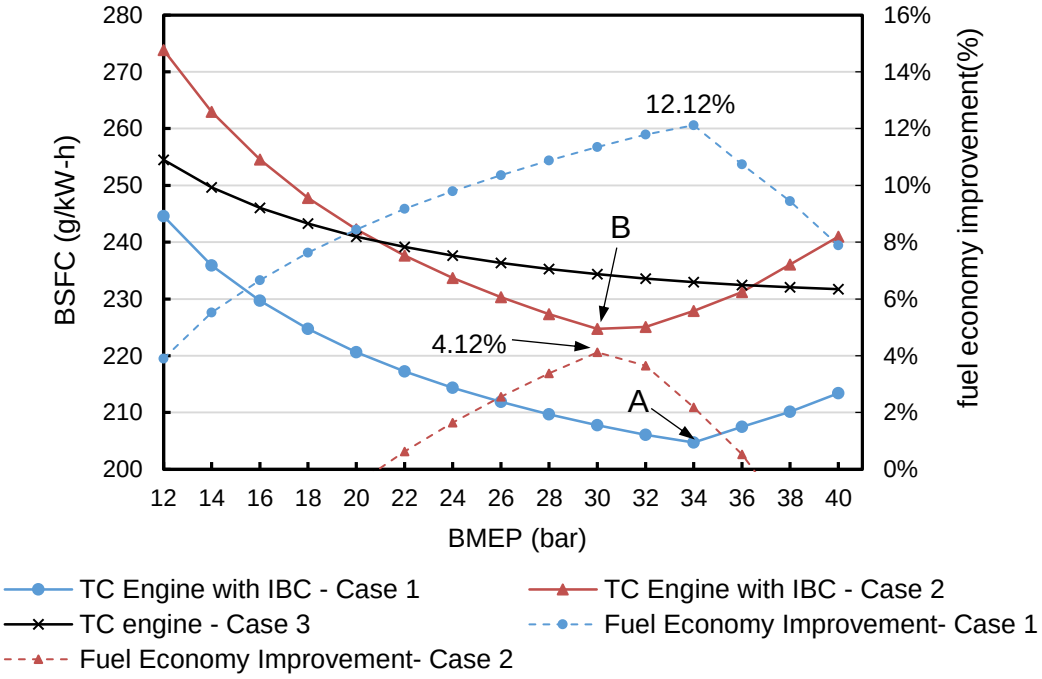

Figure 4.4 BSFC versus BMEP at different IBC turbomachinery efficiency

It is obvious from Figure 4.3 that including an IBC downstream of the turbocharger can improve the system efficiency at any chosen value of work output, in the case of the bottoming turbine (η_{it}) and compressor (η_{ic}) isentropic efficiency of 0.85 and 0.8 respectively. With increasing the power output, the efficiency increment increases to the peak of 4.98 percentage points at a BMEP of 34 bar, then

decreases steeply. The operating point with the maximum system efficiency in case 1 is referred as A. The corresponding maximum BSFC improvement is equals to 12.12%, shown in Figure 4.4. Moreover, the maximum system thermal efficiency, 41.12%, is expected at BMEP of 34 bar following by an efficiency drop.

The reduction of the system efficiency at high engine load range can be fully explained as follows. The wastegate of the turbocharger turbine tends to close in order to increase the amount of power that the turbine can deliver to the compressor, thereby increasing the boost level that the compressor provides and consequently increasing the system power output. However, it can be observed in Figure 4.5 that the turbocharger turbine wastegate in the proposed system is completely closed at BMEP of 34. Thus, to further increase the system power output, the wastegate of IBC turbine needs to open. Consequently, turbocharger turbine outlet pressure drops, thereby increasing its expansion ratio and raising the boost level of the intake charge provided by the turbo compressor.

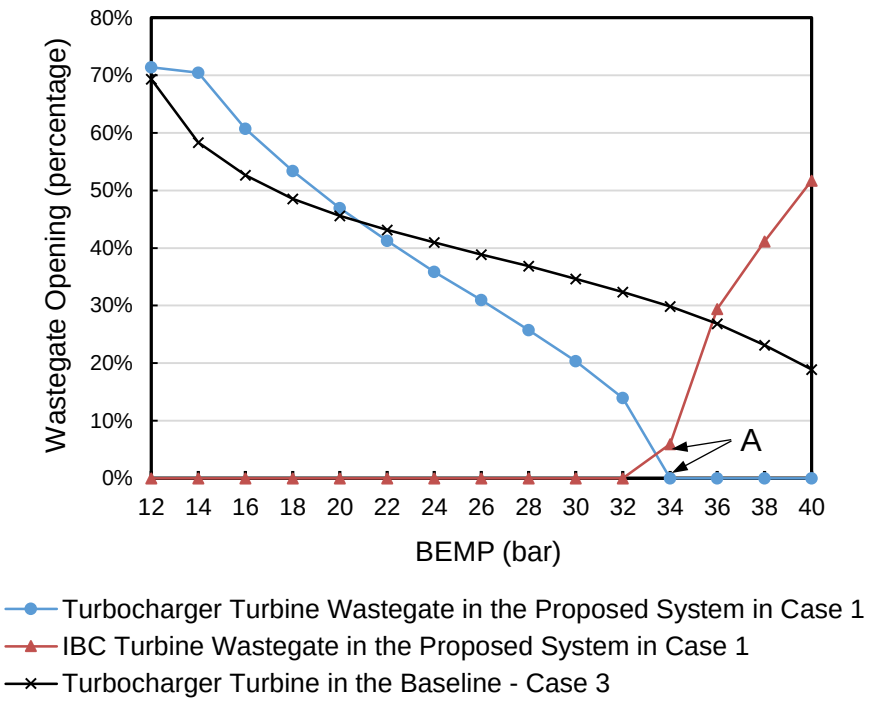

Figure 4.5 Turbine wastegate position in Case 1 and 3

By bypassing the bottoming turbine some portion of the exhaust gas available from first-stage expansion is diverted, thereby limiting the amount of power that the IBC can extract. Figure 4.6 shows the trend of power extracted by the IBC

turbine and that consumed by the IBC compressor. As can be seen in Figure 4.6, the extracted power becomes stable beyond a BMEP of 34 bar where the wastegate of the IBC turbine is open. The power consumed by the IBC compressor, which is utilized to boost the sub-atmospheric exhaust gas back to the ambient, is approximately constant with the targeted BMEP increase from 12 to 34 bar. The compressor power then increases in order to depress the exhaust pressure in order to deliver increasing BMEP via the turbocharger. Therefore, the margin between two curves in Figure 4.6, which represent the net positive bottoming energy recovery, is reduced when the target BMEP is beyond 34 bar.

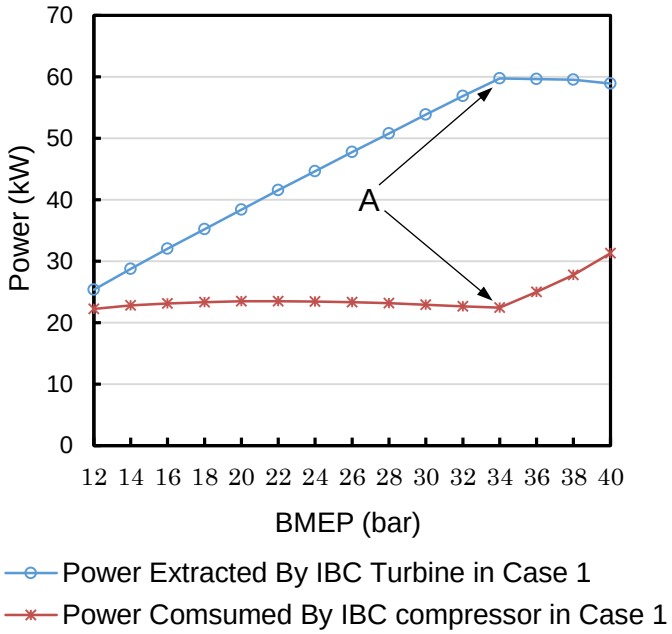

Figure 4.6 Energy flow analysis of IBC at various BMEP in Case 1

In conclusion, in order to increase the engine power output, the first-stage turbine wastegate progressively closes until it delivers the maximum power from the available pressure ratio. Interestingly, however, the IBC system can then be used to further boost the engine power output by depressing the exhaust system pressure, leading to an increased turbocharger turbine pressure ratio. This is achieved by opening the IBC turbine wastegate. Consequently, the resulting decrease in the net power provided by IBC heat-recovery system deteriorates the system efficiency.

Similar to the case of high IBC turbomachinery efficiency, the system efficiency verses system power output curve is a parabolic-like shape when η_{it} and η_{ic} decrease to 0.65 and 0.6 respectively, as shown in Figure 4.3. The maximum efficiency increment is only 1.54 percent points expected at BMEP of 30 bar where 4.12% BSFC improvement is predicted. This operating point is referred as B. Furthermore, the system efficiency of the baseline and the combined cycle becomes competitive with each other at this low-level turbomachinery efficiency. The systematic performance deterioration caused by IBC is existed when the targeted BMEP is below around 21 bar or beyond approximate 36 bar. This demonstrates the importance of turbomachinery efficiency to maintain a broad window of operating conditions where IBC cycle can produce positive output work.

Figure 4.7 shows the influence of the employment of the IBC on the outlet temperature and pressure of the turbocharged engine with the various system power outputs and two levels of IBC turbomachinery efficiencies. It can be seen that, for both case 1 and 2, the increase of the expected power output can contribute to a reduced outlet temperature of the topping cycle. This can be explained as follows. The wastegate of turbocharger turbine will close to achieve higher BMEP target. The resulting higher expansion ratio lowers the temperature of the exhaust gas at the turbocharger turbine outlet, which is directly connected to the IBC turbine. Thus, a temperature drop with increased BMEP is expected. Moreover, it seems that the bottoming turbomachinery efficiency only slightly impact the outlet temperature of the primary cycle. The maximum difference in terms of the outlet temperature between two considered cases is only 7.4 ℃. On the other hand, both case 1 and 2 demonstrates that the IBC inlet pressure increases with the increase of the expected power output until the bottom turbine wastegate is open leading to a turbocharger outlet pressure that remains stable at approximately 1.7 bar. Additionally, the IBC with lower turbomachinery efficiency can increase the back pressure of the topping cycle. This indicates that lower IBC component performance not only limits the energy-recovery capabilities of the IBC but also deteriorates the topping cycle performance due to the increase of the back pressure. More importantly, a reduction of the outlet pressure of the topping cycle caused by the IBC is observed in low-grade engine load.

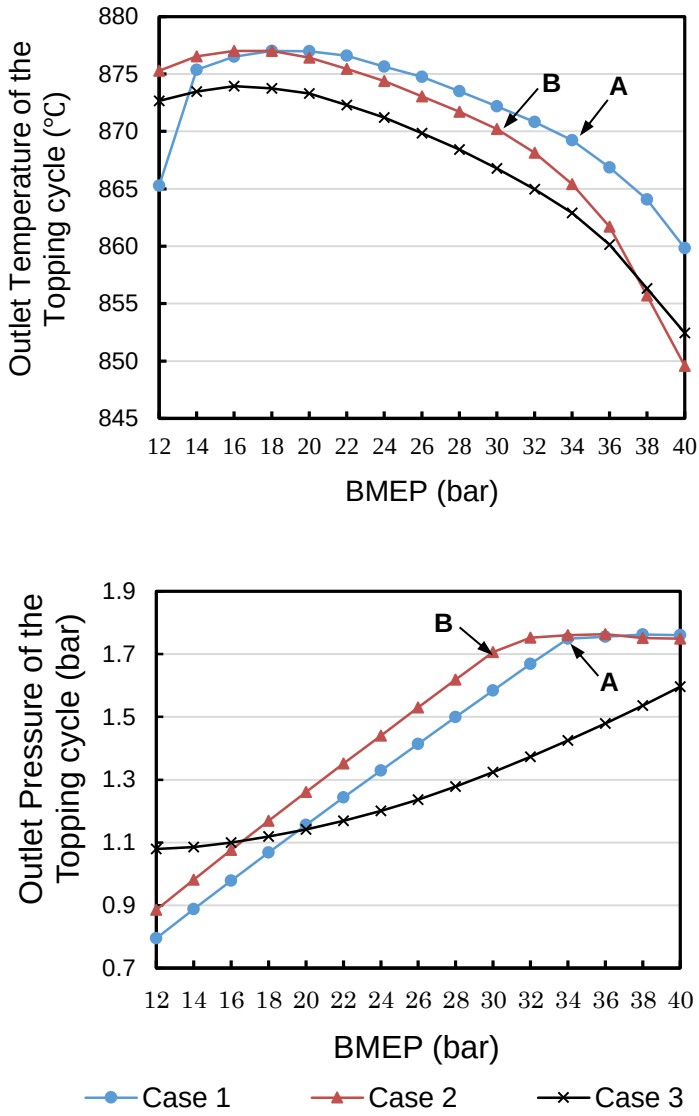

Figure 4.7 Comparison of three cases in terms of outlet boundary conditions of the topping cycle

4.4.3 Working Condition: Fully Closed Turbine Wastegate

With the benefit of the previous analysis, the best performance that the proposed system can achieve is to operate the system where the wastegates of the topping and bottoming turbines are closed. Therefore, a further study is warranted to evaluate the influences of the IBC turbine pressure ratio and turbomachinery efficiency on the system performance under these working conditions (closed wastegates).

The maximum efficiency that the proposed system can deliver is evaluated with a bottoming cycle expansion ratio of 2, 3 and 4 as shown in Figure 4.8. The trend with increasing turbomachinery efficiency is clear and expected at any chosen IBC expansion ratio. That is, a significant rise in system efficiency is demonstrated as the component efficiencies increase. Moreover, the efficiency improvement is more sensitive to the turbomachinery efficiency with a higher IBC expansion ratio. The graph also shows that optimal values of IBC expansion ratio at which the system efficiency attains its maximum value are varied with the turbomachinery efficiency. For example, at the lowest turbomachinery efficiency, the proposed system with the IBC expansion ratio of 2 can achieve a higher value of maximum system efficiency, compared to that of 3 and 4. However, when the best chosen efficiency of IBC turbomachinery is attained, the best system performance is predicted in the case of IBC expansion ratio of 4. Thus, the lower IBC expansion ratio can promote the system efficiency at the low level of turbomachinery efficiency while higher expansion ratio should be applied when component efficiencies are high.

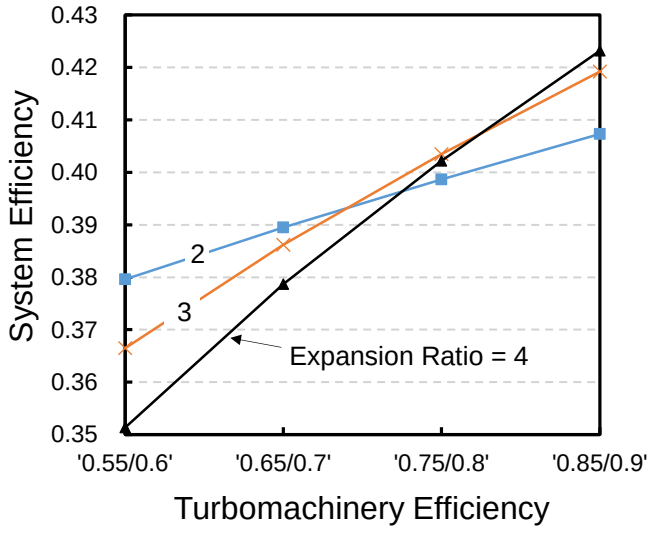

Figure 4.8 System performance investigation at optimal operating point with different IBC expansion ratio and turbomachinery efficiency (compressor/turbine)

Figure 4.9 shows the system efficiency increment provided by IBC compared to the baseline engine efficiency. The target BMEP is set as the same as that produced by the baseline turbocharged engine. With the IBC applied, both

topping and bottoming turbine wastegates are closed. The maximum efficiency increment is 6.15 per cent points when IBC expansion ratio is 4 and the turbomachinery efficiency is 0.9 and 0.85 for the turbine and compressor respectively. However, adopting an IBC deteriorates the system performance when IBC expansion ratio is 4 and the IBC turbomachinery efficiency is the below approximately 60%.

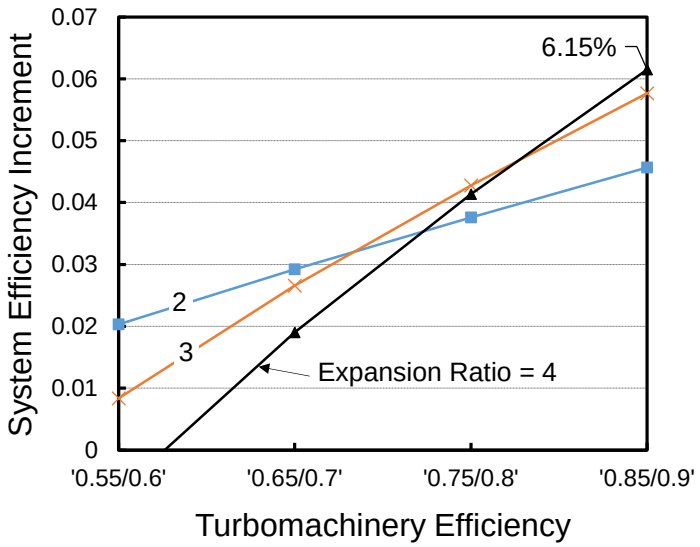

Figure 4.9 Corresponding system efficiency increment at optimal operating point of IBC

4.4.4 IBC Turbine Pressure Ratio Optimisation over the Whole Engine Operation Map

In order to present the performance of IBC at the other engine operating points, the IBC thermodynamic model fully described in Chapter 3 was coupled with the baseline GT-power model – the turbocharged SI engine. As IBC unit is installed immediately downstream of the turbocharger turbine, the turbocharger turbine outlet condition (turbine outlet temperature, pressure and mass flow rate) is considered as the inlet condition of the IBC thermodynamic model. Therefore, the baseline engine model which is built without the IBC bottoming cycle has been simulated in steady state using GT-power software in order to present the condition of the exhaust gas at the turbocharger turbine outlet. In order to perform this study, the following assumptions have been made:

- The exhaust back pressure on the compressor outlet is taken as 0.99 bar.

- A range of turbomachinery efficiencies are selected between 0.65 – 0.8 for both the compressor and turbine. These are considered here as a sensitivity study only. The author recognize that the top end of this range may be difficult to achieve in practice, but the wish to show the trend with rising component efficiencies.

- The temperature of the coolant in the IBC heat exchanger is assumed to be 300 K. The pressure loss caused by the heat exchanger is not considered here. It should be noted that the pressure loss across the heat exchanger can lower the inlet pressure of the IBC compressor, thereby increasing the power consumed by the IBC compressor to pressurize the exhaust gas from sub-atmospheric pressure to the ambient. Therefore, the pressure loss across the heat exchanger will deteriorate the performance of IBC.

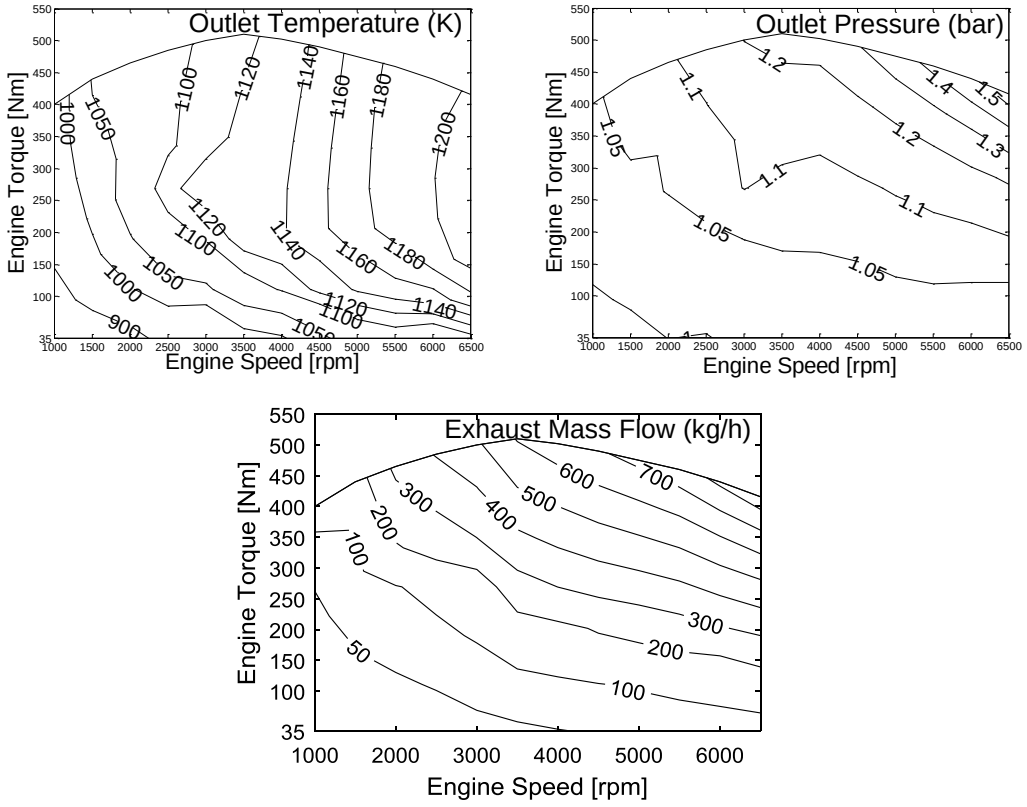

Figure 4.10 Temperature (top left), pressure (top right), and mass flow (bottom) of the exhaust gas at the turbocharger turbine outlet

Figure 4.10 shows that changing the vehicle speed and engine loads causes the exhaust gas temperature at the turbocharger turbine outlet to vary from ~850K to ~1220K. The maximum outlet pressure of the turbocharger turbine presented in Figure 4.10 is above atmospheric pressure – that is, up to 1.55 bar. This is due to a module placed downstream of the baseline engine model in order to represent the influence of the after-treatment devices. Figure 4.10 also shows the exhaust mass flow rate against engine speed and loads. As the IBC unit is installed immediately downstream of the turbocharger turbine, the outlet condition of the turbocharger turbine is considered as the inlet condition of the IBC thermodynamic model. The IBC turbine pressure ratio has been optimised at each engine operating point to deliver the maximum recovered power. Figures 4.11 and 4.12 show BSFC improvement potential from the IBC at different IBC turbomachinery efficiencies (turbine/compressor) and the corresponding optimised IBC turbine pressure ratio, respectively.

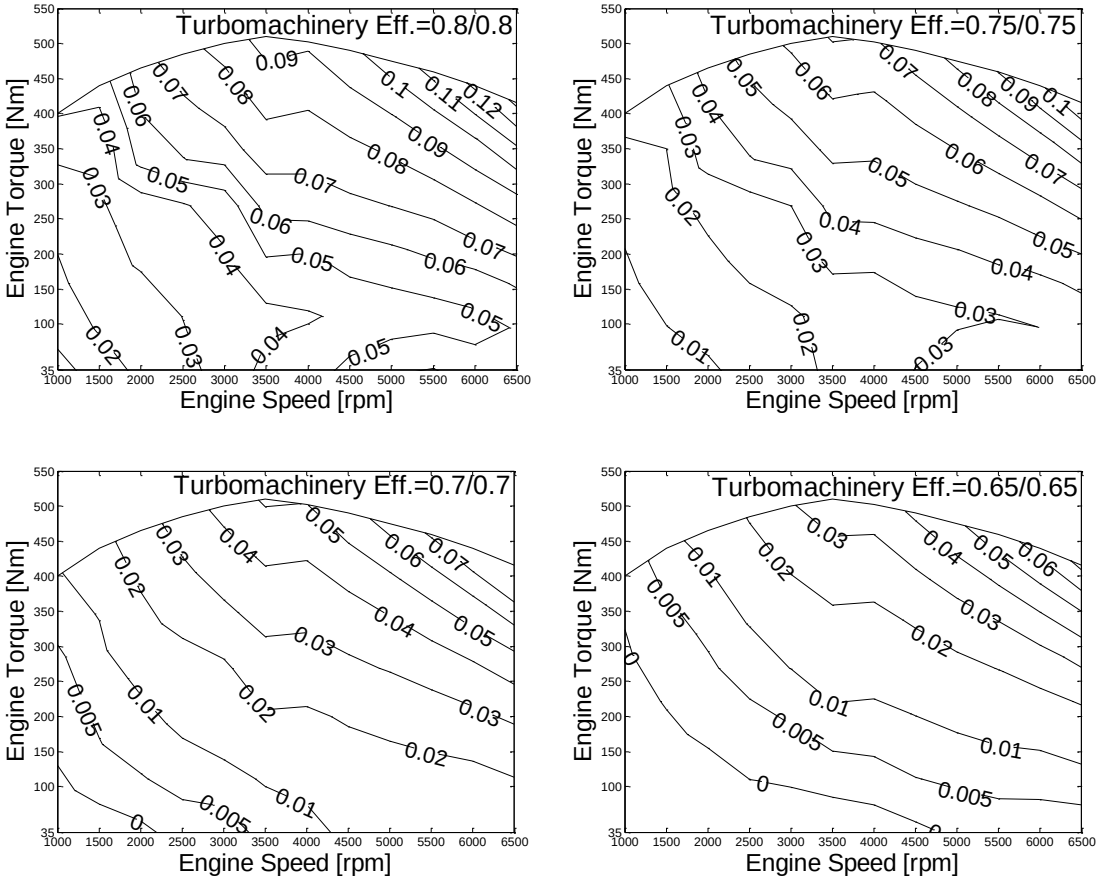

Figure 4.11 BSFC improvement (fraction) due to the employment of IBC bottoming cycle

It can be seen in Figure 4.11 that the maximum BSFC improvement of approximately 13% is delivered by IBC with the turbomachinery efficiency of 0.8/0.8 (turbine and compressor, respectively) when the engine speed is 6500 rpm at full load condition. The amount of the power produced by the IBC is significantly deteriorated by the reduction of the turbomachinery efficiency, thereby decreasing the BSFC improvement. The maximum BSFC improvement with the turbine/compressor efficiency of 0.65/0.65 is 7.1%. It should be noted that the IBC power output can be negative at low engine speed and part-loads, depending on the IBC turbomachinery efficiency. The range of the engine operating points where there is no net work produced by IBC system increases with decreasing IBC turbomachinery efficiency.

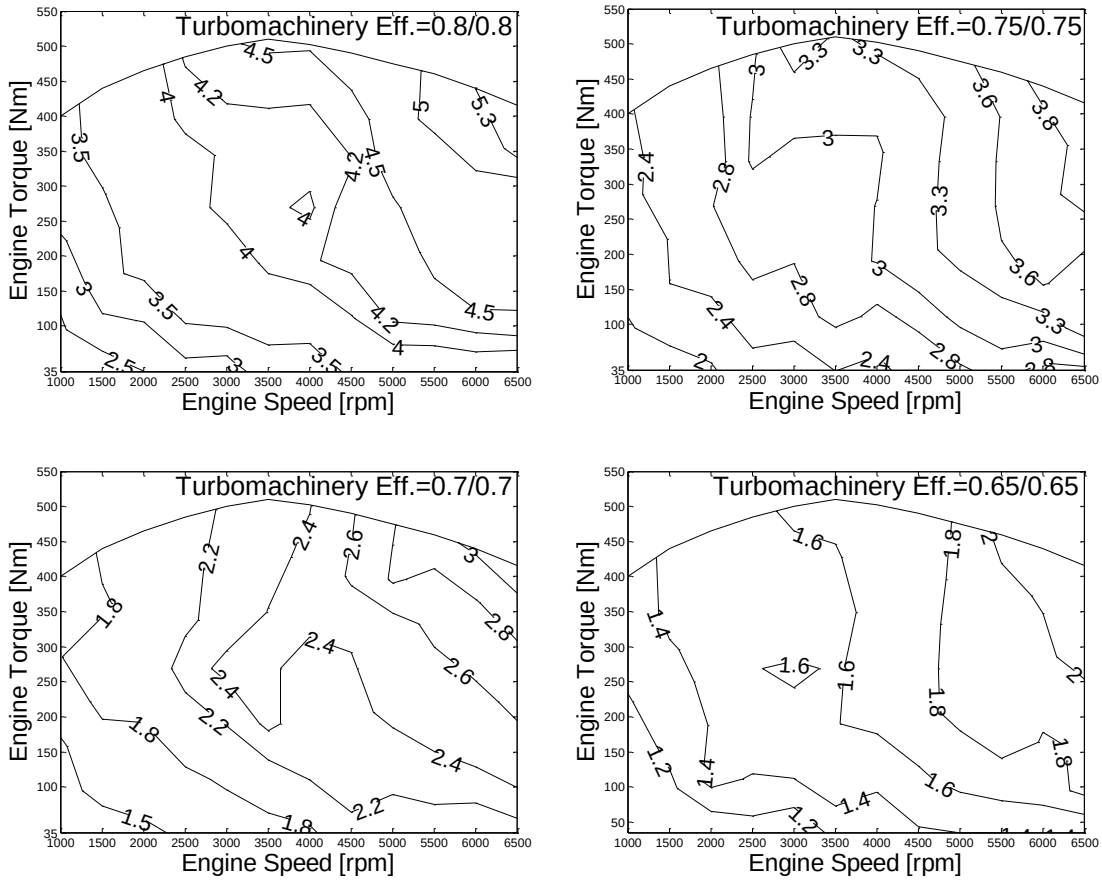

Figure 4.12 Optimised IBC turbine pressure ratio in the engine map

It should be noted that increasing the inlet pressure of IBC system can contribute to improvement of IBC performance. Therefore, engine BSFC improvement shown in Figure 4.11 could be further enlarged by increasing IBC inlet pressure.

However, increasing IBC inlet pressure leads to a higher back pressure of the engine which can negatively influence its performance. Hence, a system compromise is required to select the optimum IBC inlet pressure.

4.4.5 IBC Compressor/Turbine Matching at Engine Mini-Map Points

The performance evaluation of IBC system has been presented at the steady-state engine operating points in pervious sections. The promising improvement achieved by IBC system was found in the simulation results. However, IC engine operation conditions in practice are highly dynamic. In other words, the exhaust conditions available from the turbocharger turbine outlet vary within the wide range of the pressure, temperature, and mass flow rate. Based on the previous 0D and 1D simulation results, it has been clearly revealed that the inlet condition of IBC system, which is the outlet condition of the primary cycle, can significantly impact the performance of the IBC turbine and compressor and, thus, affect the amount of the energy recovered by IBC system. Therefore, IBC system coupled with the selected SI engine should be investigated over engine transient condition, to fully present its capability of the energy recovery. At vehicle level, various types of driving cycles are introduced by different countries and organizations to assess the performance of vehicle, such as engine fuel consumption and polluting emissions. These driving cycles are designed to represent the real-life driving. Thus, these cycles are also used as an important input in designing and evaluating future powertrain systems and vehicle concepts. In order to reveal the benefits of IBC system in real-life driving, a driving cycle should be selected to design and optimise the IBC system.

However, there are three roadblocks to perform the transient simulations of the combined system over driving cycles. First, running an engine model in a transient mode causes high computation cost. Second, a sophisticated control strategy should be developed for the combined system, to maximize the benefits achieved by IBC system. Most important, the control unit is required to ensure that the engine is always able to meet the torque demand at any operating condition. Thus, the control strategy must adjust the wastegates of the

turbocharger turbine and IBC turbine, even the IBC bypass system if required, to control the back pressure caused by the existence of the IBC system. This is because that the back pressure is able to cause the reduction of the combustion efficiency, thereby harming the engine performance. In consequence, the engine is no longer able to deliver the torque demand, even when the power recovered by IBC system is directly fed back to engine. However, the control strategy only can be developed when the system characters have been fully studied. Moreover, the development of the control strategy is out of the scope of this project. The final roadblock is that SI engine GT-power model available in this research does not have transient simulation capability. In GT-power, in order to perform the transient simulation, all inputs must be controlled depending on operating conditions by using either some forms of look-up or predictive models. In addition, it is critical to calibrate the engine model against the transient engine test data, in order to gain transient capability. However, since the selected SI engine model in this research is only calibrated against the steady-state engine test data, the transient simulations of the proposed system – SI engine and IBC system cannot be performed.

In conclusion, the performance of IBC system with the selected SI engine should be evaluated over a transient condition which should be a legislated driving cycle. However, the three roadblocks described above hinder the required simulations. Thus, an alternative investigation – mini-map investigation was proposed. Mini-map consists of a set of steady-state operating points with weighting, which is designed to represent for the chosen driving cycle. Thus, the simulation results at such mini-map can be used to reveal the benefits of IBC system over the corresponding driving cycle. This is an industry common practice.

4.4.5.1 Engine Mini-map Operating Points

The mini-map introduced in this research was generated by the vehicle simulation tool, referred as CalSim. It is an internal JLR MATLAB/Simulink-based vehicle modelling tool.

The engine test data used in this section is same as the one shown in Section 3.5.4.1. The test has been conducted over the WLTP in an SUV vehicle with 2-litre turbocharged SI engine. Figure 4.13 shows the time distribution of engine operating points on the engine map, against the corresponding mini-map points. The main descriptive parameters of WLTP Mini-mapping points with weighting are listed in Table 4.3.

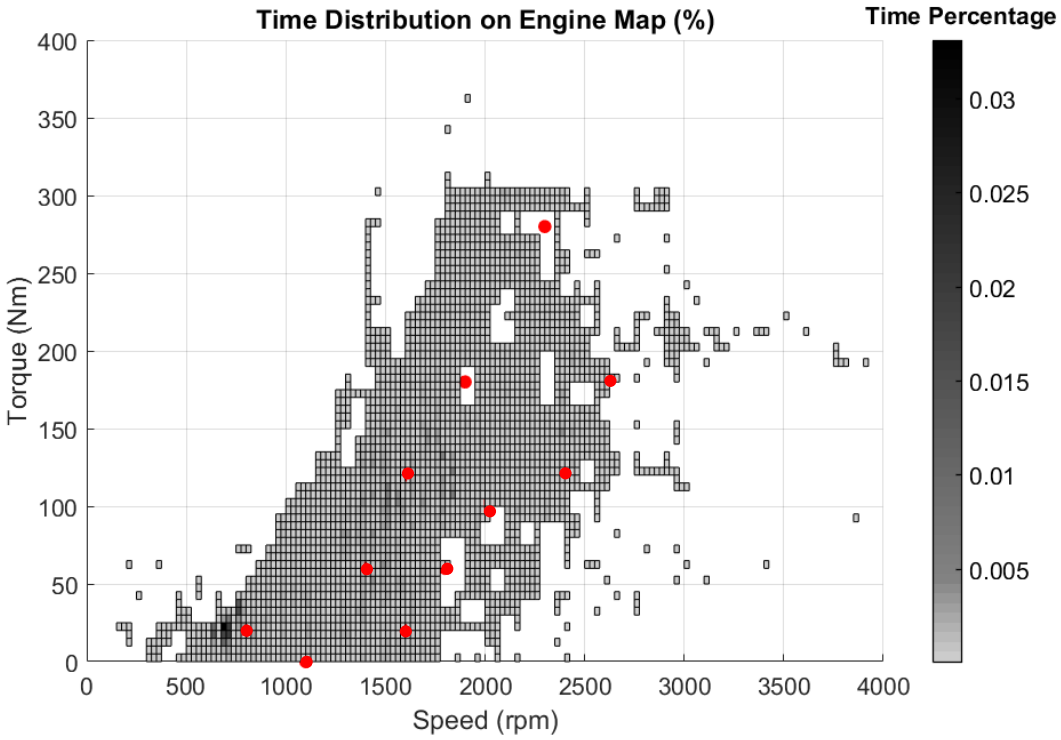

Figure 4.13 Time distribution of engine operating points on the engine map

As there is no engine steady-state bench test conducted at any mini-map point, the exhaust temperature and mass flow rate shown in Table 4.3 were predicted at a pipe directly downstream of the turbocharger turbine in the calibrated SI engine GT-power model described in Section 4.3. Since the chosen SI engine GT-power model is well calibrated at other steady-state conditions, the predicted exhaust temperature and mass flow rate are representative and reliable, which could be introduced as the inlet boundary conditions of IBC system to perform the following analysis.

Table 4.3 Descriptive parameters of WLTP Mini-mapping points

Case Number	Engine Speed	Brake Torque	BMEP	Mini-map Weightings	Brake Power	Exhaust Temp.	Exhaust Mass flow
[-]	[rpm]	[Nm]	[bar]	[%]	[kW]	[K]	[kg/h]
1	800	20	1.3	17.39%	1.7	717.9	12.7
2	1100	0	0.0	4.55%	0.0	636.6	8.9
3	1400	60	3.8	7.16%	8.8	830.9	41.3
4	1600	20	1.3	8.33%	3.4	753.5	24.1
5	1600	120	7.6	7.86%	20.1	945.0	81.9
6	1800	60	3.8	8.05%	11.3	885.9	53.5
7	1900	180	11.3	5.23%	35.8	1007.1	140.6
8	2000	100	6.3	5.31%	20.9	950.9	88.4
9	2300	280	17.6	2.89%	67.4	1088.2	277.5
10	2400	120	7.6	9.97%	30.2	1008.3	123.5
11	2600	180	11.3	5.25%	49.0	1057.3	189.8

4.4.5.2 IBC Turbine and Compressor Matching

The IBC turbine and compressor matching should be conducted at one mini-map point, then evaluated at the rest of mini-map points. In the previous study, Figure 4.11 shows that for the selected SI engine, IBC power output can be negative at engine low-load and low-speed conditions. This is because that at these engine operating points, the exhaust mass flow and temperature are too low to recover the wasted heat energy. Thus, IBC system should be designed to work at the condition when the exhaust mass flow and temperature are relatively high. In addition, JLR reckons that mini-map point 11 is considered as the engine operating point when the vehicle is in cruising mode. Thus, mini-map point 11 is selected as the design point for IBC system, as in this research IBC is mainly designed to recover the wasted heat energy at vehicle cruising mode. However, IBC performance will still be evaluated over entire WLTP driving cycle.

In the matching process, there are two design targets. The first design target is to remain the SI engine unaffected. Thus, the back pressure generated by IBC system must be fixed as 1 bar. The best modelling approach to achieve the inlet

pressure of 1 bar is that only IBC model is utilized in the matching process and the corresponding inlet pressure is imposed as 1 bar. By doing so, there is no need to predict SI engine performance in the matching process. The second target is to maximize the power generated by IBC system. Thus, the real characteristic maps for the turbocharger in SI engine are adopted and optimised by changing their size.

4.4.5.3 IBC Model Description

The IBC model in the matching process is built in GT-power and described below:

1. The single-stage IBC GT-power model is built in isolation from the SI engine, shown in Figure 4.14. The real characteristic maps of the SI engine turbocharger are introduced as the baseline for IBC system.

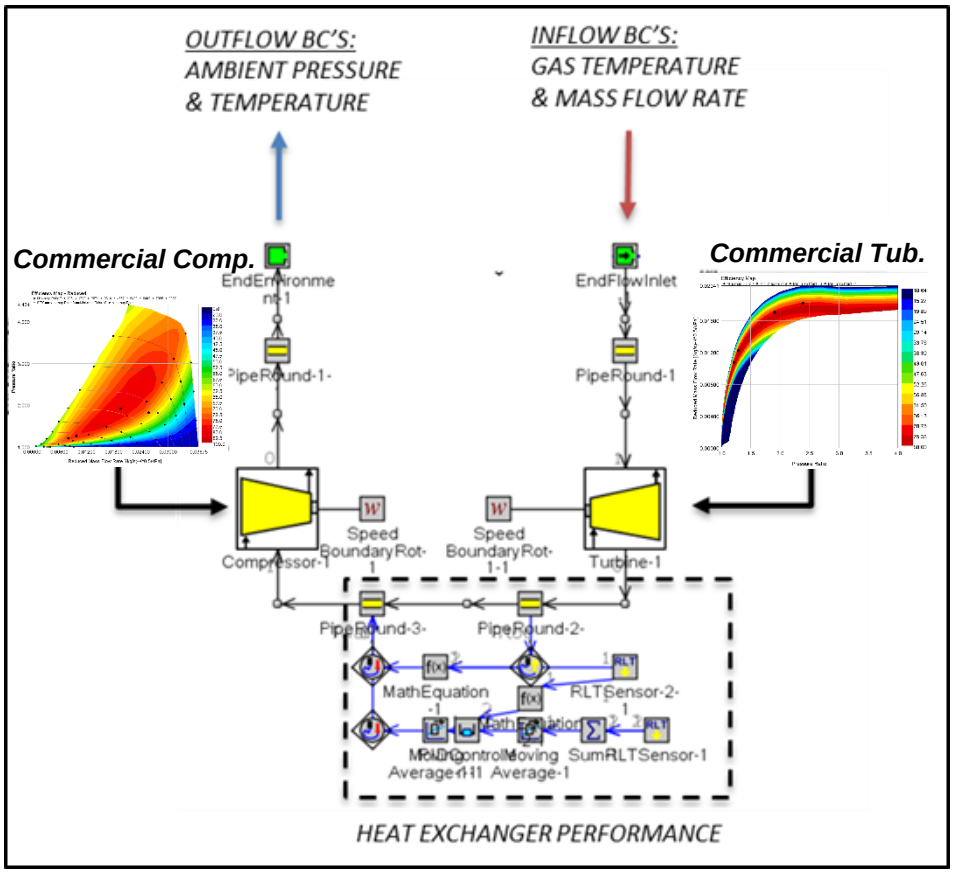

Figure 4.14 Single-stage IBC GT-power model

2. The exhaust mass flow rate and temperature at mini-map 11 is introduced as the inlet boundary conditions of the IBC model.

3. Simple heat exchanger model is employed. The HE effectiveness is fixed as 0.9 and the coolant temperature is 315 K. The resulting pressure loss is fixed as 0.01 bar.

4. The outlet boundary conditions of the IBC system are fixed as the parameters of standard atmospheric state – the pressure of 1 bar and temperature of 298 K.

5. It is assumed that an electric generator is connected to the IBC shaft, to convert the mechanical energy generated by IBC system to the electric energy. Thus, 30% recovered energy is assumed as the energy loss due to the friction loss at the IBC shaft and the efficiency loss in the electric generator.

6. GA optimisation approach is utilized to maximize the power generation of IBC system, by sizing the IBC compressor and turbine. The attributes 'Mass Multiplier' within the GT-power turbine and compressor modules are applied to achieve the map sizing, respectively. The third optimal variable is the IBC shaft speed, as it is able to affect the IBC power generation and the resulting back pressure. Since the inlet pressure must be fixed as 1 bar to keep the SI engine unaffected, it must be introduced as the constraint function in the optimisation process.

4.4.5.4 Optimisation Results

The optimal variables and corresponding predicted results are list in Table 4.4. The original turbocharged SI engine at mini-point 11 is referred as the baseline, which standalone IBC system is as the IBC. It should be noted that the power generated by IBC in Table 4.4 has taken account of 70% combined efficiency of the shaft mechanical and the electric generator efficiencies.

Table 4.4 Results of turbine and compressor matching

Optimisation Results	Turbine/Compressor Mass Multiplier = 0.60/0.57 Shaft Speed = 112320 rpm		
	Baseline	IBC	Improvement
BMEP (bar)	11.3		
Power (kW)	48.97	1.46	2.98%
BSFC (g/kW*h)	252.3	245.0	2.90%
	Pressure Ratio	Efficiency	Power (kW)
IBC Compressor	1.94	79.87%	5.20
IBC Turbine	1.93	75.80%	7.29

Since the optimisation is performed with the IBC system in isolation from the SI engine, the BSFC in IBC column is calculated based upon the SI engine power and IBC power, showing in Eq. 4.5.

$$BSFC_{engine} = \frac{r}{P_{engine}}$$
$$BSFC_{engine+IBC} = \frac{r}{P_{engine} + P_{IBC}} \tag{4.5}$$

where r is the fuel consumption rate in grams per second (g/s). P is the net power produced by SI engine and IBC, respectively.

Thus, the BSFC improvement caused by IBC is

$$BSFC\ Improvement = \frac{BSFC_{combined} - BSFC_{engine}}{BSFC_{combined}}$$
$$= \frac{P_{IBC}}{P_{engine} + P_{IBC}} \tag{4.6}$$

As shown in Table 4.4, the 2.9% of BSFC improvement has been achieved by matching the compressor and turbine characteristic maps. It should be noted that the IBC inlet pressure is fixed as 1 bar. In other words, no back pressure is generated by the employment of IBC system, thereby leaving the engine

performance unaffected. However, in Section 4.4.1, the compressor/turbine maps size optimisation at the engine operating point of 4500 rpm speed and 30.9 bar BMEP shows that the maximum power of the combined system is achieved when the inlet pressure of IBC is higher than 1 bar.

In this section, the reason of why the IBC inlet pressure is fixed as 1 bar is explained below. The previous study shows that the recovered power by IBC system can be higher than the resulting engine power loss when the IBC inlet pressure is beyond atmospheric pressure. However, the rise of the exhaust back pressure can cause a massive increase of exhaust residual gas fraction. In addition, this is also the reason for the irregular combustion phenomena, referred as knocking. The knock margin is reduced when engine operates at the lower engine speed range with high engine torque. Thus, the mini-map 11 is the quite sensitive operating condition for the engine knocking. However, the SI engine GT-power model available in this research is no capable of predicting the irregular combustion. Moreover, the effects of the back pressure in engine combustion is out of the research scopes. Therefore, in the matching process of the compressor and turbine maps, the inlet pressure was remained at 1 bar, despite the fact that the additional back pressure is beneficial to the systematic performance of the SI engine with IBC system.

The re-sized compressor and turbine maps are introduced in IBC system in order to evaluate its benefits at the rest of mini-map points. The combined GT-power model – SI engine with IBC system is utilized to perform the corresponding simulations. A PID controller is utilized to remain IBC inlet pressure at 1 bar, by changing the IBC turbo speed. Although the pressure loss across the heat exchanger should vary the exhaust mass flow rate, it is fixed as 0.01 bar over all mini-map points due to the absence of the detailed heat exchanger model. However, the heat exchanger was designed and manufactured by the additive manufacturing by a research partner in this project. At the experiment stage, it was tested individually, then along with the whole IBC system.

It should be noted that the 30% of total recovered power is considered as the mechanical loss and electric generator power loss, and deducted from the power

generated by IBC at all mini-map points. The heat exchanger effectiveness is fixed as 0.9.

The corresponding simulation results are shown in Table 4.5. It shows that IBC with the optimised compressor and turbine is only able to produce net power at mini-map points 7, 9, 10, and 11. This is because that the exhaust mass flow rates at mini-map points 1 – 6 and 8 are significantly lower than that at mini-map 11 where the IBC compressor and turbine are matched. In a consequence, efficiencies of IBC compressor and turbine drop too low to generate net power at mini-map points 1 – 6 and 8.

Table 4.5 Performance evaluation of optimised compressor and turbine

Optimisation Results	Turbine/Compressor Mass Multiplier = 0.60/0.57			
	OP 7	OP 9	OP 10	OP 11
Engine BMEP (bar)	11.3	17.6	7.6	11.3
Combined System BMEP (bar)	11.3	17.5	7.6	11.3
Engine Power (kW)	35.78	67.17	30.40	48.97
IBC Power (kW)	0.50	3.94	0.33	1.50
Engine BSFC (g/kW*h)	255.19	269.06	269.78	252.23
Exhaust Mass Flow (kg/h)	140.6	262.17	123.5	189.8
IBC Inlet Pressure (bar)	1.00	1.31	1.00	1.00
IBC Turbine Eff.	78.69%	72.41%	77.18%	75.82%
IBC Turbine PR	1.30	2.39	1.21	1.90
IBC Turbine Power (kW)	2.27	13.13	1.45	7.23
IBC Compressor Eff.	75.93%	69.20%	73.96%	79.76%
IBC Compressor PR	1.31	1.82	1.21	1.92
IBC Compressor Power (kW)	1.56	8.19	0.98	5.08
BSFC Improvement (%)	1.38%	5.13%	1.06%	2.98%
IBC / Engine Power Ratio	0.014	0.054	0.011	0.031

The simulation results show that the maximum net power recovered by IBC is 3.94 kW at mini-map point 9. Although the turbine and compressor efficiencies are relatively low at mini-map point 9, the high exhaust mass flow rate is beneficial to the power recovery. Moreover, since the turbine and compressor maps were matched at mini-map point 11, the high exhaust mass flow rate at mini-map point 9 contributes to the fact that the corresponding IBC inlet pressure is above atmospheric pressure. Consequently, with the back pressure of 1.31 bar, the SI engine is only able to deliver 67.17 kW brake power, which is 0.3 kW less than the case without any back pressure. Thus, at mini-map point 9 the IBC net power is required to compensate the engine performance deterioration. Then, any surplus power is considered as the performance improvement caused by the employment of IBC system. However, 5.13% of BSFC improvement is still expected at mini-map point 9, even though 0.3 kW of engine power reduction is caused by the back pressure of 1.31 bar. Overall, based upon the weighting at mini-map point 7, 9, 10, and 11, IBC with optimised compressor and turbine map can only deliver 0.66% BSFC improvement over the entire WLTP driving cycle. However, it should be noted that the compressor and turbine maps are optimised for the vehicle cruising mode, instead of the overall driving cycle.

At mini-map points 7, 10 and 11, the IBC system with optimised turbomachinery is able to remain the atmospheric pressure at the IBC inlet, thereby leaving the engine performance unaffected. Since the turbine and compressor marching process was conducted at mini-point 11, the highest BSFC improvement of 2.98% is found at this point. Although the quantity of the IBC net power is low at mini-map point 7 and 10, the corresponding BSFC improvement is still more than 1 percentage due to the relatively low engine power at these points.

At mini-map point 11, the IBC net powers listed in Table 4.4 and 4.5 are slightly different. This is because at matching process, IBC GT-power model built in isolation from the SI engine was utilized. Thus, the exhaust gas in the corresponding simulations was assumed as air. However, the IBC performance evaluation at mini-map points was conducted by the combined GT-power model. Thus, the exhaust gas properties were predicted by the combustion model embedded in SI engine model. In conclusion, the IBC net power discrepancy is

caused by the different working fluids feeding into IBC system. The re-sized turbine and compressor characteristic maps are shown in Figure 4.15.

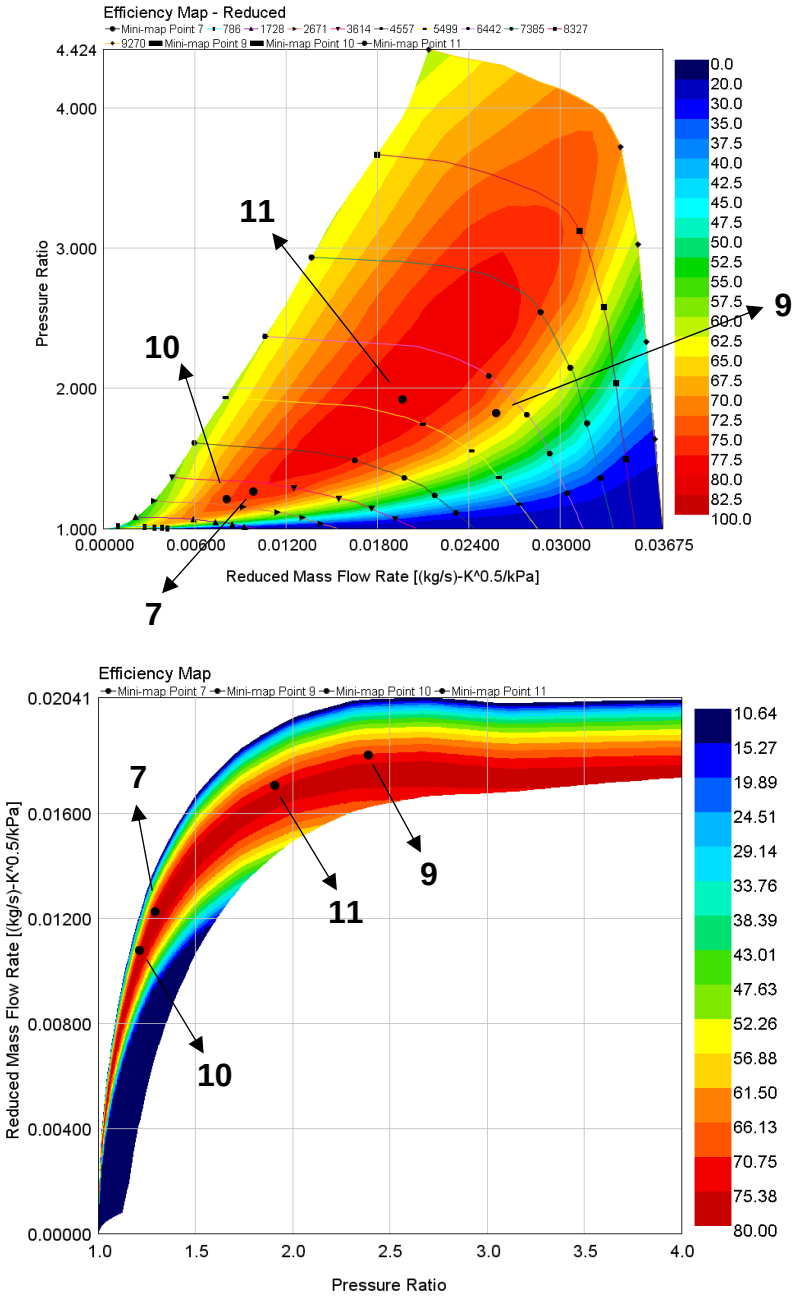

Figure 4.15 Compressor (top) and turbine (bottom) characteristic maps with operating points

4.4.5.5 Compressor and Turbine Selection

In the previous section, the compressor and turbine maps were re-sized to deliver the optimal performance of the IBC system. Thus, a commercial compressor and

turbine can be selected by matching the optimal turbomachinery map size and, thus, considered as the baseline design for the later study. Due to the limited access to the commercial turbomachinery characteristic maps, only two commercial compressors have similar operating ranges of mass flow rate and pressure ratio to that of the optimised one, while only three for turbines. Thus, all combination of available compressors and turbines were investigated to select the best combination that delivers the maximum IBC net power at the mini-map point 11.

The IBC GT-power model presented in the turbomachinery matching process was utilized to perform the compressor and turbine selection. The exhaust mass flow rate and temperature were introduced at the IBC inlet, while the IBC outlet was set as the ambient. The coolant temperature was fixed as 315 K. However, the HE pressure drop and effectiveness were assumed as 0.05 bar and 0.96, respectively. These assumptions represent the worst-case scenario according to the heat exchanger 3D CFD analysis performed by the project partner. Regarding the power loss, 30% power differential between turbine and compressor was considered as the friction loss at the IBC shaft and the efficiency loss in the electric generator.

In order to eliminate the negative effect of the back pressure on the engine performance, the IBC shaft speed was controlled to deliver the inlet pressure of 1 bar. The predicted IBC net power was selected to represent its performance and, thus, it was considered as the only criteria to select the compressor and turbine.

The 1D simulations results are presented in Table 4.6. There is no performance prediction for the combination of compressor candidate 1 and turbine candidate B, as the resulting IBC inlet pressure is unable to reach at 1 bar. The highest IBC net power of 0.91 kW is found at the case of combination of the compressor candidates 2 and turbine candidate B. The resulting BSFC improvement is 1.82%, which is lower than 2.98% of the optimal compressor and turbine shown in Table 4.5. This is because that the higher heat exchanger pressure drop, 0.05 bar, was assumed in the analysis of compressor and turbine selection. In addition,

comparing to 79.76% efficiency delivered by the optimised compressor, the compressor candidate 2 of 75.7% contributes to the lower predicted IBC net power. Even worse, the relatively low turbine efficiency of 70% further deteriorates the IBC performance.

Table 4.6 Performance evaluation of all combinations

Mini-map Point 11:	Exhaust Temp.=1057.3 K Exhaust Flow Rate=189.8 kg/h			Engine Power=49 kW BSFC=252.3 g/kW*h		
Compressor Candidates	1			2		
Turbine Candidates	A	B	C	A	B	C
IBC Net Power (kW)	0.69		0.82	0.72	0.91	0.76
IBC Shaft Speed (krpm)	140.5		129.6	136.2	125.4	102.7
IBC Inlet Pressure (bar)	1.0		1.0	1.0	1.0	1.0
Turbine Eff.	71.7%		73.6%	68.1%	70.0%	69.4%
Turbine PR	1.83		1.69	2.23	2.00	1.60
Turbine Rack Position	0.52		1.00	0.47	1.00	1.00
Turbine Power (kW)	6.45		5.82	7.92	7.11	4.95
Comp. Inlet Pressure (bar)	0.50		0.54	0.40	0.45	0.57
Comp. Inlet Temp. (°C)	60.85		61.18	60.10	60.51	61.62
Compressor Eff.	69.9%		71.1%	75.2%	75.7%	76.3%
Compressor PR	1.98		1.82	2.46	2.17	1.71
Compressor Power (kW)	5.47		4.65	6.89	5.81	3.87
BSFC Improvement (%)	1.38%		1.64%	1.45%	1.82%	1.52%
IBC / Engine Power Ratio	0.014		0.017	0.015	0.019	0.015

As a result, the commercial compressor candidate 2 and turbine candidate B were selected as the baseline design to perform the later study, due to the resulting highest IBC net power. However, relatively low efficiencies of the selected compressor and turbine were found. In other words, compressor and

turbine optimisation should be taken to improve their performance at the operating condition of mini-point 11. Modifying blade height is the common method to adjust the performance of the existing compressor and turbine without major changes of the blade shape. Thus, the compressor and turbine blades will be trimmed or extruded to improve their performance and described in detail in the next chapter.

4.5 1D Simulation Conclusion

The inverted Brayton bottoming cycle applied to a turbocharged SI engine has been modelled in GT-power. The intent is to investigate the potential performance of an IBC to recover residual heat from the exhaust gas stream available from a current automotive plant. Although some studies of heat recovery cycles have indicated that bottoming ORC technology have a higher capability of extracting energy from the exhaust in comparison with the Brayton cycles, the appeal of the latter is its relative simplicity and the use of readily available radial turbomachinery components. Currently, two main Brayton cycles, the pressurized and inverted cycle, are considered potential exhaust-gas heat-recovery systems. The pressurized Brayton cycle utilizes a separate working fluid to obtain heat from the primary cycle through a gas-to-air heat exchanger. However, the inverted Brayton cycle utilizes the exhaust gas as a working fluid and the heat transfer process simply cools the gases prior to compression - which may prove simpler to implement. More importantly, the predicted performance of the inverted Brayton cycle is superior to that of the pressurized Brayton cycle. Nonetheless, there are practical difficulties such as fouling, condensation and sub-atmospheric operation that are not considered in this work.

A validated turbocharged engine incorporating a bottoming IBC has been modelled in GT-power. The optimisation process has been presented at the engine speed of 4500 rpm and BMEP of 30.9 bar, in terms of three IBC operating parameters – torque applied on the IBC turbomachine shaft, compressor mass-flow multiplier and turbine mass-flow multiplier, in order to perform the

subsequent parametric study and provide guidance for the design of a practical IBC. In this study, the characteristics maps of the turbocharger in the topping cycle have been considered as the reference maps for IBC turbomachinery. This demonstrated that 2.25 percentage points of system efficiency increment can be expected due to the employment of an IBC with scaled turbocharger component maps. Since standard turbocharger maps where used, performance with a more appropriate match is expected to yield further system efficiency improvement. It should be noted that although adopting an IBC as a bottoming heat-recovery cycle does not require pressure from the topping power plant to operate, this research demonstrates that a small increase in the back pressure of the primary cycle is to be expected if the system is optimised for BSFC. This outcome results from the optimal trade-off between the heat recovered power and the resulting power loss due to pumping work.

The further study has been focused on the IBC performance at various engine loads with two levels of the IBC turbomachinery efficiency. The bottoming expansion ratio is fixed at 3:1. In this case, the employment of an IBC with high turbomachinery efficiencies leads to varying degrees of performance improvement depending on the engine operating point. However, with a decrease in the turbomachinery efficiencies, the range of engine loads where IBC could boost the system performance is reduced. The maximum efficiency of a combined system is expected when both the topping and bottoming turbine wastegates are closed. The corresponding maximum efficiency increment is 4.98 percent points. Moreover, adopting an IBC as the bottoming cycle significantly influences the back pressure of the topping cycle, while only slight changes of the topping cycle outlet temperature is predicted caused by the employment of IBC.

The parametric study of the proposed system performance at the operating point where the wastegates of the topping and bottoming turbines are closed indicated that up to 6.15 percent points of efficiency improvement can be expected at IBC expansion ratio of 4 and an IBC compressor and turbine efficiency of 0.85 and 0.9 respectively. It also was found that the IBC with the high turbomachinery efficiency should operate at high expansion ratio in order to achieve higher

performance of the combined power cycle, while that with low efficiency - low expansion ratio can recover more energy from the exhaust gas. In this scenario, the deterioration in the system efficiency when the low efficiency IBC with expansion ratio of 3 is adopted, predicted in case 2, can be avoided by changing the torque on the IBC shaft to lower the IBC expansion ratio.

The simulation of IBC thermodynamic model coupled with SI engine GT-power model revealed that the IBC system can deliver a reasonable BSFC improvement over whole engine operating up to a maximum value of 13% at 6500 rpm under full load conditions with IBC turbomachinery efficiencies of 80%. Nevertheless, the IBC performance can be negatively affected by a reduction of the turbomachinery efficiency such that at some part load engine operating points, the net IBC power output is negative.

Afterwards, the commercial radial turbomachinery for IBC system has been re-matched based on the real-world driving cycle. However, given the lack of the transient GT-power models, the absence of control strategy, and high computation cost, the matching process was performed at one of mini-map points. Mini-map points were a set of steady state engine operating points with weights, generated by the research partner – JLR, to present engine performance of the real work driving cycle. In this research, mini-map points over WLTP driving cycle was chosen to evaluate the IBC performance. The commercial turbomachinery was re-sized at mini-point 11. The resulting IBC net power of 1.5 kW was expected. However, due to the wide range of exhaust mass flow rate at mini-map points, the net power only can be delivered at mini-map point 7, 9, 10, and 11 with the optimal compressor and turbine. Then, an existing compressor and turbine was selected based upon the optimised size of the turbomachinery. However, the 1D simulation results show that both the selected compressor and turbine suffer relatively low efficiency at mini-map point 11. Thus, blade trimming will be applied to the selected compressor and turbine to improve their performance in the next chapter. The trimmed turbomachinery performance will be evaluated by 3D modelling in order to achieve the final design for the IBC system prototype.

Chapter 5 – Compressor and Turbine Design

5.1 Introduction

In Chapter 4, a commercial compressor and turbine were selected for the IBC prototype, based upon 1D simulation results. However, two issues hider the directly employment of the selected turbomachinery. First, both compressor and turbine suffer suboptimal efficiency at the IBC design operating point. Second, there are uncertainties about the influence of inlet boundary conditions in the turbomachinery characteristic maps. In 1D simulations, the turbomachinery characteristic maps provided by the manufacturer is imposed and utilized to predict the corresponding performance. These characteristic maps are measured by the standard turbomachinery mapping process, that is, the boundary conditions at the compressor inlet and the turbine outlet are fixed as the ambient during the mapping process. This is because the presented test conditions are able to fully represent the operating condition when the compressor and turbine are used as the turbocharger for IC engines. However, regarding IBC system, the ambient condition is expected at the compressor outlet and turbine inlet, instead of the compressor inlet and turbine outlet. Thus, given the uncertainties above and the poor efficiencies of the selected compressor and turbine, turbomachinery 3D modelling performed by ANSYS CFX were conducted in this chapter to predict and optimise the IBC compressor and turbine performance. Moreover, the study about the effect of the inlet boundary conditions on turbomachinery performance characteristic maps will be presented in Chapter 6.

At the beginning of this chapter, the 3D model settings were described and selected in detail, to ensure that 3D simulation results are reliable. Five critical steps for completing 3D simulations were followed in this research, 1) generating model geometry and flow domain which are able to fully represent a physical nature of the simulation target, 2) generating computational grids with the trade-off between the computational cost and the simulation accuracy, 3) establishing the boundary and initial conditions, 4) setting up the proper solver, and 5) performing the simulations.

Then, impeller trimming approach was applied to compressor and turbine in order to improve their performance at the design point. It is a common practice in the turbocharger industry to modify an existing impeller design to meet a new flow or pressure ratio at the design point. The resulting benefit is that the sophisticated knowledge of designing a new compressor or turbine from scratch is excluded in the performance improvement process. In addition, less time and effort are required by trimming impeller blade. Thus, given the limited time for the compressor and turbine design in this research, both selected commercial compressor and turbine were re-sized by trimming impellers in order to achieve optimal performance at the desired operating conditions.

Afterwards, the performance of various trimmed compressors and turbines were estimated by ANSYS CFX. The optimal compressor and turbine designs were manufactured and employed in IBC prototype.

In parallel with the experiment tests of IBC prototype, a procedure of the compressor in-house design and optimisation was built. This procedure generated a high-performance compressor design that delivered the T-S efficiency of 77.46%, which is 8.08 percentage points higher than the trimmed commercial compressor. The presented procedure also can be utilized to design turbine in order to achieve high performance at the design condition. However, due to the limited time, the turbine design is excluded in this research.

5.2 3D Modelling Methodology

In this chapter, 3D simulations were performed primarily using computational fluid dynamics (CFD). Basically, it uses numerical analysis and data structures to analyse and solve problems that involve fluid flows. Regarding the physical aspects of any fluid flow, the following three fundamental principles are employed: (1) mass is conserved; (2) Newton's second low: $F = ma$; (3) energy is conserved. These fundamental principles can be expressed in terms of mathematical equations, which are typically partial differential equations.

This section will provide some general information on CFD theory. First, the governing equations describing fluid flow are introduced. Second, the most common turbulence models using in CFD are briefly described. Finally, boundary conditions and meshing methodology are given, as they play vital roles in CFD simulations.

5.2.1 Governing Equations

In CFD, instead of getting an analytical solution for the whole flow field, the complex fluid domain is subdivided into a collection of subdomains, with each subdomain represented by a set of element equations to the original problem. In any closed system, the laws of conservation of mass, momentum and energy must apply to every subdomain. In particular, the Navier-Stokes equations denote conservative equations for physical quantities of mass, momentum, and energy. The4 continuity equation for any element is:

$$\frac{\partial \rho}{\partial t} + \frac{\partial (\rho u)}{\partial x} + \frac{\partial (\rho v)}{\partial y} + \frac{\partial (\rho w)}{\partial z} = 0 \tag{5.1}$$

or

$$\frac{\partial \rho}{\partial t} + \nabla \cdot (\rho \vec{V}) = 0 \tag{5.2}$$

In turbomachinery applications, gravitational effects are ignored, so the momentum equations become:

$$\rho\frac{Du}{Dt}=\frac{\partial(\rho u)}{\partial t}+\nabla\cdot(\rho u\vec{V})=-\frac{\partial p}{\partial x}+\frac{\partial\tau_{xx}}{\partial x}+\frac{\partial\tau_{yx}}{\partial y}+\frac{\partial\tau_{zx}}{\partial z}$$

$$\rho\frac{Dv}{Dt}=\frac{\partial(\rho v)}{\partial t}+\nabla\cdot\left(\rho v\vec{V}\right)=-\frac{\partial p}{\partial x}+\frac{\partial\tau_{xy}}{\partial x}+\frac{\partial\tau_{yy}}{\partial y}+\frac{\partial\tau_{zy}}{\partial z} \tag{5.3}$$

$$\rho\frac{Dw}{Dt}=\frac{\partial(\rho w)}{\partial t}+\nabla\cdot(\rho w\vec{V})=-\frac{\partial p}{\partial x}+\frac{\partial\tau_{xz}}{\partial x}+\frac{\partial\tau_{yz}}{\partial y}+\frac{\partial\tau_{zz}}{\partial z}$$

Finally, ignoring internal heat generation and gravity, the conservation of energy equation is:

$$\begin{aligned}\rho\frac{D}{Dt}\left(e+\frac{V^2}{2}\right)&=\frac{\partial}{\partial t}\left[\rho\left(e+\frac{V^2}{2}\right)\vec{V}\right]\\&=\frac{\partial}{\partial x}\left(k\frac{\partial T}{\partial x}\right)+\frac{\partial}{\partial y}\left(k\frac{\partial T}{\partial y}\right)+\frac{\partial}{\partial z}\left(k\frac{\partial T}{\partial z}\right)-\frac{\partial(up)}{\partial x}-\frac{\partial(vp)}{\partial x}\\&-\frac{\partial(wp)}{\partial x}+\frac{\partial(u\tau_{xx})}{\partial x}+\frac{\partial(u\tau_{yx})}{\partial y}+\frac{\partial(u\tau_{zx})}{\partial z}+\frac{\partial(v\tau_{xy})}{\partial x}\\&+\frac{\partial(v\tau_{yy})}{\partial y}+\frac{\partial(v\tau_{zy})}{\partial z}+\frac{\partial(w\tau_{xz})}{\partial x}+\frac{\partial(w\tau_{yz})}{\partial y}+\frac{\partial(w\tau_{zz})}{\partial z}\end{aligned} \tag{5.4}$$

This system of equations comprises the Navier-Stokes equations for three-dimensional, viscous flow. The purpose of the CFD flow solver is to discretize the Navier-Stokes equations. There are many different discretization techniques. However, the purpose of all these discretization methods is to replace the derivatives with a difference approximation and, thus, convert the partial differential equations into a system of algebraic equations which can be easily solved. [118]

It should be noted that there are two sources of error which can influence the numerical solution of Navier-Stokes equations. The first source is the discretization error. It is defined as the difference between the exact analytical solution of the partial differential equation and the exact solution of the corresponding difference equation. Simply, the discretization error is the

truncation error for the difference equation plus any errors introduced by the numerical treatment of the boundary conditions. Truncation error is the error made by truncating an infinite sum and approximating it by a finite sum. The second source of error is defined as round-off error. It is the numerical error introduced after a repetitive number of calculations in which the computer is constantly rounding the numbers to some significant figure. [119]

5.2.2 Turbulence Modelling

The simulation of the turbulent flow is a significant problem in computational fluid dynamics, as the outstanding feature of the turbulent flow is that the molecules move in a chaotic motion along complex irregular path. In addition, turbulence typically operates on a wide range of length scales. Thus, the range of length scales and complexity of involved in turbulence make most modelling approaches prohibitively expensive. In consequence, the trade-off between the computational time and the simulation accuracy should be took.

Despite the performance of modern supercomputers, a direct simulation of turbulence by the time-dependent Navier-Stokes equations, referred as the Direct Numerical Simulation (DNS), is only applicable when the relatively simple flow with low Reynolds numbers is investigated. To be specific, the mesh resolution and time scale must be smaller than a viscously determined scale known as the Kolmogoroff scale [120]. Therefore, instead of precisely resolving the turbulent flow field, various turbulence models were developed to simulate the turbulence in approximate manner. Since there is no single turbulence model which is able to predict reliably all kinds of turbulent flows, it is extremely important to select a proper turbulence model based on the simulation problems, accuracy requirements, and computational efforts.

In this research, the $K-\omega$ Shear Stress Transport (SST) turbulence model was used for the modelling. This turbulence model was proposed by Menter in 1994 [121], by combining the $K-\omega$ model of Wilcox [122] with a high Reynolds number $K-\varepsilon$ model. In $K-\varepsilon$ model, the turbulent simulation is based on the solution of equations for the turbulent kinetic energy K and turbulent dissipation

rate ε. The one of key features of $K-\varepsilon$ model is that damping function is required in order to stay valid through the viscous sublayer to the well. However, the weakness of the damping function is that the corresponding numerical stability is quick low. On the contrary, although the $K-\omega$ model was developed based on the $K-\varepsilon$ model, the $K-\omega$ model requires no the damping function. [123]

One major feature of the $K-\omega$ SST turbulence is that merits of the $K-\omega$ model and the $K-\varepsilon$ model are combined. To be specific, since there is no damping function in the $K-\omega$ model, it allows the $K-\omega$ formulation to apply all the way down to the wall through the viscous sub-layer. On the other hand, the SST formulation also switches to a $K-\varepsilon$ behaviour in the free-steam and, therefore, avoids the common $K-\omega$ problem that it is too sensitive to the inlet free-stream turbulence properties. Furthermore, the additional advantage of the $K-\omega$ SST model is that the accuracy of the flow field prediction is improved, especially with strong adverse pressure gradients and separating flow.

5.2.3 Meshing

In CFD, the computational grid size and type must be appropriate based upon the complexity of model geometry and simulation requirements, as the computational solutions of partial differential equation will be approximated in each grid. Thus, the rate of convergence, solution accuracy, and computational cost are significantly impacted by the quantity of the computational grid.

Basically, the computational grid is generated by partitioning space into elements. Thus, it is a discrete representation of the geometry of the problem. There are 3 primary types of grids, showing as follows:

- **Structured grids:** Structured grids are identified by regular connectivity. By generating this type of the computational grid, the possible element choices are restricted to the quadrilateral in 2D and hexahedra in 3D. The regularity of the computational grid results in the regularity of the connectivity, thereby achieving high space efficient. Given the

characteristics of the structured grid, it is typically used for the model with low level of geometry complexity.

- **Unstructured grids:** Unlike structured grids, unstructured girds are identified by irregular connectivity. It cannot easily be expressed as a two-dimensional or three-dimensional array in computer memory. This allows for any possible element that a solver might be able to use. Compared to structured meshes, this model can be highly space inefficient since the neighbourhood connectivity must be explicitly stored. However, the advantage of this grid type is that there is no constraint on the geometry complexity. Furthermore, another benefit of the unstructured grids is that grid refinement and coarsening can be handled in a relatively native and seamless manner. In addition, it is advisable to employ unstructured grids near walls in order to resolve the boundary layers accurately. [98]

- **Hybrid grids:** A hybrid mesh is a mesh that contains structured portions and unstructured portions. It integrates the structured meshes and the unstructured meshes in order to use the most appropriate grid in any combination. Those parts of the geometry that are regular can have structured grids and those that are complex can have unstructured grids. Note that these grids can be non-conformal which means that grid lines do not need to match at block boundaries.

In addition, dimensionless wall distance, referred as y^+, is extremely important for the simulation accuracy and stability. This is because that the fluid flow field near the boundary well is very complex. Thus, in order to capture the complex flow phenomenon correctly, a fine mesh near domain walls has to be applied. The y^+ value is a common metric used to measure grid quality near the well. This is a non-dimensional measurement which is defined as:

$$y^+ = \frac{u_\tau y}{v} \tag{5.5}$$

where y is the distance to the nearest wall. u_τ is the turbulent eddy viscosity.

A smaller value of y^+ corresponds to a finer near-wall grid and is a very useful measure in turbomachinery, since velocities in the flow passage are very high and consequently velocity gradients at walls are very high.

5.2.4 Convergence

Since the nature of the fluid flow problems is highly nonlinear, the governing Navier-Stokes equations only can be solved analytically when the restrictive conditions are imposed. As a result, CFD solutions must be calculated iteratively to reach a valid solution, either in a time-independent sense in the cases of steady-state, or at each time step in the cases of transient simulations.

In this study, only steady-state simulations were performed. Generally, there are three criteria that could be utilized to assess the convergence of a steady-state CFD analysis, shown as following:

- Residual mean square (RMS) error values should be reduced to an acceptable value, typically 10^{-4} or 10^{-5}.

  In CFD analysis, residual value is used to measure the local imbalance of a conserved variable in each control volume. Since RMS error directly quantifies the error in the solution of the system equations, it is the key parameters to evaluate the convergence of the CFD simulations. In addition, it should be noted that the RMS error will never be zero in any CFD simulation. However, the lower the residual value is, the more numerically accurate the solution. Typically, RMS error levels of 1E-4 are considered to be loosely converged. Levels of 1E-5 are well converged, while levels of 1E-6 are tightly converged. The following plot is an example of residual monitors. It shows that the various RMS errors gradually decrease down to levels of 1E-5 when the simulation iteration reach at 300 time steps.

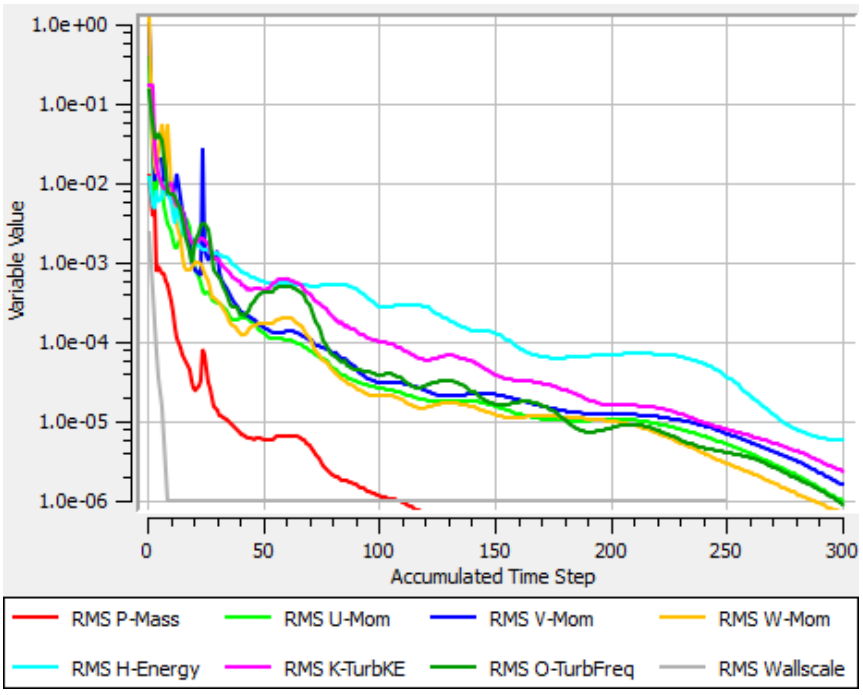

Figure 5.1 Example: residual monitors

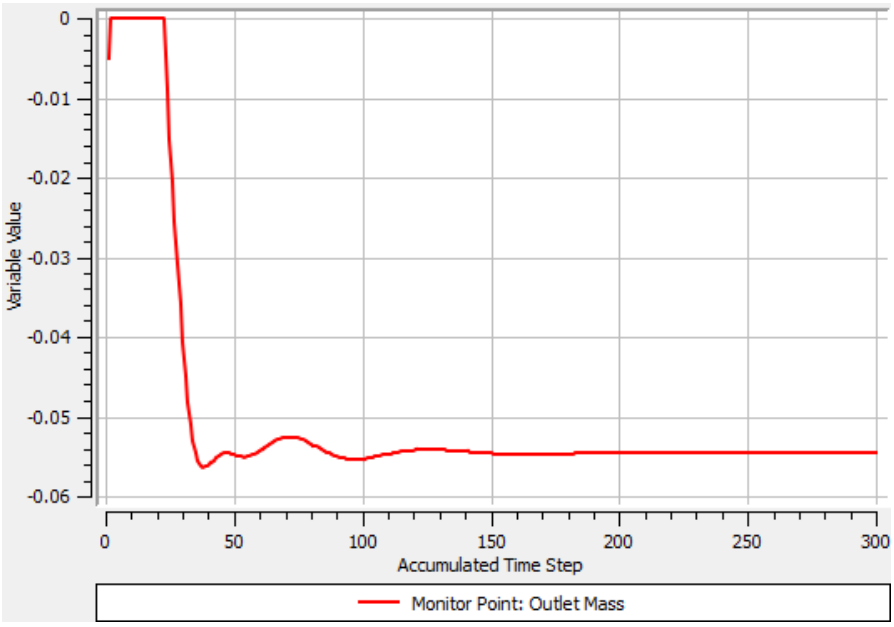

Figure 5.2 Example: quantities of interest monitors

- Quantities of interest have reached a steady solution.

  Theoretically, the solution field should not change iteration to iteration for an analysis to be deemed converged in a steady state analysis. Thus, monitoring integrated quantities of interest can help user judge whether the simulations

reach converged solutions. As a result, prior to starting a simulation, the users must clearly define what our values of interest are, such as force, drag, average temperature, or mass flow rate. Figure 5.2 shows the monitor value – mass flow rate at system outlet, changes less and less between iterations. After 200 iterations, the change of the mass flow rate is negligible, which indicates that the simulation is converged with respect of the monitored parameter.

- The domain has imbalance of less than 1%.

Since the CFD code is designed to solve conservation equations, overall property conservation of each domain should be achieved in order to generate reliable simulation results. Similar to RMS error, the CFD solution imbalances will never be exactly zero, as all physical systems are represented by a set of numerical equations. However, the imbalances should be sufficiently small before considering the solution converged. Typically, the aim for solution imbalances is below 1%. Note that more sensitive applications may require tighter convergence. As can be seen in Figure 5.3, after the initial start-up period, the solution imbalances gradually decrease as the solution progresses.

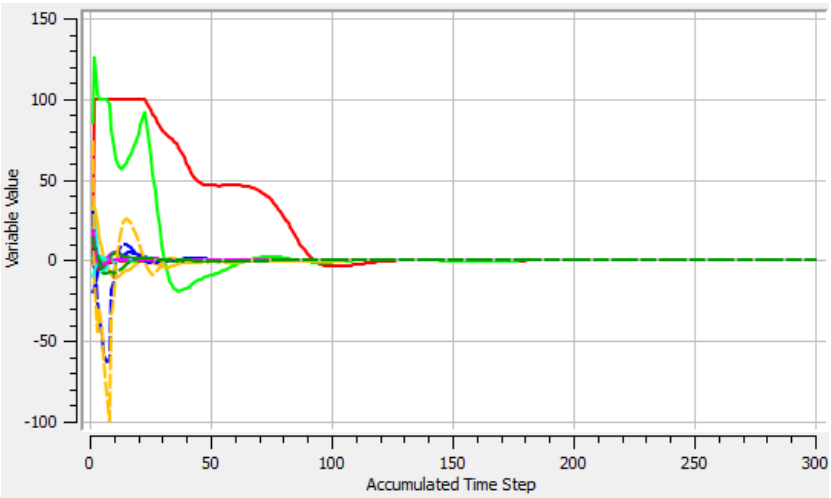

Figure 5.3 Example: solution imbalances

5.2.5 Boundary Conditions

Boundary conditions in CFD modes are vital for the behaviour of the corresponding simulation. Thus, they must be defined properly and accurately, based upon the physical nature of simulation case and simulation requirements. The primary types of boundary that must be considered are the wall boundary, and the flow inlet and exit boundaries.

At inlets and outlets of the fluid domain, the user can define the boundaries as ‘inlet’, ‘outlet’, or ‘opening’. If ‘inlet’ and ‘outlet’ are selected to apply as the boundary conditions of the fluid domain, the one-way flow boundary conditions are expected. In other words, the solver enforces the inflow or outflow by erecting artificial walls on those faces where the fluid attempts to flow opposite to the defined flow direction. On the contrary, ‘open’ boundary condition allows the fluid free to flow into or out of the boundary. It is typically selected when the full prescription of information at the boundary is not readily available.

The following combinations of boundary conditions are all valid configurations commonly used in CFD simulation. They are listed from the most robust option to the least robust.

- **Most Robust:** Velocity/mass flow at an inlet and static pressure at an outlet. The inlet total pressure is an implicit result of the prediction.

- **Robust:** Total pressure at an inlet and velocity/mass flow at an outlet. The static pressure at the outlet and the velocity at the inlet are part of the solution.

- **Sensitive to Initial Guess:** Total pressure at an inlet and static pressure at an outlet. The system mass flow is part of the solution.

- **Very Unreliable:** Static pressure at an inlet and static pressure at an outlet. Since the inlet total pressure level and the mass flow are both an implicit result of the prediction, this combination is not recommended.

- **Not Possible:** Total pressure cannot be specified at an outlet. The total pressure boundary condition is unconditionally unstable when the fluid flows out of the domain where the total pressure is specified.

Unlike ‘inlet’, ‘outlet’ and ‘open’ boundary conditions, ‘wall’ boundary condition is required to bound fluid and solid regions. Since all the fluid has to be contained inside walls, ‘wall’ boundary condition is natural extension into the numerical simulation process. However, walls allow the permeation of heat and additional variables into and out of the domain through the setting of flux and fixed value conditions at wall boundaries. In turbomachinery simulations, walls are usually taken to be adiabatic. Thus, there is no heat transfers across the well.

Since the working fluid is defined as the viscous flow in turbomachinery simulations, the most common type of wall boundary condition implementation is the no-slip boundary. It means that the fluid immediately next to the wall assumes the velocity of the wall. In the CFD simulation, walls can be specified as stationary or moving with an imposed velocity.

It is very common in turbomachinery 3D simulations that only one passage impeller is modelled in steady-state condition. The resulting benefit is to reduce the computational effort and resource, as the employment of the single-passage modelling reduces the model size and the quantity of the computational grids. Thus, it should be assumed that the flow field entering in one side of the interface in the single passage impeller is equal to the flow field exiting from the second side of the interface. Given the assumption above, rotational periodic boundary conditions are often used to ensure that the flow patterns at both periodic boundaries are identical. Note that the periodic boundary condition is not only applied in turbomachinery 3D simulation, but in the case when the physical geometry, expected flow pattern, and the thermal solution are of a periodically repeating nature.

There are two types of periodic boundaries:

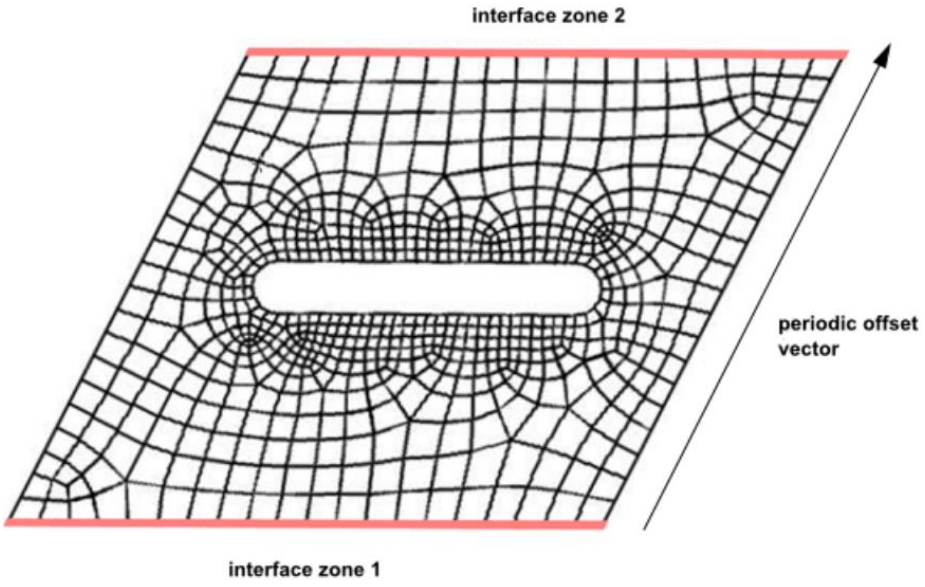

Figure 5.4 Use case of transnational periodic boundary condition

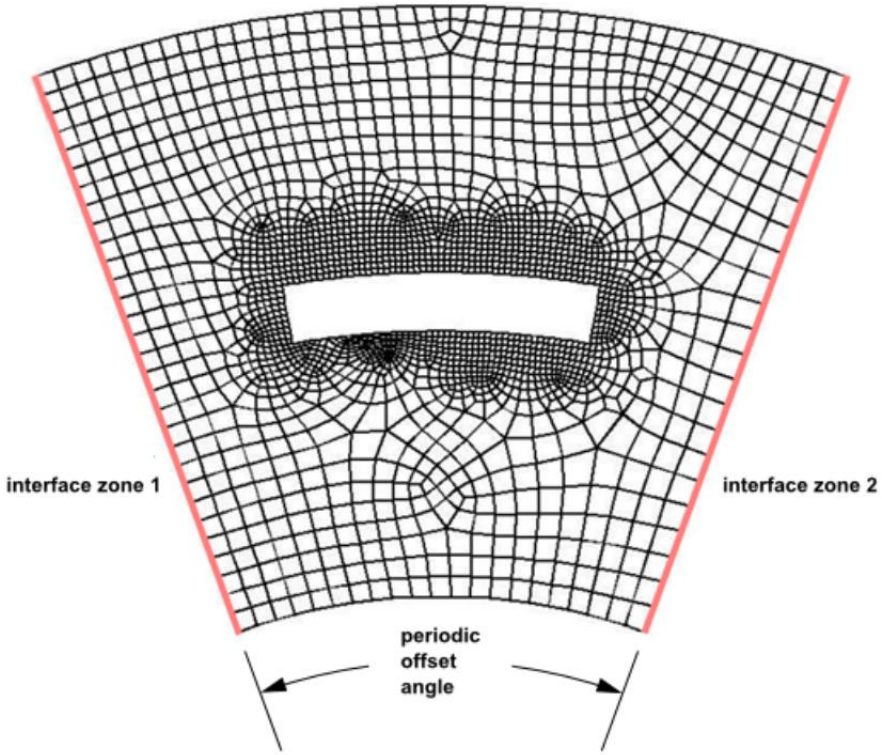

Figure 5.5 Use case of rotational periodic boundary condition

- Transnational periodic boundary condition: In this case the two sides of the interface must be parallel to each other such that a single translation

transformation can be used to map interface zone 1 to interface zone 2, showing in Figure 5.4.

- Rotational periodic boundary condition: In this case the two sides of the periodic interface can be mapped by a single rotational transformation about an axis. The example use case is shown in Figure 5.5. The rotational periodic boundary condition can apply to interface zone 1 and interface zone 2 shown in Figure 5.5. This type of periodic boundary condition only can be used when the boundaries are of equal shape and equal area.

5.3 Model Description

In this section, the compressor and turbine models used in this research were fully described and simulated in the commercial software package ANSYS-CFX R16.1. The code solves the three-dimensional Reynolds-averaged Navier-Stokes (RANS) equations in a fully implicit manner using a hybrid finite-element / finite-volume discretization approach. All simulations can be completed by the following five steps: generating model geometry and flow domain, generating computational grids, establishing the boundary and initial conditions, setting up the proper solver, and performing the simulations.

5.3.1 Centrifugal Compressor

The commercial centrifugal compressor 2, presented in Chapter 4, is selected as the baseline, as the matching process show that this compressor can deliver the best systematic performance compared with the other available compressors. The following subsections shows the four steps of the model setup for the selected compressor.

5.3.1.1 Model Geometry and Flow Domain Generation

A detailed description of the impeller geometry was obtained from the project partner. That geometry was imported into BladeGen software which is a

commercial package of ANSYS. The detailed geometry included: x, r coordinates for hub and shroud profiles, leading and trailing edge coordinates for both the main blade and the splitter blade, as well as thickness and either beta or theta values at multiple spanwise locations along the meridional length of the impeller blade. Based upon the required parameters presented above, an accurate 3D model of the passage geometry can be generated by BladeGen. A representative view of the 3D geometry of a single passage and a meridional profile are presented in Figure 5.6. Note that the vaneless diffuser is included in the single flow passage domain, highlighted in Figure 5.8. In practice, the compressor rotor is a rotating part while the diffuser is stationary. Thus, the single flow passage domain has to be divided into sub-domains when the computational grids are created. The meshing details are presented in the next section.

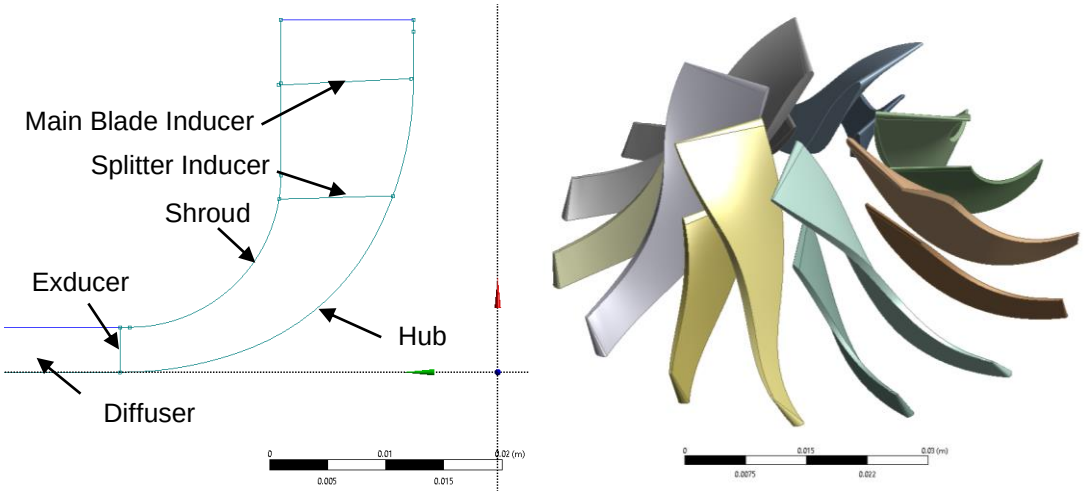

Figure 5.6 Meridional contour of the compressor flow path (right) and 3D view of main blades and splitters (left)

The selected commercial compressor consists of 7 main blades with 7 splitters, followed by a vaneless diffuser. The dimensions of the main blades are such that its inlet and exit tip diameters are 35 mm and 65 mm, respectively. The blade height at the impeller inlet and exit are 10.26 mm and 3.85 mm, respectively. Its tip clearance of 0.1 mm at the inlet and exit can be found. As described in the Introduction chapter, the tip clearance is a small gap between the blade tip and the stationary shroud. Thus, this type of tip clearance is referred to as unshrouded.

On the contrary, if the shroud is physically connected to the blades and, therefore, rotating with the rotor at same speed, it is referred as shrouded.

In this research, the entire compressor 3D model, shown in Figure 5.7, consists of three distinct regions: an inlet domain, a single flow passage, and the volute. In practice, the flow fields in each compressor flow passage are distinctive due to multiple reasons, such as the location of the volute tongue and the uneven flow at the rotor inlet. However, given the numerous computational cost associated with full compressor rotor modelling, it is common to complete the simulation with the single flow passage. More importantly, single passage simulations are enough to resolve all the important flow mechanisms at stable steady-state operating point. In order to complete the single flow passage simulation, the rotational periodic boundary condition available in ANSYS CFX should be applied at two periodic boundaries in azimuthal direction, highlighted in Figure 5.8.

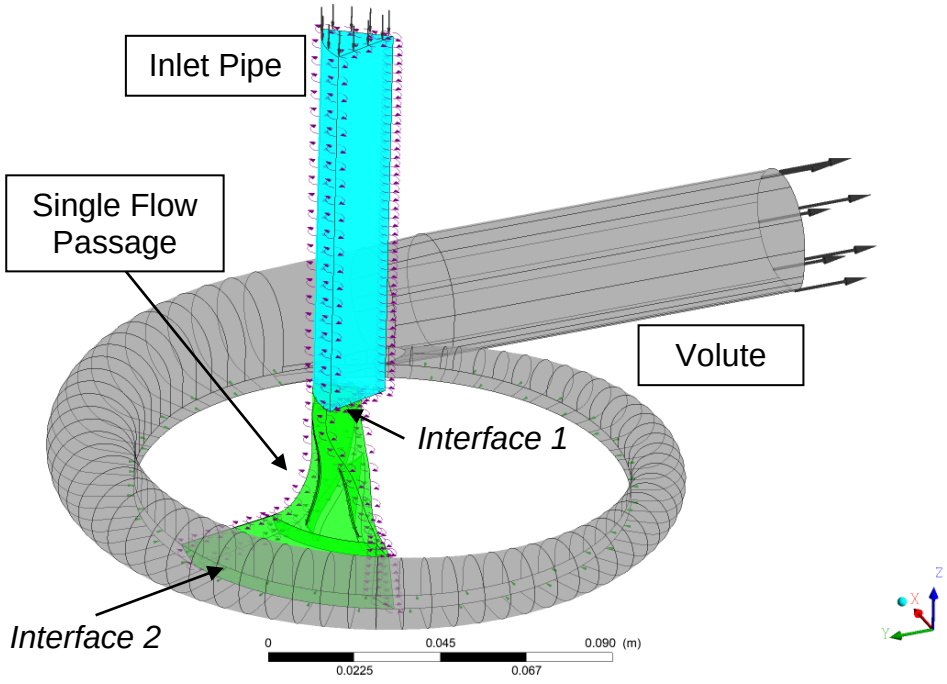

Figure 5.7 Computational domain including inlet pipe, single flow passage and volute

It can be seen in Figure 5.7 that the inlet pipe is extended to ensure that there is no flow recirculation at the domain inlet. The flow recirculation near the rotor inducer typically occurs when the centrifugal compressor operates near surge.

Thus, the location of the inlet boundary is extended sufficiently long to ensure enough distance between the domain inlet and possible recirculation regions. In addition, only 1/7 of the inlet pipe is built so that the proportion of inlet pipe can align with that of the single flow passage.

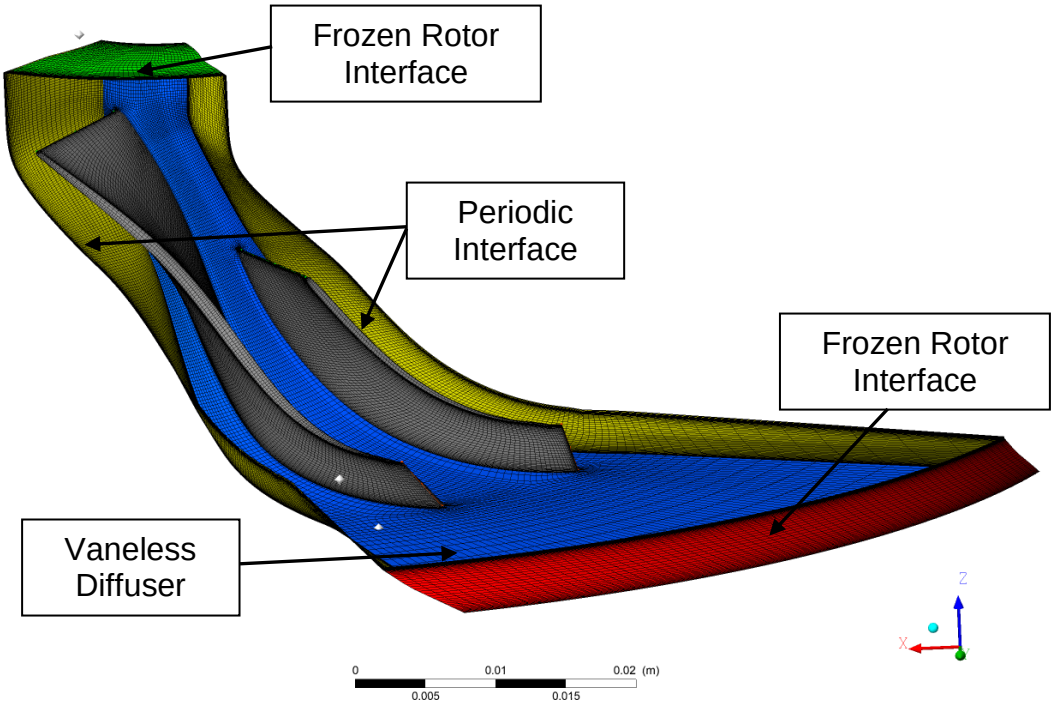

Figure 5.8 Single flow passage with meshes

The volute domain is created based upon the geometry of the commercial compressor volute. However, the compressor impellers are trimmed to deliver optimal performance at design operating point. Thus, the volute shape has to be modified according to the flow field at its inlet boundary. The cross-section of the compressor volute is demonstrated in Figure 5.9. The cross-section shape is defined by a circular arc in three quadrants and a square in the fourth quadrant. In order to define and vary the volute shape, the area to radius ratios A_c/r_c is selected as the design variable for optimisation. Area to radius ratio for this shape is

$$\frac{A_c}{r_c} = \frac{R^2\,(1 + 3\pi/4)}{r_3 + R(1 - 1/9\pi)} \tag{5.6}$$

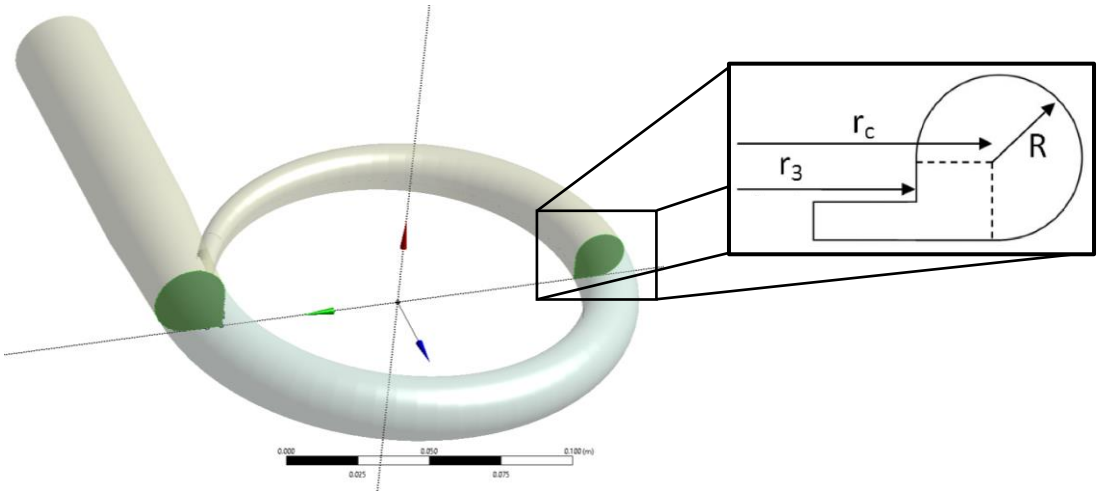

Figure 5.9 Volute domain with the highlighted cross-section shape

5.3.1.2 Meshing

The three domains described in previous section were meshed separately and assembled in the pre-processor, shown in Figure 5.10. Due to the advantages of unstructured grids described in Section 5.2.3, unstructured grids are employed in the flow domain of the inlet pipe and volute. For the inlet pipe, an unstructured grid consisting of tetrahedral elements are generated using ANSYS MESHING. Near wall gradients in the inlet pipe domain are resolved using six prismatic elements, to better catch flow details near wall. The boundary wall refinement is also implemented for the volute domain. Due to the relatively complex, spiral volute domain was meshed into unstructured tetrahedral grids by ANSYS MESHING. It should be noted that in the optimisation process, the shape of the volute varies to maximize the compressor efficiency at the design operating point. Therefore, in order to remain the simulation fidelity at each design, mesh generations for different volute models are performed by the same considerations. For example, the maximum thickness and growth rate of boundary layer meshes are defined to have the same topology for all cases. Due to the identical meshing method throughout this study, the meshing quantity in the volute domain is a monotonic function of the volute volume which changes with its geometry.

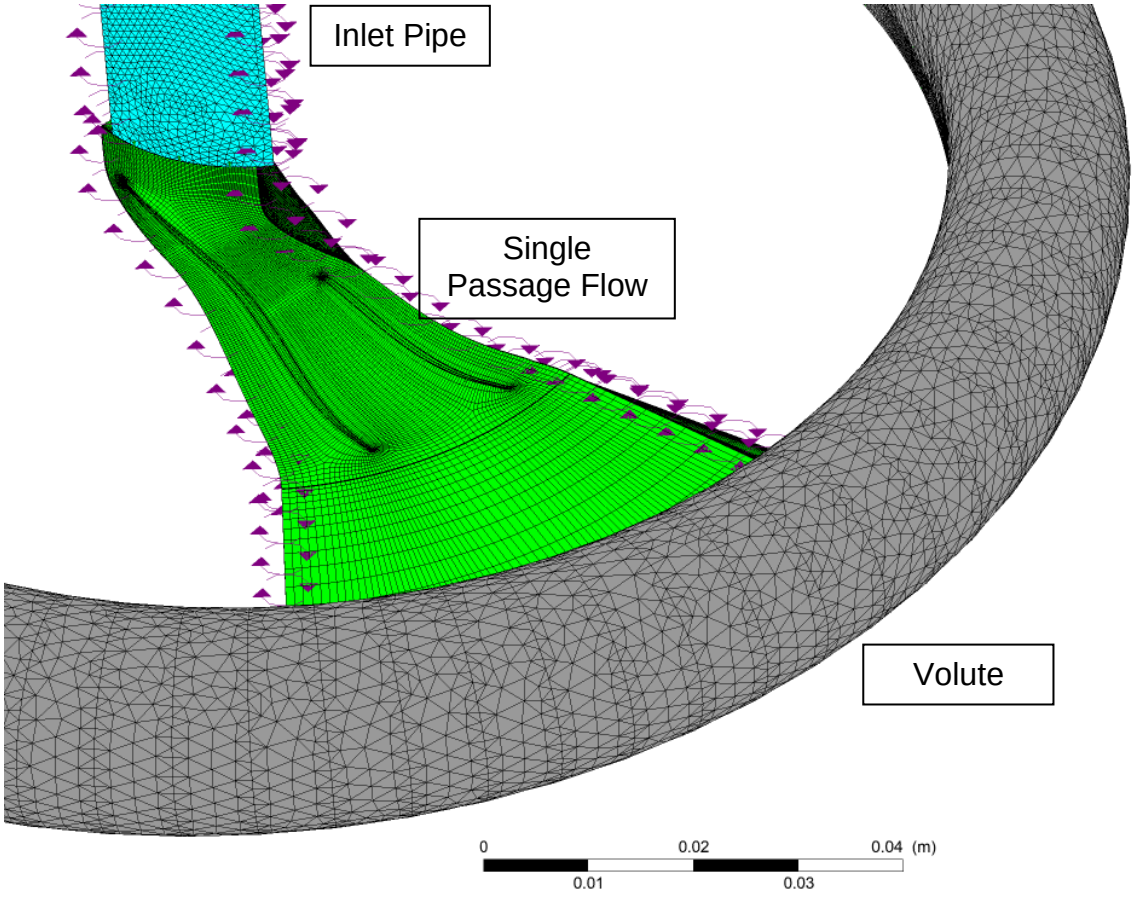

Figure 5.10 Inlet, single flow passage, and volute mesh

For the single flow passage domain, the structured hexahedral mesh is generated in ANSYS TURBOGRID. The corresponding detail of the computational grids is shown in Figure 5.11 with enlargements of the areas of interest. Cell biasing is applied to refine the mesh near the wall regions – all blade surfaces, hub and shroud. The tip clearance region is a zone of very high gradients and, therefore, there are 10 elements between the blade tip and the shroud. Typically, the meshing quality near wall is judged on the basis of the dimensionless wall distance from the wall to the first node, referred as y^+. However, y^+ is only calculated based on the flow gradients near wall which is solved by the CFD simulation. Thus, it is impossible to adjust the y^+ value when the flow domain is meshed. Therefore, several iterations should be performed between the refinement of the mesh near wall and the calculation of y^+ value. To obtain a good balance between computational accuracy and resource intensity, the meshes were kept to the y^+ value of around 1 near the blade surface.

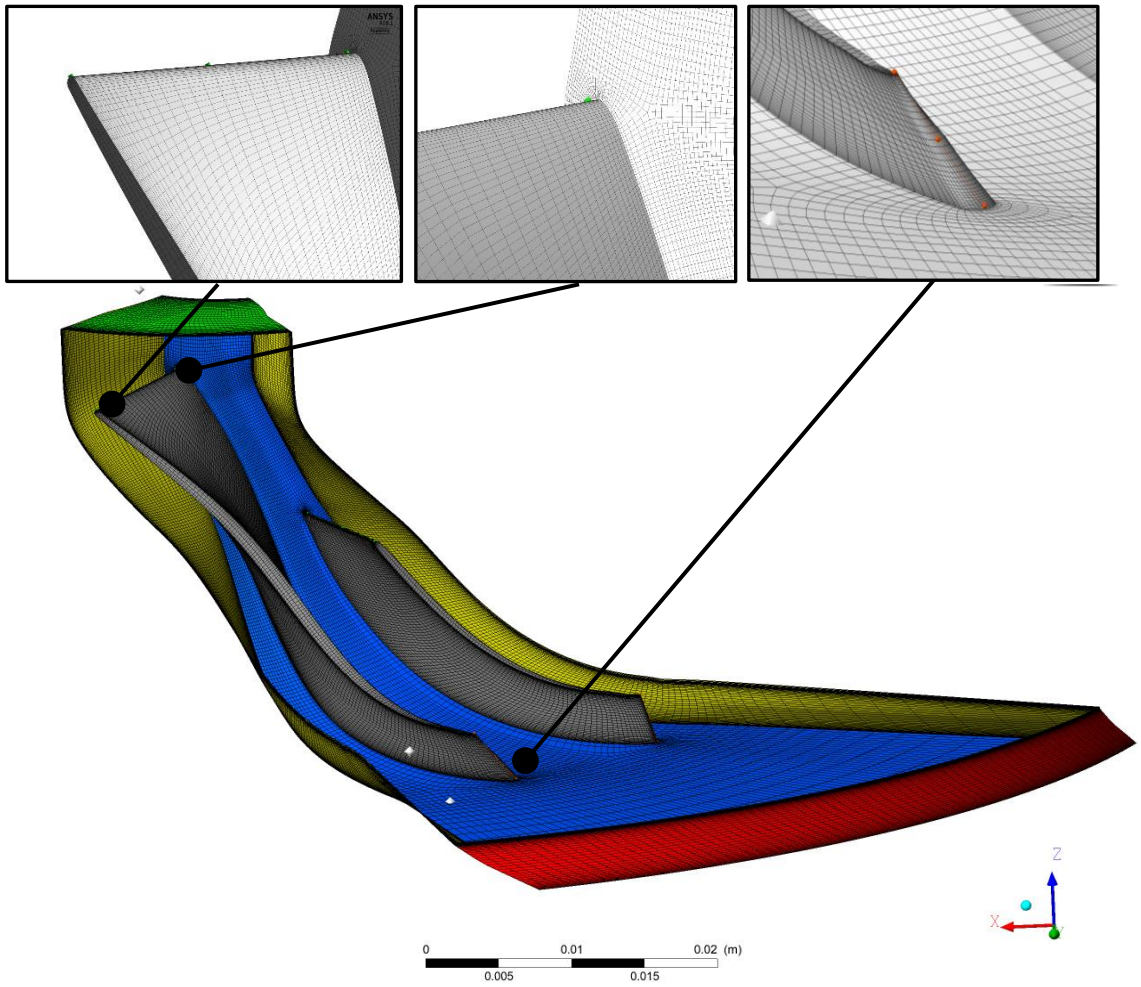

Figure 5.11 Single flow passage with detailed view of interest

5.3.1.3 Boundary Treatment and Fluid Domain Properties

As discussed in previous section, the selection of boundary conditions is very important, as boundary conditions must represent the physical nature of the bounds of each domain. Note that all the boundary conditions in all simulations are set to represent the steady-flow condition in the laboratory, instead of the actual on-engine operating conditions. The main difference is that the exhaust gas discharged by IC engine is highly pulsating. However, only stable flow is available in the laboratory in the University of Bath due to the limitation of the test facility.

In ANSYS CFX, the setup of the CFD model properties was performed in CFX-Pre. The identical setup described as following are applied to all trimmed compressor models.

In Section 4.4.5.5, the turbomachinery matching process shows that the commercial compressor candidate 2 was selected as the baseline design for the optimisation. Therefore, a total pressure of 45 kPa and a total temperature of 60 °C are imposed as the compressor inlet condition at the design operating point, shown in Table 4.6. Thus, the total pressure and total temperature are imposed at the inlet plane of the inlet pipe and *'inlet'* is selected as the boundary condition. The inlet flow angles were fixed as normal to the inlet boundary. The compressor exit is set at the outlet plane of the volute domain with *'outlet'* boundary condition. Since the total-to-static compression ratio of 2.22 is the design target, the area-averaged static pressure of 100 kPa is set as at the outlet plane. The working fluid is considered as a calorically perfect gas. Walls exposed to the environment are assumed to be adiabatic, as it is assumed that the heat transfer to the surroundings is neglected in all simulations. No-slip wall boundary conditions are applied to all the walls. This simply means that the velocity relative to the motion of the wall is set to zero.

Throughout this study, the flow is assumed to be fully turbulent with turbulence closure being ensured by Menter's k-ω SST model, as this turbulence model has proven to give relatively accurate results when experiencing flow separation under adverse pressure gradients [124].

Both inlet and volute domain are stationary, while the single flow passage is set as a rotating frame of reference with a rotational speed of 125,000 rpm which is the design operating condition. The interface between stationary and rotating domain must be selected properly to ensure that there is no change in the flow transferred from one domain to next. Thus, there are two important interfaces in the described compressor model. *Interface 1* is the intermedium plane between the exit of the inlet pipe and the inlet of the single flow passage, while *Interface 2* is between the outlet of the single flow passage and the inlet of the volute, highlighted in Figure 5.7. The *'frozen rotor'* is recommended by Copeland [23], to

apply to such interfaces. This is because that *'frozen rotor'* is suitable for the case that the frame of reference is changed but the relative orientation of the components across the interface is fixed. In addition, the two connected frames of reference have a fixed relative position throughout the calculation. This type of interface is most useful when circumferential variation of the flow is large relative to the rotating speed of the domain. Thus, given the description of *'frozen rotor'* interface, both *Interface 1* and *2* is set as *'frozen rotor'*. As can be seen in Figure 5.8, rotational periodic boundary is used on the periodic pairs of the single flow passage and inlet pipe domain, respectively.

As described above, the single flow passage is set as a rotating domain. However, the shroud and diffuser walls containing in the single flow passage are stationary in practice. Thus, counter-rotating wall velocity is imposed to them, rendering them stationary in the absolute frame of reference.

Table 5.1 summarizes the boundary conditions used throughout the steady state simulations.

Table 5.1 CFD boundary conditions for compressor modelling

Analysis Type	Steady State
Medium	Air, ideal gas
Walls	Adiabatic, Hydraulically Smooth
Inlet	Stagnation Temperature and Pressure
Outlet	Static Pressure Outlet
Interface	Frozen rotor
Turbulence Model	Menter's $k-\omega$ SST
Advection Scheme	High Resolution
Turbulence Numerics	High Resolution

5.3.1.4 Solver

The solver used to compute the flow field was ANSYS CFX, a Reynolds-Average Navier-Stokes solver. Each computational model run for a minimum of 1,000 iterations. A convergence solution was deemed to be reached when the RMS residuals decrease below a threshold of 10E-5 and domain imbalances have dropped below 1%. Moreover, total-to-static (T-S) isentropic efficiency and T-S pressure ratio need to settle to stationary levels. Isentropic efficiency was defined as the ratio of the isentropic total enthalpy change to the actual total enthalpy change, while T-S pressure ratio was simply defined as the ratio of total pressure at inlet boundary to the static pressure at the outlet boundary, shown as followings.

$$\eta_{TS,is} = \frac{h_{t,is}^2 - h_t^1}{h_t^2 - h_t^1}$$
$$p_{TS} = \frac{p_s^2}{p_t^1} \quad (5.7)$$

where station 1 refers to the domain inlet and station 2 to the outlet. Total enthalpy and pressure at each station are determined as mass flow averaged properties.

5.3.2 Radial Turbine

Based on the 1D simulation analysis presented in the previous chapter, the commercial radial turbine B is chosen as the baseline. Its blades are trimmed to shift the turbine optimal operating point to the design condition. The turbine model setup is described in detail at the following subsections.

5.3.2.1 Model Geometry and Flow Domain

The detailed geometry and computational domain are provided by the project partner, to represent the selected turbine. Similar to the compressor model, BladenGen in ANSYS is utilized to characterize the shape of the turbine impeller. The main dimensions of the selected turbine are listed in Table 5.2.

To simplify the analysis, the turbine model was divided into different regions: volute, single turbine passage, straight outlet pipe. The volute is designed to feed the stator as uniformly as possible and significantly affect turbine performance. Thus, it has to be scaled to maximize the turbine performance, as the turbine blades are trimmed to adjust flow capacity. In order to re-size the volute, the volute parameter - area to radius ratios A_c/r_c is selected as a design variable. The definition of area to radius ratios is expressed in Eq. 5.6. The original volute is shown in Figure 5.12 as an example.

Table 5.2 Primary geometric information of the commercial turbine

Impeller inlet diameter (mm)	62.00
Impeller outlet diameter (mm)	47.00
Impeller inducer height (mm)	9.60
Impeller exducer height (mm)	17.10
Tip clearance (mm)	0.15
Number of blades	11

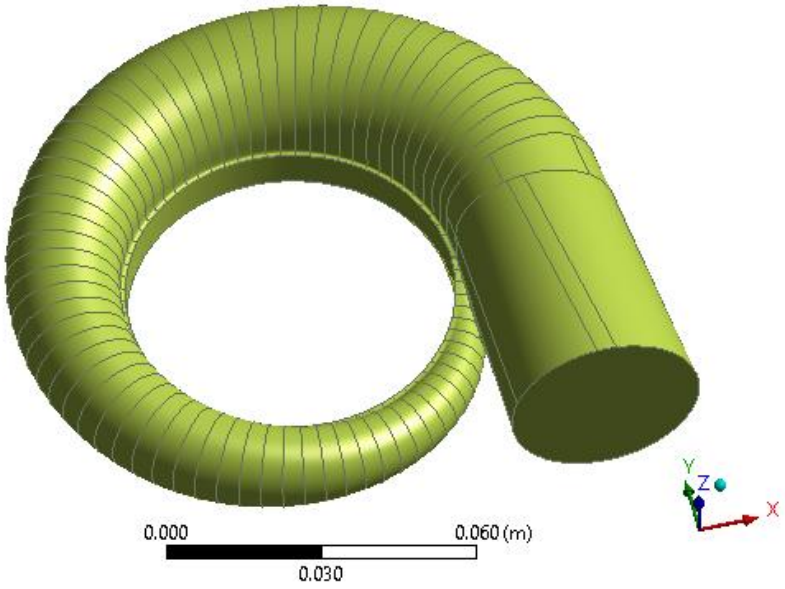

Figure 5.12 3D view of original volute of commercial turbine

In BladenGen, the turbine blades are created by the same methodology applied for the compressor. The corresponding single passage flow domain is plotted against to the 3D geometry of blades in Figure 5.13.

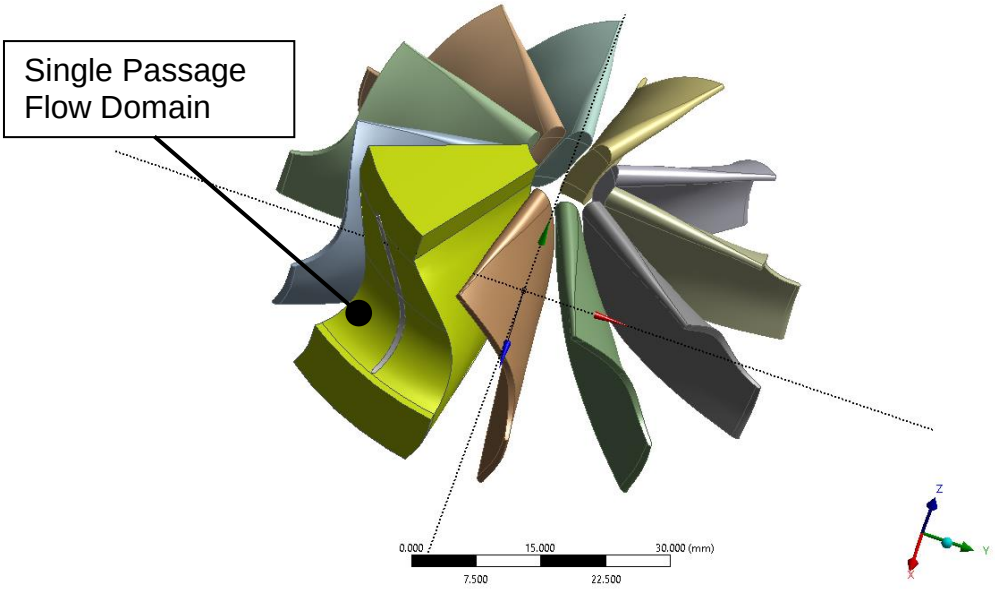

Figure 5.13 Impellers with single-passage flow domain

Given that the turbine exit flow is highly rotational, the pressure distribution near the rotor exducer shows a significantly non-uniformity. Thus, the extended duct allows the exit plane to move to a region where the unequal flows has been mixed sufficiently. The use of outlet domain extension is a practice over the CFD industry to improve the numerical stabilization of the solution. It should be noted that in IBC system there is a heat exchanger immediately downstream the turbine outlet. In other words, there is no long duct existing between the turbine and heat exchanger in the test configuration. Since only single turbine impeller is employed to predict the turbine performance, 1/11 of exit duct, shown in Figure 5.14, is introduced in order to further reduce the computational cost.

5.3.2.2 Meshing

Due to the different geometry complexity of each domain, the meshing methodology should be selected properly to faithfully reproduce the geometry. In this research, the meshing method selection is followed by the recommendation

in Copeland's study [23]. Regarding to the volute, an unstructured tetrahedral is used with boundary wall refinement. Due to the importance of the volute tongue, a smaller cell size in this region is applied. Similar to the turbine volute, ANSYS MESHING is used to obtain unstructured tetrahedral meshing in the exit duct.

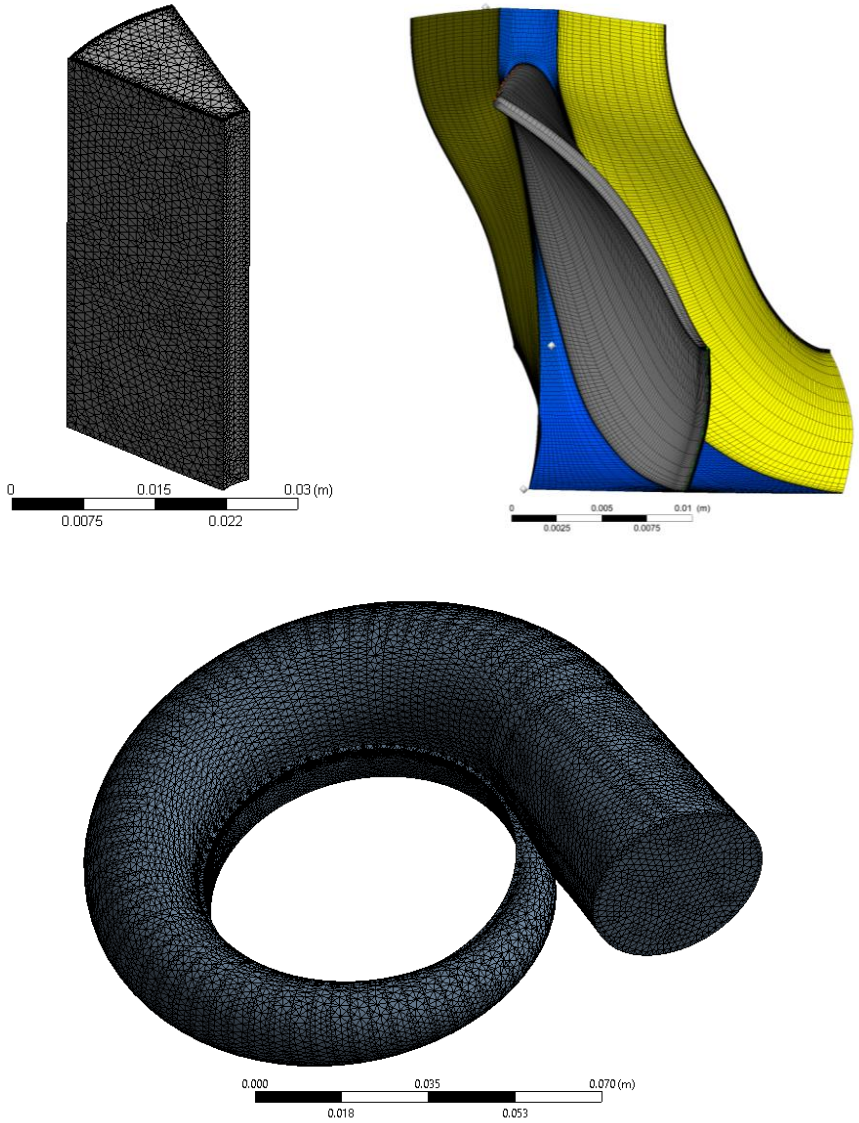

Figure 5.14 Inlet pipe (top right), impeller (top left), and volute (bottom)

Due to the relatively complex of the rotor, ANSYS TURBOGRID is utilized to generate the structured hexahedral meshing. Following the same criteria as in the compressor rotor model, the cell resolution close to the walls is increased to fully capture the complex flow characteristics. In order to quantify the wall refinement, y^+ value is calculated in simulations and targeted at around 1 near

the impeller surface. The described computational domains of the turbine model are plotted individually with the meshing in Figure 5.14.

5.3.2.3 Boundary Treatment and Fluid Domain Properties

Based on the analysis of the 3D modelling methodology, the boundary conditions for all operating points, shown in Figure 5.15, were selected as:

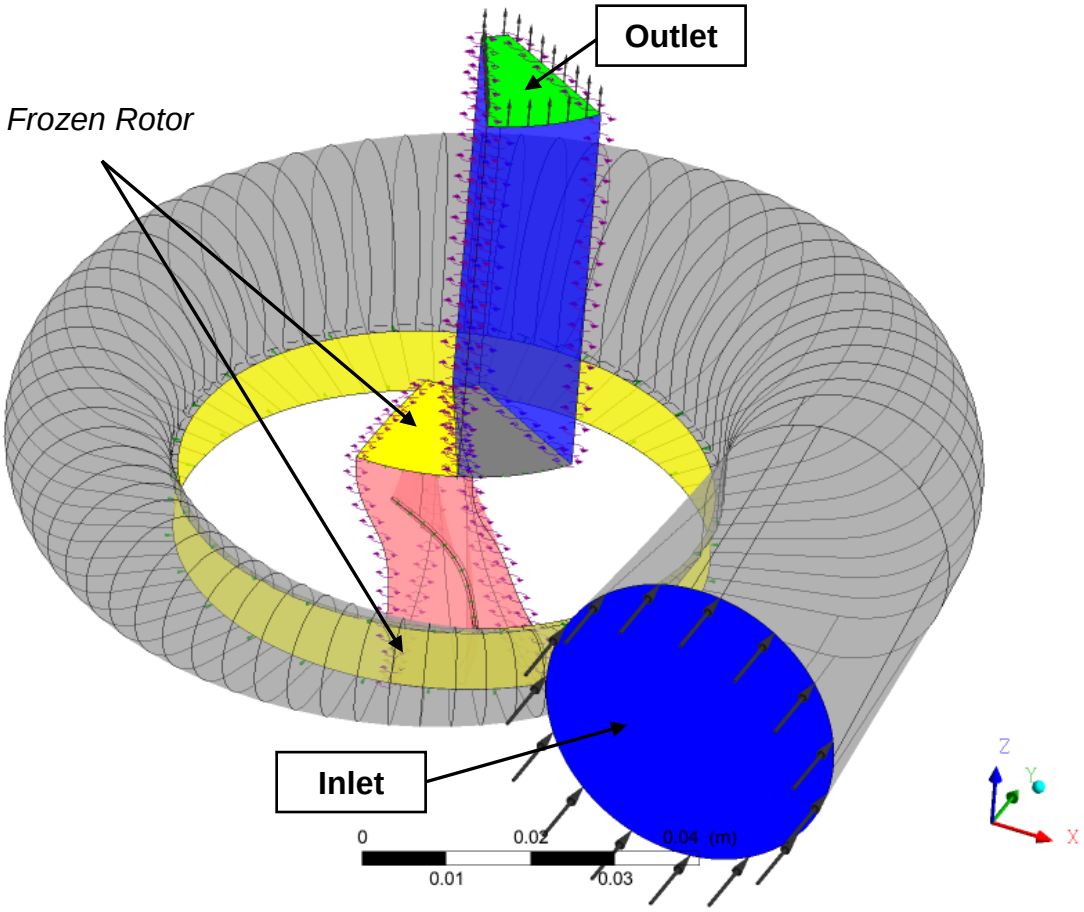

Figure 5.15 View of full turbine 3D model

Inlet

The IBC inlet plane is set at the inlet of the turbine volute. Although specifying the mass flow rate and temperature at the inlet boundary results in a more robust simulation, total pressure of 1 bar and total temperature of 1023 K with axial-flow direction are specified instead so that the calculated mass flow rate through the domain could be used to validate the trimmed turbine against the design condition.

Outlet

The turbine exit is set at the outlet plane of the exit duct with '*outlet*' boundary condition. Based on IBC 1D simulation analysis, the total-to-total (T-T) expansion ratio of 2 is the design operating condition. However, only area-averaged static pressure can be specified at the '*outlet*' boundary condition. The difference between the total and static pressure is the dynamic pressure, which represents the kinetic energy of the flowing fluid. Since the fluid velocity at the turbine outlet is quite high, the resulting dynamic pressure should be considerable. However, since the turbine model is simulated standalone, it is unknown how much static pressure can be recovered by reducing the fluid velocity due to the downstream heat exchange. Thus, three simulation cases are performed with different the area-averaged static pressure of 1.8, 2, and 2.2 bar, respectively.

Fluid Property

Similar to the compressor model, the calorically perfect gas is selected as the working fluid.

Domain Property

With respect to the turbine working condition, the exit duct and volute are set as the stationary, while the turbine single flow passage is the rotating with a rotational speed of 125,000 rpm. It should be noted that counter-rotating wall velocity is imposed to the shroud and diffuser walls, as in practice they are stationary.

Domain Interface

The detailed discussion about the interface selection is presented in the compressor model description. Thus, '*frozen* rotor' is imposed at all rotor-stator interfaces, shown in Figure 5.15. The '*periodic interface*' is applied for pitchwise boundaries of the single-flow passage and the exit duct domain.

The setup summary of the turbine was listed at Table 5.3.

Table 5.3 Turbine model setup summary

Analysis Type	Steady State
Medium	Air, ideal gas
Walls	Adiabatic, Hydraulically Smooth
Inlet	Stagnation Temperature and Pressure
Outlet	Static Pressure Outlet
Interface	Frozen rotor
Turbulence Model	Menter's $k-\omega$ SST
Advection Scheme	High Resolution
Turbulence Numerics	High Resolution

5.3.2.4 Solver

The solver and converge criteria for the turbine 3D simulations are the same as that in compressor simulations. However, instead of motoring the total-to-static related parameter, the T-T isentropic efficiency and pressure ratio in turbine simulations are required to settle to stationary levels.

5.3.3 Grid Sensitivity Study

As discussed about 3D modelling methodology, computational fluid dynamic (CFD) using a conservative finite volume method discretize the computational domain by discrete control volumes ensuring conservation of mass, momentum and energy. Consequently, the resulting computational solutions are significantly affected by the mesh quantity and quality. It is a common practice for 3D CFD community to perform the mesh sensitivity study to achieve the independence of the solution. Typically, sufficient fine-grid resolution is required to reproduce the exact solution. However, the computational effort should also be taken account to determinate the grid properties.

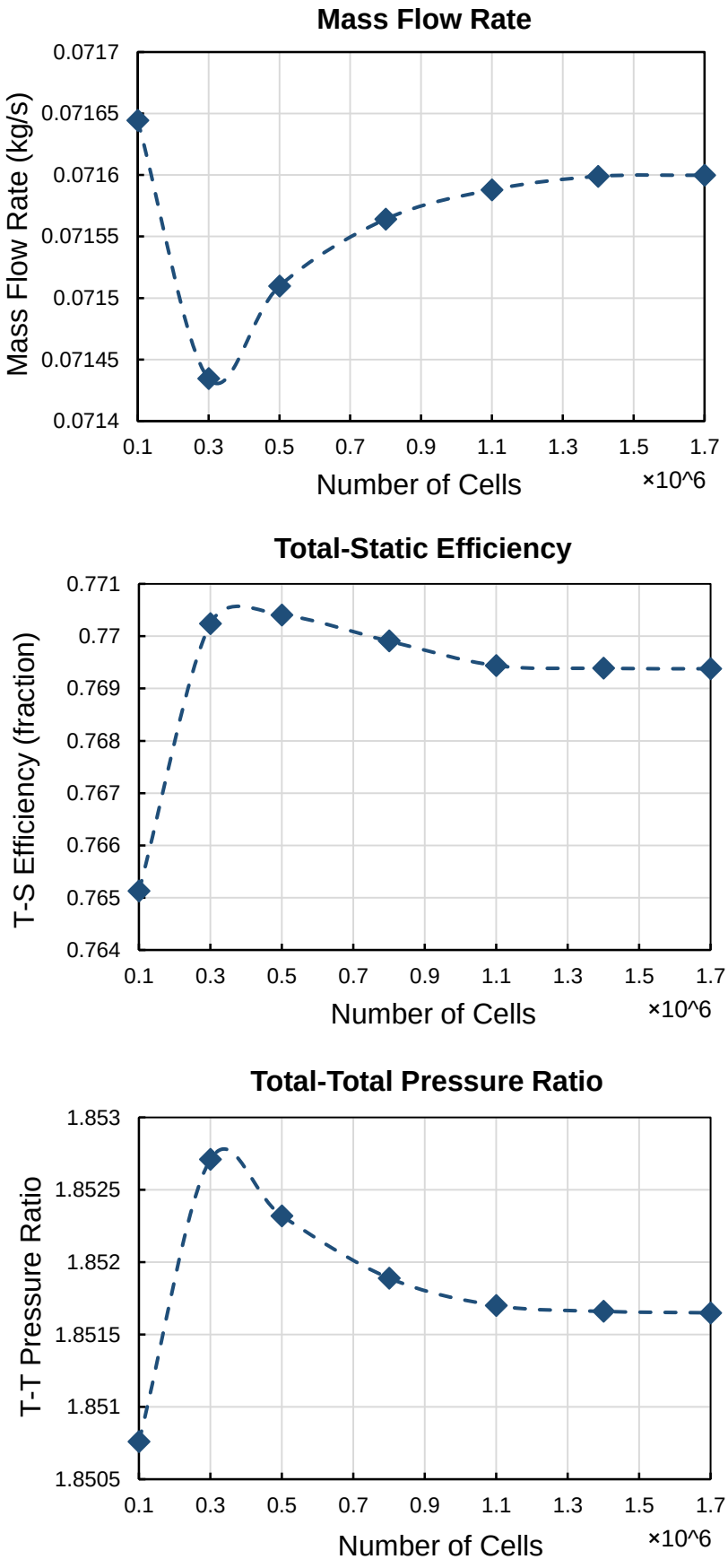

Figure 5.16 Mesh sensitivity study of the selected commercial turbine

Theoretically, the mesh sensitivity study should be performed for all domains in the compressor and turbine models. Due to the limited computational resource, only single-flow passage was selected to investigate the effect of the grid resolution. This is also because that the majority of pressure changes occur at the rotor, the diffuser for compressor, and nozzle for turbine.

Thus, for both compressor and turbine mesh sensitivity studies, 7 levels of mesh density were defined from 0.1E+6 to 1.7E+6 cells with an interval of 0.2E+6. Regarding turbine, the volute and outlet pipe were structured with 0.6E+6 and 0.1E+6 cells respectively, while the compressor inlet pipe and volute were 0.7E+6 and 0.2E+6.

The simulation results of turbine mesh sensitivity study are shown in Figure 5.16. For all variables of interest, the corresponding predictions tend to converge with increasing the mesh density. To be specific, comparing to the case with the finest mesh, 0.016% and 0.008% differential of the predicted mass flow rate and efficiency, respectively, were found for the case with 1.1E+6 cells, while 0.231% and 0.112% for that with 0.3E+6 cells. Since the differential of the predicted mass flow rate decrease from 0.050% to 0.016% by increasing the cells from 0.8E+06 to 1.1E+06, the latter was set as the mesh target for all trimmed turbines.

Regarding the compressor mesh sensitivity study, Figure 5.17 shows the effect of the mesh density on the mass flow rate, T-S efficiency, and T-T pressure ratio predicted by the proposed compressor model. As it can be seen in Figure 5.17, all parameters of interest tend to be converged with the increase of the cell number. Compare to the case with the finest rotor mesh, only 0.039% higher T-T pressure ratio is predicted by the case with the coarsest rotor mesh, while 0.681% higher mass flow rate is found. Considering the trade-off between simulation accuracy and computational time, the mesh number of 0.8E+6 is chosen for the rotor meshing target, as the resulting difference of all presented parameters are lower than 0.010% comparing to the case with the finest rotor mesh.

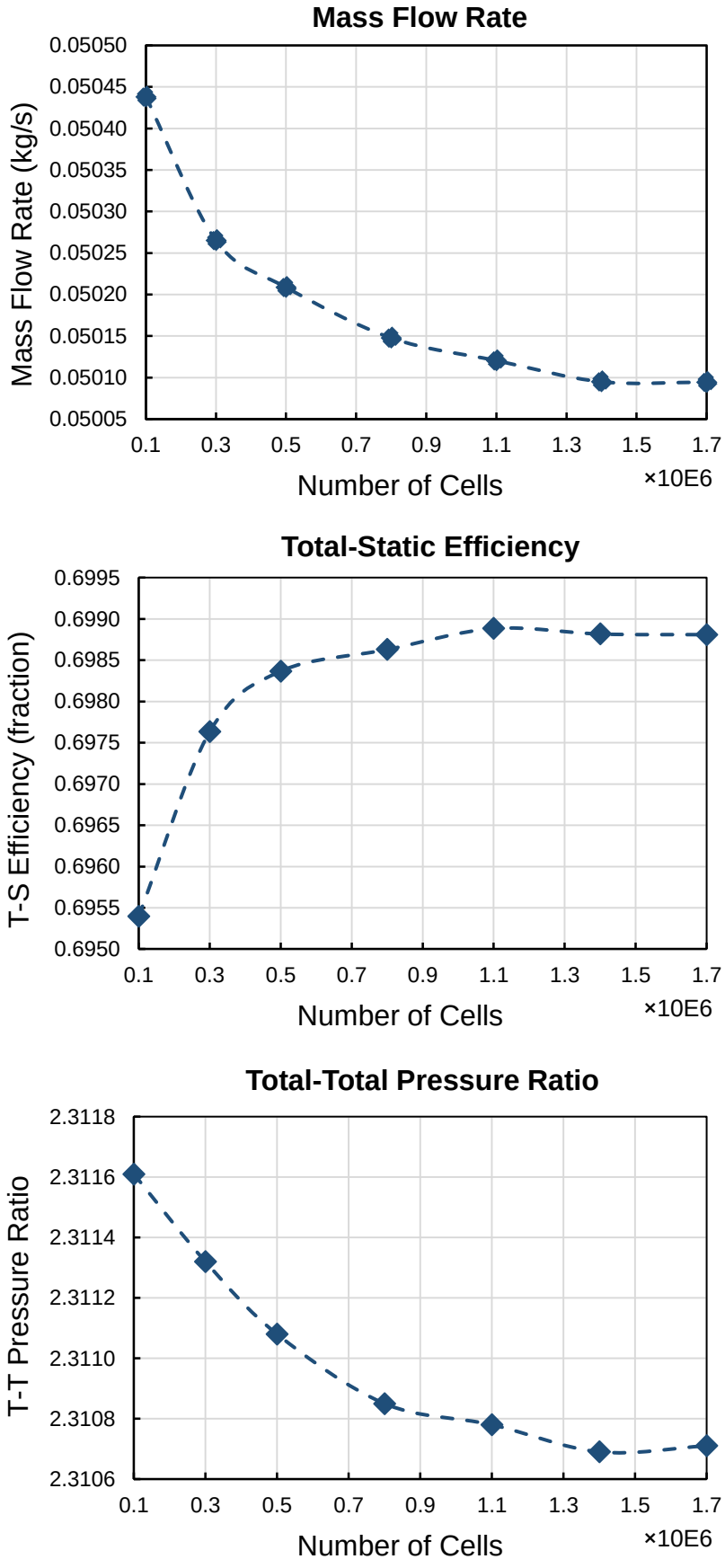

Figure 5.17 Mesh sensitivity study of the selected commercial compressor

5.4 Blade Trimming

Industrial compressor and turbine manufacturers often have to respond instantly to new blades designs or in an aftermarket situation to modification of an existing rotor. In order to deal with this, design from scratch is out of the question due to the limited time. In addition, the sophisticated knowledge of designing a new compressor or turbine is indispensable. Thus, size scaling or geometry modification are typical methods used to adjust the corresponding performance. In this research, blade trim is applied to optimise the performance of the selected commercial compressor and turbine at the IBC design operating point.

5.4.1 Compressor Impeller

The blade trimming has been widely adopted by compressor industry to expand a single high-flow design to a family of compressors in order to cover a wide flow range. It means that the trimming methods can be used to modify an existing impeller design to meet a new flow or pressure ratio design point. Thus, the selected commercial compressor can be trimmed to achieve the optimal operating performance at the design point. Figure 5.18 shows the three primary trimming methods.

Radial trimming is mainly utilized to reduce the total pressure rise across the impeller by trimming in the radial direction. There is an alternative to the radial trimming, called as axial trimming. The advantages of the axial trimming are that reducing the outlet height will lower the specific speed of the impeller and push a specific speed machine toward a more favourable value of specific speed. The third method is flow trimming. The corresponding purpose is to modify the flow coefficient of a compressor, thereby increasing the compressor efficiency at design operating region. It should be noted that the pressure ratio is unchanged by the flow trimming. However, in order to achieve the compressor performance improvement, the volute need to be resigned due to the reduction of the tip height.

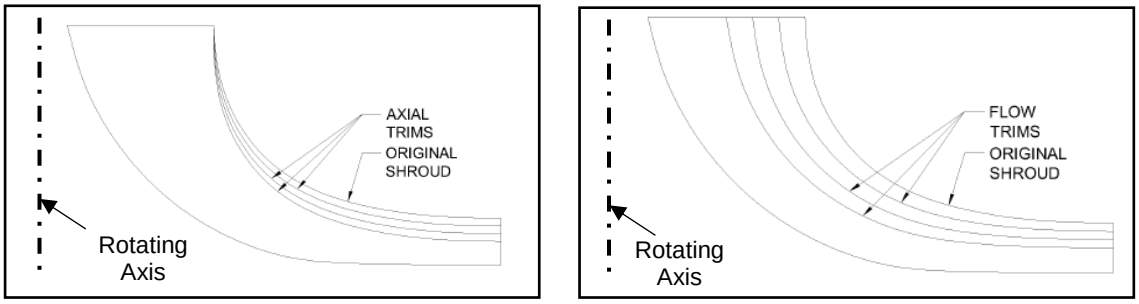

(a) (b)

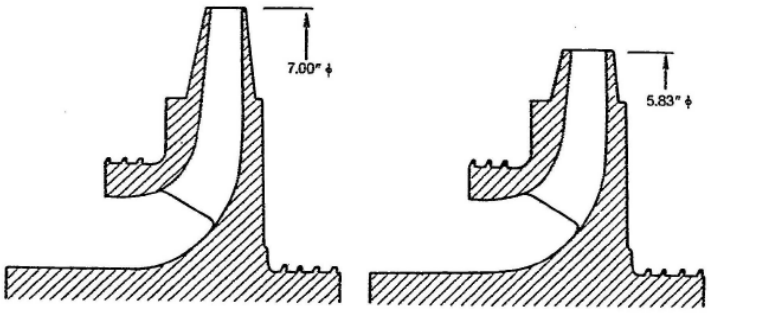

Original Design Trimmed Blades and Shroud

(C)

Figure 5.18 (a) Axial Impeller Trimming (b) Flow Trimming (c) Radial Impeller Trimming

5.4.2 Turbine Impeller

The turbine trim is a common practice used in turbochargers for adjusting flow capacity, in order to achieve the optimal performance at the desired operating condition. It is defined as the ratio of the effective outlet diameter to the turbine rotor inlet tip diameter. Thus, rotor exit and inlet tip diameter should be modified separately to perform the turbine trim.

The sensible method to quantify the modification at the turbine rotor exit is the percentage of the increased or reduced exit area, shown in Figure 5.19. The reference is the baseline turbine. The 50% reference means that the outlet exit area of the trimmed turbine is only 50% of that of the baseline turbine. '100%' trim, shown in Figure 5.19, is of course not practically feasible, but shows the maximum limit of outlet area for a radial turbine. [125]

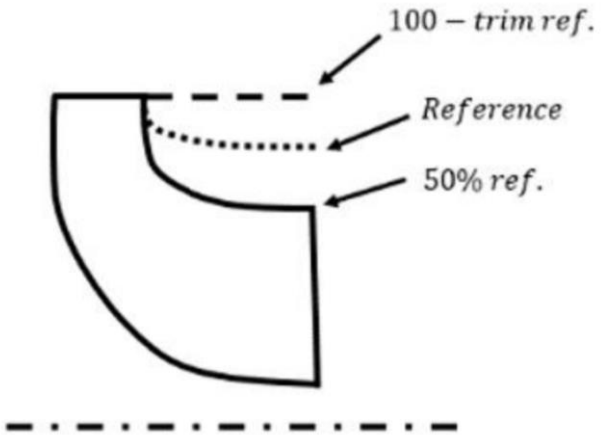

Figure 5.19 Example of turbine rotor exit trim

Second to the trim variation, the turbine inlet tip diameter could be altered by simply extending or shortening, shown in Figure 5.20. However, this parameter is slightly more difficult to assess as it is constrained by the maximum tip speed of the turbine. Note that for the turbocharger application the frame size and weight of the radial turbine is an important parameter consideration, as it can significantly affect the turbocharger transient response. However, in this research, the turbine optimisation only is conducted at one design operation point. Thus, transient response of compressor and turbine are excluded from optimisation objectives.

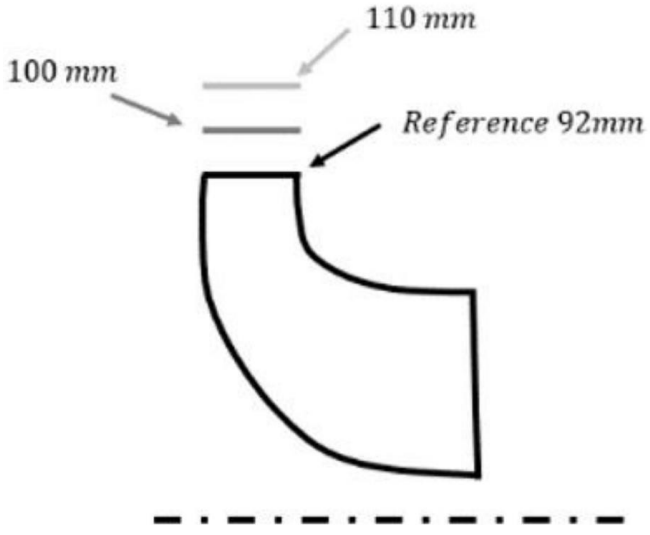

Figure 5.20 Example of turbine rotor inlet tip diameter trim

5.5 3D Simulation Results: Trimmed Compressor and Turbine

5.5.1 Compressor 3D Modelling Results

Based upon the discussion about blade trimming methods, the flow trimming was applied to vary the compressor blade height, as this method is able to modify the flow coefficient without significantly changing the pressure ratio. Thus, in this research, the compressor inducer height and exducer height were set as variables for the performance optimisation. In order to properly collect and diffuse the working fluid from the compressor rotor, the vaneless diffuser and the volute shape have to be optimised by varying the diameter and area to radius (A/R) ratios, respectively.

All trimmed compressors were evaluated by ANSYS CFX with the proposed setup in previous section. By doing so, the mass flow rate of each trimmed compressor was predicted. As a result, a DoE was set up parameterizing inducer height, diffuser diameter, and volute A/R ratio, in order to reach the optimal compressor efficiency at the design operating point. For a given inducer height, diffuser diameter, and volute A/R ratio, the parametric sweep of compressor exducer height was performed to reach the design mass flow rate.

Due to the limited computational resource, only three alternative volutes were proposed to couple with the trimmed compressor rotor. The primary parameters of all available volutes are listed in Table 5.4. The corresponding cross-section view were shown in Figure 5.9. Since the diffuser diameter specifies the inlet plane of the volute, it was considered as a design parameter for volutes.

Regarding the exducer height, three values were proposed – 3.50 mm, 3.75 mm, and 4.25 mm. A range of the inducer height was selected between 9.76 and 13.26 mm, in order to ensure that the proposed compressors deliver the design mass flow rate of 0.055 kg/s.

Table 5.4 Design variables of alternative volutes

Volute	A/R Ratio (mm)	Diffuser Dia. (mm)
A	6.0	110
B	6.6	130
C	8.0	130

In this research, five simulation cases were investigated, shown in Table 5.5. For each simulation case, the parametric sweep of compressor exducer height was performed. Then, only the compressor delivering the predicted mass flow rate of 0.055 kg/s was considered as candidates. The simulation results are listed in Table 5.5. Since the volute geometry for the original commercial compressor is unavailable in this research, the corresponding 3D simulation is unable to be performed and, therefore, there is no simulation result of the commercial compressor in Table 5.5.

Table 5.5 Compressor blade trimming simulation results

Simulation Case	1	2	3	4	5
Volute	A	B	B	C	C
Exducer Height (mm)	3.75	3.75	4.25	3.50	3.75
Inducer Height (mm)	12.61	11.22	11.16	10.71	10.87
Mass Flow Rate (kg/s)	0.055	0.055	0.055	0.055	0.055
T-S Pressure Ratio	2.22	2.22	2.22	2.22	2.22
T-S Efficiency	70.94%	72.32%	72.11%	70.55%	71.10%

In all simulation cases, the predicted T-S pressure ratio is equal to 2.22, as all 3D simulations were performed with the fixed inlet total pressure of 0.45 bar and outlet static pressure of 1 bar. With such boundary conditions, the mass flow rate through the compressor is a parameter that will be predicted by the 3D simulation. Note that the inducer height was optimised in each case to ensure that the design

mass flow rate of 0.055 kg/s was achieved. Thus, different inducer heights were expected for each case, shown in Table 5.5. According to the 0D and 1D numerical analysis of IBC system, the higher compressor efficiency is beneficial to the IBC performance. Thus, the proposed compressor in simulation case 2 that delivers the maximum efficiency of 72.11% in all cases was selected as the compressor design for the IBC prototype.

Note that its predicted efficiency is still quite low. This is because the insufficient amount of simulations cases was considered in this section. In other words, the further optimisation should be taken to improve the selected the compressor. Nonetheless, according to the project plan, there is no enough time to perform the further compressor optimisation before the scheduled IBC rig tests. In conclusion, even though the best design among all alternative compressors only delivers 72.11% total-to-static efficiency, it was still selected and manufactured for the IBC prototype.

5.5.2 Turbine 3D Modelling Results

Since the turbine design target is to increase its efficiency instead of altering the pressure ratio, only turbine exducer height is trimmed in the research to adjust flow capacity. Furthermore, the resulting flow changes require the turbine volute to be re-sized, so that the uniform flow field could be generated at the inlet of the rotor. The volute sizing can be achieved by altering its area to radius ratios. In summary, the turbine exducer height and the volute A/R ratio are selected as the design variables.

The volute employed in the selected commercial turbine is considered as the baseline. In other words, the cross-section shape of the commercial volute remains unchanged. The A/R ratio varies in a wide range from 13 to 21 mm.

In theory, the multiple heights of turbine exducer should be investigated to achieve the optimal design. However, due to the limited time available for the turbine design, only turbine rotor with the exducer height of 16.1 mm is considered as the turbine design in this research, that is, the commercial turbine rotor is trimmed down by 1 mm at the impeller exducer.

As the described model settings, total pressure of 1 bar and total temperature of 1023 K are imposed as the inlet boundary of the turbine, while only static pressure is applicable at the outlet boundary. However, the turbine design target is T-T pressure ratio. In addition, since there is no heat exchanger model simulating with the turbine, the extent to which the outlet static pressure is recovered from the available total energy is unknown. Thus, the sweep of T-S pressure ratio is investigated from 2 to 2.2 bar with an interval of 0.2 bar, to ensure that the turbine operating condition of T-T pressure ratio of 2 in tests is covered by simulations. In other words, the static pressure at the turbine outlet is set as 0.56, 0.5, and 0.45 bar.

With the described model settings, the turbine mass flow is a parameter that the CFD simulations will estimate. Thus, the turbine design candidate is selected for the IBC rig test only when the predicted mass flow rate is 0.055 kg/s and T-S efficiency is the maximum among all candidates.

Figure 5.21 shows that T-S efficiency is a function of volute A/R ratio. The blue line with circle markers represents the simulation case with T-S pressure ratio of 1.8, that is, imposing 0.56 bar as the static pressure at the turbine outlet. Whereas, the red line with square markers and the green line with triangle markers are cases with that of 2 and 2.2, respectively. The black dashed line represents the alternative turbine designs that deliver the mass flow rate of 0.055 kg/s at given operating boundaries. In Figure 5.21, except the simulation case with total-to-static pressure ratio of 1.8, T-S efficiency increases with the reduction of the volute A/R ratio. Regarding the case of T-S pressure ratio of 1.8, the optimal T-S efficiency of 79.52% is reached when the volute with A/R ratio of 13.5 mm is employed. In addition, Figure 5.21 shows that the predicted mass flow rate is a monotonically decreasing function of the volute A/R ratio, that is, the turbine mass flow rate increase with the volute volume. Since the mass flow rate at the design operating point is 0.055 kg/s, any alternative turbine design represented by the black dashed line can be considered as the turbine design for the IBC prototype. Thus, the rotor with the exducer height of 16.1 mm and the volute with the A/R ratio of 15.5 mm are selected for the final turbine design, as it delivers the optimal performance at the design operating point.

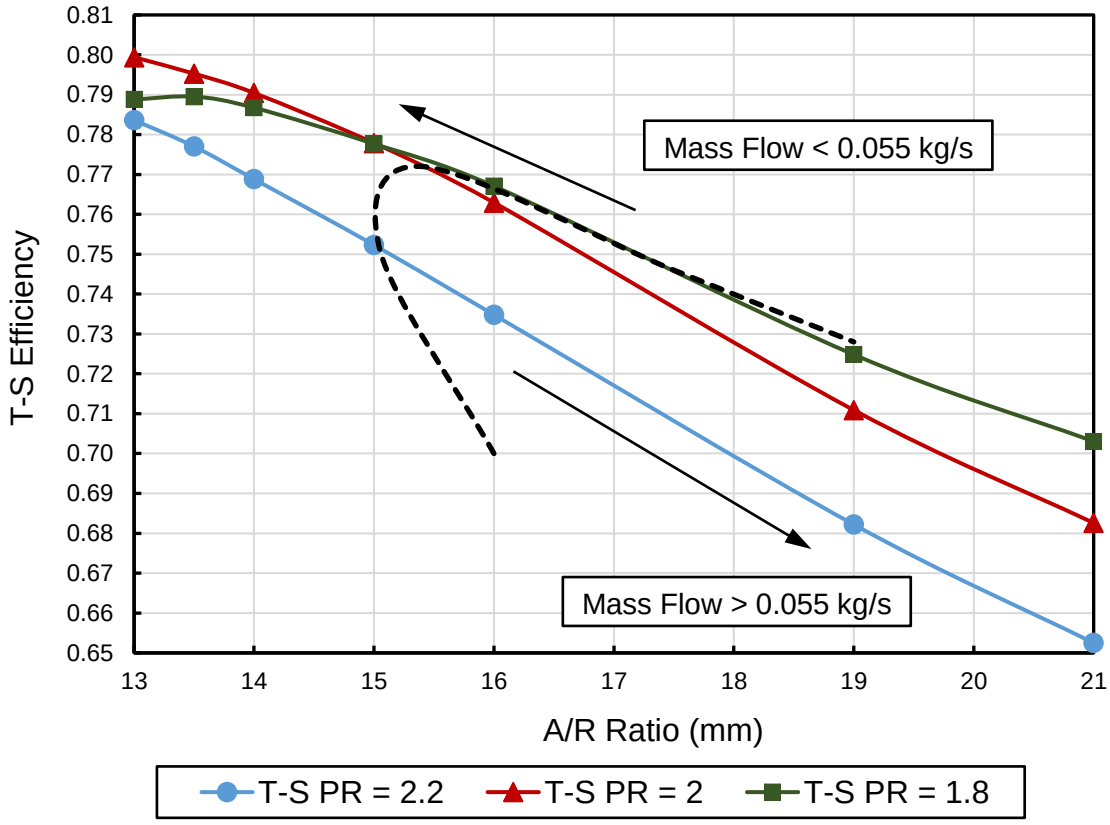

Figure 5.21 Effect of volute A/R ratio on the turbine T-S efficiency

5.6 In-house Compressor Design

In the previous section, a compressor design with T-S efficiency of 72.32% at the design operating point was selected as the IBC compressor for tests. Note that its efficiency is relatively low comparing to the maximum efficiency of typical centrifugal compressors – around 80%. Thus, during the IBC tests, a new centrifugal compressor was designed from scratch and optimised in order to deliver higher efficiency at the design operating point. Although it cannot be manufactured and tested due to the project budget limitation, the corresponding benefits for IBC systematic performance can be evaluated by 1D numerical simulations.

Similar to the compressor, the selected turbine design in the previous section should be also optimised further. However, the project plan for this research is unable to include the turbine optimisation due to the time limitation. Thus, only compressor design and optimisation were performed in this research and the corresponding approach is considered as the example to demonstrate the capability of designing and optimizing.

In this research, the compressor rotor preliminary design was generated by a program available in ANSYS, referred as VISTA CCD. It is developed to generate rotor one-dimensional meanline design of a centrifugal compressor with the given machine duty, such as mass flow, pressure ratio, etc. In addition, ANSYS have a function to convert the produced 1D impeller design to a 3D impeller geometry with some initial guesses, such as the impeller camber and thickness distributions. Based on the preliminary 3D compressor design, the compressor impeller and volute can be optimised to further improve its performance at design conditions.

The optimisation process needs to repeatedly modify the impeller shape and analyse the corresponding aerodynamic performance, until the optimal performance is achieved. Therefore, extensive potential candidates have to be investigated, which requires tremendous amount of the computational time. In addition, due to the complexities of turbomachinery blade shape, multi-variables should be utilized to define the blade geometry. As a result, the selected optimisation method should be able to solve the multi-variables optimisation problem. Moreover, the main difficulty of turbomachinery design optimisation is that the objective function has numerous local optimums, due to the complex flow structures and geometrical parameters. Thus, based on the nature of the optimisation problem in this research, genetic algorithm optimisation was selected to perform the compressor design optimisation.

5.6.1 Genetic Algorithm Optimisation

Genetic algorithm (GA) optimisation is metaheuristic inspired by the process of natural selection, which was initially introduced by John Holland in 1975 and developed by Goldberg in 1989. Then, it has been employed for solving numerical

optimisation problems in a wide variety of application fields including engineering, biology, economics, agriculture, business, telecommunications, and manufacturing [97]. Generally, the genetic algorithm is designed to drive a population of candidate solutions of an optimisation problem evolve toward better solutions. Essential differences that distinguish GA from other optimisation methods are that GA allow to cover the entire design space and thus reduce the probability to get trapped in a local minimum [98, 99]. In addition, this theory basically relies on the notion that the genetic material exchanged by specimen with favourable genetic predisposition will result in superior offspring over the course of several generations.

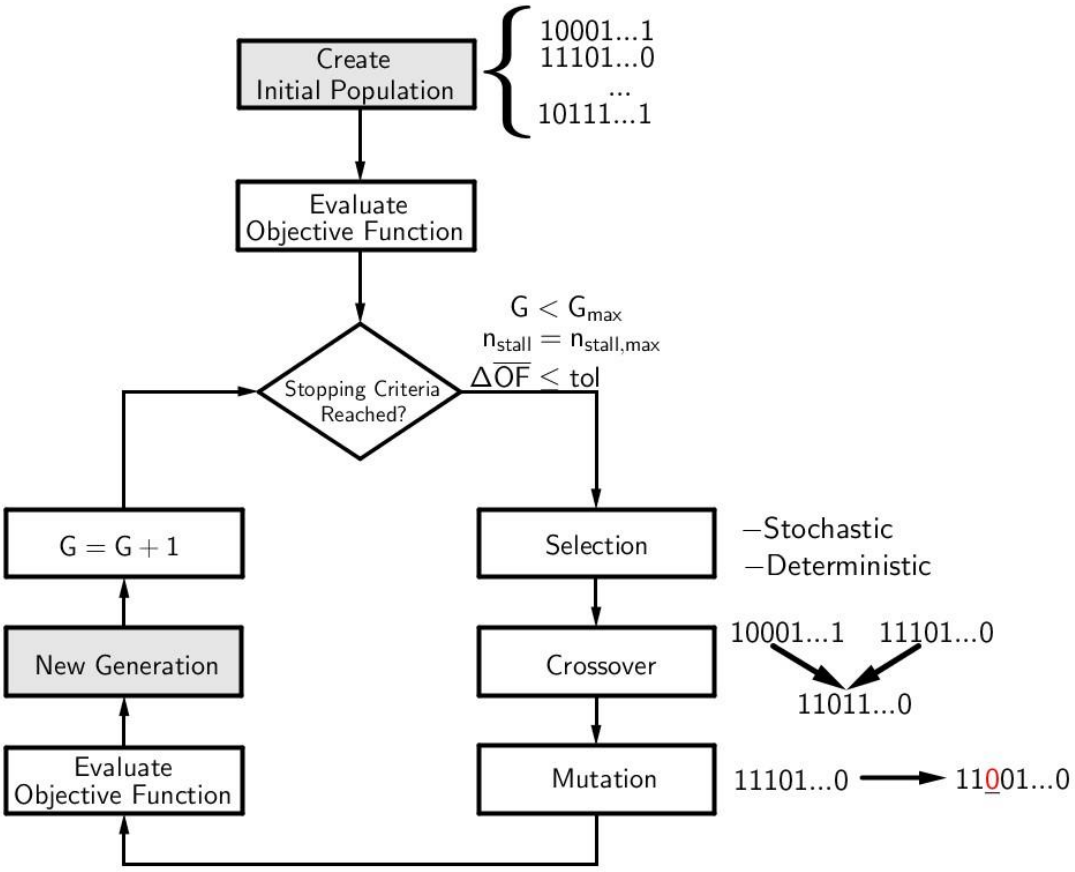

Figure 5.22 Flowchart of the genetic algorithm principle

Figure 5.22 depicts the operational principle of a standard GA. At beginning of the process, a pool of initial random population of *N* is generated within the boundaries of the design space. Each individual in the initial pool is encoded in binary as strings of 0s and 1s. Then, a solver and objective function are used to

evaluate each individual so that the favourable individuals can be selected as parents for the next generation. The corresponding binary strings, referred as genetic material, is subsequently mutated and altered by the genetic operators – crossover and mutation. By doing so, the new set of individuals are created and considered as the next generation. It is followed by an evaluation of each new individual. The whole process will be terminated when the stopping criteria is reached. In this research, the compressor optimisation stops when the maximum compressor efficiency in each generation is converged.

5.6.1.1 Initialization

As discussed above, the initial population is generated randomly within the boundary of the optimisation problem. Population size is vital parameter in GA optimisation program, especially considering the evolutionary computation and the quality of the results. The population size of candidate solutions depends on the nature of the optimisation problem. The 'small' population size could guide the algorithm to poor solutions. However, the corresponding computation cost would increase with the population size. Thus, a trade-off should be achieved in order to feed the algorithm with 'enough' candidates, thereby obtaining 'good' results. 'Enough' is directly related to instances in the search space and diversity [126]. Rao [99] claims that the size of the population should be 2 to 4 times of the number of design variables n. Schaffer, et. al. [127] intended to find out the optimum parameter setting for a binary GA. The discrete sets of parameter values for the population size, mutation rate, crossover rate, and the number of crossover points have been investigated. Due to a wide range for each GA parameter, a total of 8400 parameter combinations were adopted by GA to solve a small set of numerical optimisation problems. With the consideration of the computation cost and the final optimum solution for each parameter combination, they found that the best on-line performance resulted for the following parameter settings: population size 20-30, crossover rate 0.75-0.95, and mutation rate 0.005-0.01. It should be noted that the best parameter settings for each numerical test suite are quite similar. In other words, the best parameter settings were independent of the optimisation problem to some extent.

5.6.1.2 Selection

During each successive generation, the superior individuals are selected by the selection operator to breed a new generation. Indeed, the selection operators should be properly chosen in order to guide the evolution in a desired direction. There are many approved selection operators built in various selection criterions.

The roulette-wheel selection is frequently used in genetic algorithms, due to its simplicity of implementation and straightforward interpretation [128]. Its selection mechanism is that the fitter individuals is more likely to be selected and will go forward to for the mating pool for the next generation. In other words, this method evaluates the probability of selection based on its fitness. It can be briefly described as follows. Assuming there are N individuals in a generation and the corresponding fitness is $f_i > 0$ ($i = 1,2, \dots , N$). A percentage of total fitness is thus given as

$$p_i = \frac{f_i}{\sum_{i=1}^{N} f_i} \quad (i = 1,2, \dots , N) \tag{5.8}$$

These percentage fitness values can then be used to size the sectors of each individual in a roulette wheel. The selection of an individual is equivalent to choosing randomly a point on the wheel and locating the corresponding sector. By doing so, it is achieved that the better fitted an individual, the larger the probability of selecting and mating.

The rank selection is also fitness-based selection method. Unlike the roulette-wheel selection assigning the selection probability proportional to the individual fitness, the rank selection rates the fitness of each individual and then the individual's selection probabilities are allocated by a mapping function according to its rank [129]. Although the mapping function could be linear (linear ranking) or non-linear (non-linear ranking), the rank selection, generally, leads to populations of larger variability. This is because, with a specified mapping function, the selection probabilities would be same whether the fittest candidate is ten times fitter than the next fittest or 0.01% fitter. Thus, this selection strategy prevents premature coverage by tempering selection pressure for large fitness differentials

that occur in early generations. Conversely, the selection pressure could be amplified when the small fitness differences are found in later generation. However, this method can lead to slower convergence, because the best chromosomes do not differ so much from other ones [130]. In other words, the rank selection could be computationally expensive.

The tournament selection is probably the most widely used selection strategy in evolution algorithms due to its efficiency and simple implementation [131]. The tournament selection starts with randomly picking N individuals in the existing population and staging a tournament to determine which one get selected. N is the tournament size, commonly set to 2. The selection procedure is that a random value between zero and one, called as the probability parameter, is generated and, then, compared with a pre-determined selection probability. If the random value is less than or equal to the pre-determined selection probability, the fittest individual wins and will be selected as one of the next generation population. Otherwise, the weakest individual is chosen. The probability parameter is able to preserves diversity of each generation, although keeping diversity may deteriorate the convergence speed. In practice, the probability parameter is set to be greater than 0.5 in order to favour fittest individual. The tournament selection has several benefits: it provides easily adjustable selection pressure, keeps low probability of dominating by the large fitness individuals, and no need to scale the individuals' fitness to perform the selection.

5.6.1.3 Crossover & Mutation

After establishing the mating pool by the selection procedure, the two basic genetic operators – crossover and mutation, are utilized to produce child generation based on the parental generation in the mating pool.

The mutation operator is designed to maintain genetic diversity in each generation and prevent the algorithm trapping in a local minimum by stopping the solutions becoming too close to one another. Mutating can be achieved by altering one or more gene values in individuals' chromosomes from its initial state. By doing so, the generated individuals in child generation may change entirely

from the parental generation. In other words, the mutation is able to introduce a random walk through the entire search space and ensures that the probability of attaining any potential solution is greater than zero. The possibility of mutation is defined by a mutation rate – P_m. It should be noted that the mutation rate should be set at a low value to prevent losing 'good' individual [132].

The crossover is a process of taking more than one parental individual and producing a child individual. It evolves exchanging the genetic material of parental individuals, allowing reproduce high quality notions according to their performance and crossing these notions with many other high-performance notions from other individuals. Thus, it encourages the algorithm evolve towards better solutions.

In summary, an example of crossover and mutation is demonstrated in Figure 5.23.

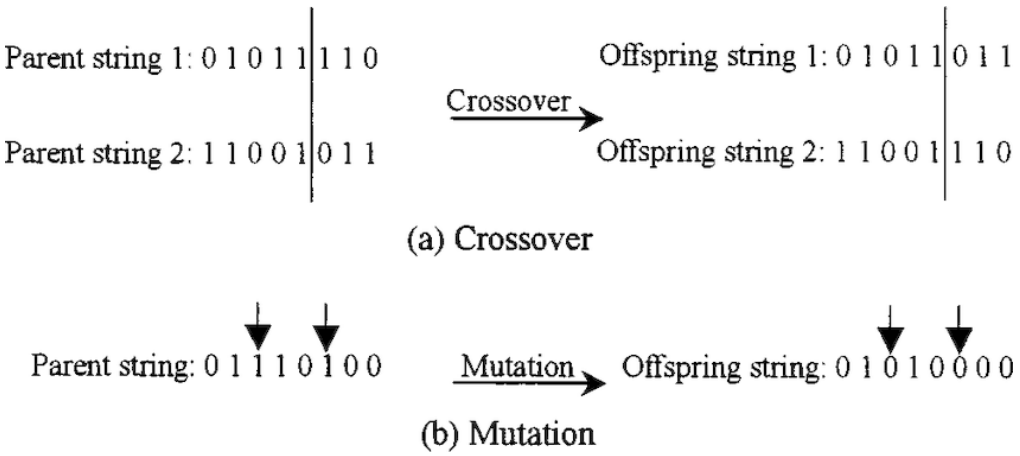

Figure 5.23 Crossover and mutation operations in genetic algorithm

5.6.2 Compressor Design and Optimisation

The in-house compressor design process consists of two stages. At first stage, the preliminary rotor geometry was generated with the design requirements and sensible guesses for the geometry parameters. Then, it was optimised with the vaneless diffuser and volute by using the genetic algorithm optimisation method. The optimised compressor design was considered as the baseline for the second stage optimisation. The aim is to optimise the compressor impeller shape to

further reduce various energy loss during the compression process. The resulting design is the final in-house compressor design that will compare with the trimmed commercial compressor.

5.6.2.1 Preliminary Design Optimisation

In this research, the preliminary rotor design was produced by ANSYS VISTA CCD, in the consideration of the compressor duty at the design conditions. However, the process still requires initial guesses on the compressor aerodynamic data and impeller geometry, such as incidence angle at shroud, hub diameter, vane inlet angle, etc. It should to be noted that the program developers claim that the VISTA CCD aims to avoid over-sophistication and the potentially frustrating data preparation. This is especially beneficial at the very beginning of the compressor design, as the only available design requirements in early phase are the required pressure ratio and mass flow, a speed constraint, and perhaps one or two geometric constraints. Thus, in order to reduce the required data, the default data settings have been sophistically tuned and, therefore, are reliable for the preliminary rotor design.

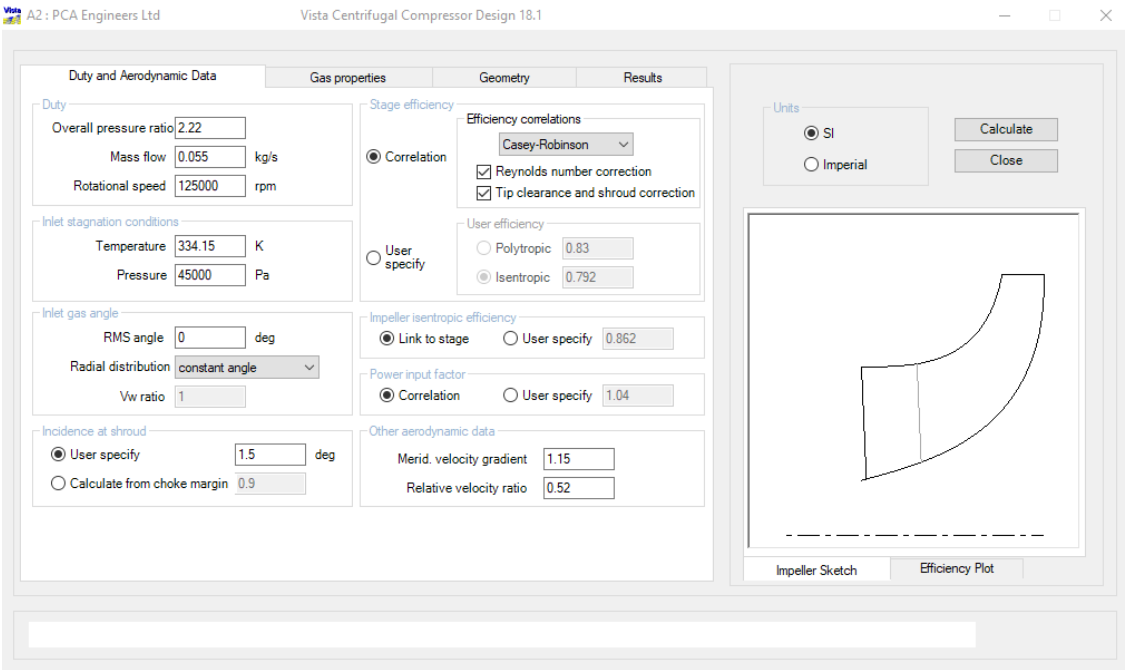

Figure 5.24 'Duty and Aerodynamic Data' settings for preliminary rotor design

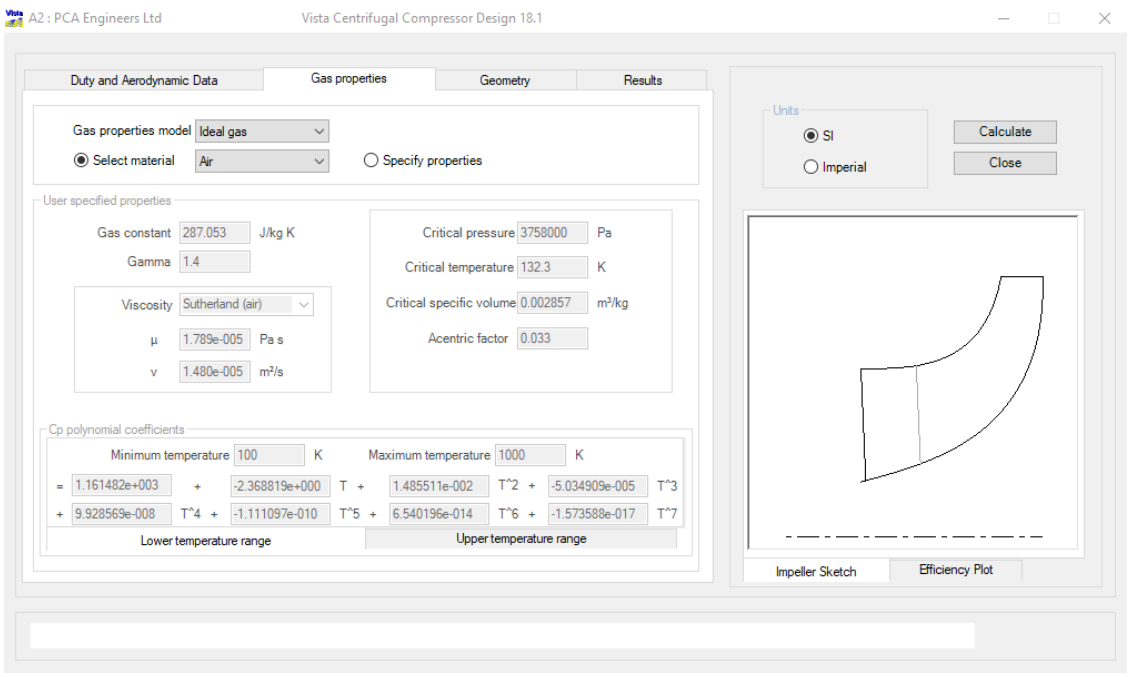

Figure 5.25 'Gas properties' settings for preliminary rotor design

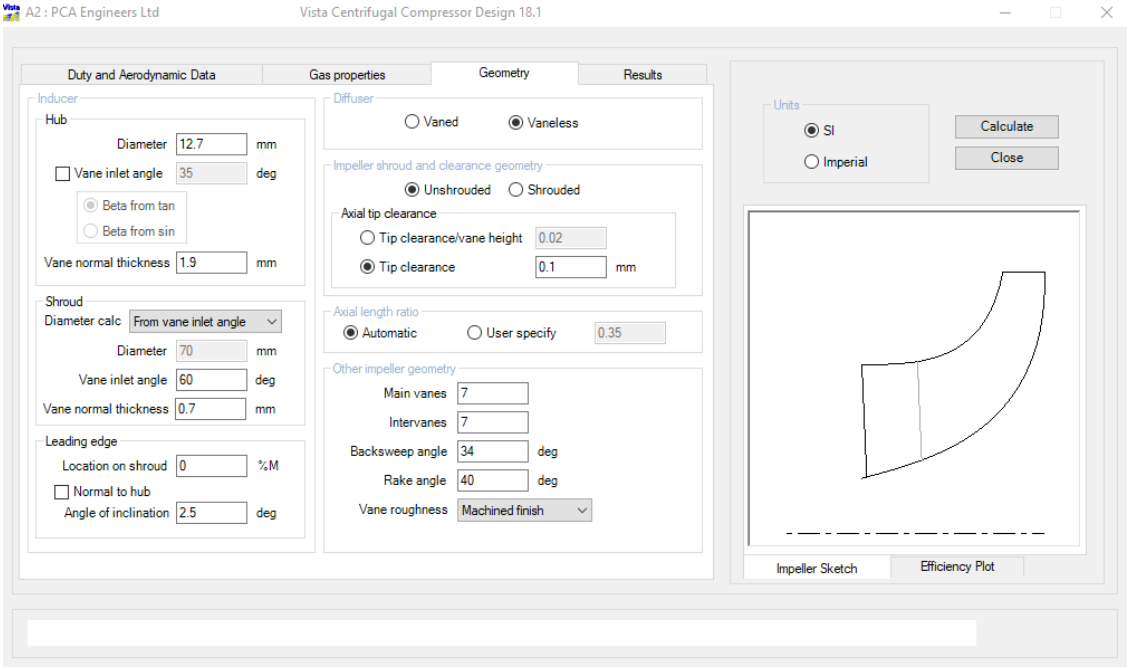

Figure 5.26 'Geometry' settings for preliminary rotor design

All user interfaces of this commercial program are shown in Figure 5.24, 5.25, and 5.26, which contain the date settings used in this research. In 'Duty and Aerodynamic Data' tab, the pressure ratio of 2.22 and mass flow of 0.055 kg/s

was considered as the design condition. At the inlet, the temperature and pressure were fixed as 60 °C and 0.45 bar. However, as the target of the in-house compressor design is to deliver required pressure ratio with the imposed inlet boundary conditions at mass flow of 0.055 kg/s, there is no constraint on the compressor rotational speed. Thus, the rotational speed was selected as the design variable. Regarding the working fluid, air was selected with the assumption of ideal gas. Due to the limited computational resource, only backsweep angle at the compressor shroud was defined as the design geometry variable. The rest of the required settings in 'Geometry' tab was specified by referring to the impeller geometry parameters of the trimmed commercial compressor. Due to the benefits of VISTA CCD described herein, the default value was kept for the data settings which were unspecified in this section.

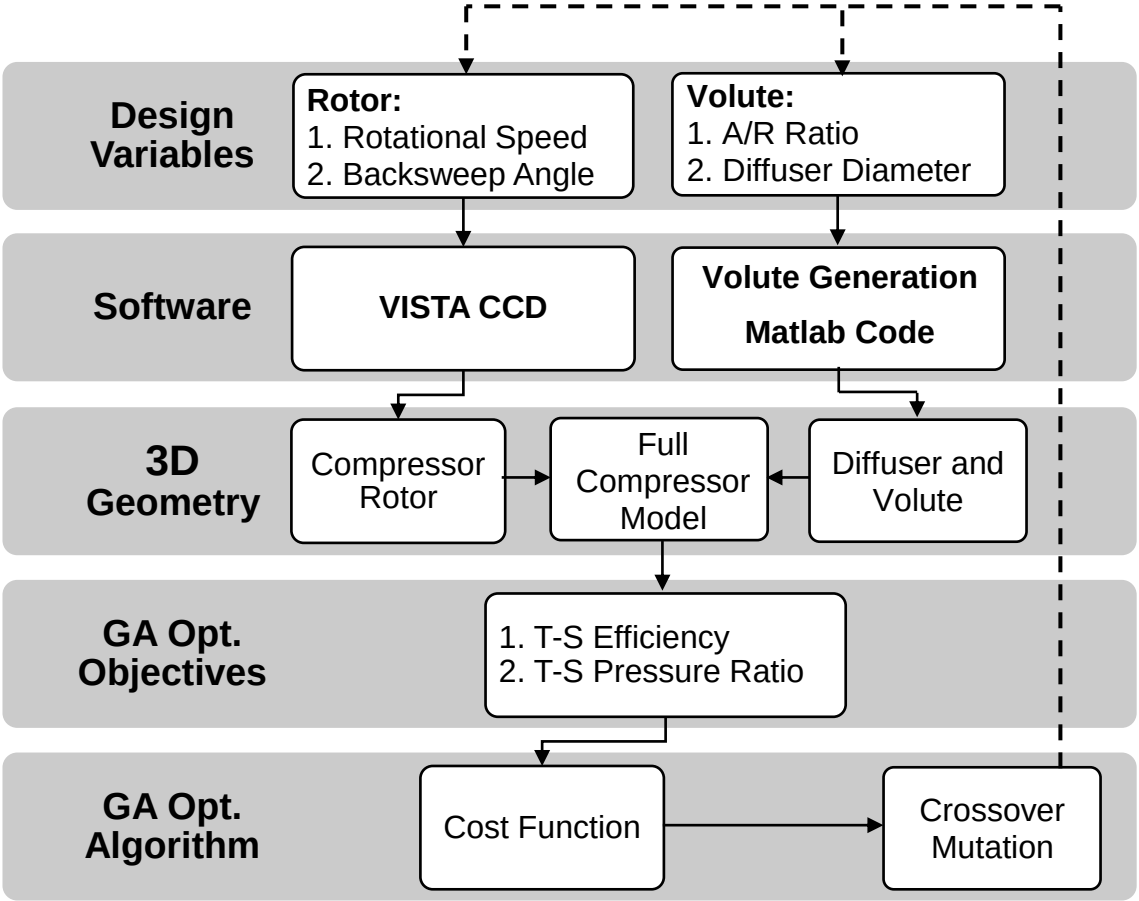

Figure 5.27 Flowchart of the compressor preliminary design optimisation process

Since VISTA CCD only produces a preliminary rotor design, the diffuser and volute are required to perform the compressor 3D simulations. In this research, the vaneless diffuser is employed downstream of the rotor. The diameter of the diffuser is considered as a design variable for optimisation. Regarding the volute, the cross-section shape is designed as same as the volute of the selected commercial compressor, shown in Figure 5.9, defined by a circular arc in three quadrants and a square in the fourth quadrant. The area to radius ratios is optimised for the compressor efficiency.

In summary, the preliminary compressor design optimisation process is shown in Figure 5.27. It shows that the GA optimisation algorithm firstly generates the value for the four selected design variables. Then, the rotational speed and backsweep angle are fed into VISTA CCD to generate the rotor geometry. The rest of the required settings for VISTA CCD are shown in Figure 5.24, 5.25, and 5.26. The A/R ratio and diffuser diameter are utilized to generate the vaneless diffuser and the volute. Afterwards, the rotor, vaneless diffuser, and volute proposed in the previous step are assembled in the pre-processor and conditioned by the described model setting in Section 5.3.1, except the outlet boundary condition. Instead of specifying the static outlet pressure, the mass flow rate of 0.055 kg/s is imposed at the compressor outlet for all compressor design candidates in the optimisation process. By doing so, the T-S pressure ratio has to be approximated by ANSYS CFX solver and included in the optimisation cost function to ensure that the optimal compressor design delivers the T-S pressure ratio falling within a range of ± 5% error in T-S pressure ratio target of 2.22. In addition, the T-S efficiency is also approximated by ANSYS CFX solver. Then, the cost function, expressed as Eq. 5.9, is used to evaluate the compressor design and, therefore, the GA optimisation algorithm is able to produce the population for the next generation. Note that high penalty, up to 10, is given when the restriction for T-S pressure ratio is unsatisfied. Regarding the GA parameter setting, the population size is set as 20, while crossover and mutation rate are selected as 0.8 and 0.01, respectively. The tournament selection is employed at the selection operator for this compressor optimisation, due to its advantage described in previous section. Regarding the optimisation stop rules, three criteria are defined as follows: 1) maximum number of generations (16) is reached, 2)

the average fitness value of the current generation is <10E6 higher than that of the previous generation, 3) the best fitness value does not change within the last three generations. The GA optimisation will stop when any one of the afore-mentioned criteria is met.

$$\text{Cost Function} = \begin{cases} -\text{T-S Efficiency}, & \text{if } 2.33 \geq \text{T-S PR} \geq 2.11 \\ 10, & \text{otherwise} \end{cases} \tag{5.9}$$

Figure 5.28 demonstrates the definitions of all presented compressor parameters in this optimisation process.

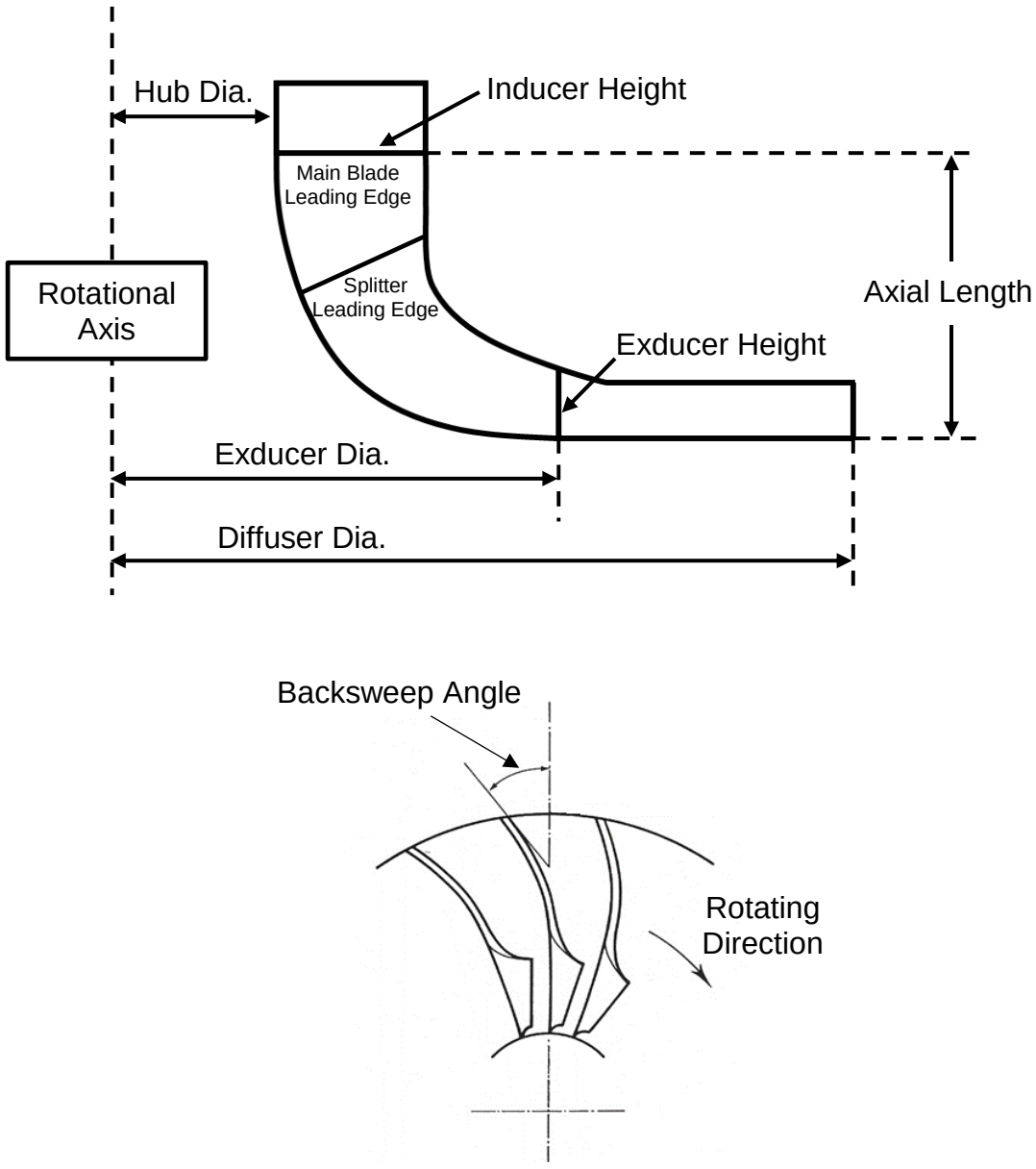

Figure 5.28 Definitions of all presented compressor parameters

Figure 5.29 shows that the compressor preliminary design optimisation took 231 different design variants, which is more 11 generations, to reach the convergence. In other words, the compressor efficiency settles down after initially showing a large spread, due to the nature of GA optimisation algorithm. However, there are still outliers until the end of the optimisation. This is caused by the existence of mutation operator.

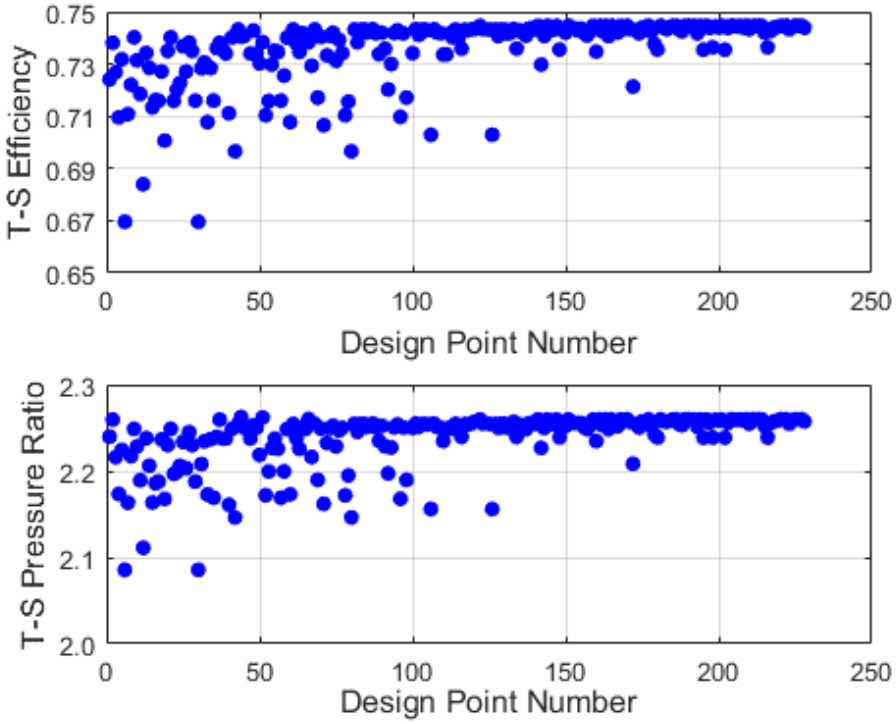

Figure 5.29 Optimisation results showing convergence of T-S efficiency and T-S pressure ratio

According to the IBC 0D and 1D simulations results, the higher compressor efficiency is, the higher net work the IBC system delivers. Thus, the candidate with the maximum efficiency of 74.47% is selected as the preliminary compressor design, which is 2.15 percentage points higher than that of the trimmed commercial compressor. The primary geometric information of the selected compressor design is listed in Table 5.5, in comparison with that of the trimmed commercial compressor. In addition, Figure 5.30 shows the geometry comparison between the preliminary compressor design and the trimmed commercial compressor – (a) blade-to-blade view near hub (20% span), (b) flow

passage shape comparison, and (c) blade 3D geometry comparison. In subplot (a), the M-Prime on the X-axis represents the radius normalized distance along the meridional curve from the leading edge (LE) and trailing edge (TE), while Theta on the Y-axis is circumferential coordinate of the blade surface in a cylindrical coordinate system. It can be clearly seen in Figure 5.30 (b) that the rotor height of the preliminary compressor design is shorter than that of the trimmed commercial compressor, while the blade passage is wider.

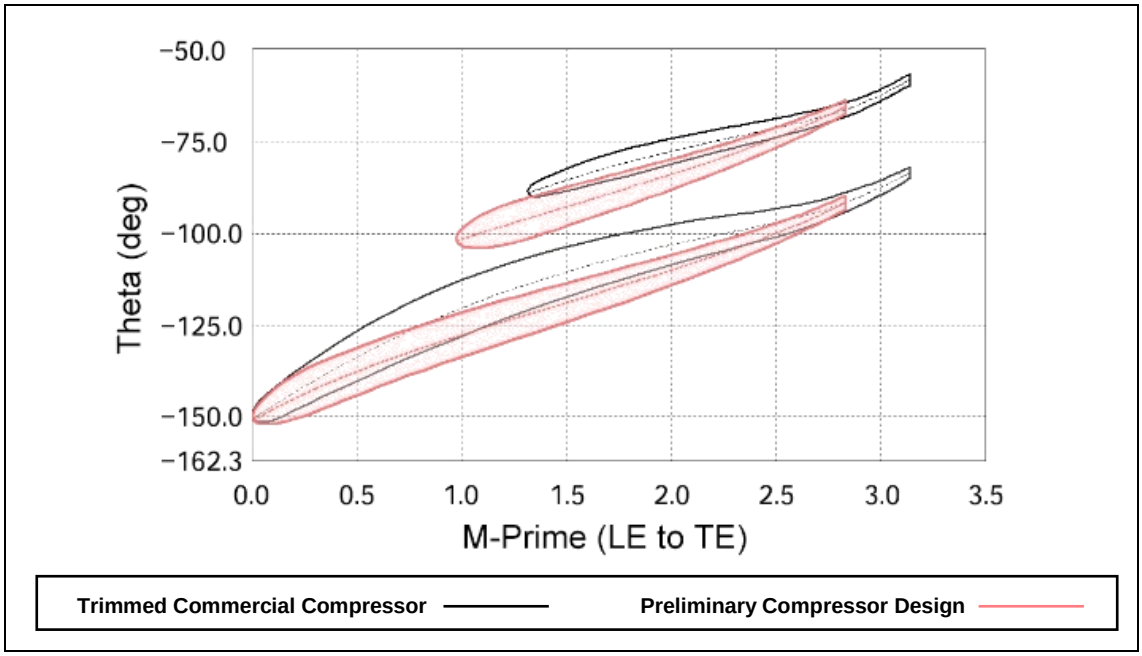

(a)

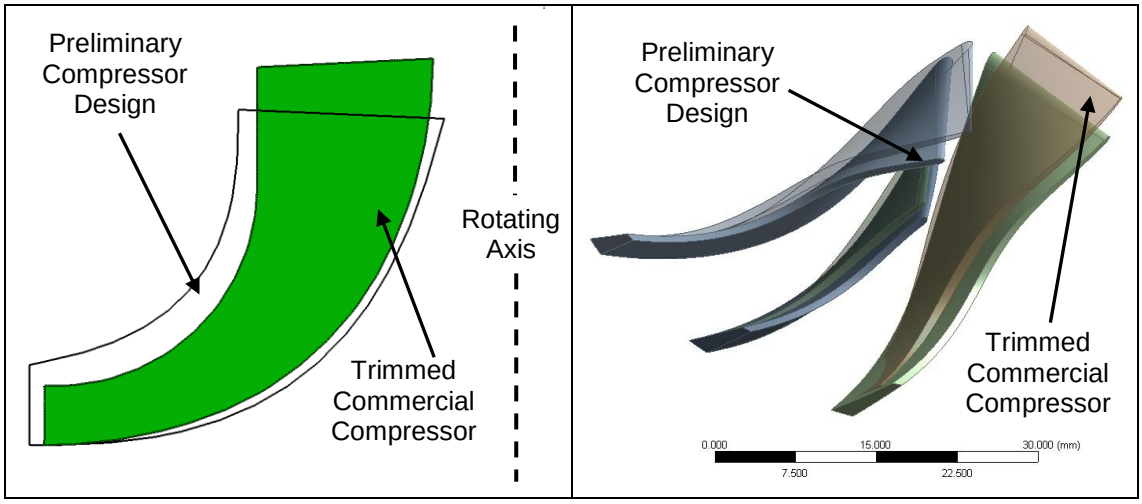

(c) (d)

Figure 5.30 Geometry comparison between the preliminary compressor design and the trimmed commercial compressor

5.6.2.2 Compressor Blade Optimisation

The second optimisation run is to improve the performance of the preliminary compressor design by optimizing the blade shape, as the blade shape of the preliminary compressor design was generated by VISTA CCD with some default settings. Thus, it is necessary to properly design and optimise the blade shape. The optimised vaneless diffuser and volute generated in the first optimisation process were employed and remained as unchanged through the second optimisation run. In addition, the 3D modelling boundary conditions were set as same as that in the first optimisation run.

The settings of GA optimisation algorithm used in the first optimisation run was also used for the blade shape optimisation, as the same amount of the design variables were employed. The design variable selection in this optimisation referred to the recommendation in Tüchler's research [133]. He performed a comprehensive compressor blade design optimisation at multiple operating points and investigated the importance of each geometric parameter of the compressor blade. However, given the computational cost, only four blade parameters were selected as the design variables, referred as 1) main blade inlet angle at shroud, 2) splitter inlet angle at shroud, 3) backsweep angle at shroud and 4) stack position for both main blade and splitter. These four design variables are depicted in Figure 5.31. It is important to note that the rotational speed of 112,900 rpm were imposed, as the previous compressor optimisation shows that the selected preliminary compressor is able to deliver highest efficiency among all candidates at the rotational speed of 112,900 rpm.

The cost function in this optimisation is expressed by Eq. 5.10 and the optimisation target is to minimize the cost function. As can be seen in Eq. 5.10, the narrower tolerance band of T-S pressure ratio, which is ± 1.5% error in T-S pressure ratio target of 2.22, was applied in cost function.

$$\text{Cost Function} = \begin{cases} -\text{ T-S Efficiency}, & \text{if } 2.25 \geq \text{T-S PR} \geq 2.19 \\ 10, & \text{otherwise} \end{cases} \tag{5.10}$$

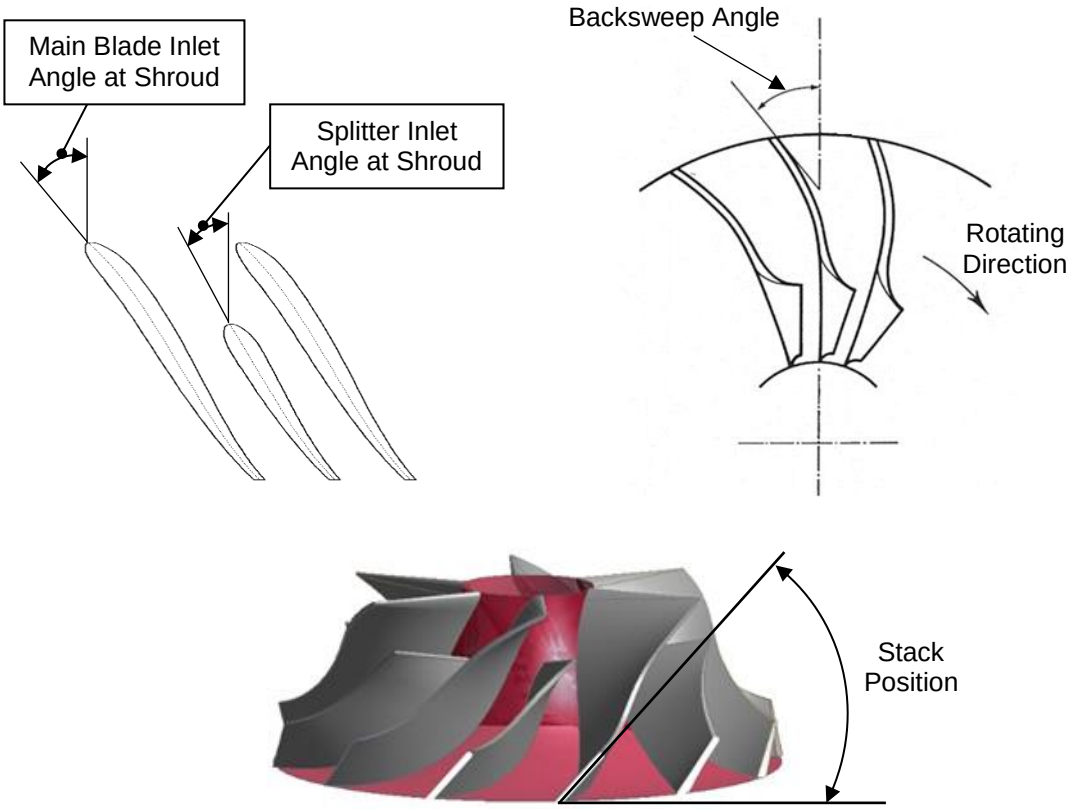

Figure 5.31 Parametrisation of the presented design variables

Figure 5.32 shows the predicted performance of all compressor design candidates generated by GA optimisation. In total, the compressor blade optimisation investigated 320 candidates, which is 16 generations. It should be noted that the maximum number of generations is set as 16. Thus, it indicates that the maximum number of generations should be increased so that the fitness value can be converged. However, the intention of developing in-house compressor design process is to demonstrate the capability of designing and optimizing. In addition, due to the limited time, the best candidate in the final generation was selected as the final in-house compressor design.

The optimisation results show that with the growth of generations, the compressor T-S efficiency gradually converged and the corresponding maximum at each generation continuously increased. Regarding compressor T-S pressure ratio, since high penalty was given to the candidates that delivered T-S pressure ratio outside of the tolerance band, the compressor design requirements were achieved when the optimisation process approached the termination.

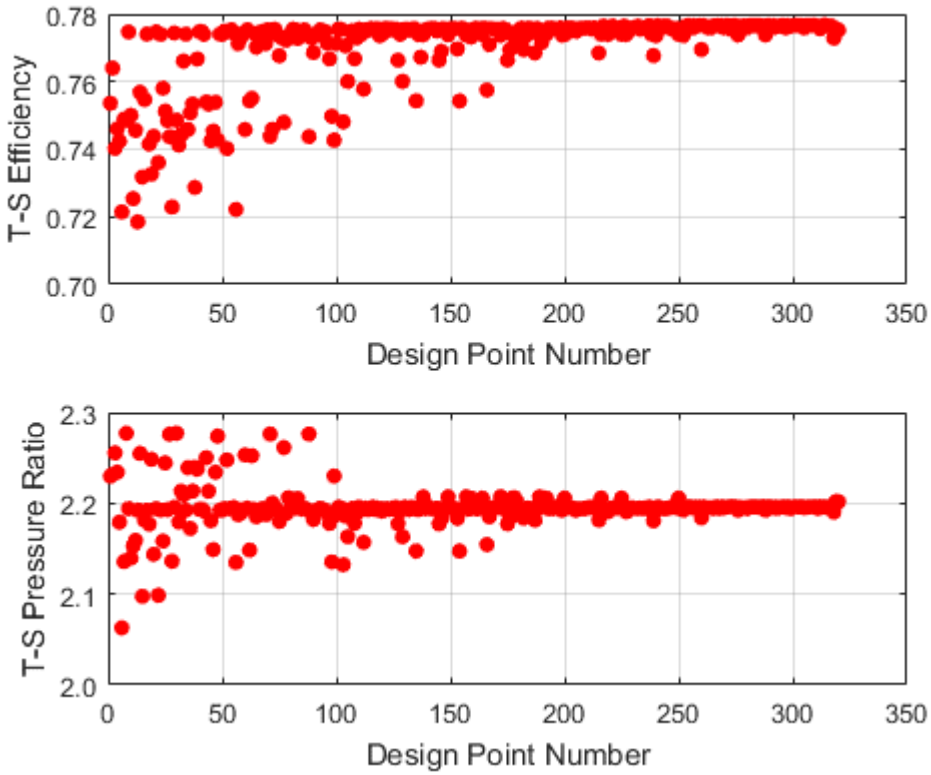

Figure 5.32 Optimisation results showing convergence of T-S efficiency and T-S pressure ratio

In this optimisation, the maximum T-S efficiency of 77.46% was expected and the corresponding blade shape was selected as the final compressor design. In other words, the compressor blade optimisation delivered 3.20 percentage points of T-S efficiency improvement, comparing to the preliminary compressor design. At design operating points, T-S pressure ratio delivered by the final compressor design is 2.20. Figure 5.33 shows the geometry comparison between the preliminary and the final compressor – (a) blade-to-blade view near hub (20% span) and (b) blade 3D geometry comparison. During compressor blade optimisation process, the hub and shroud curve are kept unchanged. Thus, the flow passage of the final compressor design is same as that of the preliminary design. It can be clearly seen in Figure 5.33 (a) that the backsweep angle near hub of the final compressor design is larger than the preliminary. To be specific, due to the compressor blade optimisation, the backsweep angle at the hub increase from 25.25 to 31.34 degree, shown in Table 5.6.

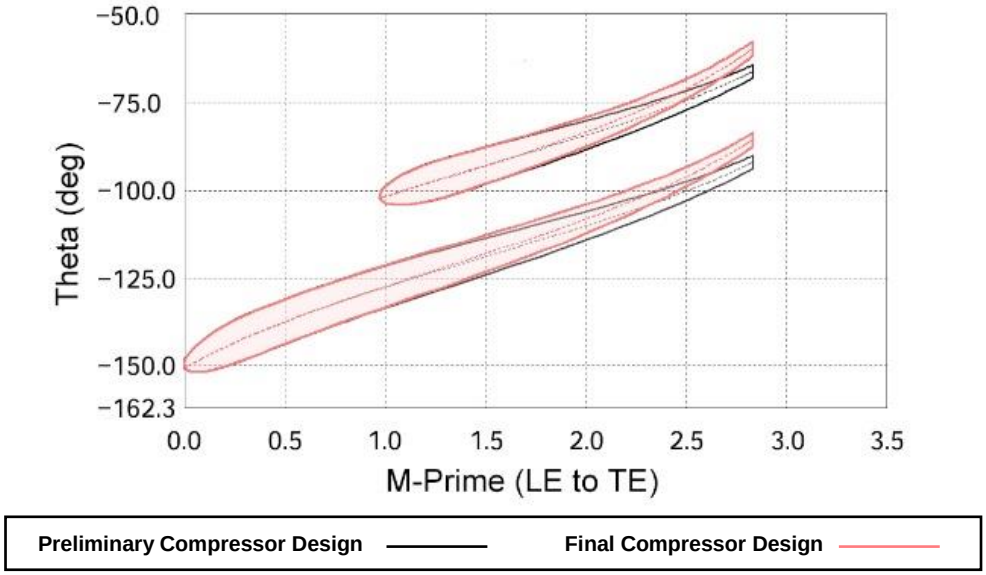

(a)

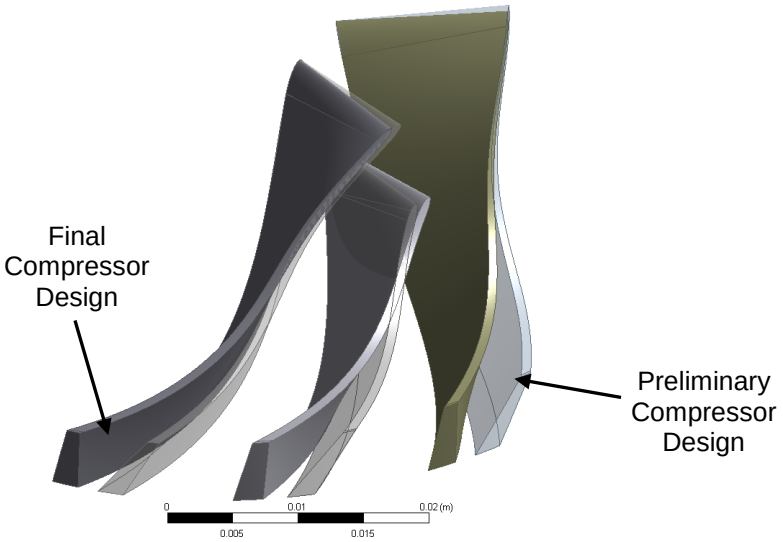

(b)

Figure 5.33 Geometry comparison between the final compressor design and the preliminary compressor design

The primary geometric information of all alternative designs is listed in Table 5.6. It should be noted that since the second optimisation run is to only optimise the impeller geometry. Thus, the compressor rotor and volute geometry maintain unchanged during the optimisation process.

Table 5.6 Primary geometric information of all alternative design

Geometric Parameters	Final Design	Preliminary Design	Trimmed Compressor
Rotational Speed (rpm)	112900	112900	125000
Backsweep Angle at Shroud (deg)	52.72	39.83	34.00
Backsweep Angle at Hub (deg)	31.34	25.25	27.78
A/R Ratio	9.27	9.27	6.50
Diffuser Diameter (mm)	114	114	130
T-T Efficiency	79.13%	75.83%	73.23%
T-S Efficiency	77.67%	74.47%	72.32%
T-S Pressure Ratio	2.20	2.26	2.24
Mass Flow Rate (kg/s)	0.055	0.055	0.055
Hub Diameter (mm)	12.70	12.70	14.47
Inducer Height (mm)	13.57	13.57	11.41
Inducer Diameter	39.75	39.75	37.29
Exducer Height (mm)	5.20	5.20	3.75
Exducer Diameter (mm)	66.94	66.94	65.00
Axial Length (mm)	21.79	21.79	25.11

5.6.2.3 Entropy Generation Analysis of Compressor Designs

In previous sections, preliminary and final optimised compressor designs are presented with the optimisation procedures. The 3D simulations show that the both in-house compressor designs have higher efficiency than that of the trimmed commercial compressor presented in Section 5.5.1. Thus, in this section, a loss examination based on the entropy generation analysis is performed to give traces of the reasons for performance improvement.

First, entropy production over inlet pipe, impeller, diffuser, and volute is evaluated for three compressor designs – trimmed commercial design, preliminary compressor design, and final optimal design. Figure 5.34 shows the breakdown of entropy production of each compressor design. The trimmed commercial compressor is selected as the baseline. Thus, all data is normalised to the total entropy production of the trimmed commercial compressor for the sake of clarity.

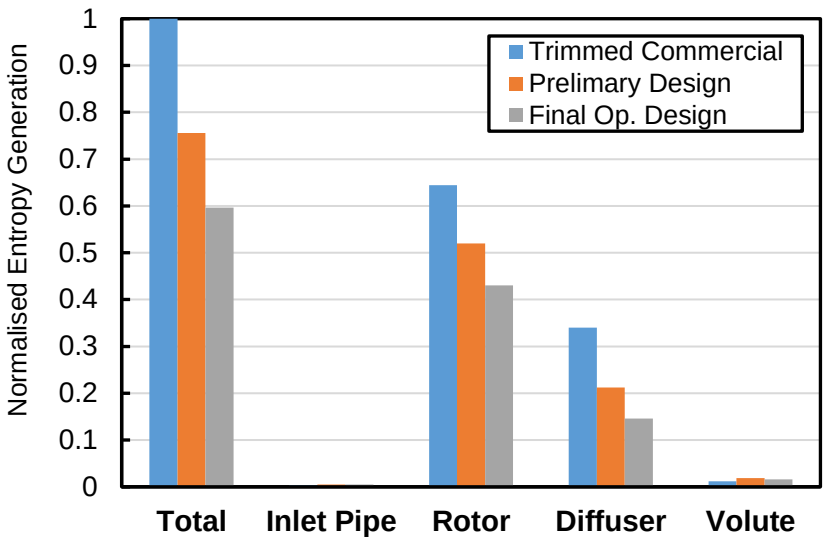

Figure 5.34 Breakdown of entropy generation at each section of compressor

It should be noted that the entropy production over the inlet pipe for all three design are too tiny to be spotted in Figure 5.34. In other words, at the design conditions, the energy loss in the inlet pipe is negligible for all three candidates. Similarly, all candidates achieve relatively low irreversibility across the volute, while the majority of the energy loss is found across the impeller and diffuser. The final optimal design reduces approximately 40% of total entropy production of the baseline, which approximately 21 and 19 percentage points of the reduction are contributed by the optimised impeller and diffuser, respectively. Since final optimal compressor design is generated based on the preliminary design by optimising the compressor blades, it can be stated that 9 percentage points reduction of the entropy generation is achieved by the blade optimisation, shown in Figure 5.34. It should be noted that although the diffusers of both preliminary and final designs are identical, the entropy generation difference of around 7 percentage points are found across the volute. This is because that optimising the compressor blade leads to the change of the flow field at the rotor outlet, which consequently causes the reduction of energy loss in the downstream diffuser. Indeed, this phenomenon is expected, as the target of the blade optimisation is to improve the overall efficiency of the compressor, that is, minimising the irreversibility at all sections of the compressor is achieved by optimising the blade geometry.

To facilitate the understanding of loss mechanisms on the local level, Tüchler [133] proposed to use the concept of the local entropy generation rate. It decomposes losses into contributions through dissipation and heat transfer. It can be further differentiated in a mean-time and a fluctuating term, expressed as follows:

$$\dot{S}_{PROD} = \dot{S}_{PROD,\overline{D}} + \dot{S}_{PROD,D'} + \dot{S}_{PROD,\overline{C}} + \dot{S}_{I,C'} \tag{5.11}$$

Table 5.7 Comparison of blade-to-blade view of Mach number and normalized local entropy generation rate near the shroud (80% span) and midspan (50% span)

	50% Span		80% Span	
	Normalized Local Entropy Generation Rate 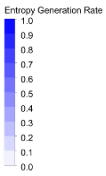	Mach Number 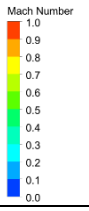	Normalized Local Entropy Generation Rate 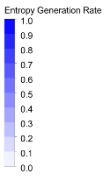	Mach Number 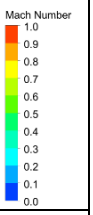
Trimmed Commercial Design	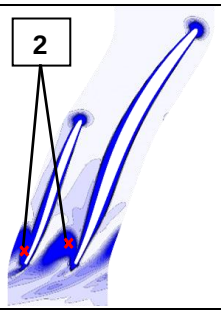	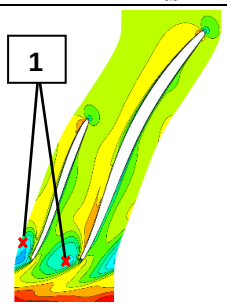	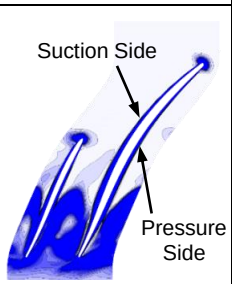	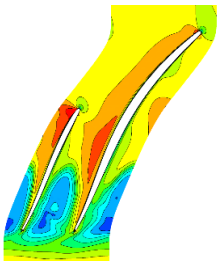
Preliminary Design	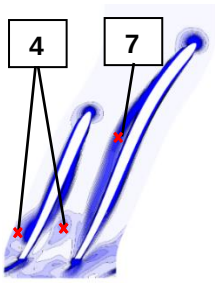	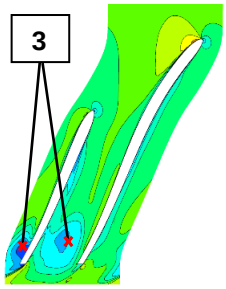	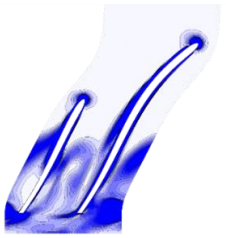	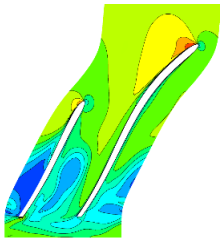
Final Optimal Design	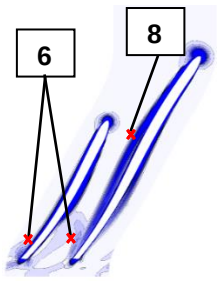	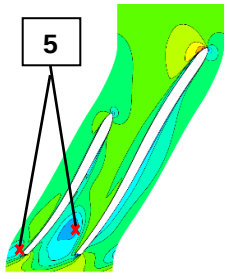	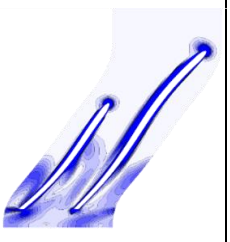	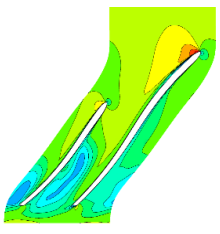

Table 5.7 shows that Mach number and local entropy generation rate are evaluated at the blade-to-blade planes near the shroud (80% span) and midspan (50% span). This evaluation is conducted at all three compressor designs in order to demonstrate the reasons of performance gains of in-house compressor designs. The local entropy generation rate is normalized to the maximum entropy generation rate at the trimmed commercial compressor.

At midspan of blade-to-blade plane, the flow field in the trimmed commercial compressor reveals separation bubbles near the trailing edge of both main blade and splitter (marked 1 in Table 5.7). These separation bubbles are characterised by subtle low flow velocity, called stall cells. Looking at the corresponding entropy generation, it can be found that there is a pronounced entropy generation at the region between the stall cells and the flow encircling it (marked 2 in Table 5.7). However, although even bigger stall cells are found at similar region for the prelimary design (mark 3) and final design (mark 5), the corresponding entropy generation is lower (mark 4 and 6 for the prelimary and final designs, respectively). This is because that for both in-house designs the velocity of the flow encircling the stall cells is lower than that of the trimmed commercial compressor. It should be noted that, for all designs, afore-mentioned stall cells are enlarged near the shroud (80% span) and build up back to the flow passage. Consequently, the larger entropy generation is found at the edge of these stall cells. However, the trimmed commercial design still suffers the highest loss than in-house designs. In addition, the entropy generation comparison between the preliminary and final design shows that the blade optimisation does lower the irreversibility occurring near the trailing edge and, therefore, improve the compressor performance.

In Table 5.7, the evaluation of the local entropy generation shows that larger region of high entropy generation near the blade surface is found at both suction and pressure sides of the main blade and splitter for in-house designs. Even though, the blade optimisation can contribute to the reduction of high entropy generation at both midspan and near the shroud, especially when the marked region 7 is compared with the marked region 8, it still means that the further blade optimisation of the final optimal design should be performed to enhance the compressor performance at the design conditions.

5.7 Conclusion

In order to achieve high turbomachinery performance, the selected commercial compressor and turbine are required to be re-sized by trimming impellers. The performance of various trimmed compressors and turbines were estimated by 3D modelling in ANSYS CFX. Then, the turbomachinery designs with the highest T-S efficiencies were selected to apply in IBC prototype.

By reviewing 3D modelling methodology of turbomachinery, the proper settings were applied to the compressor and turbine models. To be specific, the detailed description of the compressor and turbine impeller geometry was obtained from the project partner and the corresponding flow domains were generated in a commercial package of ANSYS, referred as the BladeGen code. All boundary conditions were imposed in accordance with the IBC design conditions. Since the computational grid size and type significantly affect the numerical solution for the given 3D simulation problem, meshing sensitivity studies for both the compressor and turbine were performed to achieve mesh-independent numerical solutions. By doing so, the mesh number of 0.8E+6 was chosen for the compressor rotor meshing target, while 1.1E+7 was for the turbine rotor.

Regarding the compressor impeller trimming optimisation, the selected design variables were volute A/R ratio, diffuser diameter, inducer height, and exducer height. Due to the limited time, only three volute design were proposed, which were generated based upon the selected volute A/R ratio and diffuser diameter. Since the pressure was imposed at inlet and outlet boundaries of all compressor simulations, the inducer height has to be varied to deliver the design mass flow rate for given exducer height. By completing the Design of Experiments (DoE) study of the proposed design variables, the optimal compressor design was selected for the IBC prototype and the corresponding T-S efficiency was 72.32%.

On the other hand, the multiple heights of turbine exducer should be investigated to achieve the optimal design. However, only one turbine rotor was investigated in this research. This is because that there is no enough time to investigate various blade trimming. In addition, the 3D simulation results show that this rotor

is able to deliver decent T-T efficiency at the design point. Thus, only A/R ratio of the turbine volute was optimised. Based on the optimisation results, the rotor with the exducer height of 16.1 mm and the volute with the A/R ratio of 15.5 mm are selected for the final turbine design.

Finally, a compressor in-house design and optimisation process was created in parallel to the test of the IBC prototype. Although the final in-house design will not be manufactured due to the limited budget, the presented compressor design and optimisation process can be used to design IBC compressor in the further. In addition, this procedure also can be utilized to design and optimise the IBC turbine. The compressor preliminary design was generated by VISTA CCD with some initial guesses, and optimised by using GA optimisation method. As a result, the T-S efficiency of the optimal preliminary design was 74.47%, which is 2.15 percentage points higher than that of the trimmed commercial compressor. Later, the impeller optimisation was performed to further improve the performance of the preliminary design. Four impeller parameters were selected as the design variables, referred as 1) main blade inlet angle at shroud, 2) splitter inlet angle at shroud, 3) backsweep angle at shroud and 4) stack position for both main blade and splitter. The optimisation results show that the high-performance compressor design was achieved. Its T-S efficiency was 5.35 percentage points higher than that of the trimmed commercial compressor.

Chapter 6 – Experimental Procedure and Results

6.1 Introduction

All tests throughout this study will be conducted on a steady-state turbocharger facility, also known as the gas stand, developed within Powertrain & Vehicle Research Centre in University of Bath. This gas stand is designed and developed for generating characteristic maps of radial turbochargers. In order to complete the proposed tests in this study, this gas stand will be re-configured and installed more instrumentations. The design target engine for IBC system is a 2-litre turbocharged gasoline engine. The design operating condition is the motorway cruise condition. This corresponds to the exhaust flow rate of 0.055 kg/s at temperature of 750°C, which will be imposed as the inlet condition of the IBC system in tests. However, test parameter sweeps for IBC inlet temperature, inlet pressure, coolant temperature and IBC shaft speed will be conducted to investigate IBC systemic performance at off-design condition.

Both the turbine and compressor tested in the study are trimmed versions of the commercial turbocharger which were designed and optimised in Chapter 5. The other key component – air-to-liquid heat exchanger is provided by the project partner. In order to maximize the cooling capacity and minimize the pressure drop, novel flow paths are designed by CFD analysis and manufactured by additive

manufacturing techniques. The heat exchanger design process will be not presented in this research.

It should be noted that the contents in Section 6.3 have been published as a journal paper [134] in Journal of Engineering for Gas Turbines and Power.

6.2 Test Facility

In a general summary, the basic gas stand consists of three main modules that can be distinguished within the facility: turbine module, compressor module, and lubrication module, shown in Figure 6.1. The detailed schematic diagram of test facility is demonstrated in Figure 6.2.

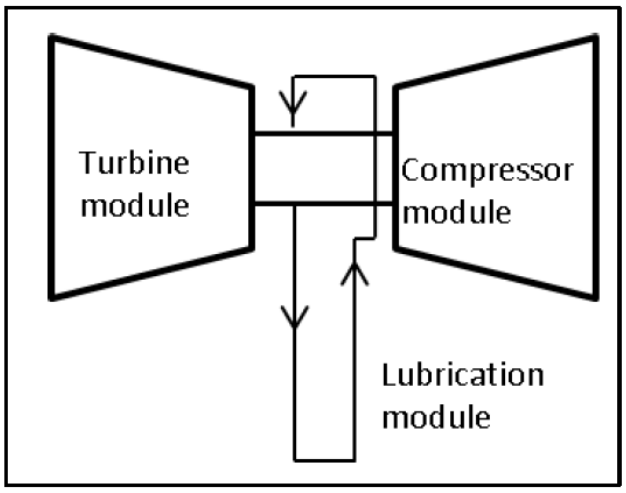

Figure 6.1 General turbocharger module arrangement

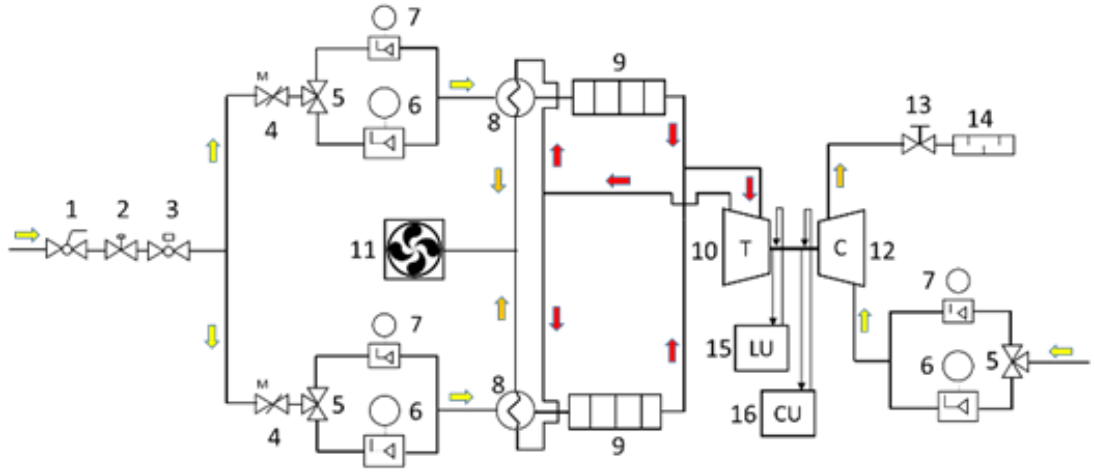

Number	Turbocharger gas stand equipment
1	Manual ball type shut off valve
2	SMC pneumatic pressure regulator
3	Ball type valve with Kinetrol electro-pneumatic positioner
4	Sierra CP motorized butterfly valve
5	Fiesto 3-way ball type valve
6	3" McCrometer V-cone mass flow meter with Siemens DSIII differential pressure transmitter
7	2" McCrometer V-cone mass flow meter with Siemens DSIII differential pressure transmitter
8	Bowman gas-to-gas heat exchanger
9	Axes Design variable power electric heater
10	Turbocharger turbine
11	Electrically controlled roof extraction fan
12	Turbocharger compressor
13	Motorized backpressure valve
14	In-line type performance silencer
15	Turbocharger lubrication unit c/w variable speed pump, electric heater, gas-to-water heat exchanger, pressure & temperature sensors
16	Turbocharger bearing housing cooling unit c/w electric heater, water-to-water heat exchanger, temperature sensors

Figure 6.2 Schematic diagram of gas stand facility

6.2.1 Basic Turbine Module

The turbine module consists of an air supply, heating system, turbine mounting bracket, and gas discharging system, shown in Figure 6.3.

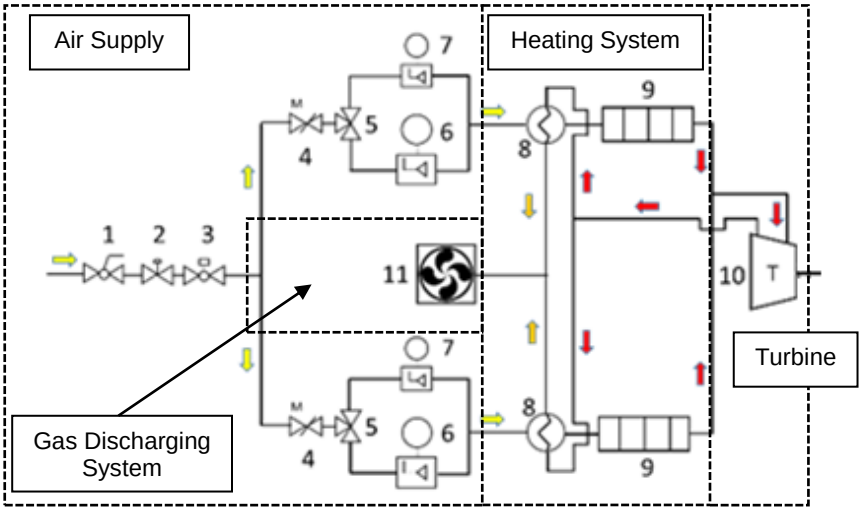

Figure 6.3 Turbine module

The pressurized air of up to 7 bar is supplied externally from the test facility by two industrial rotary type compressors, referred as Ingersoll Rand model R110N A10.0. The moisture is removed via HHDp 1800 Hankison refrigerated compressed air drier. Since the air need to be cooled to a very low temperature in the air dehumidification process, the air arriving at the test facility is dry and cold (~ 15°C). The mass flow rate and the corresponding pressure are mainly controlled by the actuated ball valve – component 3. The downstream systems are parallel pipes with motorized butterfly valves installed respectively. There are two reasons for such parallel arrangement. First, it reduces the heating burden of the downstream electric heaters. At given mass flow rate, the heated air temperature is limited due to the maximum heating capability of the electric heater. Splitting the air allows two separate electric heaters to heat the air up to the required temperature. Second, it provides two independent flows and, therefore, enables that twin-entry turbine can be tested in this facility. As can be seen in Figure 6.3, each of the parallel supply air branches include 2 differently sized differential pressure V-cone mass flow meters - component 6 and 7. By doing so, the precision of the mass air flow measurements can be increased, as the smaller V-cone is recommended to measure flows in a range between 0.015 kg/s and 0.15 kg/s while the larger one from 0.04 kg/s to 0.4 kg/s. Thus, the pressured air is directed by the 3-way valve to the small V-cone when the mass flow rate is low, while directed to the bigger one at high mass flow rate. Downstream of flow

sensors, the air is fed into the recuperator where it is heated up by the exhaust gas discharging from the tested system. Each recuperator is capable of re-using a significant amount of energy from the exhaust flow. This is not only designed to save energy, but further relieve the heating burden of the electric heaters. One of the electric heaters is designed and manufactured by Axis Design which can deliver up to 88 kW thermal power, whereas the second one by OSRAM Sylvania up to 96 kW. Note that the maximum temperature of the air at the inlet of electric heaters is 350°C. This is because that all electric connections are located in the upper part of the heaters. Thus, a temperature sensor is installed upstream of each electric heater to monitor the air temperature. If the corresponding temperature reaches the maximum tolerable temperature of 350°C, a bypass circuit is engaged to mix the exhaust flow with the cold fresh air withdrawn upstream from the main motorised mass flow control valve, to reduce temperature of the air fed into the hot side of the recuperator.

Electrically controlled roof extraction fan is employed to discharge the exhaust gas from the test cell. By doing so, it keeps the room temperature unaffected by the exhaust gas.

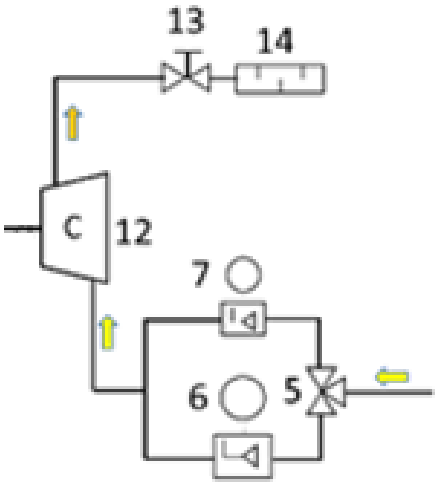

Figure 6.4 Compressor module

6.2.2 Basic Compressor Module

The basic compressor module is relatively simple, as typically compressor inlet condition in tests is ambient temperature and pressure. Furthermore, there is motorised gate valve downstream of the compressor outlet to restrict the working fluid, thereby controlling the mass flow rate and generating the backpressure. The standard arrangement of the compressor module is shown in Figure 6.4.

Similar to basic turbine module, there are two mass flow sensors, component 6 and 7, mounted upstream of the compressor inlet, which is able to achieve high measurement precision within a wide mass flow range. To reduce the noise generated during the compressor operation, an inline racing silencer, component 14, is installed at the outlet of the compressor module.

6.2.3 Lubrication Module

The lubrication module is designed to lubricate the turbocharger bearings as well as absorbing heat. The lubricating oil is conditioned by Regloplas 300s unit. It is equipped with variable speed magnetic drive pump to vary the mass flow rate and temperature of the lubricating oil. In tests, the oil temperature is controlled to remain at 90°C.

6.2.4 Test Facility Modifications

Since the basic gas stand is designed to test turbochargers, necessary modifications must be made in order to test IBC system. A CAD screenshot of the modified test configuration is shown in Figure 6.5.

The air supply and heating system of the basic gas stand remain unchanged. As a result, the working fluid of the IBC system in tests was the air rather than the exhaust gas discharging from the turbocharged IC engine. In other words, the discrepancy of the gas properties between the fresh air and the engine exhaust gas was neglected in the test. The inlet temperature and pressure of the IBC system were controlled by electric heaters and the actuated valves, respectively.

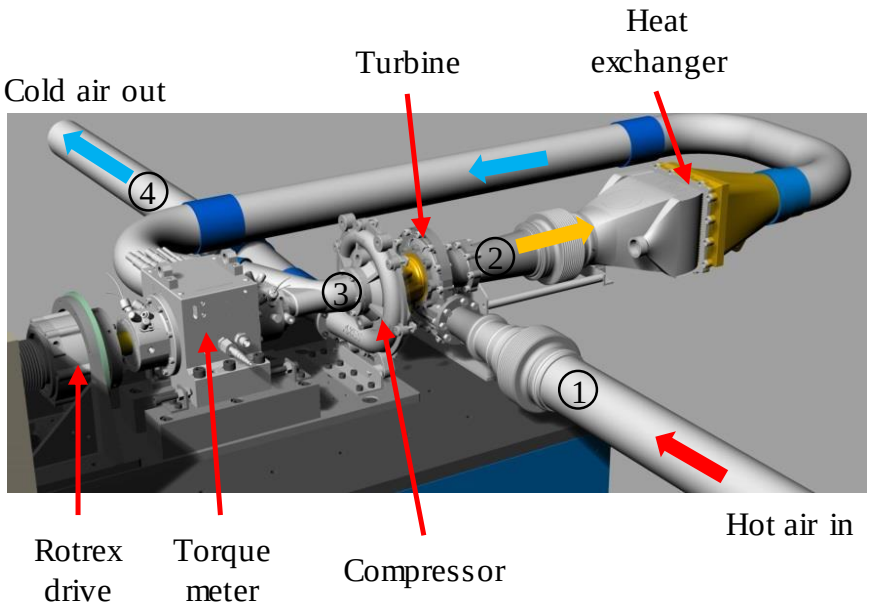

Figure 6.5 3D review of test configuration

After the expansion in the IBC turbine, the discharged air is cooled using the 3D printed Inconel heat exchanger provided by the project partner, shown in Figure 6.6. The chilled water is supplied from a cooling system as the coolant. The novel flow paths in the heat exchanger contribute to the very high performance of approximately 97% effectiveness with a pressure drop of 1.5 kPa at the gas flow rate of 0.05 kg/s. Although the prototype of the heat exchanger tested in this study was cubic, shown in Figure 6.6, its shape could be very flexible in order to fit into the modern vehicles thanks to the selected manufacturing technique of the Selective Laser Melting Additive Manufacturing (AM). In addition, the design freedom with AM also enables the use of highly efficient heat transfer surfaces that offer a better trade-off between pressure drop and effectiveness. Since afore-mentioned parameters of the heat exchanger significantly influence the inlet condition of the IBC compressor, and therefore compressor work as well as IBC power output, the heat exchanger is key to the success of the IBC system.

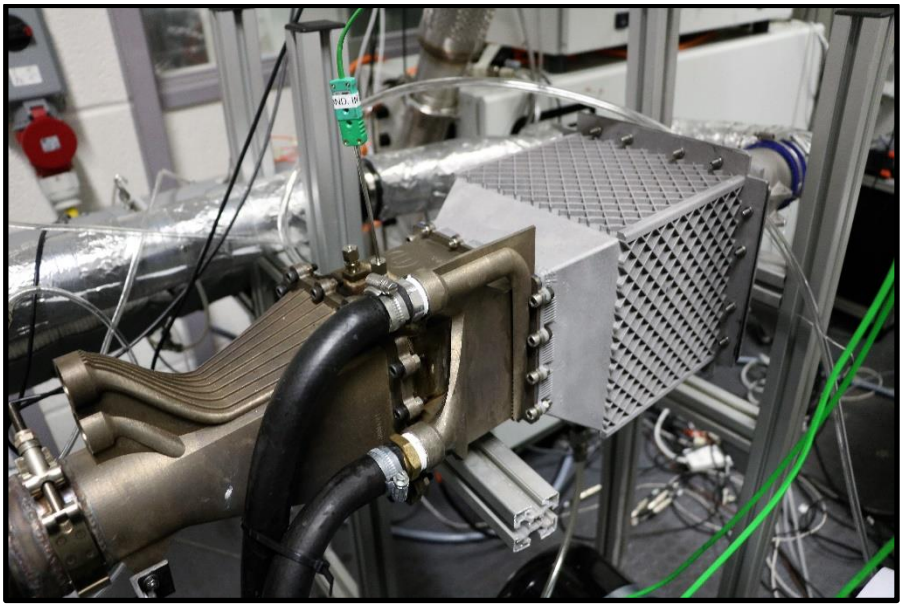

Figure 6.6 Selectively laser melted, high performance heat exchanger

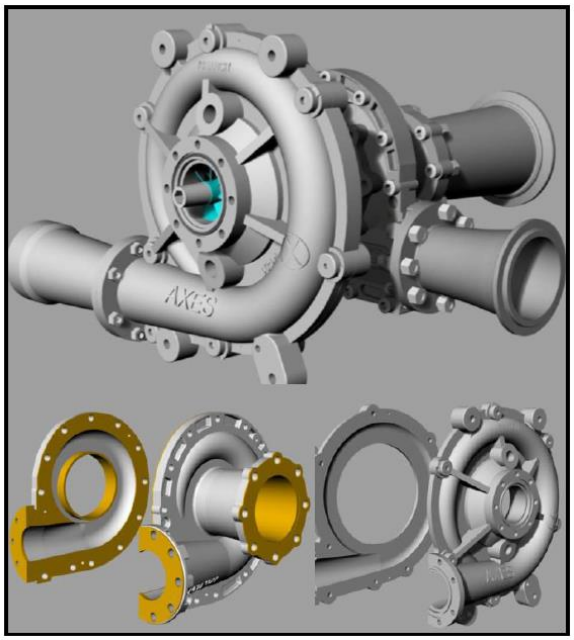

Figure 6.7 Turbomachinery housing for IBC compressor and turbine

In the proposed test, the compressor inlet is connected to the heat exchanger outlet, instead of the ambient in the normal turbocharger test. Thus, the exhaust gas from the compressor was discharged directly outside the test cell by the gas discharging system, instead of feeding into the recuperators. This is because that the air temperature at the IBC compressor outlet could be as low as around 45°C

and, therefore, it is not worthwhile to recycle the thermal energy in the exhaust gas through the recuperators. Regarding the IBC turbomachinery housing, its configuration is same as that of the normal turbocharger, shown in Figure 6.7.

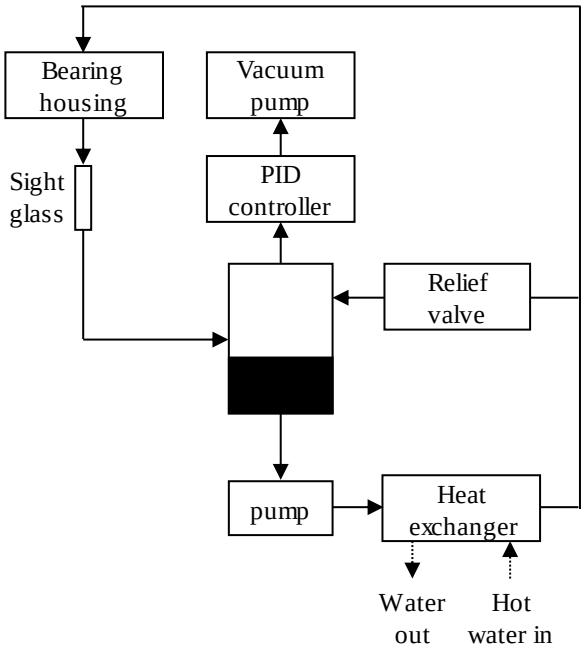

Figure 6.8 Modified lubrication system

In order to control the IBC shaft speed, a Rotrex drive dynamometer is mechanically connected to it, shown in Figure 6.5. In other words, the shaft power can be extracted from or supplied to the IBC shaft by this dynamometer. A high-speed torque meter is also attached to the IBC shaft to precisely measure the torque and speed. Thus, the measured power is the net power generated by IBC system, as the shaft friction loss has been considered by the direct measurement method. Note that energy conversion loss should be considered in the commercial IBC system, as typically shaft torque generated by the IBC system is unable to exploit directly by the vehicle system due to its high rotating speed. Thus, for the commercial IBC products, an electric generator is proposed to convert the mechanical into electric energy which could be easily stored and utilized by vehicle system. However, in the test, no energy conversion loss was considered.

Since the system between the turbine outlet and compressor inlet operates under vacuum, the lubrication system must be able to operate under vacuum to avoid

oil being sucking into the system during operation. In order to depressurize the lubrication loop, a vacuum pump is introduced, shown in Figure 6.8. The vacuum pressure is controlled by a PID controller to automatically track a pressure just below the compressor inlet pressure. The lubricating oil is heated using hot water to give the required viscosity. A sight glass is installed to monitor the oil exiting the bearing housing to ensure there is no excessive aeration. It was proved that this system was very successful to limit oil ingestion in the test.

The entire test facility for IBC system is shown in Figure 6.9.

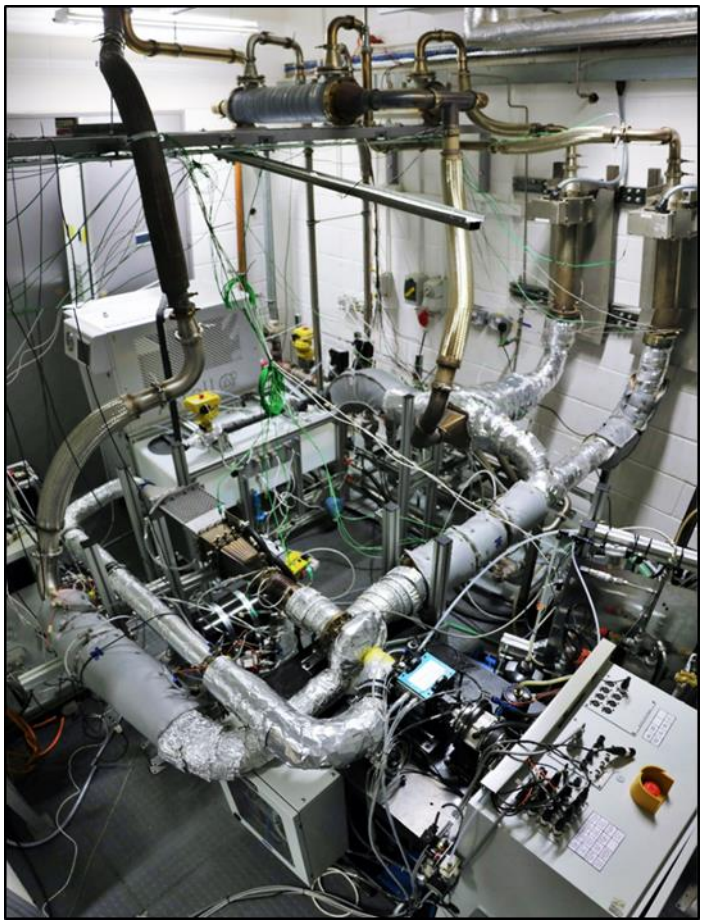

Figure 6.9 IBC with high speed dynamometer installed in hot gas stand

6.2.5 Instrumentation

Generally, the pressure transducers are considered as a cost-effective instrumentation to acquire pneumatically averaged pressures. Thus, in tests, the pressure transducers were carefully selected based upon the operative ranges

and the locations. The pneumatically averaged pressures are achieved by installing a ring connected with 4 tapings, shown in Figure 6.10. The taping is perpendicular to the tube wall whereas angle between each taping is fixed at 90 deg. In addition, all transducers were calibrated using a DPI-510 pressure calibrator before each test setup. In the IBC system, inlets and outlets of both compressor and turbine are the key location where the pressure transducers must be installed.

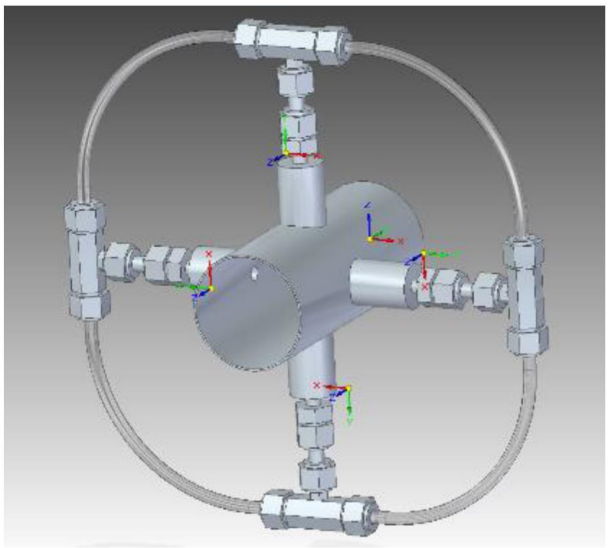

Figure 6.10 Ring for pneumatically averaged static pressure measurement

Regarding temperature measurements, turbine inlet temperature is measured by averaging four K type thermocouples and the outlet temperature using a single K type. The main reasons for theirs use are the wide operative range from -200 to 1250°C and the robustness of reading. Compressor inlet and outlet temperatures are measured by averaging four class A PRTs. The configuration of four temperature sensors is similar to that of pressure transducers. However, instead of building a ring outside the pipe, the temperature sensors are inserted perpendicularly to the pipe walls. To be specific, the temperature sensors at 0 and 180 degrees is inserted at 1/3 of the diameter of the pipe, while 90 degrees ones is at 1/2 diameter and 270 one is at 1/4 diameter. Such configuration is recommended by SAE J1723 [135]. The temperature reading is a value between the static and total temperature. ASME PTC 10 [136] reckon that if the air velocity

is below 38 m/s, the velocity temperature is negligible. Since the velocities measured were all below this value, the measured temperatures were taken to be total temperature. Note that the temperature readings were checked for credibility before each test. Faulty or disconnected thermocouples would exhibit a constant maximum value or unstable random reading.

Table 6.1 Instrumentation details

Parameter	Sensor type	Sensor Accuracy
torque	Phase shift meter	± 0.0011 Nm
rotational speed	Phase shift meter	± 0.05%
turbine inlet pressure	Pressure transducer	± 250 Pa
turbine inlet temperature	4 x K type thermocouple	± 2.5°C or ± 0.75%*T
turbine outlet pressure	Pressure transducer	± 500 Pa
turbine outlet temperature	K type thermocouple	± 2.5°C or ± 0.75%*T
compressor inlet pressure	Pressure transducer	± 80 Pa
compressor inlet temperature	Class A PRT	± (0.15 + 0.002∗T)
compressor outlet pressure	Pressure transducer	± 500 Pa
compressor outlet temperature	Class A PRT	± (0.15 + 0.002∗T)
mass flow rate	Calibrated V-cone	± 0.5%
V-cone pressure drop	Pressure transducer	± 16 Pa
V-cone upstream pressure	Pressure transducer	± 280 Pa
V-cone upstream temperature	Class A PRT	± (0.15 + 0.002∗T)

All pipework was insulated to eliminate the influence of the heat dissipation through turbocharger housing and pipes on the temperature measurements error. Although there may be no insulation in the commercial IBC products due to the corresponding cost, the insulation is necessary in tests. This is because that the pipes in test is deliberately designed to be longer than that in the commercial products in order to install various sensors. Thus, without any insulation, the heat

dissipation in tests could be much higher, thereby significantly diverting the test results from the practical use.

The air mass flow rate is measured upstream of the heaters using V-Cone flow meters, highlighted as component 6 and 7 in turbine module (Figure 6.3). The IBC shaft torque and speed are measured with a phase shift type torque meter.

Details of the instrumentation are listed in Table 6.1.

6.2.6 Performance Analysis

In the test, compressor and turbine efficiencies cannot be measured directly. Thus, following assumptions and formulas were used to calculate them.

A semi-perfect gas is assumed, that is, the specific heat c_p at constant pressure is assumed to be a function of temperature only. The compressor efficiency and work are calculated first, as the measurements related to compressor are reliable. Then, the turbine work and efficiency are calculated based on the compressor performance analysis. In the following formulas, subscripts 1 refers to the turbine inlet, 2 to turbine out, 3 to compressor inlet and 4 to compressor outlet. Since the reading of the pressure transducers is the static pressure, the following function is used to calculate the total pressure at the compressor inlet.

$$p_{3t} = p_{3s} * \left[\frac{T_{3t}}{T_{3s}}\right]^{\left(\frac{C_{p_3}}{R}\right)} \tag{6.1}$$

where subscripts t refers to total while s to static. R = 0.281 kJ/(kg K) is the gas constant of the working fluid.

C_p is the specific heat at constant pressure which is determined from the ratio of specific heat γ,

$$C_p = \frac{\gamma R}{\gamma - 1} \tag{6.2}$$

where γ for air is equals to $1.42592 - 8.03974(10^{-5})T$.[137]

The compressor total-to-static (T-S) pressure ratio $PR_{c_{TS}}$ is given by

$$PR_{c_{TS}} = \frac{p_{4s}}{p_{3t}} \tag{6.3}$$

Thus, the compressor T-S isentropic efficiency

$$\eta_{c_{TS}} = \frac{\left(PR_{c_{TS}}\right)^{\frac{\gamma-1}{\gamma}} - 1}{\frac{T_{4t}}{T_{3t}} - 1} \tag{6.4}$$

The compressor work w_c is calculated using

$$w_c = \frac{c_{p_3} + c_{p_4}}{2}(T_{4t} - T_{3t}) \tag{6.5}$$

Given the difficulty in accurately measuring the temperature of the flow at the turbine exit, the turbine efficiency and work cannot be calculated by turbine outlet measured temperature. The typical approach in turbocharger testing is to assume that the turbine work is equal to the compressor work times a factor to account for mechanical losses. However, in IBC tests, the shaft power was directly measured by the torque meter, which the shaft mechanical loss has been considered. Thus, the turbine work w_t is assumed as

$$w_t = w_c + w_o \tag{6.6}$$

where w_o is the measured torque.

The turbine total-to-total (T-T) pressure ratio is

$$PR_{t_{TT}} = \frac{p_{1t}}{p_{2t}} \tag{6.7}$$

Thus, the turbine T-T isentropic efficiency, $\eta_{t_{TT}}$ is given by

$$\eta_{t_{TT}} = \frac{w_t}{c_p T_{1t}\left(1 - \left(\frac{1}{PR_{t_{TT}}}\right)^{\frac{\gamma-1}{\gamma}}\right)} \tag{6.8}$$

6.3 Test Results and Discussion

For the results analysis below, specific work was introduced to represent the IBC performance, as the mass flow rate varied in a wide range at all test conditions. Thus, in order to eliminate the influence of mass flow rate discrepancy, the measured shaft power was divided by the corresponding mass flow rate to conduct the specific work. In addition, the work required to pump the coolant for the heat exchanger is not subtracted from the net power, as it is negligible.

The design operating speed is 125,000 rpm. However, due to the rotordynamic issues, the speed was limited to approximately 80,000 rpm. Nonetheless, the test results were still valuable, as this is the first experiment test to demonstrate the performance of the IBC system for the automotive use. In addition, the test results could be utilized to correlate 1D GT-power model, thereby increasing the simulation fidelity.

In conclusion, the baseline conditions of 70,000 rpm, 550°C IBC inlet temperature, and 10°C coolant temperature were chosen. Test boundary conditions sweeps were conducted for IBC inlet temperature, inlet pressure, coolant temperature and IBC shaft speed.

6.3.1 Test Limitations

There are two main limitations in all tests conducted in this study.

The first limitation is the method used to calculate the turbine work and efficiency. As discussed above, turbine outlet temperature cannot be used to calculate the turbine work and efficiency due to its low-accuracy measurement. Thus, turbine work was defined as the differential between the measured shaft torque and the measurement-based calculated compressor work. In other words, the turbine work presented in tests was equal to the actual turbine work minus the bearing losses. By doing so, the turbine performance is underestimated, especially when the rotational speed is high and, therefore, the bearing loss is relatively large. Thus, calculated turbine work and efficiency are lower than the actual values.

Note that thermodynamically calculated compressor performance is unaffected by the bearing loss.

The second one is related to the heat transfer. It is generally agreed that the turbocharger cannot be considered adiabatic and the heat transfer results in inaccurate measurements of turbocharger flow properties, thereby causing errors in the corresponding performance analysis. In the test, heat is transferred due to convection from the hot turbine gas to the housing. Then, it can be lost to atmosphere, lubricating oil, and cooling water. In addition, all afore-mentioned four sinks can be the intermedia to transmit heat finally to the compressor gas. Thus, the heat transfer in the test affects the performance evaluation of both compressor and turbine, due to the resulting changes of their inlet and outlet temperature. Despite of the insulation applied in the IBC prototype, heat transfer cannot be completely prevented and still can transmit from the turbine gas to compressor gas.

In terms of IBC tests conducted in this study, the net power generated by IBC system was directly measured and, therefore, unaffected by the heat transfer. The following analysis only considers the effect on the calculated compressor and turbine performance.

Starting with compressor, it can be seen in Figure 6.5 that the compressor inlet is far away from any heat resource. Thus, only heat transfer is the heat loss through pipe walls between the measurement location and the compressor inlet. It means that the reading of the temperature sensor T_{3t} is higher than the actual temperature at the compressor inlet. This results in the underestimated compressor work (Eq. 6.5) and overestimated compressor efficiency (Eq. 6.4). Note that in IBC system tests, the compressor inlet temperature was up 40°C due to the high-performance heat exchanger and low coolant temperature. Thus, with the insulation, the heat loss through pipes is negligible at compressor inlet. At the compressor outlet, the heat transfer to the compressor gas from housing tends to increase T_{4t}. However, the heat loss to ambient occurring between the compressor outlet and the measurement location gives rise to the lower T_{4t} measurements. Overall, T_{4t} could be either overestimated or underestimated.

Regarding to the turbine, in Eq. 6.6 the error in compressor work leads to an error in turbine work in the same direction at the given IBC work output. However, due to the heat transfer, T_{1t} is overestimated. Errors in both T_{1t} and the turbine work then lead to an error in the turbine efficiency.

Since all test speeds, only up to 80,000 rpm, are quite low, the effect of heat transfer on T_{4t} is the main contributor to errors in the turbocharger performance analysis. This is mainly because that at low speeds, both the compressor power and the corresponding temperature rise are small. It means that any heat transfer will give rise to a large relative error in T_{4t}. Although heat transfer to the atmosphere will be reduced due to the lower exit temperature, it could still be a very significant as a fraction of the compressor temperature rise. Moreover, at low shaft speed, the lower gas temperature in the compressor also leads to an increased temperature gradient from the turbine gas to the compressor gas, which tends to give more heat transfer to the compressor gas. Another factor is that the gas velocity will be lower at the lower rotational speed. This leads to higher residence time of gas inside the compressor and, therefore, more time for heat transfer.

In conclusion, heat transfer around compressor and turbine can significantly affect their performance and any analysis based on the test measurements. More importantly, it cannot be determined that the turbocharger performance is overestimated or underestimated by the performance analysis, due to the uncertainty in measurement of T_{4t}. Thus, CFD simulations were required to compare against the experimental results for the same reduced mass flow rate. The turbine and compressor efficiencies comparison are presented in Figure 6.11.

The results in Figure 6.11 show that the experimentally determined compressor efficiency is higher than the CFD predicted efficiency. Based on the preceding discussion, if the CFD is accurate, the main contributor to the overestimated performance is the temperature reduction at the compressor exit, causing by the heat transfer through pipe wall. According to Eq. 6.5 and Eq. 6.6, this leads to a lower compressor work and hence a lower turbine work at given net IBC work. In addition, turbine work will be further decreased by subtracting the bearing loss.

Therefore, the underestimated turbine work results in a pessimistic turbine efficiency.

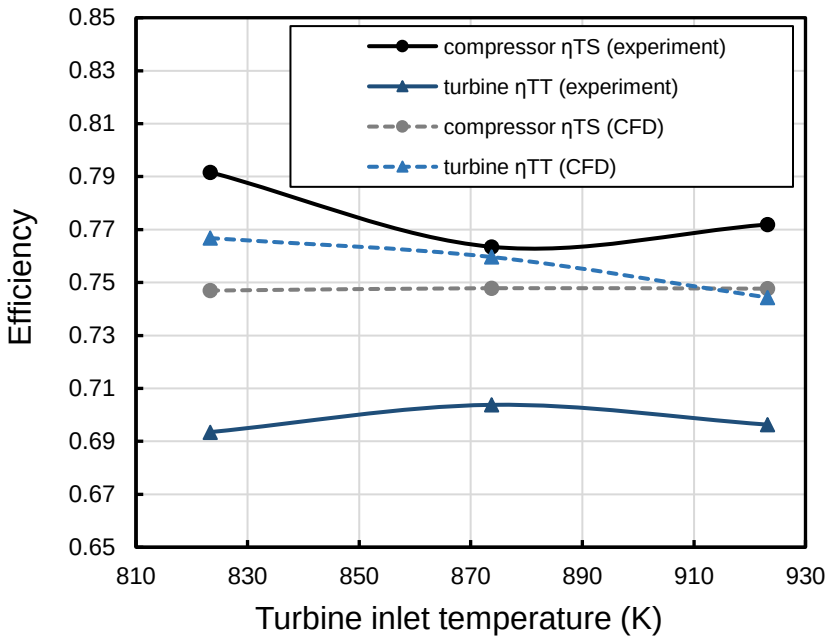

Figure 6.11 Efficiency comparison of CFD and experiment

Therefore, due to the uncertainty in the turbomachinery performance analysis, experimentally determined efficiency and work of both compressor and turbine will not be presented. Instead, CFD predicted efficiencies and work of compressor and turbine were used to present the influence of IBC boundary conditions changes. Due to the computational cost of CFD simulations, compressor and turbine 3D simulations were only performed at part of test operating points. These selected test points are enough to demonstrate the influence of the studied parameters. Whereas, all test data were utilized to correlate the 1D GT-power model, in order to achieve high-fidelity simulation results.

It is important to note that although compressor and turbine efficiencies calculated by the test data are unreliable, the IBC shaft power is known with high confidence. This is because it was measured directly by the torque meter and the only source of error is the instrumentation measurement accuracy.

6.3.2 Test Data Analysis

1D and 3D simulations presented in previous chapters show that pressure drop across the IBC system significantly affect IBC net power. However, only IBC inlet pressure was controlled in all tests, excluding the outlet pressure. Since the exhaust gas at IBC outlet is discharged directly to the ambient, it is reasonable to neglect the changes of IBC outlet pressure. Also, the test measurements show that the maximum pressure difference at IBC outlet in all tests was only up to 0.002 bar. Thus, it was assumed that the IBC outlet pressure was uncharged in all tests.

For all tests, the baseline conditions of 70,000 rpm, 550°C IBC inlet temperature, 1 bar inlet pressure, and 10°C coolant temperature were chosen. The sensitivity study for IBC inlet temperature, inlet pressure, coolant temperature and shaft speed were conducted in the test. For each parameter, a sweep was performed under the condition that the rest of studied parameters remain as same as the baseline.

Figure 6.13 shows the variation of the IBC measured specific work when the inlet pressure increases from 1 bar to 1.05 bar. Figure 6.13 (a) shows that the IBC specific work is monotonically increasing function of the inlet pressure. The 0.05 bar pressure increment at IBC inlet results in the specific work increase of 5.37 KJ/kg, which is 0.36 kW. Moreover, despite the slight increase of the turbine pressure ratio shown in Figure 6.13 (b), the net effect of raised inlet pressure is to increase the pressure downstream of the turbine and hence to reduce the compressor ratio. The pressure ratio changes are also confirmed by the 1D simulations shown in Figure 6.12. In this plot, the predicted operating points are presented against the compressor and turbine performance maps. It should be noted that since there is no mapping test data for neither compressor nor turbine, the corresponding performance maps are generated by 3D simulations. Then, the virtual performance maps of the compressor and turbine are introduced in IBC 1D models to predict their performance with imposing the test conditions at the inlet boundary. It can be clearly seen in Figure 6.12 (a) that the increasing the IBC turbine inlet pressure leads to the rise of the turbine expansion ratio, that is,

the operating conditions shifts from Point 1 to Point 3. On the contrary, sight compression ratio reduction is found in Figure 6.12 (b).

On the other hand, the CFD simulations in Figure 6.13 (c) show that the compressor efficiency reduces in few percentages with the inlet pressure rise. Overall, due to the effect of the reduction in both compressor efficiency and pressure ratio, the compressor specific work predicted by CFD simulations remains roughly same. On the other hand, the increase turbine pressure ratio leads to more turbine work, despite its efficiency drop. Therefore, raising the inlet pressure is able to increase the net IBC specific work.

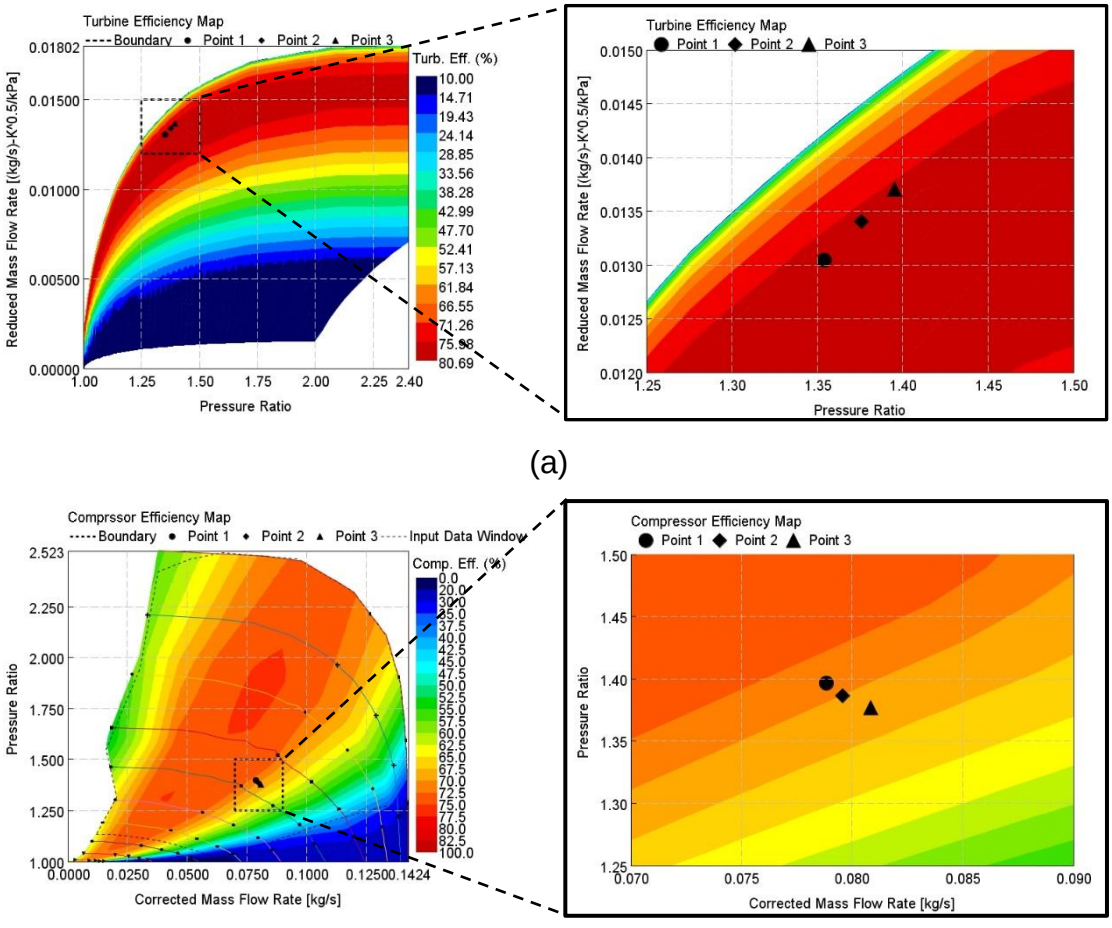

Figure 6.12 Predicted turbine (top) and compressor (bottom) operating points against their own performance maps

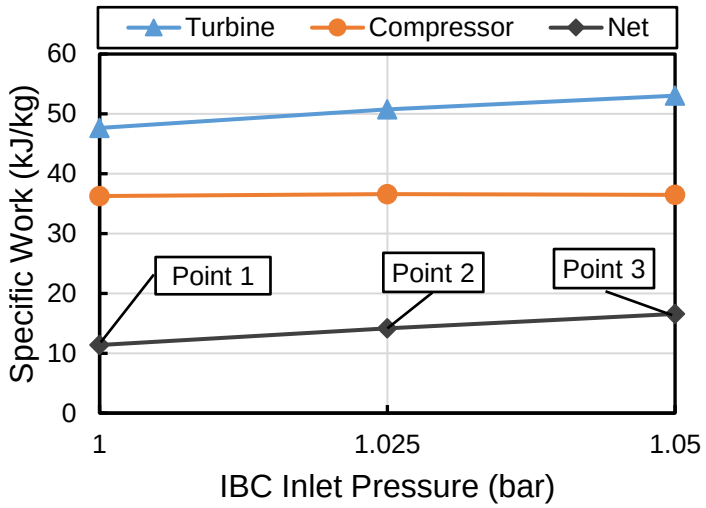

(a)

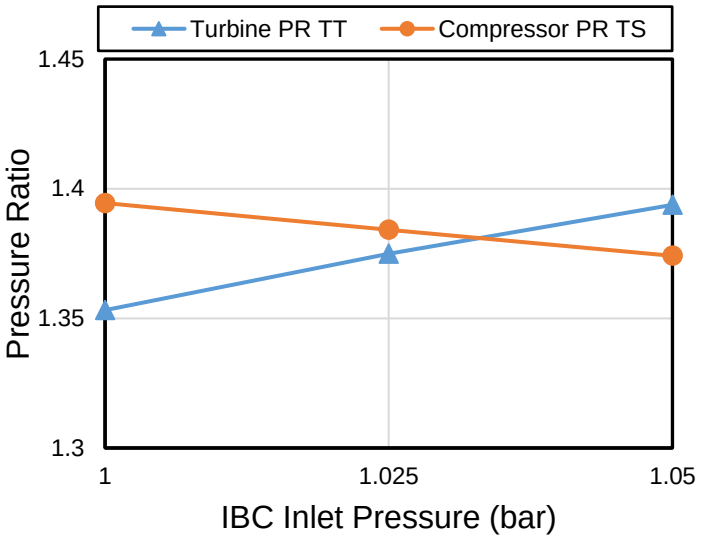

(b)

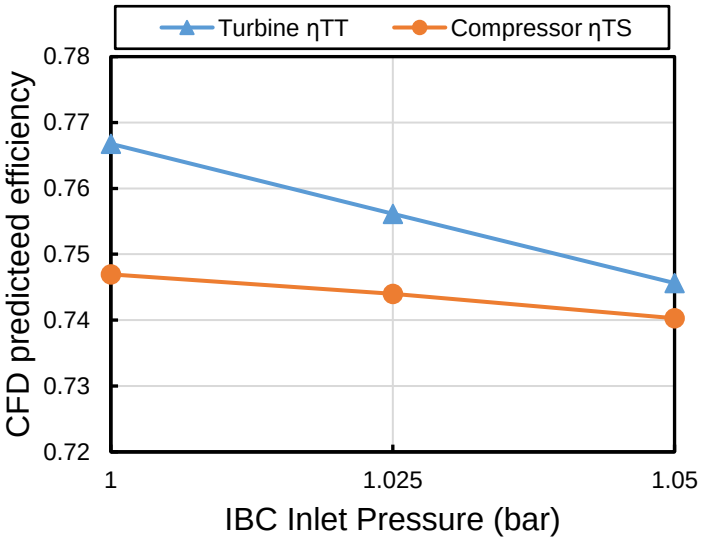

(c)

Figure 6.13 Specific work and turbomachinery performance as a function of IBC Inlet

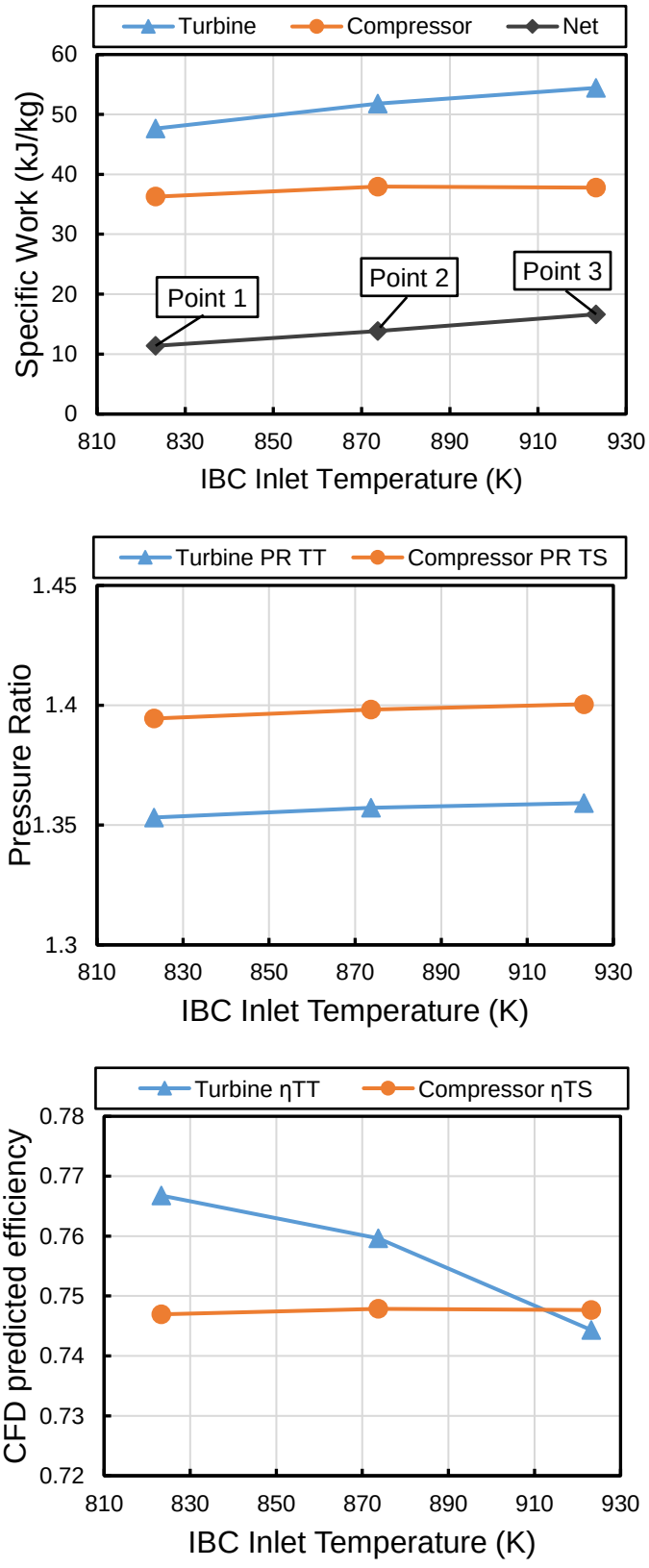

Figure 6.14 Specific work and turbomachinery performance as a function of IBC inlet temperature

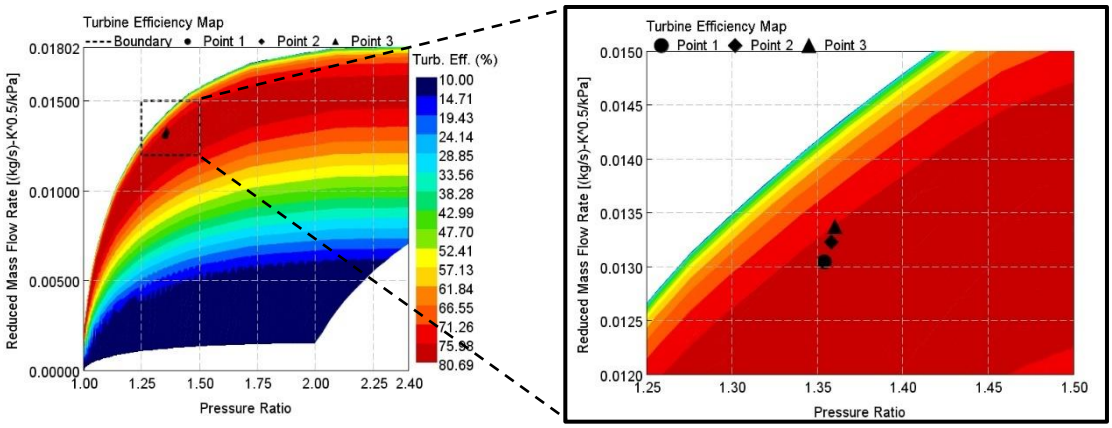

(a)

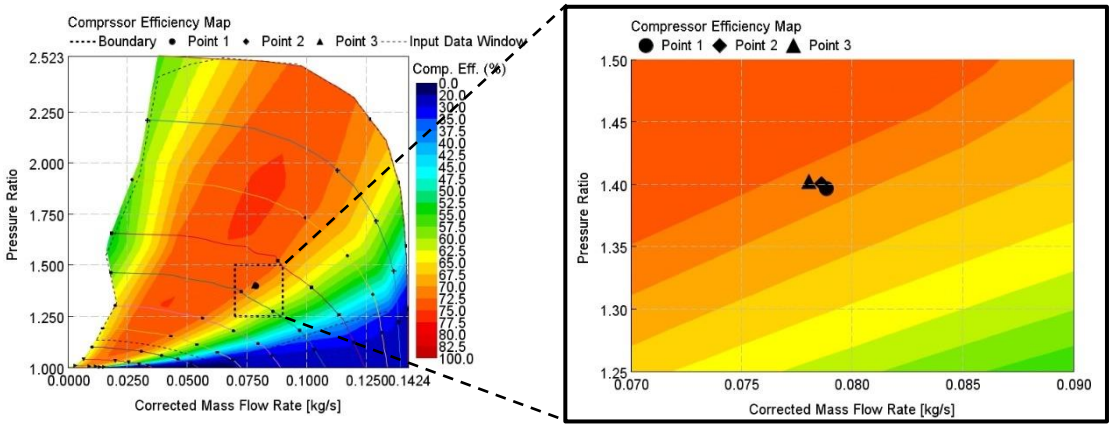

(b)

Figure 6.15 Predicted turbine (top) and compressor (bottom) operating points against their own performance maps

The effect of IBC inlet temperature is given in Figure 6.14. The test results show that the IBC inlet temperature rise contributes to increase the net specific work. This trend is aligned with the theoretical analysis, that is, the more thermal energy the working fluid contains, the more power the heat recovery system could potentially recovery. However, in practice, the turbine efficiency decreases due to the change in operating point. This tends to comprise the positive impact of raised inlet temperature on turbine work and, therefore, the net specific work. It should be noted that the turbine efficiency reduction found in this test condition is just caused by the operating region where the turbine currently operates. In other words, the inlet temperature rise does not necessarily lead to the decrease of the turbine efficiency. This can be explained as follows. In Figure 6.15 (a), 1D turbine simulation results shows that the increase of the turbine inlet temperature forces

the turbine operating point to move towards the region with higher reduced mass flow rate and higher expansion ratio, that is, from Point 1 to Point 3 in Figure 6.15 (a). However, since Point 1 is already in the peak efficiency region of the turbine performance map, the afore-mentioned operating shift leads to the reduction of the turbine efficiency. Thus, the rise of the turbine inlet temperature could contribute to the turbine efficiency growth, when Point 1 operates in the region underneath the peak turbine efficiency region. In conclusion, although turbine efficiency drop is found, the trend of increased inlet temperature leading to more net specific work is clearly demonstrated.

Figure 6.16 presents the influence of compressor inlet temperature on the IBC performance. Although the coolant temperature is selected to perform sensitive study, the compressor inlet temperature is more proper parameter to demonstrate the combined effect of both the heat exchanger and coolant temperature. As can be seen in Figure 6.16 (a), the IBC net work is a monotonically decreasing function of the IBC inlet temperature. This is because that, generally the lower the working fluid temperature at the compressor inlet, the less the work required by IBC compressor for the given pressure ratio. The net specific power does indeed trend upwards.

Note that the compressor reduced mass flow is expressed as follows,

$$\dot{m}_{reduced} = \dot{m}\sqrt{T_{c,in}}/P_{c,in} \tag{6.9}$$

where $\dot{m}$ is the mass flow rate. $T_{c,in}$ and $P_{c,in}$ is the compressor inlet temperature and pressure.

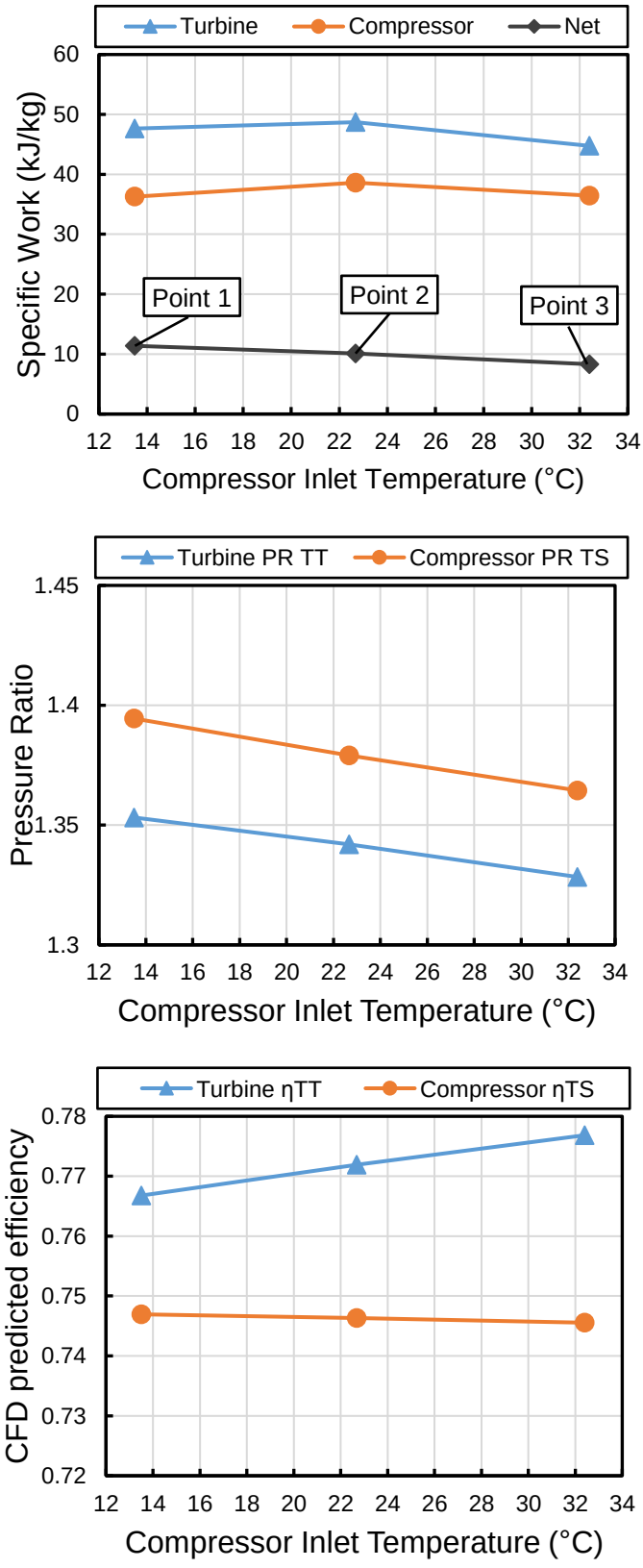

Figure 6.16 Specific work and turbomachinery performance as a function of compressor inlet temperature

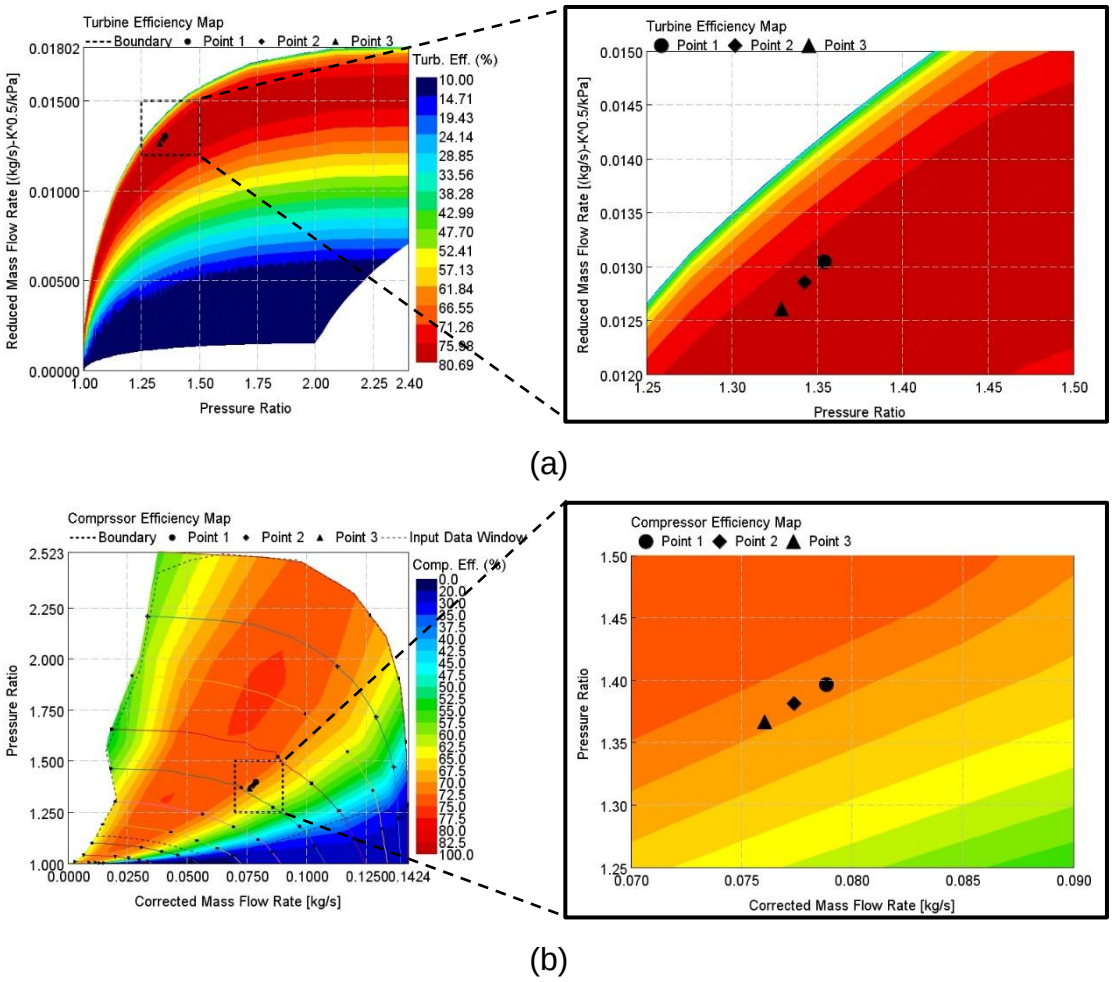

Figure 6.17 Predicted turbine (top) and compressor (bottom) operating points against their own performance maps

Thus, based on the definition of the compressor reduced mass flow, it decreases with the inlet temperature at given inlet pressure, thereby leading to the increase of compression ratio at given rotation speed. However, in IBC test, the IBC compressor outlet is directly connected to the ambient, that is, the outlet pressure is fixed. Thus, as the result of increasing compression ratio, the compressor inlet pressure will decrease. According to Eq. 6.9, the consequence of compressor inlet pressure should be the increase of the reduced mass flow and, therefore, the decrease of the compression ratio. In conclusion, for IBC system, the reduction of compressor inlet temperature has paradoxical effects on the compression ratio. However, Figure 6.16 (b) shows the measured compressor pressure ratio decreases with the increase of the compressor inlet temperature.

It means that at given IBC shaft speed, the changes of reduced mass flow rate are dominated by the compressor inlet temperature. Increasing the IBC compressor inlet temperature leads to the reduction of the compression ratio. This observation can also be found in Figure 6.17 (b). This plot shows the compressor performance predicted by 1D simulations.

In addition, the compressor efficiency is unchanged but the increase in turbine efficiency is an effect that should tend to increase net specific power rather than reduce it. This is caused by the reduction of turbine pressure ratio which is the consequence of compressor pressure ratio drop.

In Figure 6.18 (a), the test results show that the increase of the rotational speed is beneficial to the IBC net work. Figure 6.19 shows the predicted compressor and turbine operating points against their own performance maps. It can be clearly seen in Figure 6.18(a) that although both compressor and turbine work increase with the rotational speed, the higher rise in turbine work leads to the overall IBC performance improvement. Since both compressor and turbine efficiencies, predicted by CFD simulations, only change slightly, it can be gleaned that the resulting increase of the pressure ratio is the dominant contributor to the net work increase. This confirms the thermodynamic analysis presented in Section 3.5.1.4 that specific work increases with the reduction of turbine outlet pressure when both compressor and turbine efficiencies remain unchanged. The thermodynamic analysis also shows that at given IBC inlet temperature and turbomachinery efficiencies, the optimum turbine pressure ratio can be found to deliver the maximum specific power. Thus, it is clear that the present IBC system has not reached optimal operating pressure ratio at the rotational speed of 80,000 rpm.

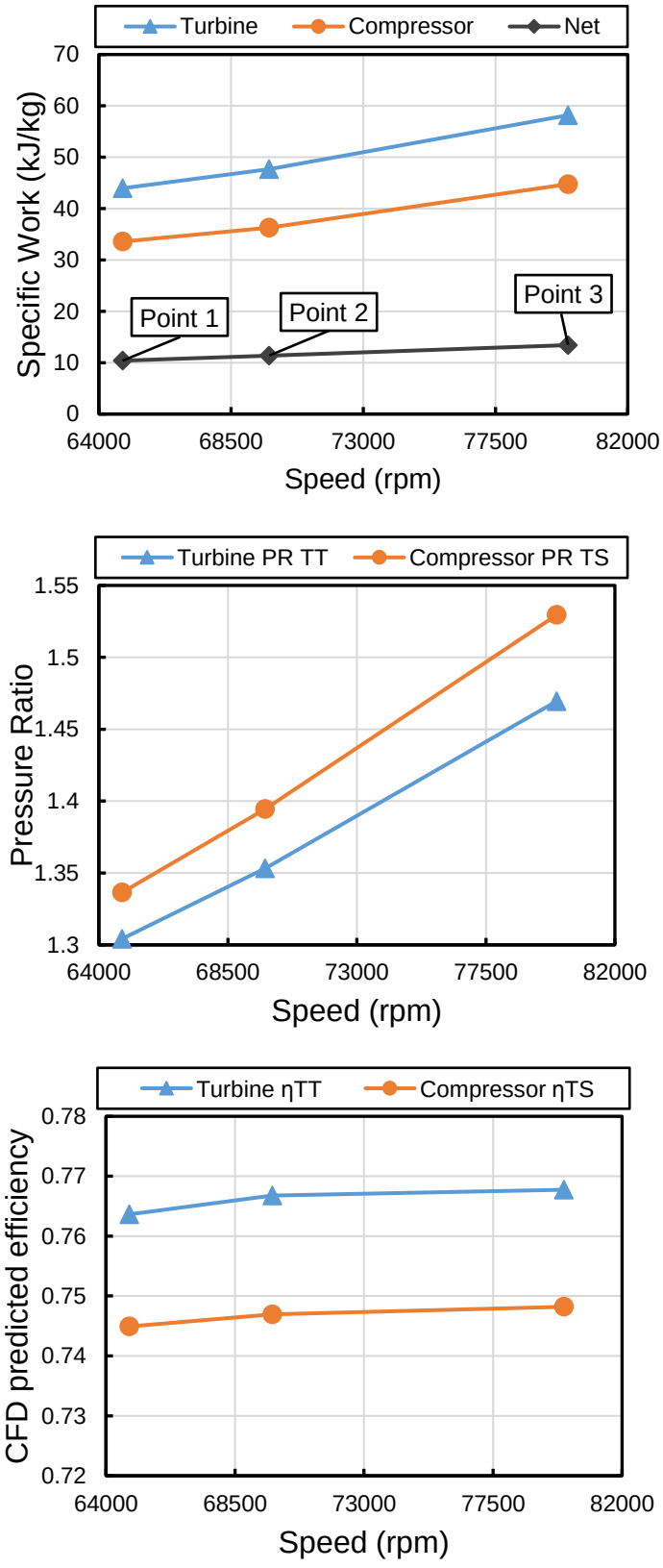

Figure 6.18 Specific work and turbomachinery performance as a function of IBC rotational speed

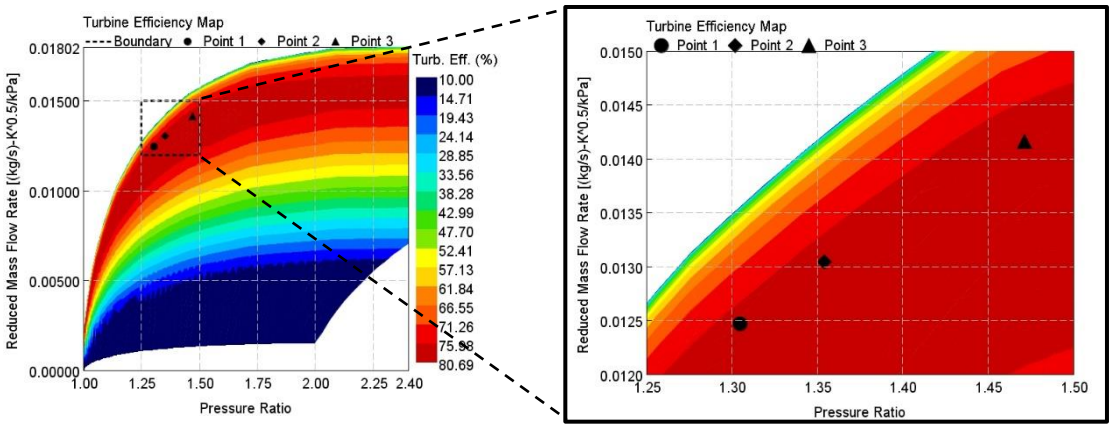

(a)

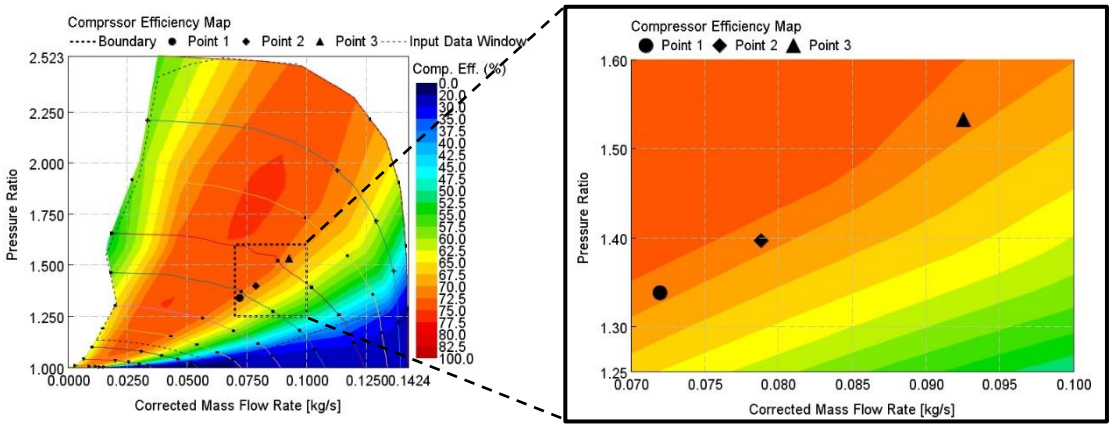

(b)

Figure 6.19 Predicted turbine (top) and compressor (bottom) operating points against their own performance maps

The heat exchanger performance is shown in Figure 6.20. Thanks to Selective Laser Melting additive manufacturing, over 99% of effectiveness is delivered by the tested heat exchanger while only imposing a 2.5 ~ 3.5 kPa pressure drop. The IBC thermodynamic analysis shows that the higher effectiveness and lower pressure drop of the heat exchanger are desirable for the IBC performance. Thus, the present heat exchanger has extraordinary performance that boosts the IBC net work.

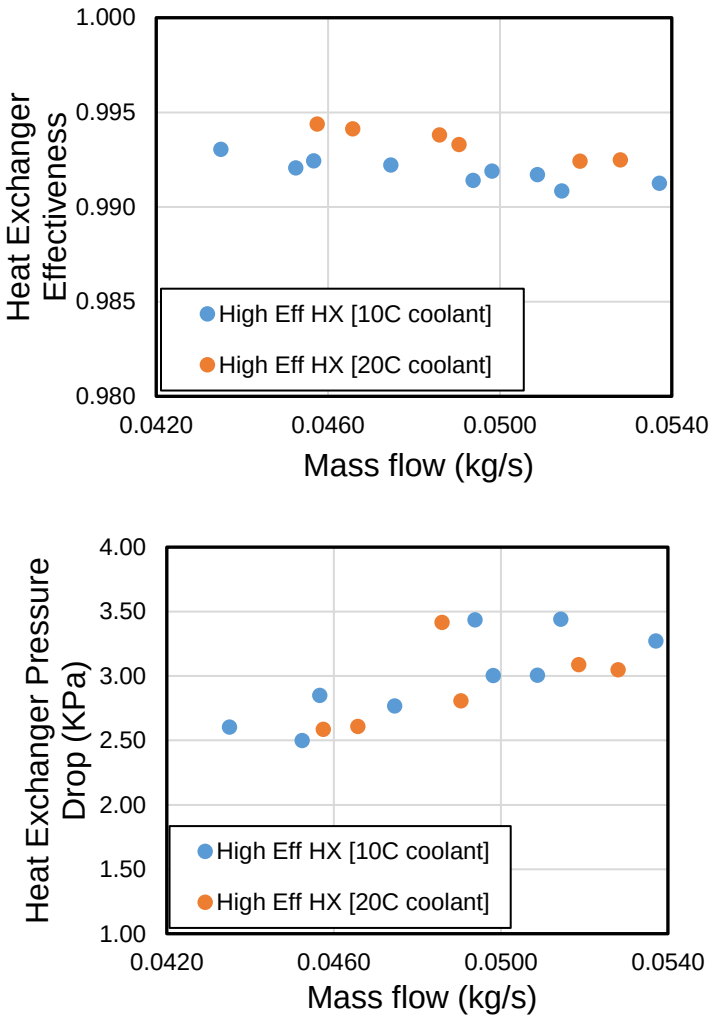

Figure 6.20 Heat exchanger effectiveness and pressure loss versus exhaust mass flow rate

6.4 1D Model Correlation

Since a Rotrex drive dynamometer and high speed torquemeter are attached to the IBC shaft, IBC shaft speed is unable to reach at the design speed of 125,000 rpm. Thus, 1D GT-power model must be correlated against the test data to predict IBC performance at the design point of the present system. Moreover, a correlated 1D GT-power model can estimate the IBC performance over a broader range of operation, such as over engine mini-map points presented in Section

4.4.5.1. Finally, a high-fidelity GT-power model can be used as a baseline and, therefore, perform the system design and optimisation with new operating points.

6.4.1 Model Description

A single-stage IBC GT-power model shown in Figure 6.21 is used to correlate against the test data. Note that there is no engine model in the proposed model. By doing so, the test inlet conditions can be directly imposed at the inlet of IBC model. The characteristic maps of compressor and turbine were generated by CFD simulations and inserted into compressor and turbine module, respectively. The efficiency and pressure ratio maps of compressor and turbines are shown in Figure 6.22. Although there are discrepancies between the real characteristic maps and the CFD predicted ones, the lack of the compressor and turbine mapping test data encourages the use of virtual turbomachinery maps.

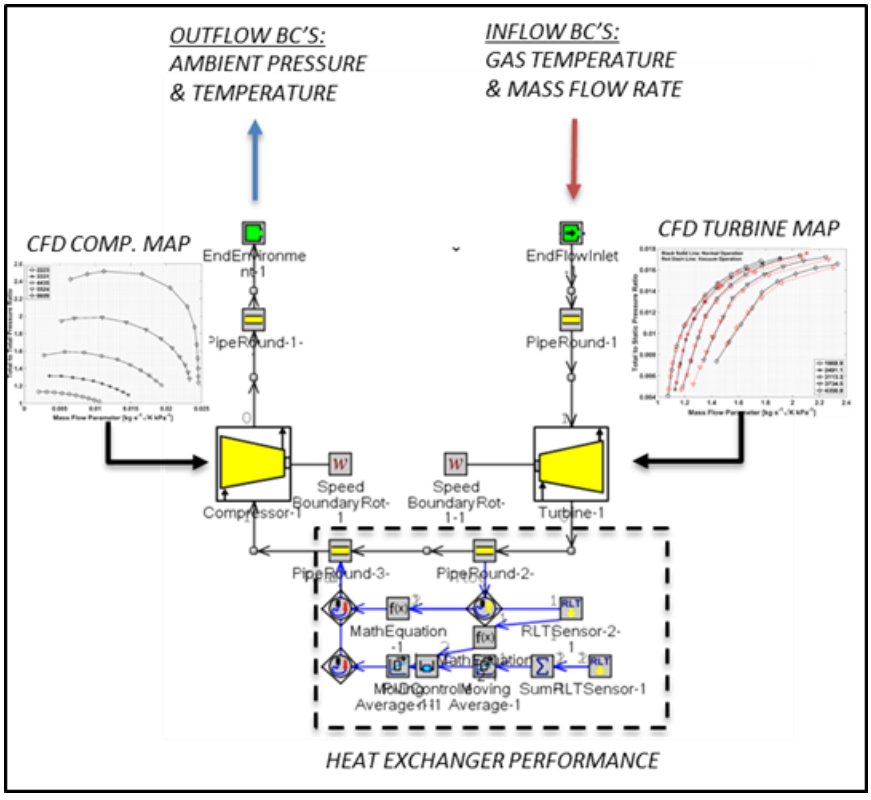

Figure 6.21 Numerical model of IBC system

It is important to note that in IBC system the pressure between turbine outlet and compressor inlet is subatmospheric, which is abnormal working conditions of the

conventional turbocharger. Thus, the typical approach to mapping compressor and turbine is doubtful for IBC application. In order to select a proper mapping approach in this study, a corresponding investigation was performed by turbine 3D simulations. As can be seen in Figure 6.22, there are two different characteristic maps for turbine efficiency and pressure ratio. The black solid lines represent the characteristic map generated by typical mapping approach that the turbine outlet pressure is set as ambient, while the red dash lines are the approach with the subatmospheric at the turbine outlet. Clearly in Figure 6.22, pressure ratios mapped by two approaches are diverse, especially at higher mass flow parameter. In terms of efficiency, larger discrepancy is found at higher reduced turbomachinery speed. In conclusion, characteristic maps generated by typical mapping approach is unable to represent the turbomachinery performance in IBC system. Thus, in this research, both compressor and turbine mapping were performed with the subatmospheric at the compressor inlet and turbine outlet, respectively.

Regarding the variations in inlet conditions, the mass flow rate and temperature from test were imposed in the IBC GT-power model, while the resulting inlet pressure was calculated by the code. At the IBC outlet, the flow temperature and pressure were fixed as the measurements from the test.

The heat exchanger in the proposed model was represented by a single pipe, instead of a heat exchanger module with detailed structure. This is because that the standalone performance of the heat exchanger is out of research scopes. The parameters of interest are the heat exchanger outlet temperature and pressure which can be accurately predicted by a single pipe with the proposed pressure drop and heat exchanger effectiveness. To be specific, the attribute ‘Friction Coefficient Multiplier’ in the ‘Pipe’ module can be controlled to ensure that the imposed pressure drop is achieved in the simulation. Whereas, the attribute ‘Imposed Wall Temperature’ can used to heat or cool the working fluid to the temperature set point, by imposing an unrealistic large heat transfer rate between the fluid and the wall. By doing so, the heat exchanger outlet temperature and pressure can be manipulated directly based on the correlated heat exchanger

effectiveness and pressure drop. The correlated process was described in the following section.

Shaft speed was specified to represent the conditions in the test. However, the mechanical loss only can be estimated by comparing the predicted power to the experimental values, as it is difficult to measure the shaft friction loss in tests. To be specific, 1D simulations were firstly performed without any shift loss. Then, it assumes that any power difference between the prediction and the measurement is caused by the shaft friction loss.

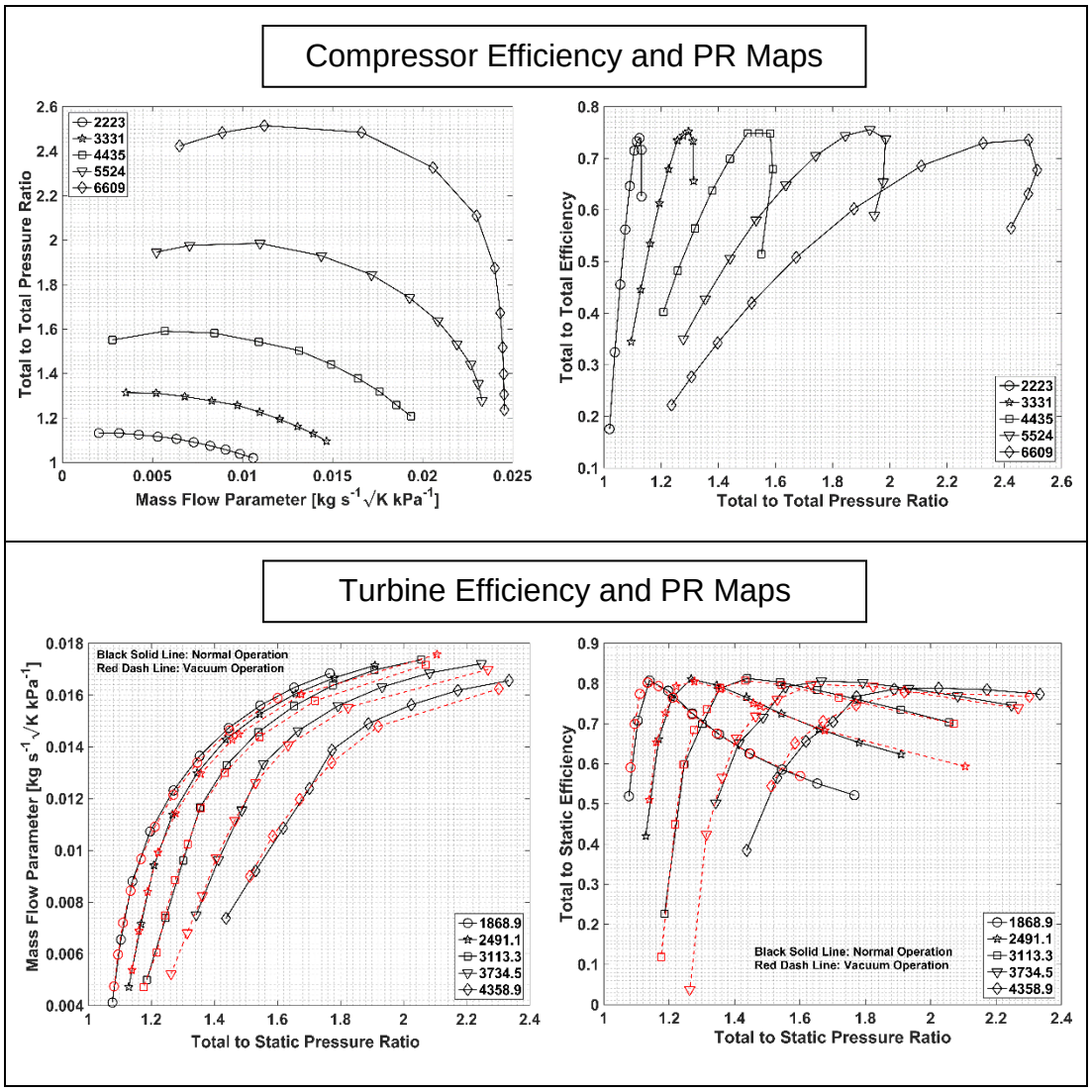

Figure 6.22 CFD predicted efficiency and pressure ratio of compressor (top) and turbine (bottom)

6.4.2 Model Correlation

Shaft friction torque, heat exchanger effectiveness and pressure drop in IBC GT-power model were three key parameters required to correlate against the test data. First, heat exchanger effectiveness and pressure drop were fitted by the mass flow rate, in order to ensure that the simplified heat exchanger model is able to represent its performance in tests. Then, in absent of the bearing friction model, the shaft power was predicted by the IBC model that has contained the correlated heat exchanger model. By doing so, the friction torque can be conducted by comparing the predicted power to the experimental values.

6.4.2.1 Heat Exchanger Correlation

In order to simplify the heat exchanger model, a single pipe was introduced as the heat exchanger in IBC 1D GT-power model. The pipe outlet temperature and the corresponding pressure drop were manipulated by varying the 'Pipe' attributes 'Imposed Wall Temperature' and 'Friction Coefficient Multiplier', respectively. It was achieved by two independent PID controllers.

In IBC system, the pressure drop and effectiveness of the heat exchanger are key parameters which must be correlated. However, due to the lack of the detailed heat exchanger model, it has to assume that the effectiveness in simulation is a linear function of the mass flow rate of the working fluid at the hot side, while pressure drop is a quadratic function of that, given in Eq. 6.12 in Chapter 3. Based on the test data, the best fits for effectiveness and pressure drop are shown in Figure 6.23.

In Figure 6.23, the coefficient of determination, denoted R^2, is presented with the regression lines for heat exchanger effectiveness and pressure drop. The coefficient of determination is the proportion of the variance in the observations that predictable from the predictors. It is a statistical measure of how well the regression predictions approximate the real data points. Its value is typically between 0 and 1. The value of 0 indicates that the statistical model explains none of the variability of the response data around its mean, while 1 means it explains all the variability. Thus, generally higher the coefficient of determination the better

quality of the regression line. However, the value of R^2 is lower than would be desired, that is, 0.3113 and 0.1144 for the regression lines of heat exchanger pressure drop and effectiveness, respectively. This is because that a single parameter, mass flow rate in this study, is unable to fully describe the heat exchanger performance. A better statistical model can be built by introducing more predictors. Since a simplified heat exchanger was employed in 1D model, the fitted regression lines presented in Figure 6.23 were still introduced to predict the heat exchanger performance. The poor quality of the regression lines was considered as the model limitations.

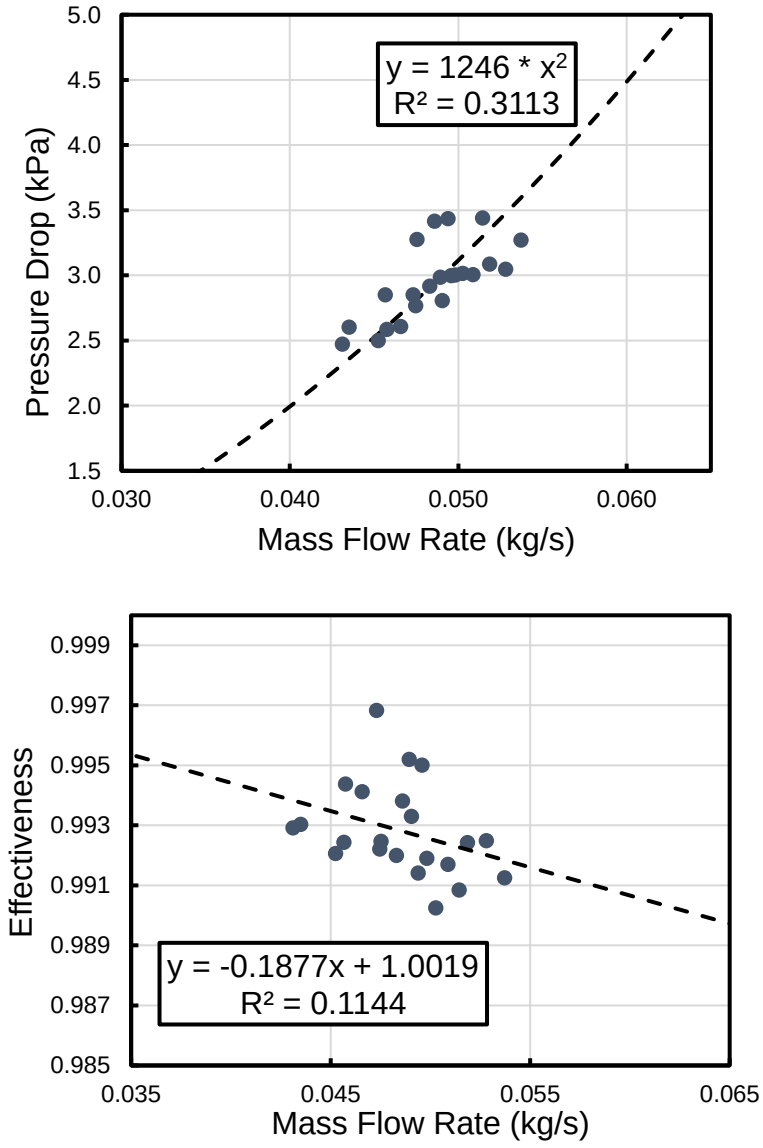

Figure 6.23 Fitting curves for heat exchanger pressure drop and effectiveness

6.4.2.2 Mechanical Loss Correlation

Since there is no bearing friction loss model in the proposed IBC GT-power model to predict the mechanical loss, it could be estimated by the power difference between the predicted power and the experimental value, with the assumption that the frictional power is a linear function of the speed. In other words, a constant friction torque was applied for the whole test points in simulations.

In order to perform the mechanical loss correlation, the experimentally measured conditions – IBC inlet temperature, inlet pressure, speed, coolant temperature, and flow rate were introduced into the model, shown in Table 6.2. The regression lines presented in Figure 6.23 were employed to predict the heat exchanger effectiveness and pressure drop. The IBC outlet boundary condition was assumed as the ambient conditions.

First, the IBC shaft power was predicted without any bearing loss at all test conditions and the corresponding results are listed as model prediction shaft power in Table 6.2. Then, the power difference between the predicted power to the experimental values, referred as ΔP, was calculated at each test conditions. Thus, the corresponding friction torque can be calculated as follows,

$$T_{loss} = \frac{\Delta P}{2\pi \left(n_{rpm}/60\right)} \tag{6.10}$$

where n_{rpm} is the turbomachinery speed.

Given the assumption of the constant friction torque, the average friction torque is calculated over all test conditions and, therefore, applied to the shaft as a fixed loss. By doing so, the friction torque has been correlated, referred as average T_{loss} in Table 6.2.

Table 6.2 Main IBC test and corresponding simulation results

Test Condition					Test Results	Model Prediction		Avg. T_{loss} = 0.0234 N-m	Model Prediction with Bearing Loss		
Inlet Prs.	Inlet Temp.	Coolant Temp.	IBC Speed	Mass Flow Rate	Shaft Power	Shaft Power	ΔP	Calculated Torque Loss	Shaft Power	ΔP	Error
kPa	C	C	rpm	kg/s	kW	kW	kW	N-m	kW	kW	%
100.2	550	10	70	0.0475	0.534	0.676	0.14	0.0195	0.51	-0.03	-5%
102.8	549	10	70	0.0509	0.717	0.916	0.20	0.0272	0.74	0.03	4%
105.3	550	10	70	0.0537	0.892	1.107	0.21	0.0294	0.94	0.04	5%
100.2	550	10	65	0.0452	0.475	0.571	0.10	0.0141	0.41	-0.06	-13%
100.4	549	10	80	0.0514	0.687	0.868	0.18	0.0216	0.67	-0.01	-2%
102.8	599	10	70	0.0498	0.842	1.046	0.20	0.0279	0.87	0.03	4%
100.2	654	10	65	0.0435	0.644	0.776	0.13	0.0195	0.62	-0.03	-4%
100.2	650	10	70	0.0457	0.767	0.903	0.14	0.0186	0.73	-0.03	-5%
100.3	649	10	80	0.0494	0.977	1.182	0.21	0.0247	0.99	0.01	1%
100.3	650	20	80	0.0486	0.868	1.081	0.21	0.0255	0.89	0.02	2%
100.2	550	20	70	0.0466	0.475	0.595	0.12	0.0165	0.42	-0.05	-11%
105.3	550	20	70	0.0528	0.803	1.012	0.21	0.0286	0.84	0.04	5%
105.3	550	30	70	0.0519	0.708	0.923	0.22	0.0295	0.75	0.04	6%
102.8	550	30	70	0.0490	0.554	0.735	0.18	0.0248	0.56	0.01	2%
100.2	550	30	70	0.0457	0.387	0.520	0.13	0.0182	0.35	-0.04	-10%
100.3	650	30	80	0.0475	0.709	0.949	0.24	0.0288	0.75	0.05	6%
100.0	601	10	80	0.0503	0.824	1.027	0.20	0.0242	0.83	0.01	1%
100.0	600	20	80	0.0496	0.741	0.934	0.19	0.0231	0.74	0.00	0%
100.0	600	30	80	0.0489	0.663	0.857	0.19	0.0232	0.66	0.00	0%
100.0	600	40	80	0.0483	0.578	0.784	0.21	0.0246	0.59	0.01	2%
100.0	600	50	80	0.0473	0.450	0.677	0.23	0.0272	0.48	0.03	7%
97.6	600	10	65	0.0431	0.529	0.644	0.12	0.0169	0.49	-0.04	-8%

6.4.2.3 Performance Evaluation of Correlated Model

The correlated IBC 1D model were utilized to predict the IBC performance at test points, in order to evaluate its fidelity. Thus, IBC inlet temperature, flow mass rate, speed, and coolant temperature available from the test measurements, shown in Table 6.2, were imposed as the boundary conditions of the correlated IBC model. The heat exchanger was represented by a simple pipe. Its effectiveness and pressure drop were a function of the working fluid, expressed in Figure 6.23. Moreover, a fixed friction torque of 0.0234 N-m was applied at the turbomachinery shaft.

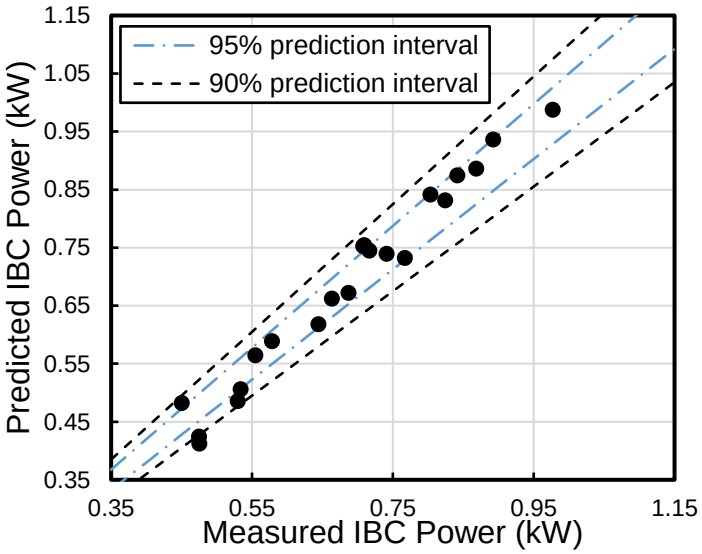

Figure 6.24 Scatter plot for measured and predicted IBC power

The simulation results, referred as 'Model Prediction with Bearing Loss', are shown in Table 6.2. The predicted IBC power is plotted against the experiment measurements in Figure 6.24. The black dashed lines represent the 90% proportional prediction interval while blue dashed lines are 95%. It can be found in tests that the maximum power generated by the IBC prototype is 0.997 kW, while the minimum power is 0.387 kW. In comparison to the 1D simulation results in Chapter 4, the measured IBC net power was relatively low. This is mainly because the presented IBC prototype is designed at the operating condition with higher shaft speed and pressure ratio, thereby theoretically higher IBC net power. Figure 6.24 shows that, at 68.18% of total test points (15 of 22), the absolute prediction error in IBC net power is equals or lower than 5%, while that at 86.36% of total test points is equals or lower

than 10%. The negative prediction error listed in Table 6.2 represents that the correlated IBC model underestimated the IBC performance. The largest prediction error of -13% was found at the lowest turbocharger speed and the lowest inlet temperature in tests. However, the corresponding ΔP is only 0.06 kW. Thus, the prediction error in IBC net power were accepted to be satisfactory.

Since only inlet temperature and mass flow rate were imposed as the IBC inlet boundary conditions, the inlet pressure of IBC system was predicted based upon operating conditions. The scatter plots of prediction versus test observation of IBC inlet pressure, turbine pressure ratio, and compressor pressure ratio are shown in Figure 6.25. Regarding the IBC inlet pressure, the prediction errors at all test conditions were below ± 2%, shown in Figure 6.25 (a). Moreover, only ± 5% prediction errors of turbomachinery pressure ratio were found in Figure 6.25 (b) and (c). It also can be found that the predicted compressor and turbine pressure ratios are constantly higher than the measurements. It should be noted that the compressor and turbine performance at mapping points are predicted by 3D simulations. In this research, mapping points are grouped by the rotational speeds. At each selected rotational speed, a large range of mass flow rate is imposed at the inlet boundary of the compressor and turbine 3D models. Regarding the compressor, the surge and chock lines are defined by the converged simulation points at each rotational speed with the lowest and highest mass flow rate, respectively. The predicted performance of all converged mapping points is introduced into the compressor and turbine module in 1D IBC model. Afterwards, compressor and turbine performance maps are generated in 1D code by the interpolation and extrapolation of these imposed mapping points. Thus, there are two sources of errors in compressor and turbine performance predictions: 1) 3D simulation errors, 2) map interpolation and extrapolation errors in 1D code. Since there is no test data at the selected mapping points for compressor and turbine, it is hard to assess the reasons why 1D simulations always predict higher pressure ratio of compressor and turbine than the measurements. Further tests should be conducted to investigate this observation.

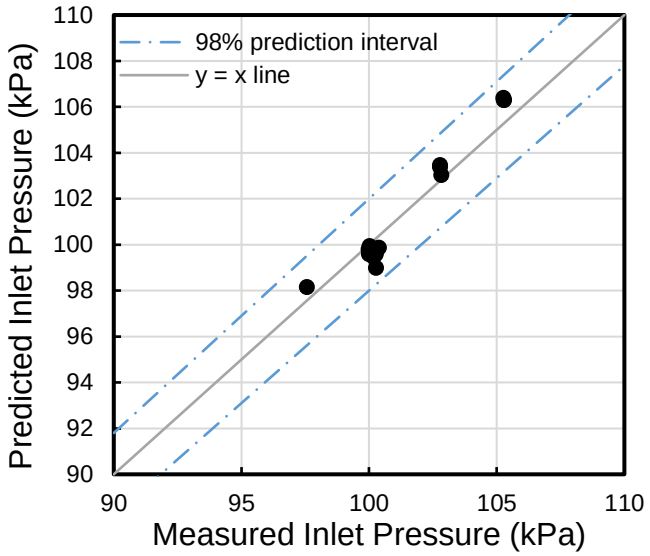

(a)

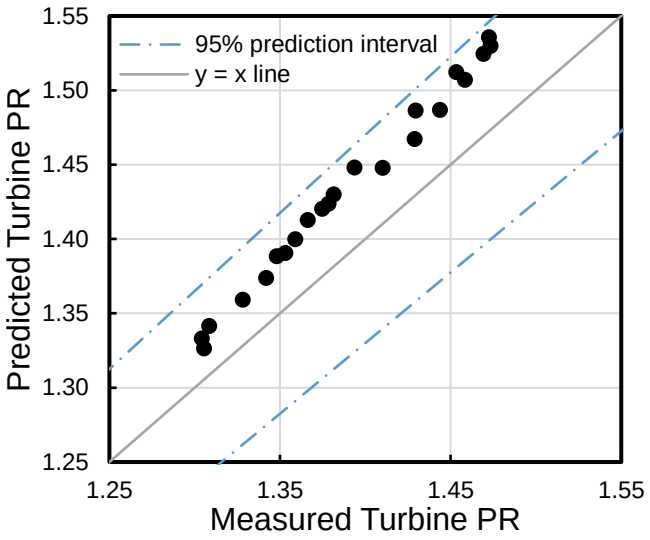

(b)

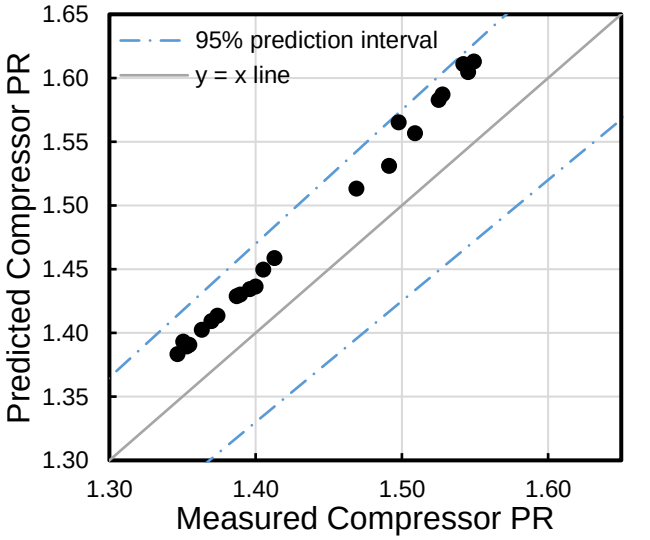

(c)

Figure 6.25 Scatter plot for prediction versus test observation of IBC inlet pressure (top), turbine pressure ratio (middle), and compressor pressure ratio (bottom)

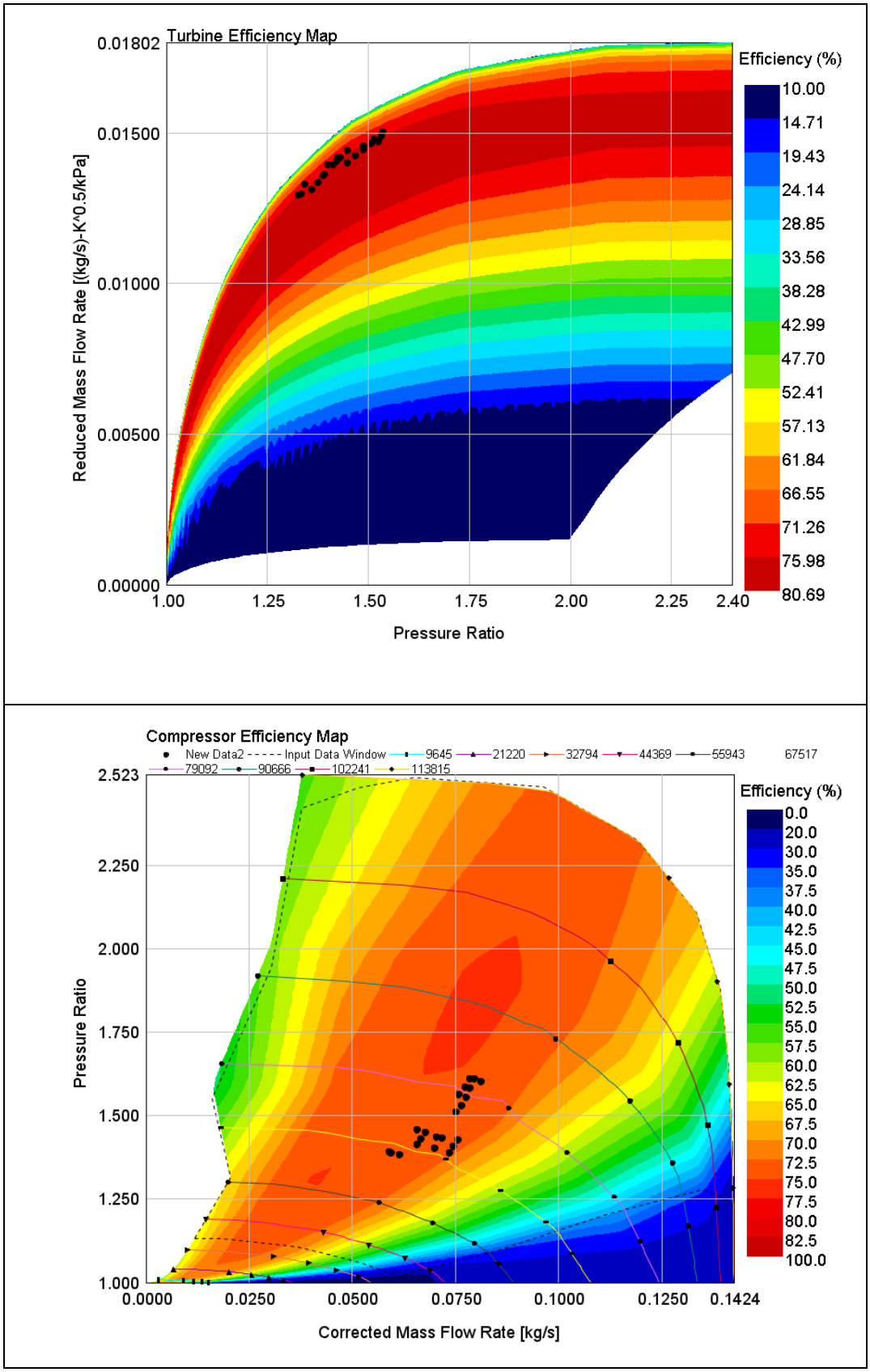

Figure 6.26 Predicted compressor and turbine operating points at all test cases

In Figure 6.26, the compressor and turbine predicted operating points were plotted in the efficiency maps, respectively. It shows that both compressor and turbine operated at off-design conditions in all test cases, that is, the maximum turbomachinery efficiencies have been not reached in tests. This contributes to the relatively low measured IBC net power. Moreover, the IBC inlet temperature in the test was only up to 650 K which is much lower than the design condition of 1023 K inlet temperature. According to the sensitivity studies performed by the thermodynamic analysis in Section 3.5.1.1, low inlet temperature is also the contributor to the deterioration the IBC net power.

In conclusion, although the correlated IBC GT-power 1D model delivered up to 13% prediction error of IBC net power at all test cases, 86.36% of total test points have prediction errors lower than 10%. Furthermore, the correlated IBC model is capable of accurately predicting the pressure at any component inlets and outlets. Thus, pressure ratios of compressor and turbine predicted by IBC model were highly correlated to the test measurements, only with errors less than ± 5%. Overall, the simulation results indicate that the presented correlated IBC model is able to deliver high fidelity simulations on IBC performance.

6.4.3 Model Prediction at WLTP Mini-map Points

Given that the correlated IBC 1D model has enough accurate to simulate the IBC performance, the performance of the tested IBC prototype was predicted at mini-map point 7, 9, 10, and 11 by the correlated model. The mini-map points are steady-state operating points which are able to present the chosen driving cycle. In Section 4.4.5.1, the generation process of the mini-map points of 2-litre turbocharged engine over WLTP driving cycle were described in detail.

In simulations, the coolant temperature was fixed as 60°C and 70% combined efficiency of the shaft mechanical and the electric generator efficiencies was considered. The turbomachinery speed was controlled to remain the IBC inlet pressure at 1 bar, in order to leave the turbocharged SI engine unaffected. However, since the mass flow rate at mini-map point 9 is too high to reach at

1 bar inlet pressure, the corresponding IBC speed was controlled to minimize the IBC inlet pressure.

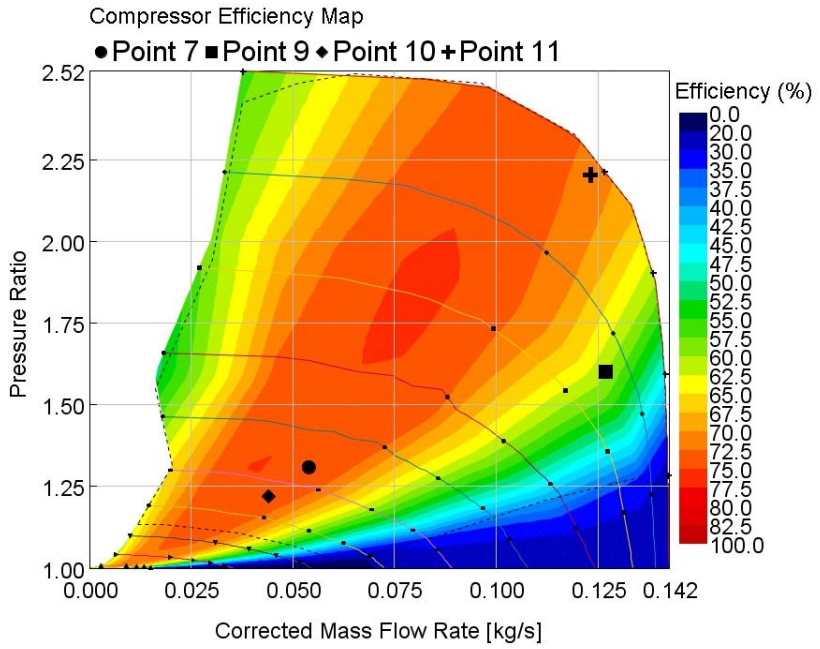

(a)

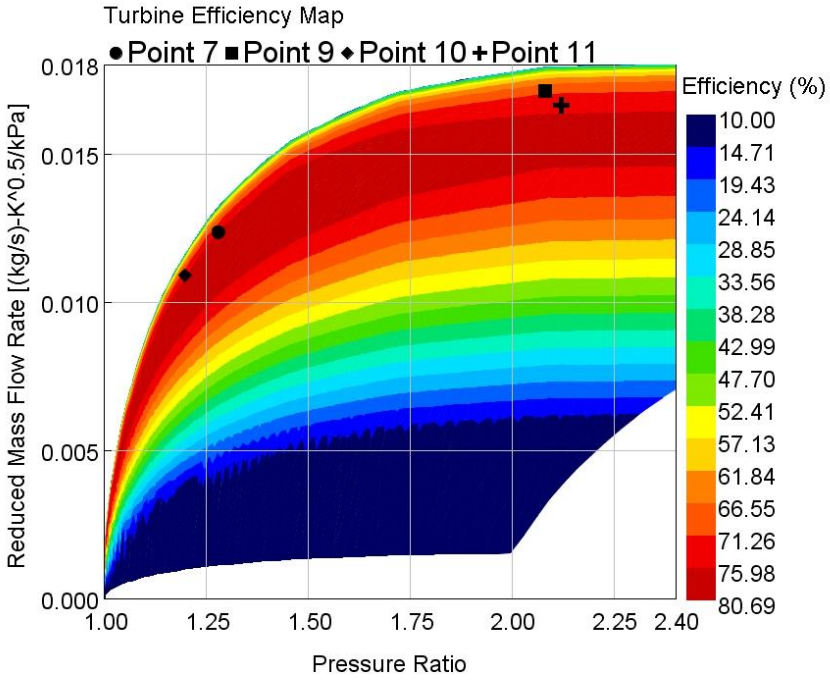

(b)

Figure 6.27 Predicted compressor (a) and turbine (b) operating points at mini-map point 7, 9, 10, and 11.

Figure 6.27 shows the predicted compressor and turbine operating points against the compressor and turbine performance maps, respectively. Note that the both compressor and turbine in IBC prototype were designed at mini-point 11 by trimming blades of the existing commercial compressor and turbine, respectively. However, it can be clearly seen in Figure 6.27 that neither compressor nor turbine operates in the peak efficiency region at the point 11 where the exhaust conditions of the engine mini-map point 11 is considered as IBC inlet conditions. This is mainly because that trimming blade height of compressor and turbine is only able to deliver suboptimal designs. In order to make both IBC compressor and turbine operate at the peak efficiency region, fully optimisation should be performed at all stages of compressor and turbine, such as blade geometry and volute.

The simulation results predicted by the correlated IBC model are listed in Table 6.3. At point 11, the IBC rotational speed is 121,605 rpm which is lower than the design condition of 125,000 rpm. This is partially due to the mass flow discrepancy between the mini-point 11 and the design condition. To be specific, the exhaust mass flow rate at mini-map point 11 is 0.053 kg/s, while the mass flow rate of the design point is fixed as 0.055 kg/s. It was decided by project partners. Furthermore, the map interpolation and extrapolation method for compressor and turbine will approximate the corresponding performance at the operating points where there is no imposed data for the performance map. Therefore, simulation errors are introduced by the map interpolation and extrapolation method. Consequently, both compressor and turbine operating points at mini-map point 11 are slightly different than the design conditions. The simulation results in Table 6.3 shows that the compressor and turbine efficiencies were found as 71.15% and 74.81%, respectively. However, 3D simulations presented in Section 5.5 shows that the compressor and turbine efficiencies at design conditions were 72.11% and 77.20%. Despite the relatively low turbomachinery efficiencies, the IBC net power of 1.37 kW was predicted at mini-map point 11. The resulting BSFC improvement is 2.72%. Note that only 70% of power differential between compressor and turbine is considered as the IBC net power due to the consideration of the mechanical and the electric generator loss.

Table 6.3 IBC performance prediction at mini-map points

	OP 7	OP 9	OP 10	OP 11
Engine BMEP (bar)	11.3	17.6	7.6	11.3
Engine BSFC (g/kW*h)	255.19	269.06	269.78	252.23
Exhaust Temperature (K)	1007.1	1088.2	1008.3	1057.3
Exhaust Mass Flow (kg/s)	0.039	0.077	0.034	0.053
Engine Power (kW)	35.78	67.17	30.4	48.97
IBC Power (kW)	0.44	3.34	0.28	1.37
IBC Inlet Pressure (bar)	1.00	1.44	1.00	1.00
IBC Shaft Speed (rpm)	63,483	103,445	53,738	121,605
Turbine Eff.	75.18%	69.54%	74.47%	74.81%
Turbine PR	1.28	2.08	1.20	2.16
Turbine Power (kW)	2.02	10.82	1.31	8.38
Comp. Inlet Temp. (K)	331.57	335.77	331.07	332.85
Comp. Inlet Pressure. (bar)	0.76	0.62	0.82	0.45
Compressor Eff.	74.27%	59.89%	73.82%	71.15%
Compressor PR	1.31	1.60	1.22	2.24
Compressor Power (kW)	1.40	6.05	0.90	6.42
HE Effectiveness	99.46%	98.79%	99.55%	99.20%
HE Pressure Drop (kPa)	1.90	6.93	1.47	3.46
BSFC Improvement (%)	1.21%	4.72%	0.94%	2.72%
IBC / Engine Power Ratio	0.012	0.050	0.009	0.028

At mini-point 9, the minimum inlet pressure predicted by the correlated IBC model is 1.44, with the turbomachinery speed of 103,445 rpm. Although the predicted turbomachinery efficiencies are lower than 70%, IBC net power still reaches at 3.34 kW due to the benefit of the high inlet pressure. As a result, the BSFC improvement of 4.72% at mini-map point 9 is the largest among all

mini-map points. Nevertheless, it is important to note that high back pressure has a significant adverse effect on the operation and reliability of the engine. Since the combustion model in the validated SI engine GT-power model, presented in Chapter 4, is unable to fully capture the influence of the back pressure, there is no need to perform the simulation of the combined system of SI engine and the correlated IBC model.

The mass flow rate at mini-point 7 and 10, 0.039 kg/s and 0.034 kg/s respectively, is much lower than the design mass flow rate of 0.055 kg/s. Thus, the low net power was expected at the mini-point 7 and 10. However, the corresponding BSFC improvements are moderate, 1.21% and 0.94% for mini-map point 7 and 10 respectively. This is because the relative low engine power is delivered at these two operating conditions.

Regarding the overall WLTP driving cycle, only 0.44% BSFC improvement can be delivered by IBC prototype based upon the weighting of all listed mini-map points in Table 6.3. Such low BSFC improvement over entire WLTP cycle is caused by the fact that the IBC device in this research is designed for the vehicle cruising, instead of the overall driving cycle.

6.5 Conclusion

In this research, the IBC prototype has been successfully demonstrated experimentally. This is the first experiment of IBC system designed for the automotive use. The parametric studies of IBC shaft speed, coolant temperature, inlet temperature and pressure were conducted in the test. Moreover, it is also one of few works in the public domain that provide IBC experimental results.

In the test, the design turbomachinery speed of 125,000 rpm cannot be reached due to the rotordynamic issues. Thus, shaft speed was limited up to 80,000 rpm. However, the maximum specific work output of 19.78 kJ/kg was still found with the test condition of 100.3 kPa inlet pressure, 605 K inlet

temperature, 10°C coolant temperature, and 80,000 rpm turbomachinery speed. The corresponding measured net power is 0.98 kW. Since the IBC net power was measured by the torquemeter which was mechanically connected to the IBC shaft, any mechanical loss has been subtracted from the IBC power.

Furthermore, the test results show increasing turbine inlet temperature and pressure contribute to the increase of the specific work output. In addition, lower coolant temperature results in higher heat rejection from the working fluid and, therefore, the lower inlet temperature. The resulting benefit shown in the test results is the rise of the specific IBC work output. Moreover, the specific work also increased with speed. The test results were in line with what would be expected from the thermodynamic analysis and 1D GT-power simulations.

However, due to the heat transfer from the turbine to compressor, the experimentally determined turbomachinery efficiencies were unreliable. In addition, heat loss through the pipe wall and turbocharger housing caused the errors in temperature measurements. Thus, turbine and compressor CFD simulations were conducted to predict the corresponding performance. The comparison between simulations and tests shows the experimentally determined compressor efficiency was overestimated, while the turbine efficiency was underestimated. As a result, CFD predicted turbomachinery efficiencies were plotted and analyzed to determine the true trend in efficiency. It is very important to note that the IBC net power was measured by a torquemeter which is mechanically connected to IBC shaft. Thus, despite the challenges in characterizing the individual efficiencies thermodynamically, the IBC net power was measured with high confidence.

Afterwards, all test data was utilized to correlate the IBC GT-power model. In order to simplify the IBC GT-power model, a simple pipe was introduced to represent the heat exchanger. Two regression lines were fitted to approximate the experimentally determined heat exchanger effectiveness and pressure drop. In terms of the IBC shaft friction loss, an assumption of constant friction torque was applied due to the lack of the detailed bearing model. The 1D

simulations show that the predicted IBC net power had a maximum error of -13%. However, the absolute prediction error at 86.36% of total test points (19 out of 22) was lower than 10%. More importantly, the predicted turbomachinery pressure ratio and IBC inlet pressure had maximum error of ±5%. In conclusion, the comparison with the test data provided enough confidence in the simulation fidelity of the correlated GT-power IBC model.

Thus, the correlated GT-power IBC model was employed to evaluate the mini-map points generated by 2-litre turbocharged engine over WLTP driving cycle. Note that the mini-map 11 is the design point of the tested IBC prototype. The simulations results show that the IBC net power of 1.37 kW was expected, which provided 2.72% BSFC improvement. Due to the low mass flow rate at mini-point 7 and 10, only 0.44 kW and 0.28 kW IBC net power were predicted, respectively. Moreover, the IBC inlet pressure at mini-map point 9 is unable to remain at 1 bar. This is mainly because the mass flow rate at the mini-map 9 is much higher than the design conditions. Thus, benefiting from the high IBC inlet pressure, the predicted IBC net power was as high as 3.34 kW.

Chapter 7 – Summary

7.1 Research Conclusion

In this research, inverted Brayton cycle (IBC) has been comprehensively studied by simulations and tests. It was considered as the exhaust-gas heat-recovery systems for a commercial 2-litre turbocharged gasoline engine. Based upon intensively 0D, 1D, and 3D simulations of the IBC system, the IBC prototype was designed, manufactured, and tested in this research. This is the first experiment of IBC system designed for the automotive use. More important, decent heat-recovery capability of the IBC system was demonstrated experimentally.

The basic IBC system consists of a turbine, a heat exchanger, and a compressor in sequence. The use of IBC turbine is to fully expand the exhaust gas available from the upper cycle to below atmospheric pressure, thereby harvesting the wasted energy. The remaining heat in the exhaust after expansion is rejected by the downstream heat exchanger. Then, the cooled exhaust gases are compressed back up to the atmospheric pressure by the compressor and discharged to the ambient. The net work produced by IBC system is defined as the power differential between the power harvested by the IBC turbine and that consumed by the IBC compressor. The use of the heat exchanger is to minimise the inlet temperature of the IBC compressor. The resulting higher gas density leads to the lower power consumption of the compressor for the given compression ratio. However, the heat exchanger

outlet temperature is limited by the effectiveness of heat exchanger and the temperature of the coolant.

At the beginning of this research, a model of an air-standard, irreversible Otto-cycle and the IBC using finite-time thermodynamics (FTT) was presented to study heat recovery applied to an automotive IC engine. The other two alternatives power cycles, the pressurized Brayton cycle and the turbo-compounding system, were compared with the IBC to specify the strengths and weaknesses of three alternative cycles. The performance of the system was defined as the specific power output and thermal efficiency was considered using parametric studies. The simulation results show that the performance of the IBC can be positively affected by five critical parameters – the number of compression stages, the cycle inlet temperature and pressure, the isentropic efficiency of the turbomachinery and the effectiveness of the heat exchanger. There existed an optimum pressure ratio across the IBC turbine that the IBC delivers the maximum specific power. In the view of the specific power, installing a single-stage of the IBC appeared to be the best balance between performance and complexity. Three alternative cycles were compared in terms of the thermal efficiency. The results indicated that the pressurized and inverted Brayton cycles can improve the performance of the turbocharged engine only when the turbomachinery efficiencies are higher than a value which changes with the operating condition. High performance of the IBC turbomachinery is required to ensure that the turbocharged engine with the IBC is superior to that with the other two alternative heat-recovery power cycles. The further IBC performance investigation was performed over driving cycle. The exhaust boundary conditions of a 2-litre gasoline turbocharged engine were measured over WLTC driving cycle and imposed as the inlet boundary conditions of the IBC thermodynamic model. Since there was no compressor and turbine characteristic maps employed in the thermodynamic model, the turbomachinery efficiencies and pressure ratio were assumed as the constant over the whole driving cycle. The simulation results show that the maximum resulting average BSFC improvement was 3.02% when the IBC turbomachinery efficiencies was 0.8/0.8 and the expansion ratio was 2. With the decrease of the of turbomachinery efficiency,

the IBC net work was deteriorated. Even, there was no net work at all when the IBC turbomachinery efficiency descended below a certain value. Then, the optimisation of the expansion ratio in the single-stage IBC was performed over WLTP driving cycle. The simulation results show that an increase in the optimum expansion ratio can be expected when the WLTP driving cycle move from the 'Low' part to the 'High' part. Since the average exhaust mass flow rate increases from the 'Low' part and 'High' part as well, this trend could be matched to a fixed geometry turbo machine that is designed to operate at the optimum expansion ratio during the whole WLTP driving cycle.

Later, the validated 2-litre turbocharged SI engine model was coupled with the IBC 1D model, in order to quantify the resulting performance improvement of a real IC engine. A commercial code, referred as GT-power, was utilized to perform the proposed 1D simulations. It allows the use of the real compressor and turbine characteristic maps in the IBC model, thereby producing the sensible evaluation of the IBC system at various operating conditions. The first design point was the high speed, high load engine working condition, that is, the engine speed of 4500 rpm and BMEP of 30.9 bar. By re-sizing the available commercial turbomachinery maps, 2.25 percentage points of system efficiency increment can be expected due to the employment of an IBC. The corresponding BSFC improvement was up to 5.91%. Then, the parametric study of IBC system with the scaled turbomachinery maps was performed at various engine loads with the engine speed of 4500 rpm. The simulation results show that, with increasing the engine power output, the system efficiency increment increased to the peak at a certain engine load, then decreased steeply. The engine operating condition that delivers the maximum performance improvement was shifted by varying the turbomachinery efficiencies. However, the optimal performance of the combined system was always achieved where the wastegates of the topping and bottoming turbines were closed. Thus, the parameter sweep of turbomachinery efficiencies and pressure ratio was conducted under conditions of the fully closed wastegates. The maximum efficiency increments of 6.15 per cent points was found when IBC expansion ratio was 4 and the turbomachinery efficiency was 0.9 and 0.85 for the turbine and compressor respectively. Afterwards, an engine operating

condition that represented the vehicle cruising mode was selected as the design point for the IBC prototype. In order to select proper commercial compressor and turbine for the design condition, the turbomachinery sizing optimisation was performed, and the resulting optimal maps were considered as the reference for the turbomachinery selection. As a result, the selected commercial compressor and turbine was able to generate the net power of 0.91 kW which was equivalent to the BFSC improvement of 1.82%. However, the selected turbine only delivered the efficiency of 70.0%, while slightly higher compressor efficiency of 75.7% was found. Thus, it is necessary to trim the compressor and turbine blades so that higher turbomachinery performance can be expected at the design point of the IBC prototype.

Then, the commercial software package ANSYS-CFX were utilized to evaluate the performance of all trimmed turbomachinery design. All simulations were completed by the following five steps: generating model geometry and flow domain, generating computational grids, establishing the boundary and initial conditions, setting up the proper solver, and performing the simulations. Since the computational grid size and type significantly affect the numerical solution produced by 3D CFD simulations, it is a common practice to complete the mesh sensitivity study to achieve the mesh-independent numerical solution. In this research, considering the trade-off between the computational cost and simulation accuracy, the mesh number of 0.8E+6 was chosen for the compressor rotor meshing target, while 1.1E+6 was set for the turbine rotor. In order to improve the efficiency of the existing compressor, parameter sweeps were performance for the impeller inducer height, exducer height, diffuser diameter, and volute A/R ratio. Since the pressure was imposed at the inlet and outlet boundaries for all compressor simulation, the compressor designs were selected as candidates only when the corresponding predicted mass flow rate met the design target of 0.055kg/s. As a result, the candidate design with the highest efficiency of 72.32% was selected as the compressor design for the IBC prototype. Regarding turbine design, the impeller exducer was supposed to be trimmed to achieve the optimal efficiency at the design point. However, the rotor design with 1mm trimming down at the exducer delivered relatively high efficiency. In addition, due to the project plan, there

was no enough time to perform a proper investigation on the blade trimming. Thus, the selected commercial turbine impellers were trimmed down 1mm at the exducer and the trimmed rotor was selected as the turbine rotor design. As the turbine volute is vital to the turbine performance, a parameter sweep for the turbine volute ratio was conducted. The simulation results show that the volute with A/R ratio of 15.5 mm should be employed with the trimmed commercial turbine rotor, as it delivered the highest efficiency among all alternative designs at the turbine design condition. Afterwards, the selected trimmed commercial compressor and turbine were manufactured as the turbomachinery of the IBC prototype. In parallel, a compressor in-house design and optimisation process was created to generate a high-performance compressor design. At the first stage of the design and optimisation process, CFX VISTA CCD code was utilized to generate the preliminary rotor design with the boundary conditions of the desired operating point. In addition, initial guesses for the compressor geometry are essential in the early design stage. Thus, some default settings were used in VISTA CCD. Four design variables – rotational speed, backsweep angle, volute A/R ratio, and diffuser diameter were optimised to achieve the optimal preliminary compressor design. Genetic algorithm (GA) was applied to solve the compressor optimisation problem. As a result, the resulting optimal design was able to deliver total-to-static (T-S) efficiency of 74.47% at the design point, which was 2.24 percentage point higher than that of the trimmed commercial compressor. The further performance optimisation was carried out by varying the compressor blade geometry. The parameterization of the compressor blade occurred in ANSYS Design Modeller. Due to the limited time, only four parameters were selected as the design variables, referred as 1) main blade inlet angle at shroud, 2) splitter inlet angle at shroud, 3) backsweep angle at shroud, and 4) stack position for both main blade and splitter. The optimisation results show that the final optimal compressor design was able to deliver T-S efficiency of 77.46%, which was 2.99 and 5.23 percentage points higher than the preliminary design and the trimmed commercial compressor, respectively. Note that the presented design and optimisation process also can be applied to design the turbine in-house.

Finally, the selected trimmed compressor and turbine were manufactured and assembled with the 3D printed heat exchanger provided by a project partner. This IBC prototype was tested in the gas stand in University of Bath. This is the first experiment of IBC system designed for the automotive use. The parametric studies of IBC shaft speed, coolant temperature, inlet temperature and pressure were conducted in the test. However, due to the rotordynamic issues, the design turbomachinery speed of 125,000 rpm cannot be reached in the test. Thus, the baseline test conditions were 70,000 rpm, 550°C IBC inlet temperature, 1 bar inlet pressure, and 10°C coolant temperature. The test results show that the IBC specific work of 11.37 kJ/kg was expected at the baseline test condition, which is 0.54 kW IBC net power. It is very important to note that there was a high-speed torque meter mechanically attached on the IBC shaft to precisely measure the shaft speed and torque. In other words, the measured shaft power was the IBC net power which the shaft mechanical loss has been subtracted. The parametric study shows that the IBC specific work was monotonically increasing function of the inlet pressure, inlet temperature, and shaft speed. While, the IBC performance benefited from the reduction of the coolant temperature. In the parametric study, the maximum specific work output of 19.78 kJ/kg, that is, net power of 0.98 kW, was expected at the test condition of 100.3 kPa inlet pressure, 605 K inlet temperature, 10°C coolant temperature, and 80,000 rpm turbomachinery speed. Then, all test data was utilized to correlate the IBC GT-power model. Regarding the 1D heat exchanger model, two regression lines were fitted to approximate the experimentally determined heat exchanger effectiveness and pressure drop. In terms of the IBC shaft friction loss, an assumption of constant friction torque was applied due to the lack of the detailed bearing model. The IBC net power predicted by the correlated IBC GT-power model had a maximum error of -13%. However, the absolute prediction error at 86.36% of total test points (19 out of 22) is lower than 10%. More important, the predicted turbomachinery pressure ratio and IBC inlet pressure had maximum error of ± 5%. In conclusion, the comparison with the test data provided enough confidence in the simulation fidelity of the correlated GT-power IBC model. Thus, the correlated GT-power IBC model was employed to evaluate the performance of IBC prototype at the design condition. The simulations results show that the

IBC net power of up to 1.37 kW was expected, which provided 2.72% BSFC improvement. The high improvement in the system performance indicates that the IBC system is a promising WHR technology for automotive use.

7.2 Further Work

Simulation

1. The effect of engine back pressure on the engine performance need to be investigated. This research demonstrates that the increase of IBC inlet pressure is beneficial to the IBC power generation. However, it can negatively influence the engine performance. Hence, a system compromise is required to select the optimum IBC inlet pressure. In this research, since the non-predictive combustion model was employed to simulate the engine combination, the negative effect of the back pressure on the engine performance cannot be properly investigated. Thus, the optimisation of the IBC inlet pressure is not performed in this research.

2. The control strategy for the IBC system needs to be developed. Since the automotive engines behave in a highly transient manner, a sophisticated control strategy should be developed in order to ensure that the employment of the IBC system do not compromise the engine transient behaviours.

3. The IBC bypass system needs to be investigated. In this research, the turbomachinery matching process was conducted at the engine mini-map point 11. However, due to the high mass flow rate at the mini-map point 9, the IBC inlet pressure was unable to maintain 1 bar. Thus, bypassing a portion of the exhaust gases is required at some operating conditions. Moreover, when the IBC turbomachinery efficiency descends below a certain value, there is no work generated by IBC and, therefore,

the IBC system should be bypassed. In conclusion, the bypass system is necessary for the IBC applications.

Experiment

1. The test facility needs to be further improved in order to overcome the rotordynamic issues. In this research, the shaft speed was limited up to 80,000 rpm, due to the shaft vibration problems.

Reference

1. Gopal, N.K., et al., *Thermodynamic analysis of a diesel engine integrated with a PCM based energy storage system.* International Journal of Thermodynamics, 2010. **13**(1): p. 15-21.
2. Gomes, C., *Improving US Household and Business Fundamentals Point to Higher Sales Ahead*. 2018, Scotiabank Economics: GLOBAL ECONOMICS.
3. Yu, C. and K. Chau, *Thermoelectric automotive waste heat energy recovery using maximum power point tracking.* Energy Conversion and Management, 2009. **50**(6): p. 1506-1512.
4. Stabler, F. *Automotive applications of high efficiency thermoelectrics*. in *Proceedings of DARPA/ONR/DOE High Efficiency Thermoelectric Workshop*. 2002.
5. Taylor, C., *Automobile engine tribology—design considerations for efficiency and durability.* Wear, 1998. **221**(1): p. 1-8.
6. Liu, J., et al., *Characteristics of engine exhaust gas energy flow.* Journal of Central South University (Science and Technology), 2011. **42**(11): p. 3370-3376.
7. Liu, J., et al., *Comparison and analysis of engine exhaust gas energy recovery potential through various bottom cycles.* Applied Thermal Engineering, 2013. **50**(1): p. 1219-1234.
8. Özkan, M., et al., *Experimental study on energy and exergy analyses of a diesel engine performed with multiple injection strategies: Effect of pre-injection timing.* Applied Thermal Engineering, 2013. **53**(1): p. 21-30.
9. El Chammas, R. and D. Clodic, *Combined cycle for hybrid vehicles*, in *SAE 2005 World Congress & Exhibition*. 2005, SAE Technical Paper.
10. Nag, P.K., *Engineering thermodynamics*. 2013: Tata McGraw-Hill Education.
11. Kuo, P.S., *Cylinder pressure in a spark-ignition engine: a computational model.* J Undergrad Sci, 1996. **3**: p. 141-145.
12. Cho, S.-Y., et al., *Optimal design of a centrifugal compressor impeller using evolutionary algorithms.* Mathematical Problems in Engineering, 2012.
13. TOUSSAINT, M. and P. Podevin. *GUIDE-VANES UPSTREAM THE IMPELLER OF CENTRIFUGAL COMPRESSOR*. in *5th European Conference on Turbomachinery Fluid Dynamics and Thermodynamics*. 2003.
14. Gonzalez, C. *What's the Difference Between a Pump and a Compressor?* 2015 [cited 2018 12/10]; Available from: https://www.machinedesign.com/whats-difference-between/what-s-difference-between-pump-and-compressor.

15. Aungier, R. and S. Farokhi, *Axial-Flow Compressors: A Strategy for Aerodynamic Design and Analysis.* Applied Mechanics Reviews, 2004. **57**: p. B22.
16. Schwind, R. and S. Abdallah, *A Look at Compressor Impeller Technologies for Turbochargers Focusing on Surge Mitigation.* Global J Technol Optim, 2015. **6**: p. 185.
17. Rakopoulos, C., et al., *Evaluation of the effect of engine, load and turbocharger parameters on transient emissions of diesel engine.* Energy Conversion and Management, 2009. **50**(9): p. 2381-2393.
18. Jaatinen-Värri, A., et al., *Centrifugal compressor tip clearance and impeller flow.* Journal of Mechanical Science and Technology, 2016. **30**(11): p. 5029-5040.
19. Wang, T., C. Peng, and J. Wu, *Back swept angle performance analysis of centrifugal compressor.* Mechanika, 2014. **20**(4): p. 402-406.
20. Dixon, S.L. and C. Hall, *Fluid mechanics and thermodynamics of turbomachinery*. 2013: Butterworth-Heinemann.
21. Kane, J. *How They Work, and Current Turbo Technology* 2019 [cited 2018 10/10]; Available from: http://www.epi-eng.com/piston_engine_technology/turbocharger_technology.htm.
22. Watson, N. and M. Janota, *Turbocharging the internal combustion engine*. 1982: Macmillan International Higher Education.
23. Copeland, C.D., *Evaluation of steady and pulsating flow performance of a double-entry turbocharger turbine*, in *Mechanical Engineering*. 2010, Imperial College London.
24. Feneley, A.J., A. Pesiridis, and A.M. Andwari, *Variable geometry turbocharger technologies for exhaust energy recovery and boosting - A Review.* Renewable and sustainable energy reviews, 2017. **71**: p. 959-975.
25. Japikse, D. and N. Baines, *Introduction to turbomachinery*. 1994: Norwich, Vt. : Concepts ETI.
26. Lüddecke, B., D. Filsinger, and J. Ehrhard, *On mixed flow turbines for automotive turbocharger applications.* International Journal of rotating machinery, 2012. **2012**.
27. Yang, J. *Potential applications of thermoelectric waste heat recovery in the automotive industry*. in *Thermoelectrics, 2005. ICT 2005. 24th International Conference on*. 2005. IEEE.
28. Saidur, R., et al., *Technologies to recover exhaust heat from internal combustion engines.* Renewable and Sustainable Energy Reviews, 2012. **16**(8): p. 5649-5659.
29. Zhang, X. and K. Chau, *An automotive thermoelectric–photovoltaic hybrid energy system using maximum power point tracking.* Energy Conversion and Management, 2011. **52**(1): p. 641-647.
30. Mori, M., et al., *Current possibilities of thermoelectric technology relative to fuel economy*. No. 2009-01-0170. 2009, SAE Technical Paper.
31. Stobart, R.K., A. Wijewardane, and C. Allen, *The Potential for thermo-electric devices in passenger vehicle applications*. No. 2010-01-0833. 2010, SAE Technical Paper.

32. Karri, M., E. Thacher, and B. Helenbrook, *Exhaust energy conversion by thermoelectric generator: Two case studies.* Energy Conversion and Management, 2011. **52**(3): p. 1596-1611.
33. Hsu, C.-T., et al., *Experiments and simulations on low-temperature waste heat harvesting system by thermoelectric power generators.* Applied Energy, 2011. **88**(4): p. 1291-1297.
34. Crane, D.T. and G.S. Jackson, *Optimization of cross flow heat exchangers for thermoelectric waste heat recovery.* Energy Conversion and Management, 2004. **45**(9): p. 1565-1582.
35. Bhargava, R.K., M. Bianchi, and A. De Pascale. *Gas turbine bottoming cycles for cogenerative applications: Comparison of different heat recovery cycle solutions*. in *ASME 2011 Turbo Expo: Turbine Technical Conference and Exposition*. 2011. American Society of Mechanical Engineers.
36. Doyle, E., L. Dinanno, and S. Kramer, *Installation of a diesel-organic Rankine compound engine in a class 8 truck for a single-vehicle test*. No. 790646. 1979, SAE Technical Paper.
37. Leising, C., et al., *Waste heat recovery in truck engines*. 1978, *SAE Transactions:* p. 2639-2648.
38. Lodwig, E., *Performance of a 35 HP Organic Rankine Cycle Exhaust Gas Powered System*. No. 700160.1970, SAE Technical Paper.
39. Patel, P.S. and E.F. Doyle, *Compounding the truck diesel engine with an organic Rankine-cycle system*. 1976, SAE Technical Paper.
40. Heywood, J.B., *Automotive engines and fuels: a review of future options.* Progress in Energy and Combustion Science, 1981. **7**(3): p. 155-184.
41. Vaja, I. and A. Gambarotta, *Internal combustion engine (ICE) bottoming with organic Rankine cycles (ORCs).* Energy, 2010. **35**(2): p. 1084-1093.
42. Paanu, T., S. Niemi, and P. Rantanen. *Waste Heat Recovery–Bottoming Cycle Alternatives*. in *Proceedings of the University of Vaasa, Reports*. 2012.
43. Chen, H., D.Y. Goswami, and E.K. Stefanakos, *A review of thermodynamic cycles and working fluids for the conversion of low-grade heat.* Renewable and Sustainable Energy Reviews, 2010. **14**(9): p. 3059-3067.
44. Yang, K. and H. Zhang, *Performance Analysis of the Organic Rankine Cycle (ORC) System under Engine Various Operating Conditions.* Journal of Clean Energy Technologies, 2015. **3**(5).
45. Hountalas, D., et al., *Study of available exhaust gas heat recovery technologies for HD diesel engine applications.* International Journal of Alternative Propulsion, 2007. **1**(2): p. 228-249.
46. Ringler, J., et al., *Rankine cycle for waste heat recovery of IC engines*. 2009, *SAE International Journal of Engines*, 2(1), p. 67-76..
47. Korobitsyn, M., *Industrial applications of the air bottoming cycle.* Energy Conversion and Management, 2002. **43**(9): p. 1311-1322.
48. Czaja, D., T. Chmielniak, and S. Lepszy, *The selection of gas turbine air bottoming cycle for polish compressor stations.* Journal of Power Technologies, 2013. **93**(2): p. 67--77.

49. Romanov, V.V., et al. *Performances and application perspectives of air heat recovery turbine units*. in *ASME Turbo Expo 2010: Power for Land, Sea, and Air*. 2010. American Society of Mechanical Engineers.
50. Ismail, Y., et al., *Potential of Exhaust Heat Recovery by Turbocompounding*. No. 2012-01-1603. 2012, SAE Technical Paper.
51. Thompson, I., S. Spence, and C. McCartan. *A Review of Turbocompounding and the Current State of the Art*. in *3rd International Conference on Sustainable Energy and Environmental Protection, Dublin, Ireland, Aug*. 2009.
52. Hiereth, H. and P. Prenninger, *Charging the internal combustion engine*. 2007: Springer Science & Business Media.
53. Aghaali, H. and H.-E. Ångström, *A review of turbocompounding as a waste heat recovery system for internal combustion engines.* Renewable and Sustainable Energy Reviews, 2015. **49**: p. 813-824.
54. Wallace, F. and G. Winkler, *Very High Output Diesel Engines-A Critical Comparison of Two Stage Turbocharged, Hyperbar, and Differential Compound Engines*. No. 770756. 1977, SAE Technical Paper.
55. Varnier, O.N., *Trends and limits of two-stage boosting systems for automotive diesel engines*. 2012, Universidad politecnica de Valencia.
56. Vuk, C.T., *Electric turbo-compounding: a technology whose time has come.* Proceeding of DEER, 2005: p. 21-25.
57. Frost, T., A. Anderson, and B. Agnew, *A hybrid gas turbine cycle (Brayton/Ericsson): an alternative to conventional combined gas and steam turbine power plant.* Proceedings of the Institution of Mechanical Engineers, Part A: Journal of Power and Energy, 1997. **211**(2): p. 121-131.
58. Zheng, J., et al., *Exergy analysis for a Braysson cycle.* Exergy, an International journal, 2001. **1**(1): p. 41-45.
59. Tyagi, S.K., Y. Zhou, and J. Chen, *Optimum criteria on the performance of an irreversible Braysson heat engine based on the new thermoeconomic approach.* Entropy, 2004. **6**(2): p. 244-256.
60. Zheng, J., et al., *Powers and efficiency performance of an endoreversible Braysson cycle.* International journal of thermal sciences, 2002. **41**(2): p. 201-205.
61. Zheng, T., et al., *Power, power density and efficiency optimization of an endoreversible Braysson cycle.* Exergy, an International Journal, 2002. **2**(4): p. 380-386.
62. Zhou, Y., S. Tyagi, and J. Chen, *Performance analysis and optimum criteria of an irreversible Braysson heat engine.* International journal of thermal sciences, 2004. **43**(11): p. 1101-1106.
63. Agnew, B., et al., *Simulation of combined Brayton and inverse Brayton cycles.* Applied thermal engineering, 2003. **23**(8): p. 953-963.
64. Kohler, C., *Verfahren zum Betriebe von Verbrennungsturbinen mit mehreren Druckstufen*. 1919.
65. Hingst, R.D.-I., *Verfahren zur Energieerzeugung aus Gasen und Gasdampfgemischen niederen Druckes, z. B. Abgasen von Brennkraftmaschinen*. 1944.
66. Hodge, J., *Cycles and performance estimation*. 1955, London, England: Butterworths Scientific Publications.

67. Wilson, D. and N. Dunteman. *The inverted brayton cycle for waste-heat utilization*. in *ASME 1973 International Gas Turbine Conference and Products Show*. 1973. American Society of Mechanical Engineers.
68. Holmes, R.T., *An inverted Brayton cycle application to naval marine gas turbines*. 1976, Doctoral dissertation.
69. Tsujikawa, Y., et al. *Conceptual recovery of exhaust heat from a conventional gas turbine by an inter-cooled inverted Brayton cycle*. in *ASME 1999 International Gas Turbine and Aeroengine Congress and Exhibition*. 1999. American Society of Mechanical Engineers.
70. Kaneko, K.i., et al., *Utilization of the cryogenic exergy of LNG by a mirror gas-turbine.* applied Energy, 2004. **79**(4): p. 355-369.
71. Tsujikawa, Y., K.-I. Kaneko, and J. Suzuki, *Proposal of the atmospheric pressure turbine (apt) and high temperature fuel cell hybrid system.* JSME International Journal Series B Fluids and Thermal Engineering, 2004. **47**(2): p. 256-260.
72. Bianchi, M., G.N. di Montenegro, and A. Peretto. *Inverted Brayton Cycle employment for low temperature cogenerative applications*. in *ASME Turbo Expo 2000: Power for Land, Sea, and Air*. 2000. American Society of Mechanical Engineers.
73. Bianchi, M., et al. *A feasibility study of inverted Brayton cycle for gas turbine repowering*. in *ASME Turbo Expo 2003, collocated with the 2003 International Joint Power Generation Conference*. 2003. American Society of Mechanical Engineers.
74. Alabdoadaim, M., B. Agnew, and I. Potts, *Examination of the performance of an unconventional combination of Rankine, Brayton, and inverse Brayton cycles.* Proceedings of the Institution of Mechanical Engineers, Part A: Journal of Power and Energy, 2006. **220**(4): p. 305-313.
75. Alabdoadaim, M., B. Agnew, and A. Alaktiwi, *Examination of the performance envelope of combined Rankine, Brayton and two parallel inverse Brayton cycles.* Proceedings of the Institution of Mechanical Engineers, Part A: Journal of Power and Energy, 2004. **218**(6): p. 377-385.
76. Alabdoadaim, M., B. Agnew, and I. Potts, *Performance analysis of combined Brayton and inverse Brayton cycles and developed configurations.* Applied thermal engineering, 2006. **26**(14-15): p. 1448-1454.
77. Henke, M., T. Monz, and M. Aigner, *Inverted Brayton Cycle With Exhaust Gas Recirculation—A Numerical Investigation.* Journal of Engineering for Gas Turbines and Power, 2013. **135**(9): p. 091203.
78. Head, A.J. and W. Visser. *Scaling 3-36kW Microturbines*. in *ASME Turbo Expo 2012: Turbine Technical Conference and Exposition*. 2012. American Society of Mechanical Engineers.
79. Tanaka, K., et al. *The development of 50kw output power atmospheric pressure turbine (apt)*. in *ASME Turbo Expo 2007: Power for Land, Sea, and Air*. 2007. American Society of Mechanical Engineers.
80. Wan, K., et al., *Performance of humid air turbine with exhaust gas expanded to below ambient pressure based on microturbine.* Energy Conversion and Management, 2010. **51**(11): p. 2127-2133.

81. Fujii, S., et al., *Mirror gas turbines: A newly proposed method of exhaust heat recovery.* Journal of engineering for gas turbines and power, 2001. **123**(3): p. 481-486.
82. Agelidou, E., et al. *Experimental Investigation of an Inverted Brayton Cycle Micro Gas Turbine for CHP Application*. in *ASME Turbo Expo 2017: Turbomachinery Technical Conference and Exposition*. 2017. American Society of Mechanical Engineers.
83. Bailey, M.M., *Comparative evaluation of three alternative power cycles for waste heat recovery from the exhaust of adiabatic diesel engines - DOE/NASA/50194-43 - NASA-TM-86953*. 1985, National Aeronautics and Space Administration, Cleveland, OH (USA). Lewis Research Center.
84. Zhang, M. and A.W. Rizzi, *Assessment of Inverse and Direct Methods for Airfoil and Wing Design*, in *Simulation-Driven Modeling and Optimization*. 2016, Springer. p. 75-109.
85. Wang, D. and L. He, *Adjoint aerodynamic design optimization for blades in multistage turbomachines—part i: Methodology and verification.* Journal of Turbomachinery, 2010. **132**(2): p. 021011.
86. Srinivasan, K., V. Balamurugan, and S. Jayanti, *Shape optimization of flow split ducting elements using an improved Box complex method.* Engineering Optimization, 2017. **49**(2): p. 199-215.
87. Dababneh, O., T. Kipouros, and J.F. Whidborne, *Application of an Efficient Gradient-Based Optimization Strategy for Aircraft Wing Structures.* Aerospace, 2018. **5**(1): p. 3.
88. Venter, G., *Review of optimization techniques.* Encyclopedia of aerospace engineering, 2010.
89. Marta, A.C., et al. *Development of adjoint solvers for engineering gradient-based turbomachinery design applications*. in *ASME Turbo Expo 2009: Power for Land, Sea, and Air*. 2009. American Society of Mechanical Engineers.
90. Papadimitriou, D. and K. Giannakoglou, *Total pressure loss minimization in turbomachinery cascades using a new continuous adjoint formulation.* Proceedings of the Institution of Mechanical Engineers, Part A: Journal of Power and Energy, 2007. **221**(6): p. 865-872.
91. Campobasso, M.S., M.C. Duta, and M.B. Giles, *Adjoint calculation of sensitivities of turbomachinery objective functions.* Journal of propulsion and power, 2003. **19**(4): p. 693-703.
92. Walther, B. and S. Nadarajah, *Optimum shape design for multirow turbomachinery configurations using a discrete adjoint approach and an efficient radial basis function deformation scheme for complex multiblock grids.* Journal of Turbomachinery, 2015. **137**(8): p. 081006.
93. Shahpar, S. and S. Caloni, *Adjoint optimisation of a high-pressure turbine stage for a lean-burn combustion system.* Proceeding of 10th ETC, Lappeenranta, Finland, 2013.
94. Wang, D., et al., *Adjoint Aerodynamic Design Optimization for Blades in Multistage Turbomachines—Part II: Validation and Application.* Journal of Turbomachinery, 2010. **132**(2): p. 021012.
95. Becker, G., M. Schäfer, and A. Jameson. *An advanced NURBS fitting procedure for post-processing of grid-based shape optimizations*. in

49th AIAA Aerospace Sciences Meeting including the New Horizons Forum and Aerospace Exposition. 2011.
96. Mueller, L. and T. Verstraete, *CAD Integrated Multipoint Adjoint-Based Optimization of a Turbocharger Radial Turbine.* International Journal of Turbomachinery, Propulsion and Power, 2017. **2**(3): p. 14.
97. Rezazadeh, H. and A. Khiali-Miab, *A two-layer genetic algorithm for the design of reliable cellular manufacturing systems.* International Journal of Industrial Engineering Computations, 2017. **8**(3): p. 315-332.
98. Marco, N., J.-A. Désidéri, and S. Lanteri, *Multi-objective optimization in CFD by genetic algorithms.* 1999.
99. Rao, S.S., *Engineering optimization: theory and practice*. 2009: John Wiley & Sons.
100. Benini, E., *Optimal Navier–Stokes design of compressor impellers using evolutionary computation.* International Journal of Computational Fluid Dynamics, 2003. **17**(5): p. 357-369.
101. Hehn, A., et al., *Aerodynamic Optimization of a Transonic Centrifugal Compressor by Using Arbitrary Blade Surfaces.* Journal of Turbomachinery, 2018. **140**(5): p. 051011.
102. IBARAKI, S., I. TOMITA, and K. SUGIMOTO, *Aerodynamic Design Optimization of Centrifugal Compressor Impeller Based on Genetic Algorithm and Artificial Neural Network.* Mitsubishi Heavy Industries Technical Review, 2015. **52**(1): p. 77.
103. Van den Braembussche, R.A., *Numerical optimization for advanced turbomachinery design*, in *Optimization and computational fluid dynamics*. 2008, Springer. p. 147-189.
104. Kim, J., et al., *Multi-objective optimization of a centrifugal compressor impeller through evolutionary algorithms.* Proceedings of the Institution of Mechanical Engineers, Part A: Journal of Power and Energy, 2010. **224**(5): p. 711-721.
105. Mamur, H. and R. AHISKA, *A review: Thermoelectric generators in renewable energy.* International Journal of Renewable Energy Research (IJRER), 2014. **4**(1): p. 128-136.
106. Bejan, A., *Theory of heat transfer-irreversible power plants.* International Journal of Heat and mass transfer, 1988. **31**(6): p. 1211-1219.
107. Huleihil, M., *Effects of pressure drops on the performance characteristics of air standard Otto cycle.* Physics Research International, 2011.
108. Ge, Y., L. Chen, and F. Sun, *Finite-time thermodynamic modelling and analysis of an irreversible Otto-cycle.* Applied Energy, 2008. **85**(7): p. 618-624.
109. Mock, P., et al., *The WLTP: How a new test procedure for cars will affect fuel consumption values in the EU.* International Council on Clean Transportation, 2014. **9**: p. 35-47.
110. Copeland, C.D. and Z. Chen, *The benefits of an inverted Brayton bottoming cycle as an alternative to turbocompounding.* Journal of Engineering for Gas Turbines and Power, 2016. **138**(7): p. 071701.
111. Chen, Z., et al., *Modeling and simulation of an inverted Brayton cycle as an exhaust-gas heat-recovery system.* Journal of Engineering for Gas Turbines and Power, 2017. **139**(8): p. 081701.

112. Cengel, Y.A. and M.A. Boles, *Thermodynamics: an engineering approach.* Sea, 2002: p. 358.
113. Wu, H., et al., *Mean Value Engine Modeling for a Diesel Engine with GT-Power 1D Detail Model*. No. 2011-01-1294. 2011, SAE Technical Paper.
114. Chen, Z. and C.D. Copeland, *Inverted Brayton cycle employment for a highly downsized turbocharged gasoline engine*. No. 2015-01-1973. 2015, SAE Technical Paper.
115. Copeland, C.D. and Z. Chen. *The Benefits of an Exhaust-gas Heat-recovery Unit - The Inverted Brayton Cycle*. in *Proceedings of the 2nd Conference on Engine Processes*. 2015. Berlin: Universitätsverlag der TU Berlin.
116. Inc., G.T. *Flow Theory Manual 7.4*. 2013; Available from: http://www.gtisoft.com.
117. Hu, B., et al., *1-D Simulation Study of Divided Exhaust Period for a Highly Downsized Turbocharged SI Engine-Scavenge Valve Optimization*. 2014, SAE International Journal of Engines, 7(3), 1443-1452..
118. Swain, D., *Impact of impeller blade trimming on the performance of centrifugal compressors*. 2014: Michigan State University.
119. Wendt, J.F., *Computational fluid dynamics: an introduction*. 2008: Springer Science & Business Media.
120. Ferziger, J.H. and M. Peric, *Computational methods for fluid dynamics*. 2012: Springer Science & Business Media.
121. Menter, F.R., *Two-equation eddy-viscosity turbulence models for engineering applications.* AIAA journal, 1994. **32**(8): p. 1598-1605.
122. Wilcox, D.C., *Reassessment of the scale-determining equation for advanced turbulence models.* AIAA journal, 1988. **26**(11): p. 1299-1310.
123. Blazek, J., *Computational fluid dynamics: principles and applications*. 2015: Butterworth-Heinemann.
124. Menter, F.R., M. Kuntz, and R. Langtry, *Ten years of industrial experience with the SST turbulence model.* Turbulence, heat and mass transfer, 2003. **4**(1): p. 625-632.
125. Anton, N., et al. *On the choice of turbine type for a twin-turbine heavy-duty turbocharger concept*. in *ASME Turbo Expo 2018: Turbomachinery Technical Conference and Exposition*. 2018. American Society of Mechanical Engineers.
126. Diaz-Gomez, P.A. and D.F. Hougen. *Initial Population for Genetic Algorithms: A Metric Approach*. in *GEM*. 2007.
127. Grefenstette, J.J., *Optimization of control parameters for genetic algorithms.* IEEE Transactions on systems, man, and cybernetics, 1986. **16**(1): p. 122-128.
128. Lipowski, A. and D. Lipowska, *Roulette-wheel selection via stochastic acceptance.* Physica A: Statistical Mechanics and its Applications, 2012. **391**(6): p. 2193-2196.
129. Baker, J.E. *Adaptive selection methods for genetic algorithms*. in *Proceedings of an International Conference on Genetic Algorithms and their applications*. 1985. Hillsdale, New Jersey.
130. Noraini, M.R. and J. Geraghty, *Genetic algorithm performance with different selection strategies in solving TSP.* 2011.

131. Gen, M. and R. Cheng, *Foundations of genetic algorithms.* Genetic Algorithms and Engineering Design, 1997: p. 1-41.
132. Correia, D.S., et al., *Comparison between genetic algorithms and response surface methodology in GMAW welding optimization.* Journal of materials processing technology, 2005. **160**(1): p. 70-76.
133. Tüchler, S., Z. Chen, and C.D. Copeland, *Multipoint shape optimisation of an automotive radial compressor using a coupled computational fluid dynamics and genetic algorithm approach.* Energy, 2018. **165**: p. 543-561.
134. Kennedy, I., et al., *Experimental Investigation of an Inverted Brayton Cycle for Exhaust Gas Energy Recovery.* Journal of Engineering for Gas Turbines and Power, 2019. **141**(3): p. 032301.
135. *Supercharger Testing Standard*, in *SAE International Surface Vehicle Standard*. 1995, SAE Standard J1723.
136. Code, A.P.T., *Performance Test Code on Compressors and Exhausters.* American Society of Mechanical Engineers, New York, 1997.
137. *Turbocharger Gas Stand Test Code,* in *SAE International Surface Vehicle Standard*. 1995, SAE Standard J1826.